LES of Pulsatile Flow in the Models of Arterial Stenosis and Aneurysm

Md. Mamun Molla

LES of Pulsatile Flow in the Models of Arterial Stenosis and Aneurysm

A Thesis Submitted for the Degree
of

Doctor of Philosophy

in the
Faculty of Engineering
of the
University of Glasgow

By

Md. Mamun Molla
BSc., MSc. & MPhil.

Department of Mechanical Engineering
University of Glasgow
Glasgow, UK

May 2009

This work is dedicated to
my parents.

Declaration

This dissertation is the result of my own work. No part of this dissertation has already been, or is being concurrently submitted for any other degree, diploma or qualification.

.....
Md. Mamun Molla
07 May, 2009

Abstract

The Large Eddy Simulation (LES) technique is used to simulate the different types of Newtonian and non-Newtonian pulsatile blood flow in a constricted as well as in a dilated channel to gain insight of the transition-to-turbulent blood flow due to the arterial stenosis and aneurysm. In the stenosed model, a cosine shape stenosis is placed at the upper wall of a 3D channel which reduces the cross-sectional area, whereas the aneurysm which is also placed at the upper wall dilates the channel cross-sectional area. In LES, a top-hat spatial $grid$-filter is applied to the Navier-Stokes equations of motion to separate the large scale flows, which carry the majority of the energy, from the small scale known as sub-grid scale (SGS).The large scale flows are resolved fully while the unresolved SGS motions are modelled using two different dynamic models to determine the Smagorinsky constant, C_s, at each time step.

Initially, an additive sinusoidal pulsatile velocity profile is used at the inlet of the model stenosis to generate the unsteady oscillating flow and a comparison is made between the results obtained by the additive and non-additive pulsation. Secondly, the physiological pulsatile flow in the same model stenosis is investigated, where the physiological pulsation is generated at the inlet using the first four harmonics of the Fourier series of pressure pulse. A comparison between the LES and the coarse Direct Numerical Simulation (DNS) results is drawn and the effects of the various harmonics of pressure pulse, length and percentage of the stenosis on the flow field are examined. Transition-to-turbulent physiological flow through the model of a double stenosis and an aneurysm is also investigated. Finally, the physiological pulsatile flow in a model of single stenosis is investigated using the various non-Newtonian blood viscosity models and the results are compared with the Newtonian model.

For the additive sinusoidal pulsation case the maximum ratio of the SGS to molecular viscosity is 0.709 and for the non-additive case is 0.78 while $Re = 2000$. The shape of the post-stenotic re-circulation region is totally different between the additive and non-additive case. In the additive case the upper wall pressure drop is larger than the non-additive case. Due to the large amplitude of the oscillation, transition happens earlier and the peak turbulent kinetic energy occurs at the post-lip of the stenosis. The intensity of the turbulent kinetic energy is higher in the additive sinusoidal pulsation case than the physiological pulsation.

The maximum contribution of the SGS motion to the large -scale motion is 37.4% for the first harmonic physiological pulsation while 97% contribution from the first four harmonics case for $Re = 2000$. The centreline turbulent kinetic energy is slightly higher in the first harmonic case than the first four harmonics. For the

higher area reduction of the stenosis, the stress drop at the upper wall, the maximum shear stress at the lower wall and the turbulent kinetic energy increased. The intensity of the shear stress and the turbulent kinetic energy decreased when the length of the stenosis is increased. The break frequency of the energy spectra found from $-5/3$ to $-10/3$ for the velocity fluctuations and from $-5/3$ to $-7/3$ for the pressure fluctuations.

Due to the presence of the second stenosis, the stress drop, the adverse pressure gradient and the turbulent intensity of the flow enhance significantly. Inside the aneurysm a large re-circulation region exists and the flow is turbulent for a asymmetric aneurysm and maximum turbulent intensity occurs between the centre and the ending segment of the aneurysm. Owing to the effects of the non-Newtonian viscosity, the length of the post-stenotic re-circulation region increased as well as the streamwise velocity and the turbulent kinetic energy decreased.

Acknowledgements

Above all, I would like to express my gratitude to almighty Allah who has helped me accomplish this dissertation. I wish to express my sincere thanks to my supervisor, Dr Manosh Paul, for his invaluable help and steadfast support throughout the period of this research. I am also thankful to him for his wise criticisms and suggestions in preparing and improving of this dissertation. I am also thankful to Dr Donald Ballance for his agreement to become a pastoral supervisor and his help in different ways during my study.

For the financial support of this study, I thank the ORSAS committee and the Faculty of Engineering of the University of Glasgow. I would be happy to thank the Department of Mechanical Engineering, University of Glasgow for the financial support to attend the *British Applied Mathematics Colloquium (BAMC 2006)*, Keele University, UK and the *European Congress Society of Biomechanics (ESB 2008)*, Lucerne, Switzerland. I would like to thank the European Union for awarding a scholarship to attend the *EUROMEC Fluid Mechanics Conference (EFMC 2008)*, Manchester, UK. I am also very much grateful to the Head of the department Dr Donald Ballance for giving me some financial support during my writing up stage.

I would like to thank our IT administrators Mr Kenneth Stevenson (former) and Mr Walter Robinson for their effort to keep the system always running and their support to any problem in the computer systems.

I would like to thank Dr Giles Roditi, Consultant Radiologist, Glasgow Royal Infirmary, for helpful discussions on the various clinical aspects of the results.

I am delighted to acknowledge the support I have received from all my colleagues in this department. This work could not have been completed in such a peaceful way without their support. I also like to thank all my friends for their encouragements during this research. Specially, many thanks to Sreebash da, with whom I shared my office room and learnt many things from him, and Suvash in Australia, Abdul Hye for their help on both scientific and non-scientific matters.

I am grateful to my beloved parents, wife, brothers, and sisters, whose love is more than I can desire. I am also grateful to all of my well-wishers for their inspiration that leads me to go ahead.

Contents

List of Figures

List of Tables

List of Symbols

Roman Symbols

A	amplitude of the physiological oscillation, m
C_s	Smagorinsky model constant
$E_{\alpha\alpha}$	energy spectra
$\bar{f}$	generic filtered variable
f_b	break frequency, Hz
f_s	vortex shedding frequency, Hz
G	grid filter function
k_c	cut-off wave number, m^{-1}
L	height of the channel, m
L_{ij}	Leonard stress
N	number of time cycle
NH	number of harmonics
N_t	total number of time steps
N_{xyz}	number of grid nodes
p	pressure, N/m^2
Re	Reynolds number
Re_T	turbulent Reynolds number
S_{ij}	strain rate tensor
Sr	Strouhal number
t	time, s
T	Time period
T_{ij}	subtest scale stresses
u_i or u, v, w	velocity components in Cartesian coordinate, m/s
$\bar{V}_{max}$	bulk velocity depends on the flow Reynolds number, m/s
r	position vector, (x, y, z), m
x_i or x, y, z	Cartesian coordinate directions

Greek Symbols

δ_{ij}	kronecker delta
$\Delta x, \Delta y, \Delta z$	mesh spacing in the x, y, z directions
Δ	filter width
δt	numerical time step
μ	molecular viscosity of fluid, $Pa.s$
μ_{sgs}	sub-grid scale eddy viscosity
ν	kinetic viscosity of fluid, m^2/s
ν_{sgs}	sub-grid scale kinetic eddy viscosity, m^2/s
ρ	fluid density, kg/m^3
τ_{ij}	subgrid scale stresses
τ_{xy}	wall shear stress, N/m^2
ϕ	phase angle
ω	frequency of the unsteady flow, Hz
ω_z	vorticity
∇	divergence
σ	Kolmogorov velocity scale
ϵ	dissipation rate

Superscripts

$''$, etc.	turbulent fluctuations

Mathematical Accents

$\bar{.}$	grid filtering
$\tilde{.}$	test filtering
$< . >$	time averaging
$<< . >>$	phase averaging
$< . >_s$	spanwise averaging
$\|.\|$	magnitude
$\|\|.\|\|$	norm of residuals

Chapter 1

Introduction

Arterial stenosis is commonly found in the arteries of patients who have vascular disease. The term arterial stenosis refers to narrowing of an artery where the cross-sectional area of a blood vessel reduces. The most common cause is atherosclerosis where cholesterol and other lipids are deposited beneath the intima (inner lining) of the arterial wall. As the amount of this fatty material increases there is an accompanying proliferation of connective tissue and the whole forms a thickened area in the vessel wall called plaque. The vessel wall remodels to accommodate this to varying degrees but with marked plaque deposition then this will reduce the effective cross-section of the vessel and retard blood flow. When the reduction in vessel calibre is severe the result is that the blood flow transits to turbulent with a pressure drop across the stenotic region. The alteration in flow dynamics in turn produces abnormal wall shear stress both at the plaque and at the post stenotic area such that the plaque may fissure and rupture exposing the lipid plaque core to the blood stream with potential for thrombosis (blood clotting) at the site of rupture. This development of atherothrombosis may dangerously acutely occlude the vessel with, in critical territories such as the coronary arteries and cerebral vessels, potentially catastrophic results. Non-occlusive atherotrhombosis is also clinically important as the thrombotic material deposited is often unstable and a source of distal embolism, this is particularly important in the extracranial carotid arteries as a source of stroke (Ku and McCord [7], Wootton and Ku [8], Ku [9], Nichols and O'Rourke [10]).

When a stenosis in a coronary artery prevents the blood flow, it causes heart attack. Once the surface of the stenosis is damaged, there might be blood clot, which may choke blood flow in a cerebral artery or in a coronary artery. Moreover, blood may stagnate in post-stenosis, which again makes blood clot and that may be transferred to the lung (Wootton and Ku [8]). Interestingly, these are the sites

of low wall shear stress that are prone to lipid accumulations and hence plaque formations. These are thought to be through stimulating as atherogenic phenotype in the cells of the endothelium or vessels lining, Malek *et al* . [11]. Furthermore it is the pulsatile nature of the flow and the oscillating shear index that is increasingly being recognised as the important factor in this process as has been shown in 4D MRI (magnetic resonance imaging) experiments, Frydrychowicz *et al* . [12].

The blood flow through arteries is inherently unsteady and pulsatile due to the cyclic nature of heart pump, which may either be laminar or transition to turbulent. The pulsations of the flow have a significant effect on the transition to turbulence as they usually generate abnormal circulations in the flow, and the development of transition to turbulent in the arteries has clinical interest as mentioned above.

The typical Reynolds number range of blood flow in human artery varies between 1 and 4000 (Ku [9]) and the blood flow is usually pulsatile laminar in the absence of any obstruction in artery. However, the presence of a moderate or severe stenosis in the artery the laminar flow becomes transitional to turbulent at the downstream region of the stenosis. Therefore, it is very important to know accurately how the blood flows in the stenosis, since the fluid dynamics of post stenotic blood flow plays an important role in diagnosis of arterial diseases. For example, the quantification of arterial stenosis by both duplex ultrasound and quantitative flow MRI techniques relies on the measurements of the flow velocity/acceleration at/beyond the stenotic segment to infer the degree of underlying stenosis (Frydrychowicz *et al* . [12]).

Another abnormal condition of the artery is a balloon-like dilation which is known as aneurysm. Hemodynamic factors such as velocity, pressure and shear stress play an important role in the progression and rupture of aneurysm. Aneurysm may burst under the influence of internal pressure and cause severe pathological disorder, even death (Kumar and Naidu [13]). Aneurysm is a sudden expansion of the artery which produces a large cavity in which blood can re-circulate. As a result the blood flow changes from laminar to turbulent flow.

Moreover, the re-circulated blood in aneurysm increases the shear stress which is potentially dangerous for the blood cells and blood vessels. Aneurysm also causes additional risks of blood clotting and rupture of artery that leads to fast heart beating which results in death (Lasheras [14]).

Chapter 2

Review of Previous Studies

A general review of the previous studies relevant to this thesis has been made. Detailed reviews of the experimental and computational works on arterial stenosis are presented in § 2.1 and § 2.2 respectively. A brief review of the studies of arterial aneurysm is given in § 2.3 and the previous studies related to the non-Newtonian blood flow in the arteries are reviewed in § 2.4. The objectives and outline of the thesis are given at the end of this chapter.

2.1 Experimental Studies on Stenosis

From the literature review, it is found that numerous experimental studies of the steady and pulsatile turbulent flow in model arterial stenosis or constricted tube have been carried out to diagnose the post stenotic turbulent flow and to study its impact on the blood cells and inner side of blood vessels. Some of these studies focused on the investigation of the post-stenotic flow physics including studying the effects of the various shapes and percentage of the stenosis on the flow downstream of the stenosis, while some are on the investigation of the effects of the shear stress and turbulence on blood and arterial walls at the downstream region of the stenosis.

2.1.1 Post-stenosis flow physics

Clark [15; 16] studied the fluid mechanics of the nozzle type stenosis using both steady and pulsatile flow and found highly disturbed flow after the stenosis. They also reported that the disturbances of velocity depend on the flow Reynolds number. On the other hand, Cassanova and Giddens [17] concentrated on two aspects of the fluid dynamics of post stenotic flows; the characterisation of flow disorder

over a transitional Reynolds number ranging from 318 to 2540 and a pulsatile flow frequency parameter $\alpha = 15$ with emphasis upon mild and moderate degrees of stenosis and the relationship of steady and pulsatile flow through such constrictions. They concluded that the more abrupt and sharp edged stenoses create a much greater flow disturbance at a given Reynolds number than the smoothly contoured configuration. For the steady flow the visualisation studies and measurements also indicate that if the stenosis is smoothly contoured, a degree of stenosis of 50% is required to cause substantial disturbances at the Reynolds number studied. However, for the pulsatile flow, the disturbances are generated with a mild 25% stenosis. So, it is clear from this investigation that the transition in the post-stenosis is strongly dependent on the flow pulsatility. A similar result was reported by Young and Tsai [18] who investigated unsteady flow through the stenosis. They reported that the critical Reynolds number of about 1000 for the unsteady or pulsatile flow in the axisymmetric model of the stenosis is lower than the steady case of Young and Tsai [18]. That means the transition for unsteady case has happened for relatively small Reynolds number. In their steady paper [18], they also found that the pressure losses in the non-symmetric models were considerably higher than the losses in the corresponding axisymmetric models.

Following the above mentioned investigations Yongchareon and Young [19] studied the development of turbulence for both the steady and pulsatile flow through the model of arterial stenoses. Their findings are summarised in four points below: (i) the critical Reynolds number for the development of turbulence in pulsatile flow through the stenosis not only depends on the shape and size of the stenosis but also on the nature of the inlet-flow waveform, which is a similar result reported by Young and Tsai [18; 20]; (ii) the turbulence developed at a Reynolds number below the critical value for an unobstructed tube; (iii) the critical Reynolds number is reduced as the stenosis shape becomes more abrupt and the inlet flow frequency increases; and finally (iv) the axial location (critical length), at which turbulence was first observed, is a function of both the stenosis shape and the frequency parameter. Moreover, the critical length tends to decrease as the frequency parameter increases, and the location of the most intense turbulent fluctuations moves upstream when the Reynolds number increases.

The evolution of post-stenotic flow disturbances was studied by Khalifa and

Giddens [21; 22] using a laser Doppler anemometer (LDA) for the measurement of the velocity along the centreline of Plexiglas (Perspex, PMMA) tube. The pulsatile frequency parameter and the peak Reynolds number were chosen typical of a dog aorta and the disturbance velocities were characterised at various stages in the cycle and for the degrees of stenosis ranging from zero to severe. They demonstrated three types of flow disturbances: (i) a coherent structure associated with the initiation of each flow cycle; (ii) a periodic disturbance arises from the shear layer distal to the constriction; and (iii) a non-stationary turbulence created after the stenosis. A similar type of investigation was done by D'Luna *et al* . [23] using a pulsed directional Doppler system together with high resolution temporal auto regression spectral analysis for detecting the vortex shedding and coherent eddies.

Ahmed and Giddens [1; 24] investigated the flow disturbances through the axisymmetric stenosis of rigid tube using laser Doppler anemometry and a flow visualisation technique where Reynolds numbers in the range from 500 to 2000 were chosen but the upstream flow conditions were steady. They found that the flow field is transitional to turbulent when $Re \geq 1000$ and the maximum centreline velocity occurs at the centre of the 50% stenosis. They also reported that the length of the re-circulation zone or the reattachment point is shorter at $Re = 2000$ than that of $Re = 1000$. This result strongly coincides with the result of Back and Roschke's [25] who identified three distinct regimes of flow reattachment after the stenosis. At the low Reynolds number, their (Back and Roschke's [25]) results show that the reattachment point which was governed by the growth of the laminar shear layer moved downstream with increasing the flow rate, i.e. in the second regime the reattachment point moved back towards the stenosis as the instabilities developed in this shear layer. Finally, in the third regime, for relatively high Reynolds number, the shear layer was highly disturbed and the reattachment point was near the stenosis.

Later on, Ahmed and Giddens [26] studied the post stenotic flow behaviour using sinusoidal pulsatile inflow conditions with the frequency parameter, $\alpha \leq 15$. They concluded that even a mild stenosis can lead to the transition to turbulent flow at the post stenotic region under the pulsatile inflow condition. A similar conclusion was made by Cassanova and Giddens [17]. Fourteen years later, Ahmed [27] re-investigated the pulsatile flow through a smooth constriction using a two-component

laser Doppler velocimetry (LDV) technique. The results presented in the paper for the post-stenotic turbulent flow physics are similar to those in Yongchareon and Young [19].

2.1.2 Pathological Impacts

Both the wall pressure and shear stress play an important role damaging and weaken the internal wall of the artery at the post-stenotic turbulent region. For example, due to the high shear stress the materials of the blood cells could be damaged and the qualitative interpretation of cardiovascular sounds and murmurs which are generated by turbulence in flowing blood is a main diagnostic tool in the clinical practice for diagnosing the cardiovascular diseases. Due to this, many researchers in their investigations are interested in getting a better understanding of sound generation, murmur characteristics, and transmission of energy of turbulence.

Burns [28] found that the bulk of acoustic energy in murmurs is caused due to nearly periodic fluctuations in the wake of downstream of any appropriate obstacle. He suggested that in the physiological range of blood velocities a significant amount of localised acoustic energy might be generated. On the other hand, Yelling [29] investigated the hydraulic noise of a bounded jet in a model with an intrafluid which has less friction. He showed, using spectral analyses, that an insignificant amount of local turbulent pressure fluctuations were converted into sounds. A non-invasive diagnostic method (phonoangiography) was presented by Lees and Dewey [30] to determine the percentage of area reduction of a stenosis from the arterial sound produced by turbulence. They related the intensity of pressure fluctuations at the vessel wall to the arterial flow velocity as well as the arterial diameter, and these independent parameters yield information concerning the severity of stenosis.

In terms of the effects of shear stress, Fry [31] showed that the high shear stress associated with turbulence might be a strong factor causing some endothelial damage as a result of including a vascular stenosis. He also observed a critical level of wall shear stress of approximately $400 dynes/cm^2$ which is responsible for endothelial damages of the artery. On the other hand, Sutera and Mehrjardi [32] found that high shear stresses which occur in turbulent flow may result in damage to red blood cells. Moreover, Folts *et al* . [33] and Stein *et al* .[34] have suggested that high shear

stress might overstimulate platelet thrombosis which could accelerate atherosclerosis. Furthermore, Some researchers, Friedman *et al* . [35], Ku *et al* . [36] and Salam *et al* . [37], have found low shear stresses at the throat of the stenosis for which the intimal thickening might be stimulated causing remodelling of the stenosis. According to He and Ku [38] the most intimal thickening occurs where the average wall shear stress is less than $10 dynes/cm^2$.

2.1.3 Turbulence power spectra

Spectral analysis of turbulent flow quantities is an important technique to determine the feasibility of stenosis and also to understand the characteristics of turbulent fluctuations downstream of stenosis. Kim and Corocoran [39] observed turbulence spectra at the downstream of a stenosis using a hot-film anemometer technique. Their results show that the turbulence spectra are quite different from the sound spectra measured at the centre of the tube for the same flow rate and orifice diameter. But, as shown in Clark [40; 41], the energy spectrum for the velocity and pressure fluctuations follow the slope $-5/3$, which shows the existence of a turbulent inertia subrange region that is independent of the viscous effect. Although the spectrum from a pulsatile flow was very similar to the corresponding steady flow case, non-dimensional power spectra of the maximum value of turbulence wall pressure showed no dependence on the Reynolds number, but they were questionably dependent on nozzle area ratio and shape.

Lu *et al* . [42] investigated the intravascular pressure and velocity fluctuations in arterial stenosis using a laser Doppler anemometer system. Spectral analysis of the simultaneously measured pressure and flow fluctuations showed a region in which the slope of the flow energy sprectrum is $-5/3$. This then changes to $-10/3$ at the 'break' point at $f_b = 100 Hz$. However, in further study, Lu *et al* . [43] concluded that the peak frequencies in the pressure fluctuation spectra were expected to be different from those in the velocity fluctuations in most situations. Only in the region where noise is so strong that it dominates the flow field, is it possible for both spectra to have coincident characteristic frequencies. Results also show no existence of a universal spectrum of velocities within the section of nozzle and 9 diameters downstream. The spectra of u and v fluctuations found at the same point

are different, which means turbulence in such regions is non-isotropic.

A comprehensive study on the measurement of the scaling of wall pressure spectra the downstream of an axisymmetric stenosis was performed by Tobin and Cheng [44]. By using steady flow at inlet, three key observations were made by them. Firstly, the intensity of wall pressure fluctuations is highest in the region where the shear layers separate from the centre of the stenosis and re-attach to the wall downstream of the pipe. Thus, sounds associated with the wall pressure fluctuations is generated due to the shear layer, not the turbulence in the core flow. Secondly, they have identified a break or corner frequency, f_b, which corresponds to the intersection of the two lines parallel to the two major sloping portions of the recorded spectrum in the cases of no stenosis and with stenosis. Using this information, along with the diameter of the orifice and the jet velocity, they have evaluated a constant value for the Strouhal number, $Sr = \frac{f_b D}{u_j} \cong 0.578$ while the Reynolds numbers were between 1000 and 4000. Here D is the diameter of the tube, u_j is the mean jet velocity. Using this constant value they have prescribed a formula for the degree of stenosis as, $1 - \left(\frac{d}{D}\right)^2 = 1 - 0.578\left(\frac{f_b D}{U}\right)^{-1}$. Thus, under steady flow conditions, with a wall pressure spectrum at the position of maximum root mean square wall pressure and a knowledge of D and U, they were able to predict the degree of stenosis. Finally, they have compared the wall pressure spectrum with the same turbulent pipe flow spectrum used by Lees and Dewey [30] and found significant mismatch in the slope of the spectra beyond the corner frequency. Moreover, there is no evidence of a break frequency in the study of Giddens *et al* . [45] who measured instantaneous blood velocities distal to externally created stenoses in the stenotic aorta of dogs during open-chest surgery.

Jones and Fronk [46] studied the post-stenotic flows in an axisymmetric geometry with steady inflow for the range of Reynolds numbers from 600 to 1500 and prescribed $\frac{f_c D}{u_j} = Re^{0.72}(d/D)^{0.26}$ as an improved correlation for the break frequency in the pressure spectra. Using the continuity equation, $UD^2 = u_j d^2$, the above expression is represented as $\frac{f_c D}{u_j} = Re^{0.72}(d/D)^{1.74}$, which can be compared with the corresponding scaling of Lees and Dewey [30] and Tobin and Cheng [44]. From these discussions it is clear that all three scalings are quite different which indicates the need for further studies for understanding the flow physics and scaling of spectra at the post region of the stenosis.

2.2 Computational Studies on Stenosis

As discussed in the previous section, the fluid dynamics of post-stenotic blood flow plays a crucial role in the diagnosis of arterial disease. So, there is considerable interest in gaining better insight into the dynamics of post-stenotic flows from the pathological point of view. At present computational fluid dynamics (CFD) is one of the most popular tools for gaining accurate results and visualising the flow field properly. Relevant computational studies on steady and pulsatile flow through the model arterial stenosis are discussed below. First the studies which considered the laminar flow assumption will be reviewed, which will be followed by discussion of turbulent flow studies.

2.2.1 Laminar flow

In early 70s, Lee and Fung [47] and Deshpande *et al* . [48] performed 2D investigation on steady flow in arterial stenosis. In Lee and Fung [47] the constriction in the model artery was generated by a Gaussian normal distribution curve, whereas a cosine shape stenosis, which is similar to the biological type stenosis was used by Deshpande *et al* . [48] in their geometry. They found that the maximum wall pressure drop and vorticity occurred near the centre of the stenosis. But the choice of the Reynolds number in their studies was very low, for example, from zero to 25 in Lee and Fung [47] and from zero to 200 in Deshpande *et al* . [48].

Early studies of pulsatile laminar flow through the model arterial stenosis were investigated by Cheng *et al* . [49], Daly [50] and O'Brien and Ehrlich [51]. Cheng *et al* . [49] investigated pulsatile flow through a channel with square shape of stenosis, but in Daly [50] and O'Brien and Ehrlich [51] an axisymmetric cosine shape stenosis was considered. Daly [50] used physiological pulsatile flow at the inlet whereas a simple sinusoidal pulsatile flow was considered by Cheng *et al* . [49] and O'Brien and Ehrlich [51]. In their findings, Cheng *et al* . [49] and Daly [50] concluded that the pressure gradient and the shear stress drops are maximum at the throat of the stenosis. On the other hand, O'Brien and Ehrlich [51] found that at each timestep the peak wall vorticity occurred just prior to the centre of the stenosis and is proportional to the wall shear stress.

Recently, Cavalcanti [52] studied hemodynamics in the early stages of the atheroscle-

rosis or stenotic process using physiological realistic pulsatile inlet conditions where the percentage of stenosis was 2%. Even for the mild stenosis he showed that the flow velocity and the wall shear stress increase at the post-stenotic region. A comparative study of physiological and simple pulsatile laminar flows through an axisymmetric stenosed artery has recently been done by Zendehbudi and Moayeri [53]. Most recently, a simulation of laminar physiological pulsatile flow in a model axisymmetric stenosis has been performed by Marques *et al* . [54].

In regards to the three-dimensional study of laminar flow in stenosis, some recently published papers are cited here. Stroud *et al* . [55] investigated the influence of stenosis morphology on pulsatile laminar flow through stenotic vessels with Reynolds number ranging from 200 to 1200, while Melaaen [56] studied the steady flow in a constricted tube with $Re = 200$. Bertolotti and Deplano [57] analysed the steady flow pattern for a stenosed coronary bypass for a Reynolds number of 250. Dvinsky and Ojha [58] simulated the sinusoidal pulsatile laminar flow through an asymmetric stenosis. Very recently, Long *et al* . [59] investigated physiological pulsatile laminar flow through an axisymmetric arterial stenosis with a Reynolds number of 300. Dvinsky and Ojha [58] considered a cosine shape asymmetric stenosis, whereas in Long *et al* . [59] the shape of the stenosis was approximated by two integrated Gaussian functions at each of the proximal and distal ends together with a straight segment in between.

As seen, all the papers cited above are on the single stenosis. There are a few recent papers which looked into the flow in multiple stenoses but limited to laminar flow. Damodaran *et al* . [60] did a numerical study of laminar flow through tubes with multiple constrictions using curvilinear co-ordinates and finite volume approach, while the effects of the steady fluid flow through a double bell-shaped constriction in tube were numerically investigated by Lee [61] for Reynolds number ranging from 5 to 400. Lee [61] showed that the major part of the pressure drop in the constricted tube occurs due to the second constriction, and when the Reynolds number increases, the length of the re-circulation region increases between the regions of two constrictions. Huang *et al* . [62] used the Lattic-BGK method to investigate the steady flow through a tube with double stenoses while $Re = 150$. But they applied steady inlet velocity profiles which are inappropriate for representing blood flow and, as has already been mentioned in Chapter 1, the blood flow through

artery is pulsatile.

2.2.2 Turbulent flow

The aforementioned computational studies are restricted to laminar flow. But in the experimental studies it was well established that the post stenotic flow is transitional-to-turbulent. very few computational studies are available in the liturature on the transition-to-turbulent flow in the stenosis.

Axisymmetric 2D computational investigations of laminar to turbulent flow have been reported by Ghalichi *et al* . [63], Varghese and Frankel [64], Lee *et al* . [65; 66] and Li *et al* . [67] who used the Reynolds-Average Navier-Stokes (RANS) approach, particularly, the k-ω turbulence model. However, Scotti and Piomelli [68] clearly indicated that the commonly used RANS turbulent models have some limitations in modelling pulsatile flows where the inlet velocity profile/pressure gradient oscillates with time. These authors compared the performances of four different RANS models (one-equation Spalart-Allmaras [69], k-ϵ and k-ω^2 of Saffman and Wilcox [70], and k-ϵ-v^2 of Dublin [71]) in a channel flow driven by an oscillating pressure gradient with experiment, DNS and LES. They found that the RANS models gave good agreement for the velocity results, but the predictions were unsatisfactory for the key turbulent results such as Reynolds shear stresses (important results from a medical aspect), turbulent kinetic energy and dissipation rate. Moreover, these models are incapable of simulatingting instantaneous pulsatile turbulent flows as the governing equations of motion are time-averaged.

Some three-dimensional instabilities and transitional studies of simple pulsatile flow through stenosis have been studied by Mallinger and Drikakis [72; 73]. They found that the circumferential wall shear stress takes an oscillating form and the stress drop happens just after the centre of the stenosis. They also reported that the maximum longitudinal wall shear stress occurs just before the centre of the stenosis. Sherwin and Blackburn [74; 75] studied three-dimensional instabilities and transition to turbulent of steady and pulsatile axisymmetric stenotic flows in tube by Direct Numerical Simulation (DNS) based on the spectral method. For the pulsatile case they have taken a simple sinusoidal pulse with Reynolds number ranging from 250 to 800.

Very recently, Varghses *et al* [76; 77] have investigated steady and pulsatile flow in symmetric and eccentric stenoses using DNS and reported the results of the turbulence phenomena at the downstream of the eccentric stenosis for a relatively low Reynolds number of 300. They found that for such low Reynolds number is transitional to turbulent and the shear stress oscillates highley in the post stenotic region. But, DNS is computationally very costly for the typical large Reynolds numbers valid in the human arteries. So, in order to save the computational time and space, the technique of Large Eddy Simulation (LES) is applied in the thesis for modelling the transitional flow.

In DNS all the large and small scale eddies are resolved fully, whereas in LES only the large scale eddies, energy-containing scales of turbulence, are resolved while the smaller scale eddies, sub-grid scales (SGS), are modelled. DNS is suitable for low Reynolds number flow, while LES is for small to high Reynolds number flow and requires less time and mesh than DNS, since in LES the smallest scales need not to be resolved.

Application of LES to the modelling of stenotic flow is very limited. Recently, Mittal *et al* . [78; 79] have investigated the transition to turbulent pulsatile flow in a constricted channel using the LES technique. In their studies they extended the study of Tutty [80] to 3D case using the same semi-circular constriction in the upper wall of the channel, which is not a replica of the arterial stenosis. They reported the maximum shear stress at the centre of the constriction of the upper wall, but from the experimental studies of Friedman *et al* . [35], Ku *et al* . [36], Salam *et al* . [37] and Ojha *et al* . [81], it is known that the wall shear stress at the centre of the stenosis is low. So, it is clear that further computational study is required to get agreement between the experimental and computational results.

2.3 Previous Studies on Aneurysm

2.3.1 Experimental studies

Scherer [82] investigated the steady flow dynamics in axisymmetrical glass spherical model aneurysms. He found that the flow inside the aneurysm is turbulent when $Re = 2900$ and the turbulence depends on the dimension of the aneurysm. An ex-

perimental study of the physiological pulsatile flow in the asymmetric and axisymmetric aneurysms has been done by Egelhoff *et al* . [5], while Reynolds number ranging from 362 to 5696 was used with Womerseley number, $16.4 < \alpha < 21.2$. They also found turbulent flow inside the aneurysm.

Salsac *et al* . [83] did an experiment for investigating the wall shear stress on a cosine shaped model aneurysm with the physiological inlet pulsatile flow condition and found that the wall shear stresses at the systolic phase are higher than the stresses at the diastolic phase. They also investigated the effect of the length of aneurysm on the formation of the re-circulation regions and observed that for the large aneurysm the number of re-circulation zones increased. The experiment of Deplano *et al* . [84] showed that vortices inside the balloon like abdominal aortic aneurysm are highly dependent on the flow waveform, and due to these the wall shear stress and wall pressure increase.

2.3.2 Computational studies

The numerical simulation in the arterial aneurysm was initially done by Wille [85] using the finite element method by considering the laminar flow. Later Perltold *et al* . [86; 87] investigated the paths of the flow particles for pulsatile flow in an axisymmetrical balloon like aneurysm with $Re = 100$. They found a large re-circulation region inside the aneurysm and the centre of this circulation changes with the changes of time phase. Although, Kumar and Naidu [13] traced a similar re-circulation region inside the aneurysm, the investigation of Kumar [88] on 3D unsteady laminar flow in two asymmetric aneurysms using the finite volume method showed that the high wall shear stress and pressure occur at the dilation region at the systolic phase. In addition to this, the velocity is very low at the diastolic phase inside the aneurysm, which can trigger thrombus formation.

The issues of hemodynamics and thrombus formation in aneurysm have also been investigated more recently. Utter and Rossmann [89] looked into the aneurysm hemodynamics and the influence of morphology on rupture risk of aneurysm, while Rayz *et al* . [90] predicted the regions prone to thrombus formation inside the intracranial aneurysm and concluded that the regions of thrombus formation correspond to slow flow and low wall shear. Chatziprodromou *et al* . [91] found in their

investigation that the shear stress also plays an important role in the hemodynamics and wall-remodelling of a growing cerebral aneurysm. Very recently, Valencia *et al* . [92] showed that the wall shear stresses are directly correlated with the growth and rupture of the aneurysm.

The above described numerical investigations on aneurysm are confined to laminar flow. A numerical study of the turbulent pulsatile flow in an axisymmetric aortic aneurysm has recently been done by Khanafer *et al* . [93] using the k-ϵ RANS model, but it has already been mentioned in §2.2.2 that RANS is not suitable for studying pulsatile turbulent flow.

2.4 Non-Newtonian Blood Viscosity

Previous sections contain a description of the literature on the arterial stenosis and aneurysm where the blood was assumed to be a Newtonian fluid, but it is well known that blood behaves as a non-Newtonian fluid at shear rates less than 100 s^{-1} (Fung [94], Berger and Jou [95]). Considering blood as a non-Newtonian fluid several investigations on laminar blood flow in arterial system have been done by using different blood viscosity models. For example, Buchanan *et al* . [96] used the Quemada and Power-law blood viscosity models for an axisymmetric channel, while Tu *et al* . [97] employed the Herschel-Bulkley model in the same geometry.

Three different models, namely, (i) Casson model (ii) Power-law model and (iii) Quemada model have been used by Neofytou *et al* . [98; 99; 100] for studying blood flow in a sudden expansion channel, arterial stenosis and aneurysm. They found that the Quemada and Casson models exhibit similar behaviour, while the Power-law does not. So, the solution in the non-Newtonian model clearly depends on the choice of the non-Newtonian viscosity model used in the simulation. Johnston *et al* . [101; 102] who used five different non-Newtonian blood viscosity models, (i) Casson model (ii) Power-law (iii) Carreau model (iv) Walburn-Schneck and (v) Generalised power-law model, to study the wall shear stress in human right coronary artery. They found significant effects on the shear stress for the different models.

Luo and Kuang [103] recently proposed a modification to the Casson's model as the modified Casson's model is more effective in describing the shear thinning behaviour of blood within a large shear range. On the other hand, Zang and Kunag

[104] proposed a new blood viscosity model and the results agree well with the Quemada model.

Hron *et al* . [105] used the power-law model for getting effects of blood rheology in flow through the model stenosis with Reynolds number ranging from 10 to 100. Their results showed that the wall shear stress changes slightly due to the effect of non-Newtonian blood viscosity. But the study of Valencia *et al* . [106], where the Herschel-Bulkley model is employed for the unsteady laminar flow in a right internal carotid artery with an aneurysm, shows that though the complex vortex structure inside the aneurysm changes during one pulsatile cycle, the effect of the non-Newtonian properties of blood on the wall shear stress inside the aneurysm is similar for the Newtonian and non-Newtonian models.

As seen, very few studies are related to non-Newtonian blood flow in arterial stenosis and aneurysm. The papers cited above, such as, Tu *et al* . [97], Buchanan *et al* . [96], Neofytou and Drikakis [99], Hron *et al* . [105], Nag and Datta [107] and Valencia and Villanueva [108], where different blood viscosity models are used, are conducted only for laminar flow. To our knowledge, there is no single numerical/computational paper that has looked into the details of the transition-to-turbulent of the non-Newtonian blood flow in stenosis or aneurysm.

2.5 Objectives of the present study

The LES approach, which has largely been applied in other engineering field to model turbulent flow, has only recently been applied to the study of physiological transitional flow in bio-fluid mechanics. The novelty of the LES approach in the thesis is the application in a non-uniform model of arterial stenosis to investigate the transition-to-turbulent flow under various pulsatile and physiological conditions. Although a few number of papers, as cited in the last paragraph of § 2.2.1, described the flow study in a double stenosis, they are limited to steady or 2D turbulent flow. A true 3D simulation of such model with LES would provide in-depth information of flow transition through multiple stenoses.

Moreover, the papers cited in § 2.3.2 show that the simulation of flow in aneurysm are limited to laminar, except the one paper of Khanafer *et al* . [93] who used the RANS technique. So, using the LES technique with a physiological pulsatile

flow through a model of arterial aneurysm would enable us to gain insight to the transition-to-turbulent phenomena of the flow inside the aneurysm.

Furthermore, most of the previous studies are concerned with the Newtonian flow. It would be interesting to investigate how the results of transition-to-turbulent in a model of stenosis are affected by the choice of various non-Newtonian viscosity models. Again, application of LES to simulate the transition-to-turbulent physiological pulsatile non-Newtonian blood flow is novel. So, based on the above we identify the aims of the thesis, which are given below in bullet points, and the outlines of the thesis describing how these aims are met is given in the next section.

- Investigate the transition-to-turbulent flow through a model of the non-uniform arterial stenosis by applying a sinusoidal additive type oscillation at the inlet.
- Investigate the variations of the results obtained from the additive and non-additive type oscillations.
- Using physiologically realistic pulsatile flow, investigate the transition process in the same model. It would be investigated how the results are influenced by the various harmonics in pulsation.
- Investigate physiological pulsatile flow in the model of a double stenosis.
- Investigate physiological pulsatile flow through the model of a non-uniform asymmetric aneurysm.
- Finally, investigate how the non-Newtonian blood viscosity affects the flow transition in the model of arterial stenosis

2.6 Thesis Outline

In Chapter 4, the governing equations for incompressible flow and the description of Large Eddy Simulation (LES) technique are given for investigating the laminar to turbulent pulsatile flow in a 3D model of arterial stenosis. A simple channel with a cosine shape stenosis on the top wall is chosen as the computational domain, the unsteady pulsatile flow is generated in the stenosed channel by adding a sinusoidal

pulsation to fully developed streamwise velocity profile at the inlet. Reynolds numbers which are typical of those found in human large artery are chosen in the work. In LES, the large scale flows are resolved fully while the unresolved SGS motions are modelled using the Germano-Lilly [2; 3] dynamic model.

In Chapter 5, a non-additive sinusoidal pulsatile flow with non-zero mean in the same model of stenosis is studied by using LES with the Germano-Lilly [2; 3] dynamic model. The results obtained by the non-additive pulsation are compared with those of the additive pulsation (Chapter 4) and the fully developed steady flow.

In Chapter 6, physiological pulsatile flow in the same computational domain is investigated by using the LES technique. The physiological pulsation is generated at the inlet using the first harmonic of the Fourier series of pressure pulse. To reduce the back-scatter problem, that occurs in the Germano-Lilly [2; 3] dynamic model, the Piomelli-Liu [4] localized dynamic model is used for modelling the SGS motions. A grid independence test and the effects of the various timesteps on the simulated results are examined. Moreover, comparison of the LES results with a coarse DNS is shown in this chapter and the agreement found is good indeed.

In Chapter 7, the work presented in Chapter 6 is extended by considering the first four harmonics of the physiological pressure pulse. The results for the fourth harmonic case are presented first for different Reynolds numbers and the effects of the various harmonics on the transient results are investigated for $Re = 2000$. In addition, a comparison between the results of the two dynamic sub-grid models, Germano-Lilly [2; 3] and Piomelli-Liu [4], is given. The effects of different percentage and length of the stenosis on the results of the wall shear stress and the turbulent kinetic energy are also examined.

In Chapter 8, physiological pulsatile flow through a double stenosis is studied with the LES technique. The effects of the double stenosis on the transient flow field are investigated for the different flow Reynolds numbers.

In Chapter 9, physiological pulsatile flow in a model aneurysm is studied using the LES technique with the Piomelli-Liu [4] localised dynamic sub-grid model. The turbulent phenomena inside the aneurysm are compared qualitatively with the experimental results of Egelhoff *et al* . [5].

In Chapter 10, the effects of various non-Newtonian blood viscosity models on physiological pulsatile flow in the stenosis are investigated using the LES technique.

The results of the various non-Newtonian models are compared with those of the Newtonian model in Chapter 7.

In Chapter 11, the findings of the present investigation are summarised and some suggestions for future work are given.

Chapter 3

Numerical Methods

3.1 Governing Equations

Blood is a non-Newtonian fluid, but as mentioned by Pedley [109] and Fung [94] blood flow in a large arterial vessel may be modelled as a Newtonian fluid. So the Navier-Stokes equations of motion are suitable for use in investigating the flow physics of blood through the arterial stenosis. We also assume that the fluid is homogeneous and incompressible. The governing equations for a Newtonian and constant density fluid flow can be written as the continuity equation

$$\frac{\partial u_j}{\partial x_j} = 0, \tag{3.1}$$

and the momentum equations

$$\frac{\partial u_i}{\partial t} + \frac{\partial u_i u_j}{\partial x_j} = -\frac{1}{\rho}\frac{\partial p}{\partial x_i} + \frac{\partial}{\partial x_j}\left[\nu\left(\frac{\partial u_i}{\partial x_j} + \frac{\partial u_j}{\partial x_i}\right)\right]. \tag{3.2}$$

Cartesian tensor notation is used in the above equations, where x_j is the coordinate system and u_j is the corresponding velocity components, p is the pressure, ρ is the density and ν is the kinematic viscosity of the fluid.

Important to note that the above equations describe the physics of incompressible fluid motion under laminar as well as turbulent conditions. It is well known that analytical solutions of the Navier-Stokes equations exist for only a limited number of laminar flow cases, such as pipe and annulus flows or boundary layers, and that direct numerical simulation (DNS) of the transport equations is limited to laminar or very low Reynolds number turbulent flows. In a DNS of turbulent flow, the numer-

ical resolution has to be fine enough to represent the dissipative scales. The enormous spatial and temporal resolution requirements resulting from this constraint for a DNS of turbulent flow have been described by the investigators, Grotzbach [110] and Reynolds [111]. The basic idea of DNS resolutions is reviewed below, since this relates closely to the motivation for LES.

3.2 Resolution Requirements for DNS

To get an estimate for the resolution requirements of free turbulent shear flow, Kolmogprov's ([112]) first principle of similarity is adopted. It is assumed that the small scales of turbulence are locally isotropic, that is, the statistical properties of the small scale motions are presumed not to depend on the orientation of the coordinate system or spatial position in a sufficiently small domain within a flow for which Reynolds number is sufficient large. The smallest turbulent scales, dissipating the turbulent kinetic energy, are therefore presumed to have lost any orientation that might be imposed by the flow geometry. Their physical properties can then only depend on the rate of dissipation, ϵ, and the kinematic viscosity, ν. It then follows from dimensional analysis that the smallest length and time scales in a turbulent flow are characterised by the Kolmogorov length scale defined as

$$\eta \equiv \left(\frac{\nu^3}{\epsilon}\right)^{\frac{1}{4}}, \tag{3.3}$$

and the Kolmogorov velocity scale defined as

$$\sigma \equiv \left(\frac{\nu}{\epsilon}\right)^{\frac{1}{2}}. \tag{3.4}$$

An approximation for the dissipation rate can be obtained from the large scale motion if the turbulence is locally in equilibrium, that is, if the local rate of production of turbulent kinetic energy equals the local rate of dissipation. The rate of turbulence production, however, is determined by the large scale motion and can therefore be approximated as being proportional to the turbulent energy, $\frac{u_0^2}{2}$, and a time scale $\frac{l_0}{u_0}$, characterising the rate at which energy is transferred from the mean motion to the turbulent fluctuations. Here u_0 is a velocity scale while l_0 is an integral

length scale characterising the large scale turbulent motion. Thus, for turbulence in local equilibrium the dissipation rate scale is

$$\epsilon \propto \frac{u_0^3}{l_0}. \tag{3.5}$$

Though, strictly, only true for the artificial case of forced non-decaying homogeneous turbulence, this relation can be regarded as a scale relation valid for inhomogeneous turbulence as well. Available experimental evidence suggests (Tennekes and Lumley [113]) that the spectral energy transfer proceeds at a rate dictated by the kinetic energy of the large eddies, which can be approximated by $\frac{u_0^2}{2}$, and their time scale, $\frac{l_0}{u_0}$. An estimate for the Kolmogorov scales can therefore be obtained from the large scales of the problem by introducing (3.5) into (3.4).

With an approximation for the smallest turbulent length scales obtained in this manner, the computational requirements for a three-dimensional DNS of isotropic homogeneous turbulence can be estimated. For a finite difference or finite volume method, the number of grid nodes N_{xyz}, required to represent the large scale as well as the small scale motion in the three spatial directions, is

$$N_{xyz} \propto \left(\frac{l_0}{\eta}\right)^3 \propto \left(\left(\frac{l_0 u_o}{\nu}\right)^{\frac{3}{4}}\right)^3 = Re_T^{\frac{9}{4}}, \tag{3.6}$$

where Re_T is the turbulent Reynolds number of the large scale motion. Equation (3.6) now implies that the grid size for a DNS of homogeneous turbulence depends on the Reynolds number. As mentioned above, the scale relation in equation (3.5) is generally valid as an order of magnitude for all free flows, so that the spatial resolution requirements for complex engineering type applications are expected to grow with $Re^{\frac{9}{4}}$ as well, for areas away from solid surface. Here Re is the flow Reynolds number which is proportional to the turbulent Reynolds number, Re_T, characterising the large scale turbulent fluctuations. Now if the Reynolds number Re of a turbulent flow is known, one can calculate with the relation (3.6) the number of grid nodes which will be required to resolved the flow at the Kolomogorov scales. For example, when $Re = 2000$, over 20 millions grid nodes are required for DNS to resolve the flow at the Kolmogorov scales, which is still a difficult task with today's

state-of-the-art computing facility. Therefore, a modelling approach is essential for turbulent flow. In the thesis, we will use a LES approach, by which the large-scale motions are resolved by the grid resolution, while the small scales, which are filtered out from the flow using the technique discussed in § 3.3, are modelled. In addition, computations with coarse DNS will be performed and the results will be presented in Chapters 6 and 7.

3.3 The Filtering Operation

3.3.1 Spatial filtering

To obtain the LES equations, the governing equations (3.1-3.2) are filtered first using a spatial filter which separates the large scale (resolved scale) flow field from the small scale (sub-grid scale). If $f(x_j, t)$ is a generic instantaneous variable at a location, x_j, the corresponding filtered variable, known as the resolvable component of $f(x_j, t)$ and denoted by $\bar{f}(x_j, t)$, is defined as the convolution of $f(x_j, t)$ with a filter function G as (Leonard [114])

$$\bar{f}(x_j, t) = \int_D f(x'_j, t) G(x_j - x'_j, \triangle(x_j)) dx'_j, \tag{3.7}$$

where D is the entire domain; $\Delta(x_j)$ is the filter width which in LES practice is generally related to the mesh size, e.g. $\triangle(x_j) = \sqrt[3]{\triangle x \triangle y \triangle z}$. The filter function G is usually defined as the product of three one-dimensional filters,

$$G(x_j - x'_j, \triangle(x_j)) = \prod_{j=1}^{3} g(x_j - x'_j, \triangle(x_j)), \tag{3.8}$$

which must satisfy the normalisation condition,

$$\int_D G(x_j - x'_j, \triangle(x_j)) dx'_j = 1. \tag{3.9}$$

Defining the Fourier transform $\hat{f}(k_j, t)$ of $f(x_j, t)$ as

$$\hat{f}(k_j,t) = \iiint_{-\infty}^{\infty} f(x'_j,t)e^{-ik_j x_j}dx_j, \tag{3.10}$$

it can be seen from the definition of the spatial filter (3.7) that $\bar{f}(x_j,t)$ is a simple convolution of the generic variable $f(x'_j,t)$ and filter function G, which implies that its Fourier transform is

$$\hat{\bar{f}}(k_j,t) = \hat{G}\hat{f}(k_j,t), \tag{3.11}$$

where $\hat{G} = \prod_{j=1}^{3} \hat{g}(k_j, \triangle(x_j))$ is the Fourier transform of the filter function. It is important to note that this filter function determines the size and structure of the smallest resolvable eddies. Various distributions of the filter function are available in the literature, for example, see Leonard [114], Germano [2], and Ghosal and Moin [115]. But the most commonly used filter functions and their Fourier transforms are given below. The "top hat" filter,

$$G\left(x_j - x'_j, \triangle(x_j)\right) = \begin{cases} \frac{1}{\triangle(x_j)} & \text{if} \quad |x_j - x'_j| \leq \frac{\triangle(x_j)}{2} \\ 0 & \text{otherwise} \end{cases} \tag{3.12}$$

and the Fourier transform of the top hat filter is

$$\hat{g}(k_j, \triangle(x_j)) = \frac{\sin\left(k_j \frac{\triangle(x_j)}{2}\right)}{k_j \frac{\triangle(x_j)}{2}}. \tag{3.13}$$

The Gaussian filter,

$$G\left(x_j - x'_j, \triangle(x_j)\right) = \left(\sqrt{\frac{6}{\pi}}\frac{1}{\triangle(x_j)^2}\right) exp\left[-\frac{6(x_j - x'_j)^2}{\Delta(x_j)}\right], \tag{3.14}$$

and its Fourier transform is

$$\hat{g}(k_j, \triangle(x_j)) = exp\frac{-(k_j\Delta(x_j)}{24}. \tag{3.15}$$

and the Fourier cut-off filter,

$$G[x_j - x'_j, \triangle(x_j)] = \frac{\sin(k_c(x_j - x'_j))}{\pi(x_j - x'_j)}. \tag{3.16}$$

where $k_c = \frac{\pi}{\triangle(x_j)}$ and the corresponding Fourier transform is

$$\hat{g}(k_j, \triangle(x_j)) = \begin{cases} 1 & \text{if} \quad |k| \leq k_c \\ 0 & \quad \text{otherwise} \end{cases} \tag{3.17}$$

So, in the Fourier cut-off filter if $\hat{g}$ is zero for $k^2 = k_j k_j > k_c^2$, where k_c is a cut-off wave number defining the limit of wave resolution, then $\bar{f}$ will contain no contribution from wave numbers greater than k_c, that is, wave numbers greater than a cut-off value are completely removed from the flow field leaving the smallest wave numbers unaffected. In contrast, both the top hat and Gaussian filter functions affect all wave numbers without removing completely any particular part of the spectrum. In our simulation we have used the "top hat" filter given in equation (3.12) and suggested by Germano [2] as it fits naturally into a finite volume formulation (see di Mare and Jones [116]).

3.3.2 Commutation

At the time of applying the spatial filter to the Navier-Stokes equations, some rules for the manipulation of filtered quantities must be known. The following rules, as with the Reynolds averages, apply for the spatial filtering:

$$\overline{cf} = c\bar{f}, \tag{3.18}$$

where c is a constant and $f(x_j, t)$ is a spatial function. For two functions, $f_1(x_j, t)$ and $f_2(x_j, t)$, it is clear that

$$\overline{f_1 + f_2} = \bar{f}_1 + \bar{f}_2 \tag{3.19}$$

while in general,

$$\overline{\bar{f}_1 . f_2} \neq \bar{f}_1 . \bar{f}_2 \tag{3.20}$$

Unlike the Reynolds averages, applying the same filtering twice generally changes the value, so that

$$\bar{\bar{f}} \neq \bar{f} \tag{3.21}$$

But the Fourier cut-off filter is an exception. It can be seen from its definition that the Fourier base is not modified by multiple filtering application and therefore

$$\bar{\bar{f}} = \bar{f}. \tag{3.22}$$

The filtering operation always commutes with time differencing, so that

$$\overline{\frac{\partial f}{\partial t}} = \frac{\partial \bar{f}}{\partial t}. \tag{3.23}$$

But, as the filter width is a function of space, the filtering operation on spatial differentiation does not commute, i.e.

$$\overline{\frac{\partial f}{\partial x_j}} \neq \frac{\partial \bar{f}}{\partial x_j}. \tag{3.24}$$

Therefore, the commutation error arises, which is the difference between the term on each side of (3.24), i.e. $\left(\overline{\frac{\partial f}{\partial x_j}} - \frac{\partial \bar{f}}{\partial x_j}\right)$. This lack of commutativity between the filtering and differentiation causes every spatial derivative operator in the governing equations (3.1-3.2) to generate terms that can not be expressed solely in terms of the filtered fields. As suggested in Ghosal and Moin [115], the commutation error can be derived in terms of the spatial gradient as follows

$$\overline{\frac{\partial f(y)}{\partial y}} = \int_a^b G[y - y', \triangle(y)] \frac{\partial f(y')}{\partial y'} dy'. \tag{3.25}$$

Applying integration by parts, we get

$$\overline{\frac{\partial f(y)}{\partial y}} = \underbrace{G[y - y', \triangle(y)] f(y')|_a^b}_{(A)} - \underbrace{\int_a^b f(y') \frac{\partial G[y - y', \triangle(y)]}{\partial y'} dy'}_{(B)}. \tag{3.26}$$

The first term (A) vanishes, since $G[y - y', \triangle(y)]f(y') = 0$ on the integration boundaries a and b. Application of the chain rule to second term (B) gives

$$\overline{\frac{\partial f(y)}{\partial y}} = \frac{\partial}{\partial y}\int_a^b G[y-y',\triangle(y)]f(y')dy' - \int_a^b f(y')\frac{\partial G[y-y',\triangle(y)]}{\partial \triangle}\frac{d\triangle(y)}{dy}dy' \tag{3.27}$$

then

$$\overline{\frac{\partial f(y)}{\partial y}} - \frac{\partial \bar{f}}{\partial y} = -\frac{\partial \bar{f}}{\partial \triangle}\frac{d\triangle(y)}{dy}. \tag{3.28}$$

since

$$\frac{\partial G[y-y',\triangle(y)]}{\partial y'} = \frac{\partial G[y-y',\triangle(y)]}{\partial \triangle}\frac{d\triangle}{dy} - \frac{\partial G[y-y',\triangle(y)]}{\partial y} \tag{3.29}$$

Eq. (3.28) now shows that the commutation error, $\frac{\partial \bar{f}}{\partial \triangle}\frac{d\triangle(y)}{dy}$, depends on how the filter function varies with the filter width and at the same time how the filter width varies in the spatial direction.

According to Ghosal and Moin [115], if a second-order numerical scheme is used to represent the derivatives, the finite differencing error is then of the same order as the error due to the lack of commutativity of the spatial differentiation and the filtering operations. From equation (3.28), the error may be analysed for the second order central difference scheme as

$$\overline{\frac{\partial f(y)}{\partial y}} - \frac{\bar{f}_{j+1}-\bar{f}_{j-1}}{2h} + O(h^2) = -\frac{\partial \bar{f}}{\partial \triangle}\frac{d\triangle(y)}{dy}, \tag{3.30}$$

where, for the non-uniform mesh, $2h_j = y_{j+1} - y_{j-1}$. Equation (3.30) can now be written as

$$\overline{\frac{\partial f(y)}{\partial y}} - \frac{\bar{f}_{j+1}-\bar{f}_{j-1}}{2h_j} = -\frac{\partial \bar{f}}{\partial \triangle}\frac{d\triangle(y)}{dy} - O(h_j^2) \tag{3.31}$$

If the commutation terms is assumed to approximate to zero, that is,

$$-\frac{\partial \bar{f}}{\partial \triangle}\frac{d\triangle(y)}{dy} - O(h_j^2) \sim 0 \Rightarrow -\frac{\partial \bar{f}}{\partial \triangle}\frac{d\triangle(y)}{dy} \sim O(h_j^2) \tag{3.32}$$

Hence Eq. (3.32) shows clearly that the commutation error becomes $O(h_j^2)$. Ghosal

and Moin [115] proposed an alternate definition for the filtering operation by introducing a mapping, which transforms the computational space of non-uniform filter width into an alternate coordinate system where this filter width becomes constant. They have showed that the commutation error is second order in a second order accurate numerical scheme. So, Eq. (3.32) is consistent with Ghosal and Moin [115] though we have used the original filter. They also pointed out that, in LES the grid spacing is approximately equal to that of the filter width, that means, $h \sim \triangle$. Hence the equation (3.32) becomes

$$-\frac{\partial \bar{f}}{\partial \triangle}\frac{d\triangle(y)}{dy} \sim O(\triangle^2). \tag{3.33}$$

Note that the physical interpretation of the resulting filtered fields is ambiguous and is not clear how these filter definitions affect the size of the terms in the equations in relation to the commutation error. So, in keeping with the vast majority of simulations reported in the literature ([79], [116], [117], [118], etc.), the commutation error has been neglected in the present study. However, it may be proved that the effect of neglecting the commutation error on the computed flow field would be very low. In order to show this, it is used an example of the streamwise velocity, $\bar{v}$, computed in the stenosed artery in Chapter 4. A non-uniform grid size of $N_x \times N_y \times N_z = 50 \times 200 \times 50$ was used in the LES computation. The gradient of the velocity, $\frac{d\bar{v}}{dy}$, presented in Fig. 3.2a, shows that the magnitude is about (10^6) times higher than $\triangle^2$ in Fig. 3.2b. Therefore, it is quite clear that the effect of the commutation error is quite negligible.

Moreover, equation (3.28) indicates that the commutation error is proportional to the gradient of the filter width ($\frac{d\triangle}{dy}$). So, if the expansion or compression ratio of the non-uniform grid is smooth, i.e, the grid spacing varies smoothly, the commutation error can be kept to a minimum. In the sample case shown above, the mesh expansion ratio lies between 0.97 and 1.05, so that $\frac{d\triangle}{dy}$ is small.

3.4 Filtered Governing Equations

By applying the above filter function (3.12) to the Navier-Stokes equations of motion (3.1-3.2), we obtain the following filtered equations:

$$\frac{\partial \bar{u_j}}{\partial x_j} = 0, \tag{3.34}$$

$$\frac{\partial \bar{u_i}}{\partial t} + \frac{\partial \bar{u_i}\bar{u_j}}{\partial x_j} = -\frac{1}{\rho}\frac{\partial \bar{p}}{\partial x_i} + \frac{\partial}{\partial x_j}\left[\nu\left(\frac{\partial \bar{u_i}}{\partial x_j} + \frac{\partial \bar{u_j}}{\partial x_i}\right)\right] - \frac{\partial \tau_{ij}}{\partial x_j}, \tag{3.35}$$

where the effects of the small scales, appearing in the subgrid-scale stress term as

$$\tau_{ij} = \overline{u_i u_j} - \bar{u_i}\bar{u_j} \tag{3.36}$$

must be modelled and are discussed in the next section.

3.5 Subgrid-scale Modelling

The Smagorinsky model [119] is the most famous and still widely used model for the sub-grid scale stresses, which is based on the eddy viscosity assumption as

$$\tau_{ij} - \frac{1}{3}\delta_{ij}\tau_{kk} = -2\nu_{sgs}\bar{S}_{ij}, \tag{3.37}$$

where the subgrid kinetic eddy viscosity, ν_{sgs}, which is again related to the subgrid eddy viscosity, μ_{sgs}, as $\rho\nu_{sgs} = \mu_{sgs}$, is obtained by assuming that the turbulent dissipation is in equilibrium with the turbulent energy production. This yields an expression

$$\nu_{sgs} = (C_s\triangle)^2|\bar{S}|, \tag{3.38}$$

where C_s is the Smagorinsky constant and $|\bar{S}| = \sqrt{2\bar{S_{ij}}\bar{S_{ij}}}$ is the magnitude of the large scale strain rate tensors defined as $\bar{S_{ij}} = \frac{1}{2}\left(\frac{\partial \bar{u_i}}{\partial x_j} + \frac{\partial \bar{u_j}}{\partial x_i}\right)$. Thus, the Smagorinsky model takes the form

$$\tau_{ij} - \frac{1}{3}\delta_{ij}\tau_{kk} = -2(C_s\triangle)^2|\bar{S}|\bar{S_{ij}} = -2C_s^2\beta_{ij}, \tag{3.39}$$

where $\beta_{ij} = \triangle^2|\bar{S}|\bar{S_{ij}}$. A theoretical value of $C_s = 0.1$ is usually found in the literature for simulating turbulent flow with LES. However, one of the major difficulties with the Smagorinsky model is the calculation of the Smagorinsky constant for inhomogeneous flow, which means, transition to turbulent flow. The optimum value for C_s may be different at different regions inside a full flow domain, therefore, the Smagorinsky model needs an additional assumption to determine the values of C_s for transitional flow, which is described in the next section.

3.5.1 Germano-Lilly Dynamic Subgrid-scale Model

The subgrid dynamic model for transition to turbulent flow originally proposed by Germano *et al* . [2] calculates the Smagorinsky constant as a function of time and position. According to Germano *et al* . [2], a $test$-filter, which has a filter width larger than the original filter, ($\tilde{\triangle} > \triangle$), is applied to the filtered Navier-Stokes eqs. (3.34)-(3.35), giving the subgrid scale stress tensor, T_{ij}, similar to τ_{ij} of (3.36) as

$$T_{ij} = \widetilde{\overline{u_i u_j}} - \tilde{\bar{u}}_i \tilde{\bar{u}}_j. \tag{3.40}$$

The two stress tensors, τ_{ij} and T_{ij}, are now related to the following Germano identity,

$$L_{ij} = T_{ij} - \tilde{\tau_{ij}} \tag{3.41}$$

Assuming the same functional form as the Samgorinsky model, the anisotropic part of T_{ij} gives

$$T_{ij} - \frac{1}{3}\delta_{ij}T_{kk} = -2(C_s\tilde{\triangle})^2|\tilde{\bar{S}}|\tilde{\bar{S}}_{ij} = -2C_s^2\alpha_{ij}, \tag{3.42}$$

with the test-scale shears defined similarly to those for the grid scale. Here $\alpha_{ij} = (\tilde{\triangle})^2|\tilde{\bar{S}}|\tilde{\bar{S}}_{ij}$.

In eq. (3.41) the elements of L_{ij} are the resolved components of the stress tensor associated with the scales of motion between the test and grid scales. Now the right hand side of eq. (3.41) can be evaluated explicitly by subtracting (3.39) from (3.42),

$$L_{ij}^a = L_{ij} - \frac{1}{3}\delta_{ij}L_{kk} = 2C_s^2 M_{ij} = 2C_s^2(\beta_{ij} - \alpha_{ij}), \tag{3.43}$$

where

$$M_{ij} = \tilde{\triangle}^2 |\tilde{\bar{S}}| \tilde{\bar{S}}_{ij} - \triangle^2 \widetilde{|\bar{S}|\bar{S}_{ij}} = \alpha_{ij} - \beta_{ij}. \tag{3.44}$$

Following a suggestion of Lilly [3], a least square approach is used to obtain the values of C_s^*, leading to

$$C_s^2 = C_s^* = \frac{1}{2} \frac{L_{ij}^a M_{ij}}{M_{ij}^2}. \tag{3.45}$$

The Smagorinsky coefficient C_s was evaluated iteratively and was set to zero when negative. And the the ratio of the $test$ and $grid$-filter used is 2 for getting the insensitive results (Piomelli-Liu [4], Germano *et al* . [2] and Lund [120]).

3.6 Boundary Conditions

For solving the governing filtered equations (3.34-3.35) the following boundary conditions have been employed.

3.6.1 Inflow Boundary Condition

The inlet boundary condition is the very important to study the transition-to-turbulent pulsatile in the models of arterial stenosis and aneurysm which will be described in the following each chapter.

3.6.2 Wall Boundary Condition

If the domain boundary coincides with a solid impermeable wall, a no-slip condition can generally be used. This boundary condition is used for both the lower and upper walls of the model, which is defined as

$$\bar{u}_j(\mathbf{x}; t)|_\Gamma = 0. \tag{3.46}$$

However, while the prescription of a no-slip condition is straight forward, the LES of turbulent flow in the vicinity of the wall is not. Strictly an LES of all important energy levels contain scales would have to include all viscous scales in the sublayer and thus would effectively correspond to a DNS in the proximity of the wall. Good results have been obtained for the channel flow at moderate Reynolds number, by

increasing the grid resolution near the wall to capture the viscous scales in the sub-layer, and following this in the present computation fine mesh has been used near the walls.

3.6.3 Periodic Boundary Condition

For the spanwise boundaries, a periodic boundary condition is applied for modelling the spanwise homogeneous flow. In a geometrical simple problem, such as that arising from the simulation of turbulent channel flow or homogeneous turbulence, the difficulty of having to prescribe instantaneous boundary conditions is often avoided by assuming that the flow is periodic. Regardless of the complexity of the flow problem, this assumption is also useful in problems with a two dimensional pattern in the mean, where the homogeneous direction can be approximated as being periodic. Thus the field at boundary Γ_1 and Γ_2 is set to be identical, i.e.

$$\bar{u}_j(\mathbf{x};t)|_{\Gamma 1} = \bar{u}_j(\mathbf{x};t)|_{\Gamma 2} \tag{3.47}$$

and

$$\bar{p}_p(\mathbf{x};t)|_{\Gamma 1} = \bar{p}_p(\mathbf{x};t)|_{\Gamma 2}, \tag{3.48}$$

where $\bar{p}_p$ corresponds to the periodic part of the pressure.

3.6.4 Symmetric Boundary Condition

This boundary condition is only applied to compare the computational results with the experimental data of a laminar flow in an axisymmetric geometry. In order to reduce the size of the computational domain, symmetric or free slip conditions are sometimes convenient to use. These are designed to minimise the effect of the boundary on the predicted flow by allowing the flow tangential to the boundary to slide along a frictionless surface. The wall-normal velocity component, u_n, is assumed to vanish instantaneously so that

$$\bar{u}_n|_{\Gamma} = 0, \tag{3.49}$$

while for all other flow variables a zero gradient Neumann condition is imposed normal to the surface, that is,

$$\frac{\partial \bar{u}_j}{\partial n}|_\Gamma = 0. \tag{3.50}$$

3.6.5 Outflow Boundary Condition

At the outlet a convective boundary condition is used. In incompressible Reynolds average simulations of turbulent flow it is common to assume a zero gradient condition at the outlet boundary where fluid is expected to be convected out of the computational domain. The field is thus calculated to satisfy

$$\frac{\partial \bar{u}_j}{\partial n}|_\Gamma = 0. \tag{3.51}$$

Strictly, this condition is always invalid in LES, since the instantaneous velocity field at the outlet boundary will vary. However, in areas in which the mean flow is approximately parabolic, errors from such a crude condition are not expected to propagate far upstream and will only influence the solution close to the outlet boundary. Howover, it is well known that this condition can lead to spurious numerically generated reflections, Vichnevetsky [121]. In analogy with the wave travelling out of the domain, Jin and Braza [122] conjectured that a condition,

$$\frac{\partial \bar{u}_j}{\partial t} + u_c \frac{\partial \bar{u}_j}{\partial n} - \nu \frac{\partial^2 \bar{u}_j}{\partial \eta^2} = 0, \tag{3.52}$$

imposed on the outlet boundary should allow the flow structures to be convected out of the domain without any spurious reflections. Here $\frac{\partial}{\partial n}$ is the gradient normal to the outlet boundary and $\frac{\partial}{\partial \eta}$ is tangential to the outlet boundary, while u_c is the convective outflow velocity normal to the outlet boundary. This condition is similar to that of Pauley *et al* . [123] who imposed

$$\frac{\partial \bar{u}_j}{\partial t} + u_c \frac{\partial \bar{u}_j}{\partial n} = 0 \tag{3.53}$$

on the outlet boundary using either the average exit velocity or the vortex propagation speed for u_c. This condition is now well established which allows vortical structures to convect out of the domain virtually unimpeded and is used in the

present computations.

3.7 Overview of Numerical Procedures

An overview of the computational procedure employed in our simulation is presented in this section. The in-house FORTRAN code LES-BOFFIN (Boundary Fitted Flow Integrator), which was initially developed at the Imperial College London for simulating turbulent combustion reacting flow, has been modified and extended in the thesis in order to solve the incompressible governing equations with dynamic subgrid models for the pulsatile and steady flow. The code is fully implicit and second order accurate in both space and time. The BOFFIN code has previously been applied to simulate turbulent flow in other engineering contexts, for examples, see LES of a gas turbine combustor by di Mare *et al* [124], Paul *et al* . [125; 126; 127] of a turbulent non-premixed flame by Branley and Jones [128], turbulent flow past a swept fence by di Mare and Jones [116] and turbulent cross flows of jets by Wille [129].

The governing filtered equations (3.34-3.35) in the Cartesian coordinates are transformed into a curvilinear coordinate system (Thomson *et al* [130]) and the finite volume approach is used to discretise the partial differential equations to yield a system of quasi-linear algebraic equations. To discretise the spatial derivatives in eqns. (3.34-3.35), the standard second order accurate central difference scheme is used, except for the convective terms in the momentum equations (3.35) for which an energy conserving discretisation scheme is used (Morinishi [131]).

Time derivatives are discretised by a three point backward difference scheme. A constant time step is used in the computations to ensure that the maximum Courant number, ($\bar{u_j}\frac{\partial t}{\partial x_j}$), based on the filtered velocity, lies between 0.1 and 0.2 (Choi and Moin [132]).

A pressure correction algorithm is applied to couple pressure with the velocity components where the results are stored at the centre of a control volume according to the collocated grid arrangement. The Poisson like pressure correction equation is discretised by using the Rhie and Chow [133] pressure smoothing approach, which prevents the even-odd node uncoupling in the pressure and velocity fields.

A BI-CGSTAB [134] solver is used for solving the matrix of velocity vectors,

while for the Poisson like pressure correction equation a ICCG [135] solver is applied due to its symmetric and positive definite nature. More details about the numerical algorithm are given in Appendix A.

3.8 Data Processing and Flow Statistics

In the data processing, some different types of averaging procedure are used. For a generic flow filtered variable, $\bar{f}$, the mean (statistical enssemle mean) over the total number of timestep N_t is calculate as

$$< f > (x, y, z) = \frac{1}{N_t} \sum_{i=1}^{N_t} \bar{f}_s(x, y, z, t_i), \tag{3.54}$$

In order to separate the turbulent fluctuations from the pulsatile fluctuations, a phase averaging technique (Hussain and Reynolds [136], Lieber and Giddens [137] and Mittal *et al* . [79]) is applied . The phase average over $T_f = NT$, where N is the total number of periods and T is the time period, is computed as

$$<< \bar{f} >> (x, y, t) = \frac{1}{N} \sum_{n=0}^{N-1} < \bar{f} >_s (x, y, t + nT), \tag{3.55}$$

where $< \bar{f} >_s$ is the spanwise average quantity of $\bar{f}$ defined as

$$< \bar{f} >_s (x, y, t) = \frac{1}{L_3} \int_0^{L_3} \bar{f}(x, y, z, t) dz, \tag{3.56}$$

where L_3 is the total number of mesh points used in the spanwise direction. Finally, the random turbulent fluctuations are calculated using

$$f''(x, y, z, t) = \bar{f}(x, y, z, t) - << \bar{f} >> (x, y, t). \tag{3.57}$$

Thus, the root mean square (rms) values of the turbulent fluctuations are calculated using the following definition

$$< f'' >_{rms} = \sqrt{< f''^2 >}. \tag{3.58}$$

The energy spectra, E, of the turbulent fluctuations are defined as

$$E = \sum_{j=1}^{M} f''^2 e^{-2i\pi(j-1)(k-1)} \; ; \qquad k = 1, \cdots M. \tag{3.59}$$

where M is the number of time steps.

The energy spectra of the turbulent fluctuations and the vortex shedding frequency from the sampling frequency have been calculated by using MATLAB (MATLAB 7.5 [138]). The algorithm for getting the energy spectra is given below

- Load the data sets of f'' and M.
- Calculate f''^2 for the energy spectra.
- Use MATLAB FFT (Fast Fourier Transform) algorithm on f''^2 and store data as Y.
- Use MATLAB Nyquist frequency algorithm on M and store data as the vortex shedding frequency f_s.
- Finally, calculate the energy spectra, E, taking the absolute value of Y.

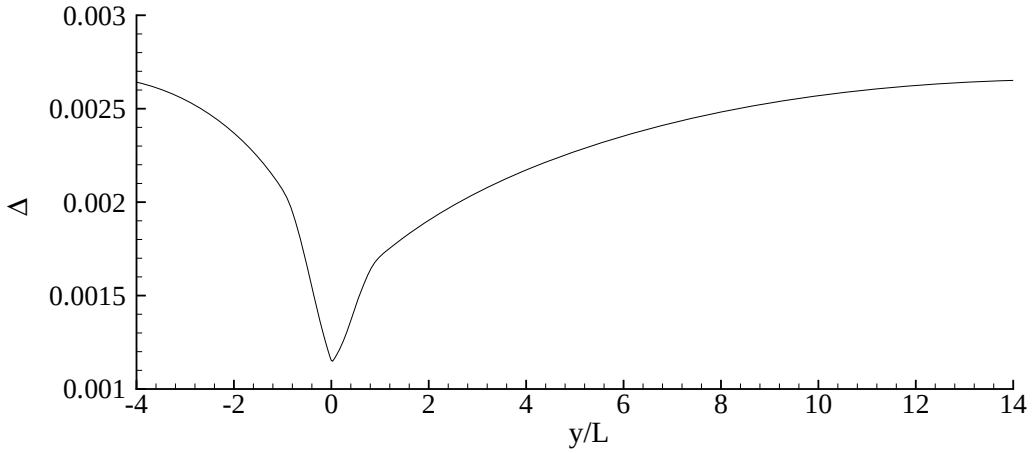

Figure 3.1: Centreline filter width, $\triangle = \sqrt[3]{\triangle x \triangle y \triangle z}$

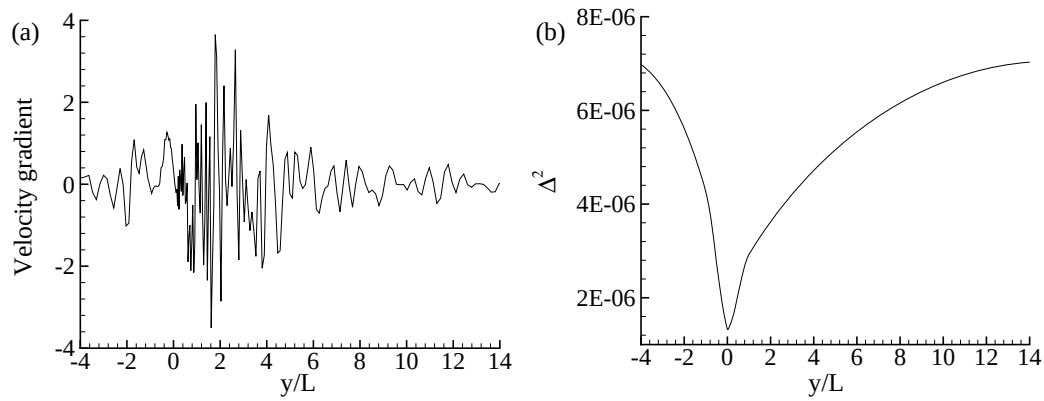

Figure 3.2: Centreline (a) velocity gradient, $\frac{\partial \bar{v}}{\partial y}$ and (b) $\triangle^2$

Chapter 4

LES of Sinusoidal Pulsatile Flow in a Model Arterial Stenosis. Part 1. Additive type Oscillation

4.1 Introduction

In recent years, Large Eddy Simulation (LES) has been used to study complex flows in many engineering applications. In the field of bio-fluid mechanics, it appears that only Mittal *et al* . [78; 79] have applied the LES technique to simulate the transition to turbulent flow in a rectangular channel with a semi-circular constriction in the upper wall. In their studies, they have found the maximum shear stress occurred at the centre of the constriction of the upper wall, but Friedman *et al* . [35], Ku *et al* . [36], Salam *et al* . [37] and Ojha *et al* . [81] reported in their experiments that the wall shear stress at the centre of the stenosis is low. So, further computational study is necessary to get agreement between the experimental and computational results.

In this Chapter, laminar transition to turbulent pulsatile flow in a 3D model of arterial stenosis is investigated by using the LES technique. A simple channel with a cosine shaped stenosis on the top wall is chosen as the computational domain. The unsteady pulsatile flow is generated at the inlet of the stenosed channel by adding a sinusoidal pulsation to fully developed streamwise velocity profile, which is termed here as an additive type oscillation. In LES spatial filtering is applied to the governing equations to separate the flow field into large scale and small scale eddies, known as, sub-grid scale (SGS). The large scale eddies which contain most

of the turbulent energy are resolved directly while the unresolved small scale eddies are modelled using the Germano-Lilly dynamic model (Germano [2] and Lilly [3]) which is described in Chapter 3. The contribution of the SGS model to the large scale motions is assessed in terms of the normalised SGS eddy viscosity.

This Chapter is organised in the following way: a description of the model geometry is presented in §4.2, mesh distribution for the flow simulations is given in §4.3 respectively. Validation with experiment and results and discussion are presented in §4.5 and §4.6 respectively. Finally, a general conclusion of this chapter is made in §4.7.

4.2 Model Geometry

The geometry shown in Fig. 4.1 consists of a 3D channel with a one sided cosine shaped stenosis on the upper wall centred at $y/L = 0.0$, where y is the horizontal distance or the distance along the flow and L is the height of the channel. In the model the height (x) and its width (z) are kept same which gives a square cross-section both upstream and downstream of the stenosis. The length of the stenosis is equal to twice the channel height. Before the stenosis the channel length is $5L$, and $15L$ is the downstream of the stenosis. The stenosis is formed using the following relation

$$\frac{x}{L} = 1 - \frac{\delta_c}{2}\left(1 + \cos\frac{y\pi}{L}\right), \quad -L \leq y \leq L \tag{4.1}$$

where δ_c is the parameter that relates to the area reduction of the stenosis. In this Chapter, δ_c is fixed to $\frac{1}{2}$, which gives a 50% reduction of the cross-sectional area at the centre of the stenosis. The smooth constriction/stenosis generated at the channel using the relation above (4.1) gives a fairly reasonable representation of an arterial stenosis (or biological stenosis), see Deshpande *et al* . [48].

4.3 Mesh Distribution

In Fig. 4.3 a crude 2D mesh configuration is shown in the $x-y$ plane. As the no-slip condition (3.46) is applied on the top and bottom walls of the channel, the meshes are refined near the top and bottom walls to increase the resolution in the sublayer.

The mesh lines are also concentrated at the centre and immediate downstream of the stenosis because these are the regions where the high level of vortices and turbulent fluctuations are generated. A uniform spacing is used at the spanwise directions. Note that to generate the dense meshes near the top and bottom walls as well as in the immediate downstream region a $\tanh$ function is used, which is similar to the approach in Moin and Kim [139].

4.4 Inflow Boundary Condition

A sinusoidal pulse is added to the fully developed streamwise velocity profile to generate time-dependent pulsatile flow at the inlet of the model. The formulation of the pulsatile velocity takes the following form

$$\bar{v}(x,t) = 6\bar{V}_{max}\frac{x}{L}\left(1-\frac{x}{L}\right)\left[1+A\sin\left(\frac{2\pi t}{T}\right)\right], \tag{4.2}$$

where $\bar{V}_{max}$ is the bulk velocity which depends on the flow Reynolds number defined as $Re = \frac{\bar{V}_{max}L}{\nu}$. In eq. (4.2), $T = 2\pi$ and A are the time period and amplitude of the sine pulse respectively. In Fig. 4.2 the inlet velocity profile is shown for one pulsation when $Re = 1500$ and $A = 0.3$ which corresponds to the 30% sinusoidal pulsation.

4.5 Validation with Experiment

Although the main focus of the thesis is to study the blood flow in a non-uniform stenosis (Fig. 4.1), it would be interesting to see how the computational results compare with the experimental results of Ahmed and Giddens [1] who studied flow in an axisymmetric model of stenosis. It is note that no experimental data in the non-uniform stenosis considered here is available to make a direct comparison with the present computational results. However, various mesh and timestep independence tests are performed in the thesis in order to check sensitivity of the numerical results.

The model of the stenosis [1] has an area reduction of 75% and 50% respectively at the centre of the stenosis and the respective flow Reynolds numbers in the experiment are 500 and 1000. The boundary condition at the inlet is treated as a

fully developed laminar pipe flow without adding any pulsation to this, while the lower wall of the model shown in Fig. 4.1 is treated as a symmetric plane.

The governing flow field computed downstream of the stenosis is laminar with a negligible effect coming from the SGS, which is essentially a DNS computation. The comparison, presented in Figs. 4.4 and 4.5 for the streamwise velocity at different downstream locations while $Re = 500$ and 1000 respectively, show clearly that the overall agreement of the present computational results against the experiment [1] is quite good indeed. However, the computational velocity profiles at $y/L = 0.0$ for both the stenoses and at $y/L = 0.5$ for the 50% stenosis are slightly deviated in the middle portion of the computational domain, but they have a good agreement at the centre and near the wall where the stenosis appeared. Similar types of small disagreement with the results of Ahmed and Giddens [1] are reported in the study of Vargheses *et al* . [77].

4.6 Results and Discussion

The computational results of LES obtained by using the mesh arrangement of $50 \times 200 \times 50$ (along $x \times y \times z$) with the timestep of $\delta t = 10^{-3}$ and time period of $T = 2\pi$ for the three different flow Reynolds numbers of 1200, 1300 and 1500 are presented here. A mesh independence test is performed, and the results of this test are presented in §4.6.3 and § 4.6.4. Initially, the amplitude (A) of the sinusoidal oscillation is fixed to 0.3 which corresponds to a 30% oscillation in the inlet velocity with a peak-to-mean ratio of 1.3. Then the amplitude is varied for $Re = 1000$ and the results are presented in §4.6.6. The simulations are carried out up to the peak phase of the eleventh cycle of pulsation, where it is checked that the primary mean flow eventually reaches a stationary state.

4.6.1 Contribution of SGS Model

The contributions of the SGS model in the LES are illustrated in Figs. 4.6 and 4.7 at the peak phase of time cycle, $t/T = 10.25$. Fig. 4.6(a-c) depict the contour plots of the dynamic Smagorinsky constant, C_s, for $Re = 1200$, 1300 and 1500 respectively, while the corresponding SGS eddy viscosity, μ_{sgs}, normalised by the

molecular viscosity, μ, is shown in Fig. 4.7(a-c). We note that the equivalent peak Reynolds numbers at this phase are $Re_p = 1560$, 1690 and 1950 respectively. The maximum value of C_s for $Re_p = 1950$ is found about 0.103 which is very close to the typical value of the Smagorinsky constant 0.1 usually used for LES simulation of turbulent flow in a channel. However, the magnitude of C_s decays as the Reynolds number is decreased, e.g. 0.055 and 0.035 are found for $Re_p = 1690$ and 1560 respectively.

In Fig. 4.7(c), the maximum eddy viscosity of about 0.709 for $Re = 1500$ ($Re_p = 1950$) explains the fact that the SGS model contributes up to 70.9% extra dissipation into the flow. The level of SGS dissipation also depends on Re, e.g. when $Re = 1300$ ($Re_p = 1690$) the dissipation of about 21.1% is found in the simulation, while for $Re = 1200$ ($Re_p = 1560$) it is about 3.3% which is negligible compared to those achieved for $Re = 1500$ and 1300. This finding is reasonable given the fact that because of the low Reynolds number less energy is dissipated through the SGS, and a DNS technique could be used for simulating the pulsatile flow when $Re \leq 1200$. Moreover, Fig. 4.7 also shows that the SGS dissipation is significantly large at the post stenosis region where the flow transients to turbulent.

4.6.2 Instantaneous Flow Field

To represent the post-stenotic flow field at the peak phase ($t/T = 10.25$), the $\bar{u}$-$\bar{w}$ (cross flow) velocity vectors at different positions along the flow are plotted in Fig. 4.8(a-h) for $Re_p = 1950$. At the post lip of the stenosis, i.e. at (a) $y/L = 1$, the flow is clearly transitional with the presence of strongly re-circulated chaotic/turbulent flow close to the upper wall, while the flow is laminar close to the lower wall. However, this transitional flow pattern breaks down further downstream of the stenosis and the nature of the flow in this region is completely turbulent. In particular, the level of circulations seen in frames (b-e) is quite strong and, in the pathological context, this could cause potential damage to blood cells as well as the inner surface of the stenosed artery. However, the intensity of the circulations gradually reduces to the far downstream of the stenosis due to the process of re-laminarisation, as seen in frames (f-h).

The spanwise average vorticity, $< \omega_z >_s = (\frac{\partial \bar{v}}{\partial x} - \frac{\partial \bar{u}}{\partial y})$, at different phases over the

last cycle of pulsation are presented in Fig. 4.9 for the Reynolds number $Re = 1500$. The exact locations of these phases, at which the frames are plotted in this figure, are denoted by S_i (where $i = 1, 2, \cdots 10$) and shown in Fig. 4.2. In each frame, a total of 14 unequal contour levels between the maximum and minimum values of $< \omega_z >_s$ are plotted as shown in the colour bar. The dashed contours where vortex-cell rotates in the anti-clockwise direction correspond to the negative values (blue colour) of $< \omega_z >_s$, while the solid lines are for the positive values (red colour) of $< \omega_z >_s$ and the vortex rotates in the clockwise direction.

Two large vortices generated immediately downstream of the stenosis are quite strong, one of which rotates in clockwise and other in the anti-clockwise direction. In the first five frames it is also observed that due to the transition/separation of the shear layer from the throat of the stenosis the anti-clockwise vortices are generated, whereas the second shear layer separating from the opposite wall leads to formation of the clockwise vortices (seen clearly in frames (e-g)). These vortex pair rolls downstream of the stenosis as the phase increases and the breakdown of the clockwise vortices occurs further downstream, see in frames (i-j).

Some detailed structures of the spanwise-average vortices can also be revealed through the cross-sectional plots in Fig. 4.10. The contour levels and the Reynolds number in this figure remain the same as in Fig. 4.9. Frame 4.10(a), which is plotted at the throat of the stenosis, shows that the flow close to both the top and bottom walls is still laminar, but the transient state begins to develop in the middle of the channel. In the next two frames, which are plotted close to the post lip of the stenosis, the vortex-cells develop near the upper wall. The strength of those vortices increases in the post lip and further downstream the vortex cells occupy almost the whole cross-sectional area of the channel.

The effects of the Reynolds number on the development of the spanwise vortices are shown in Fig. 4.11(a-c) for $Re = 1200$ ($Re_p = 1560$), $Re = 1300$ ($Re_p = 1690$) and $Re = 1500$ ($Re_p = 1950$) respectively. These results are taken when the flow rate becomes maximum, i.e. when the flow pulsation attains its peak position, S_p. The patterns of the vortices developing at the downstream of the stenosis are quite similar in every frame, but the vortex-cells shift slightly downstream when the Reynolds number increases.

4.6.3 Mean Flow Characteristics

The mean streamwise velocity profiles for the different Reynolds numbers, $Re_p = 1560, 1690$ and 1950, are depicted in Fig. 4.12 at the different axial positions. Note that the velocity results in the figure have been normalised by the bulk velocity obtained from $Re = 1500$ ($Re_p = 1950$). At the inlet the mean velocity profiles have a parabolic shape (frame a) since the flow before the stenosis is fully developed laminar. But the separated shear layers from the throat break down this parabolic shape in the post lip region due to the adverse pressure gradient. However, towards the far downstream region, the velocity profiles take the non-parabolic or turbulent velocity profile shape.

Fig. 4.13 illustrates the mean streamlines for (a) $Re = 1200$ ($Re_p = 1560$), (b) $Re = 1300$ ($Re_p = 1690$) and (c) $Re = 1500$ ($Re_p = 1950$). The large recirculation regions, near the post lip of the stenosis, which are caused by the backflow, are of great pathological significance as these are the regions of low shear which increase the residence time of blood at the post stenosis, consequently, they increase the chances of heart attack and brain stroke. The effects of the Reynolds number can also be observed in the figure, the recirculation region increases slightly with the increment of the Reynolds number, which is clearly noticeable between $Re = 1300$ and 1500. For instance, when $Re = 1300$ the recirculation region is found between $y/L \sim 0$ and $y/L \sim 1.9$, or in other words, the separated boundary layer from the throat reattached at $y/L \sim 1.9$ on the upper wall. Whereas for $Re = 1500$ the reattachment point moves slightly downstream and is located at $y/L \sim 2.1$. In addition, for the $Re = 1500$ case, another small recirculation region generates very close to the post lip of the stenosis because of the high velocity at the inlet, which could again cause blood clot and stagnte the blood flow.

In Fig. 4.14 the normalised mean centreline velocity for the different Reynolds numbers is depicted, and a comparison between the two mesh arrangements, $50 \times 200 \times 50$ and $70 \times 200 \times 50$, is made for only $Re = 1500$. The solid line with filled square symbol represents the solutions of the higher resolution mesh. As seen in the figure the comparison agrees quite well and the flow resolution is not very sensitive to these two mesh arrangements. Based on this assessment and to minimise the computational time and space, the first set of mesh arrangement, $50 \times 200 \times 50$, was chosen for the simulations of other Reynolds numbers less than 1500.

In the figure we also see that the centreline velocity increases with the Reynolds number because the flow rate increases through the channel. The peaks occurring at about the same downstream location of $y/L \sim 0.4$ fall down abruptly at the post lip of the stenosis, which is again corresponding to the fact that the adverse pressure gradient takes place near the post lip of the stenosis (Fig. 4.16). The second peaks located between $y/L \sim 1.2$ and $y/L \sim 2$ are linked to the intense clockwise vortices found at that region. The velocity after $y/L \sim 3.0$ oscillates because of the high vortex of the flow, however further downstream the centreline velocity vary only a little.

The mean pressure distributions, normalised by $\rho \bar{V}_{max}^2$, at the upper wall, the centreline and the lower wall are presented in Fig. 4.15 for the different Reynolds numbers. The high level of pressure drops found at the throat of the stenosis is of a great concern as these are again potential sources of stoke or heart attack. Moreover, the blood in the post stenosis re-circulated for a long time risking thrombosis because of these pressure drops with the adverse pressure gradient (Fig. 4.16). The corresponding shear stress distributions in Fig. 4.17 show that the upper wall shear stress drops just prior to the centre of the stenosis where the acute pressure drops took place. These low shear stresses usually stimulate re-modelling of the arterial wall which increases the percentage of the arterial stenosis and consequently increases the level of turbulence in the post stenotic region. However, the upper wall shear stresses rise in the post stenosis region with the maximum between $y/L = 1$ and $y/L = 2$ and the further downstream they are close to zero. The centreline profiles in frame (b) show an acute stress drop at the post lip of the stenosis and the oscillating form in the downstream region is due to the presence of the turbulence. The oscillating shear stress remains persistent in the lower wall firmly between $y/L \sim 2.2$ and $y/L \sim 6.0$, and the shear stresses in the lower wall rise to maximum at the centre of the stenosis in contrast to the sharp drops seen in the upper wall. Ii is also noted here that, from the medical point of view, these high and oscillating wall shear stresses in the post stenosis zone could cause damage to the materials of red blood cells (Sutera and Mehrjardi [32]) and also to the endothelium or inner side of post-stenotic blood vessel (Fry [31]).

4.6.4 Turbulent Characteristics

In this section, turbulent characteristics of the flow downstream of the stenosis are presented. Fig. 4.18 shows the centreline profiles of the turbulent kinetic energy, $TKE = \frac{1}{2} < u_j'' u_j'' >$, for $Re = 1200$, 1300 and 1500. These results have been normalized by $\bar{V}_{max}^2$ where $\bar{V}_{max}$ was taken from $Re = 1500$. A comparison between the two mesh arrangements, $50 \times 200 \times 50$ and $70 \times 200 \times 50$, is also made for $Re = 1500$. The results again show that the turbulent fluctuations are not severely sensitive to these mesh orientations.

There is no turbulent kinetic energy upstream of the stenosis since the flow is laminar there, but due to the effect of the stenosis the turbulent kinetic energy grows rapidly in the immediate post-stenotic region and the severe level occurred at the post-lip of the stenosis (Fig. 4.19). However, the TKE decays gradually downstream and finally approaches zero far downstream where the flow is re-laminarized. It is interesting to point out here that this high level of TKE at the post-stenotic region is closely linked to the interaction between the two shear layers, which separate from the stenosis and produce the intense pair-wise vortices in the post stenosis zone, as already seen in Fig. 4.7. Consequently, the level of turbulent fluctuations in the post-stenotic flow becomes prominent and the intensity of the turbulnet fluctuation revealed through the results in Figs. 4.20 as a root mean square (rms) of the centreline velocity, they usually give a quantitative measure of the turbulence intensities. From the medical point of view, this result is quite important since the velocity fluctuations have a significant consequence in activating the blood platelets and damaging the blood cell materials and subsequently they could create many pathological diseases (Ku [9]). Moreover, the results of the SGS eddy viscosity (seen in Fig. 4.7) have also a close correlation with this as they were also predicted to be high at this post-stenotic region. The high level of pressure fluctuations in Fig. 4.21 are responsible for the post-stenotic dilatation due to the arterial damage and are also a potential source of arterial murmur which is a key factor for identifying an arterial stenosis through acoustical techniques (Ask *et al* [140]). The murmur due to the arterial stenosis is usually diagnosed by placing an external "transducer" which transmits through the arterial wall.

Figs. 4.22 and 4.23 respectively show results of the streamwise velocity and pressure fluctuations for $Re = 1500$ plotted in the different axial positions over the

last three cycles. Again no fluctuation is seen at the pre-stenosis and the centre of the stenosis, but due to the flow transition both the velocity and pressure fluctuations grow rapidly in the post stenosis, followed by gradual decay further downstream. We also notice that the cycle-to-cycle growth of these fluctuations is non-periodic.

4.6.5 Turbulent Energy Spectra

Some additional information of the random turbulent fluctuations seen in the post stenotic region will now be revealed through the turbulent energy spectra plotted in Figs. 4.24 and 4.25 for $Re = 1500$. In Fig. 4.24(a-b), the normalised energy spectra, $E_{v''v''} = E(f_s)\bar{V}_{max}/L$, for the centreline velocity fluctuations, $v''^2/\bar{V}^2_{max}$, are plotted against the Strouhal number, $Sr = f_s L/\bar{V}_{max}$, of the vortex shedding frequency, f_s, at the different locations of the post stenotic region. The frequency spectra, $E(f_s)$, are computed by using the FFT (Fast Fourier Transform) scheme. The lines corresponding to $(Sr)^{-5/3}$ and $(Sr)^{-10/3}$ are included in the figure as in Lu *et al* [42] and Mittal *et al* . [79].

According to Tennekes and Lumley [113] three regions are usually present in power spectra: one of which is the large subrange containing the energies of the injected flow in a very small frequency region; the second one is the inertial subrange where the eddy structure is independent of viscosity and the spectrum slope is $-5/3$, which is also called the broadband frequency region; and the rest is the viscous dissipation subrange for the high frequencies. The range of the broadband frequency found in frames (a-e) of Fig. 4.24 are approximately the same, but it is small in the far downstream location, frame (f). In addition, the change of slope of the power spectra from $-5/3$ to $-10/3$ at the region of large Strouhal number, which is also consistent with the results of Lu *et al* . [42], represents the transfer of energy from the turbulent flow to the acoustic fluctuations and is the main cause of arterial murmurs. A further change of slope from $-10/3$ results in the viscous dissipation subrange where the kinetic energy converts into heat through the action of viscosity. However, this region is very small in our investigation.

Fig. 4.25 presents the corresponding normalised energy spectra, $E_{p''p''}$, for the pressure fluctuations, $p''^2/(\rho\bar{V}^2_{max})^2$, along with the straight lines of $(Sr)^{-5/3}$ and $(Sr)^{-7/3}$. In every frame the spectra containing the inertial/broadband region in-

dicate the energy contained eddies of the turbulent flow in the post stenosis, and the change of slope from $-5/3$ to $-7/3$ represents the transfer of energy from the pressure fluctuations spectra to the sound spectra which is again a further source of murmurs of the arterial stenosis. Moreover, likewise the velocity spectra, the broadband frequency found in frames (a-e) is larger than that of the spectra of slope $-7/3$, and in frame (f) the broadband region is very small where the turbulent intensity is relatively low.

4.6.6 Effects of the Amplitude of Oscillations

The effects of the amplitude of the inlet pulsatile oscillation on the development of transition to turbulent flow downstream of the stenosis are investigated in this section. Fixing the Reynolds number to 1000, the amplitude (A) of the oscillation is varied between 0.1 and 0.4 with an interval of 0.1, which corresponds to 10%, 20%, 30% and 40% oscillations respectively to the mean flow. The results of the variation of the amplitude are presented in Fig. 4.26 in terms of the mean and turbulent kinetic energy. As seen in Fig. 4.26(a), the mean kinetic energy grows rapidly in the immediate post stenosis region as the percentage of the oscillation increases. The turbulent kinetic energy in Fig. 4.26(b) is also strongly affected by this. In particular, the maximum turbulent kinetic energy for 30% and 40% oscillations occurs between $y/L = 0.0$ and $y/L = 2.0$, while for 10% and 20% it occurs between $y/L = 4.0$ and $y/L = 6.0$. So for the large oscillation the transition to turbulent happens earlier with large turbulent intensity, whereas the transition delays for the small oscillation.

4.7 Conclusion

In this Chapter, Large Eddy Simulation with a dynamic sub-grid model has been applied to study a simple sinusoidal pulsatile flow through a 3D model of arterial stenosis. In particular we have investigated the pulsatile nature of the transition to turbulent flow downstream of the stenosis. In the model, the stenosis was placed eccentrically at the upper wall of the channel which reduced the cross-sectional area of the channel by 50%. Three different Reynolds numbers, 1200, 1300 and

1500, based on the bulk velocity, were chosen for this study – the choices of these Reynolds numbers are realistic for human arteries, Ku [9].

We have found that the flow characteristics, the turbulent kinetic energy, the root mean square of the turbulent fluctuations, etc, are highly dependent on the flow Reynolds number, and they are enhanced by the increment of the Reynolds number. The level of turbulent fluctuations found downstream of the stenosis could activate the blood platelets and damage the blood cell materials and consequently, they could create many pathological diseases.

For $Re = 1500$ (corresponding to peak Reynolds number, $Re_p = 1950$), we have found that the SGS contributes a maximum of about 70.9% energy diffusion into the flow downstream of the stenosis where the flow becomes turbulent. This is again an important finding in the application of LES for studying pulsatile flow in the arterial stenosis. However, the contribution of SGS reduces as the Reynolds number is reduced and it is quite small for $Re = 1200$. When $Re \leq 1200$ the numerical results can be treated as DNS solutions.

The shear stresses for the upper wall drop at the centre of the stenosis, where the adverse pressure gradient exists – the same phenomena were reported by Ojha *et al* [81], Tutty [80], Mallinger and Drikakis [72] and Frydrychowicz *et al* [12]. However, Mittal *et al* [79] found high shear stresses at the upper wall, which is opposite to present finding and the above three papers reported. It is also found the shear stresses on the lower wall are quite high, which could smash up the inner lining of the artery. These findings, however, are consistent with the results of Mittal *et al* . [79]. In addition, the presence of a permanent recirculation region seen in the immediate downstream region of the stenosis and the earlier transition to turbulent for the pulsatile flow when the amplitude of the oscillation is increased agree quite well with the experimental studies of Ojha *et al* [81].

In this Chapter, an additive type sinusoidal pulsatile velocity profile is used for generating the time dependent pulsation at the inlet. In the next Chapter, (Chapter 5) a non-additive type pulsatile profile will be used and results will be compared with those of the additive pulsatile case.

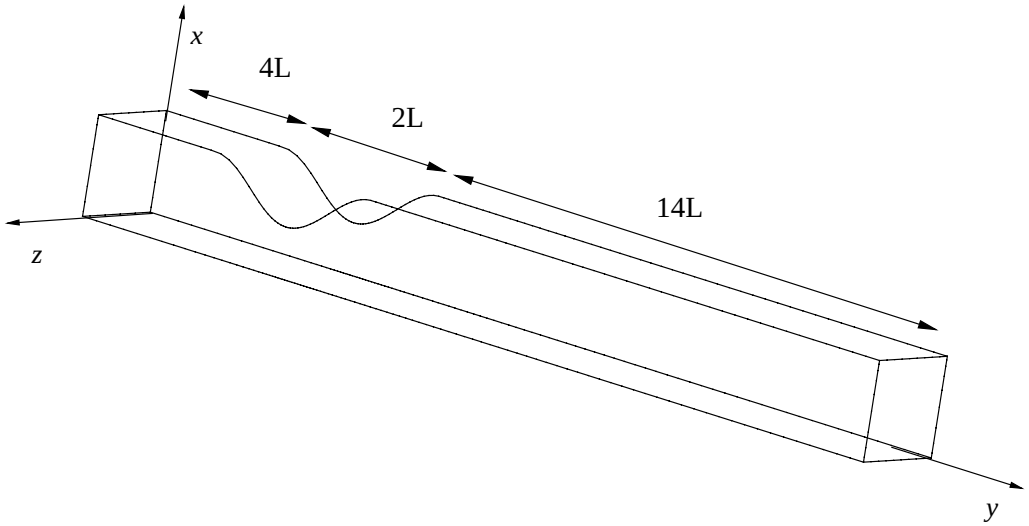

Figure 4.1: A schematic of the model with coordinate system.

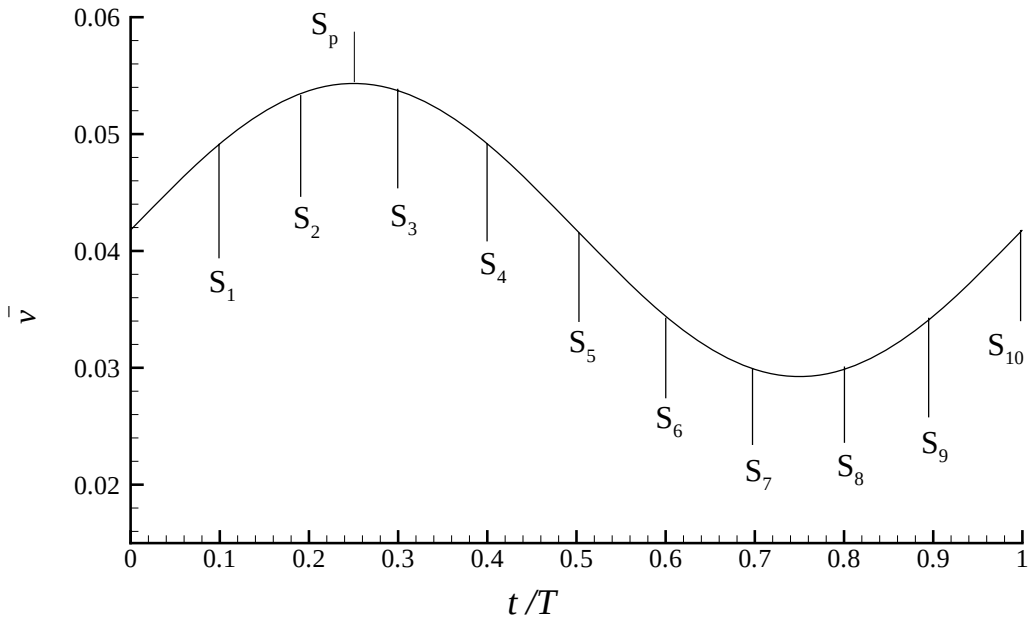

Figure 4.2: Inlet pulsatile velocity profile, $\bar{v}$. Different phases are marked by S_i ($i = 1, 2, \cdots 10$) and S_p is the peak phase.

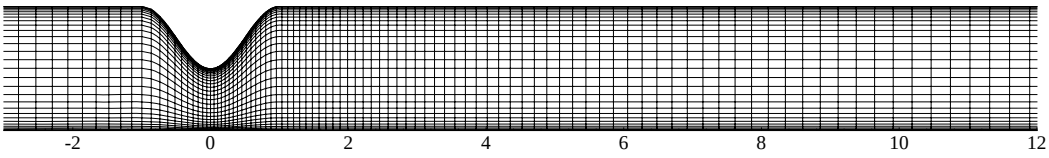

Figure 4.3: A crude mesh distribution in $x - y$ plane.

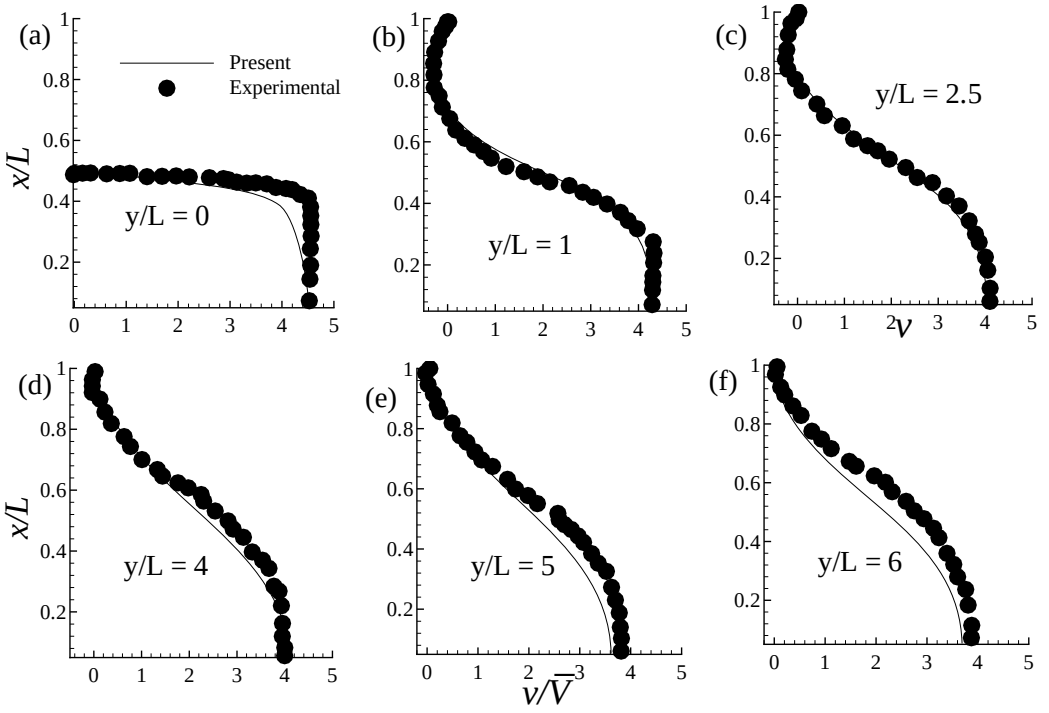

Figure 4.4: Streamwise velocity comparison with the experimental data of Ahmed and Giddense [1] for 75% stenosis while $Re = 500$.

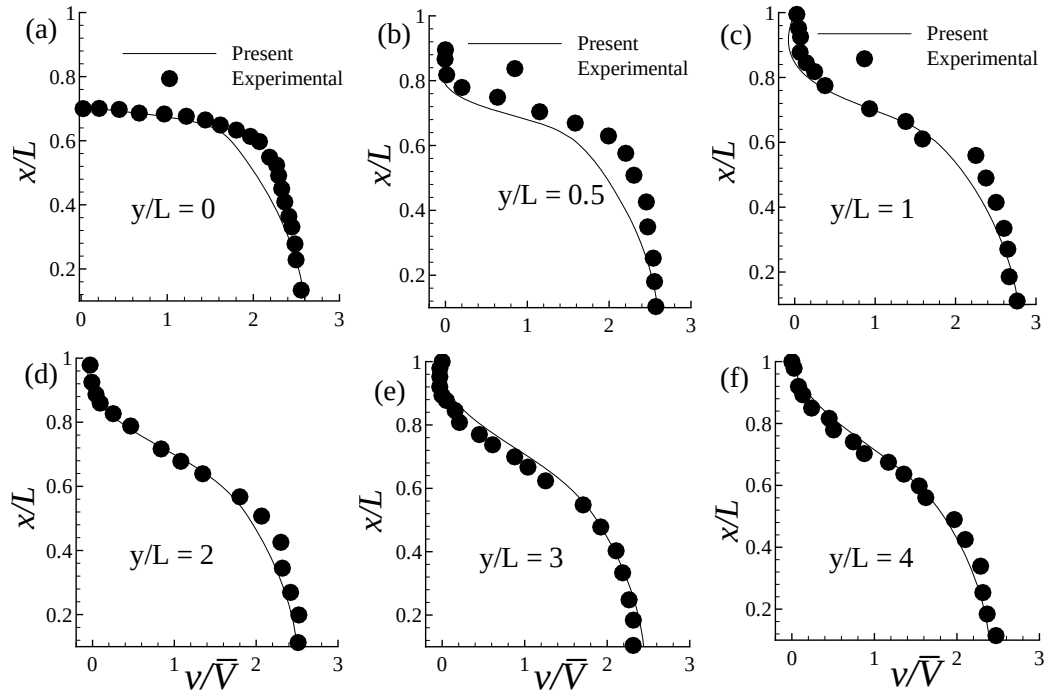

Figure 4.5: Streamwise velocity comparison with the experimental data of Ahmed and Giddense [1] for 50% stenosis while $Re = 1000$.

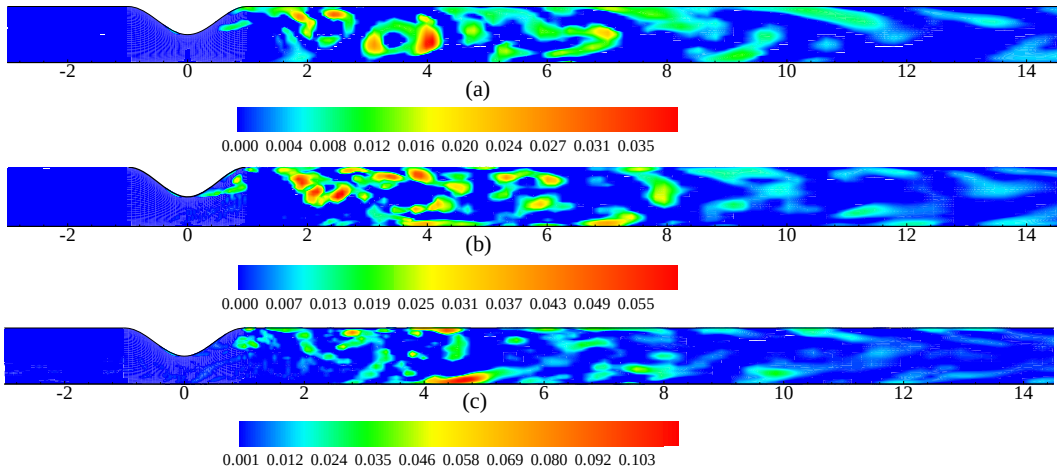

Figure 4.6: Dynamic Smagorinsky constant, C_s, at $t/T = 10.25$ for (a) $Re = 1200$, (b) $Re = 1300$ and (c) $Re = 1500$.

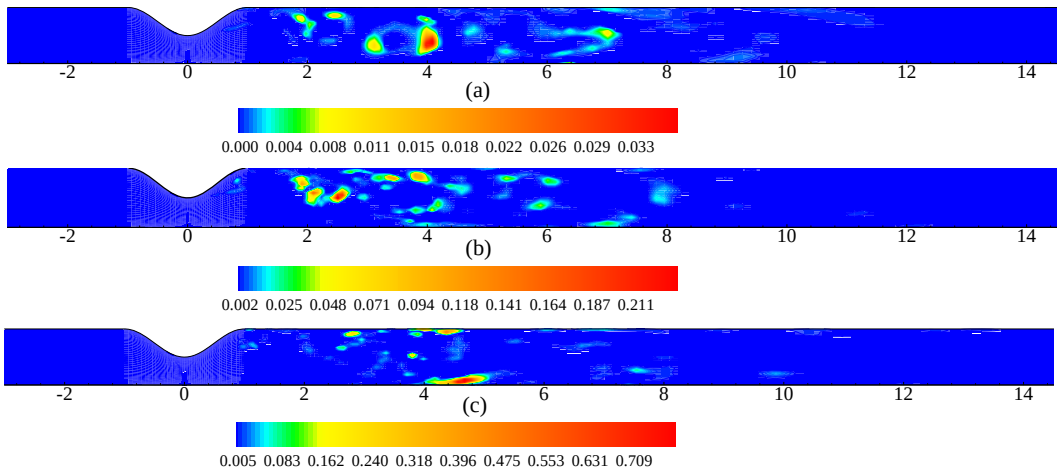

Figure 4.7: Normalised SGS eddy viscosity, μ_{sgs}/μ, at $t/T = 10.25$ for (a) $Re = 1200$, (b) $Re = 1300$ and (c) $Re = 1500$.

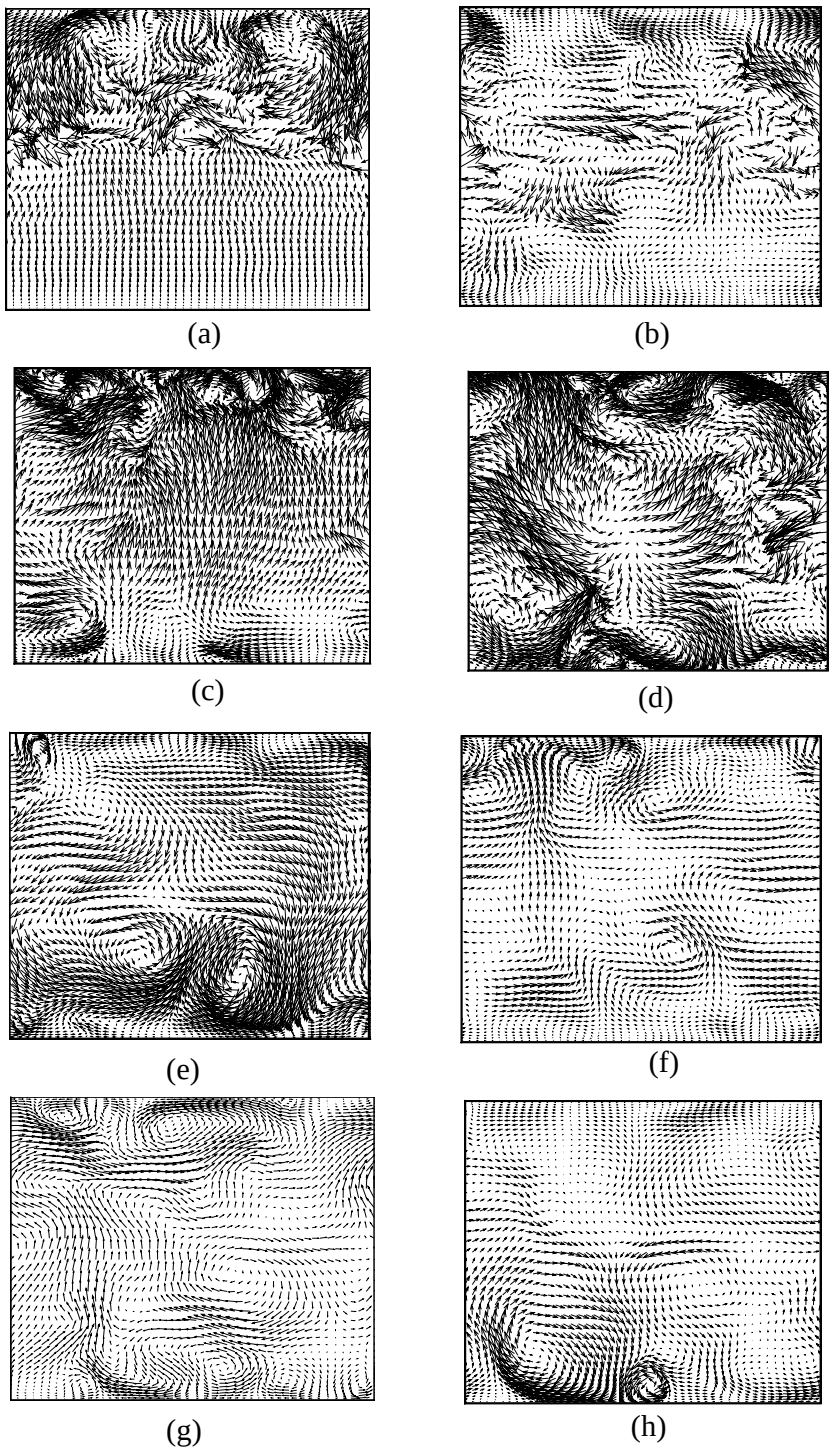

Figure 4.8: Instantaneous vectors based on the velocity componenets $\bar{u} - \bar{w}$ are plotted at (a) $y/L = 1$, (b) $y/L = 2$, (c) $y/L = 3$, (d) $y/L = 4$, (e) $y/L = 5$, (f) $y/L = 6$, (g) $y/L = 7$ and (h) $y/L = 8$ while $Re = 1500$ and $t/T = 10.25$.

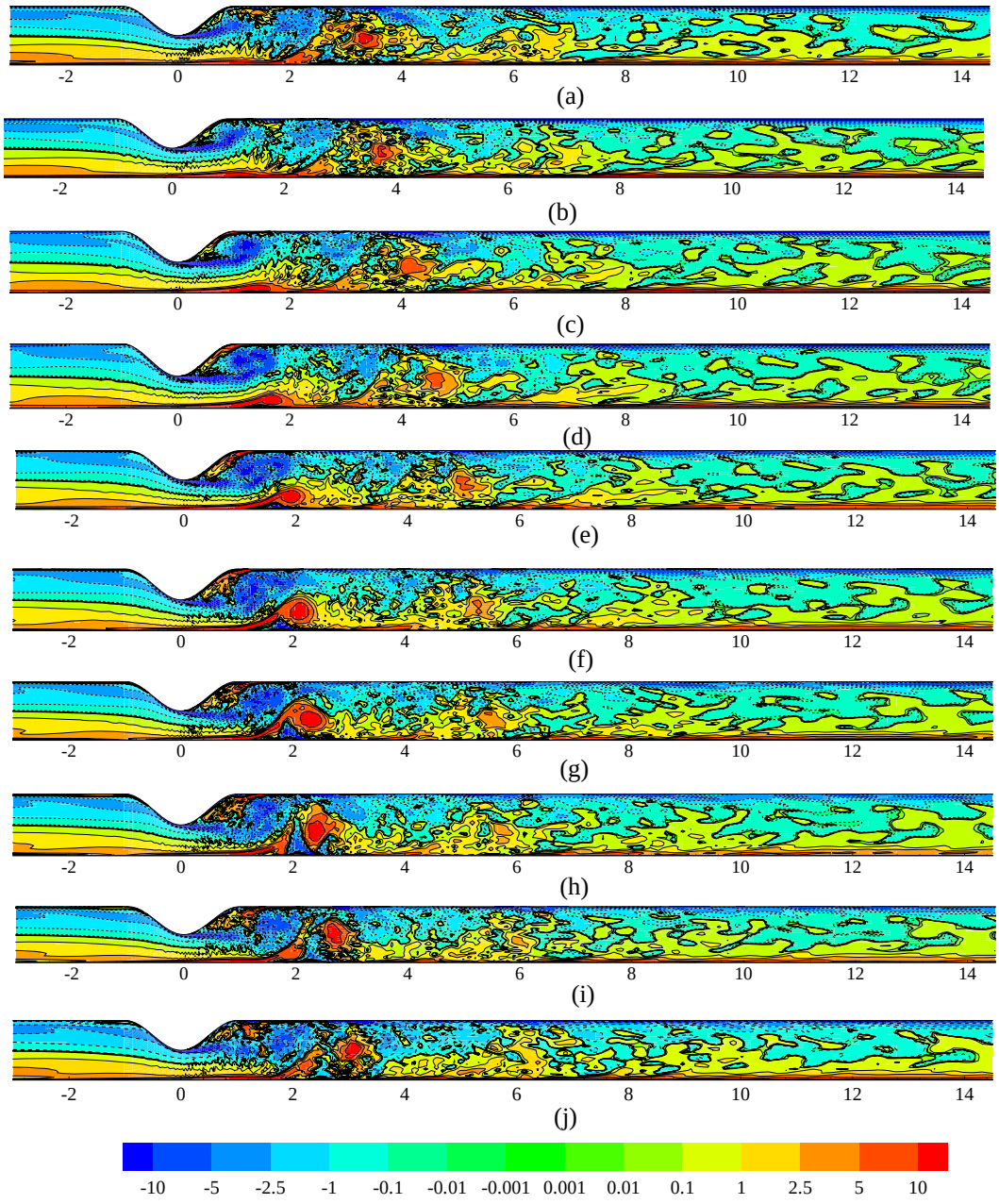

Figure 4.9: Sequence of the spanwise average vorticity, ω_z, at different positions of phase while $Re = 1500$. Here (a) S_1, (b) S_2, (c) S_3, (d) S_4, (e) S_5, (f) S_6, (g) S_7, (h) S_8, (i) S_9, and (j) S_{10}, see Fig. 4.2.

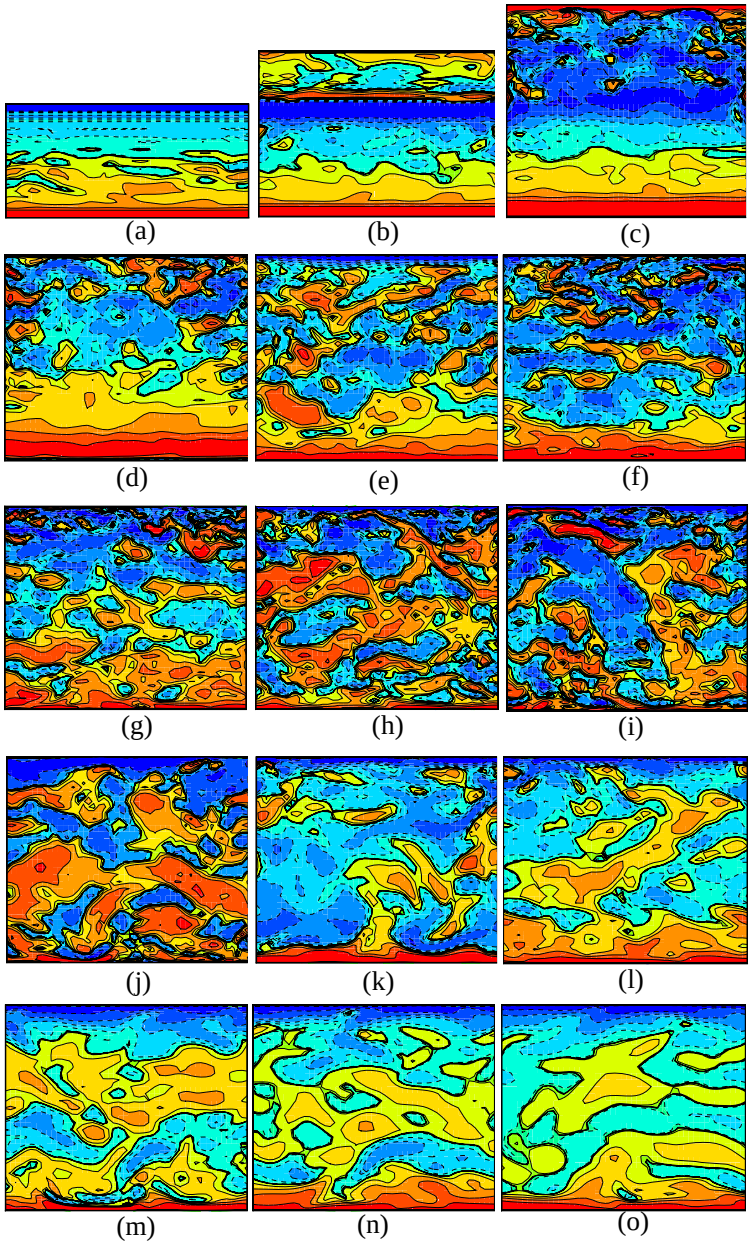

Figure 4.10: Instantaneous cross-sectional vorticity, ω_z, plotted at (a) $y/L = 0$, (b) $y/L = 0.5$, (c) $y/L = 1$, (d) $y/L = 1.5$, (e) $y/L = 2$, (f) $y/L = 2.5$, (g) $y/L = 3$, (h) $y/L = 3.5$, (i) $y/L = 4$, (j) $y/L = 4.5$, (k) $y/L = 5$, (l) $y/L = 6$, (m) $y/L = 8$, (n) $y/L = 10$ and (o) $y/L = 12$ while $Re = 1500$ and $t/T = 10.25$.

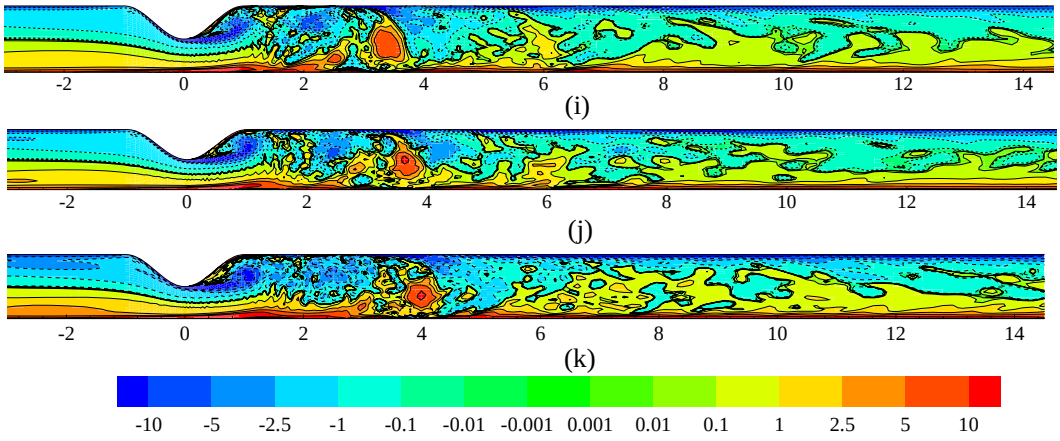

Figure 4.11: Spanwise avarage vorticity, ω_z, at $t/T = 10.25$ for (i) $Re = 1200$, (j) $Re = 1300$ and (k) $Re = 1500$.

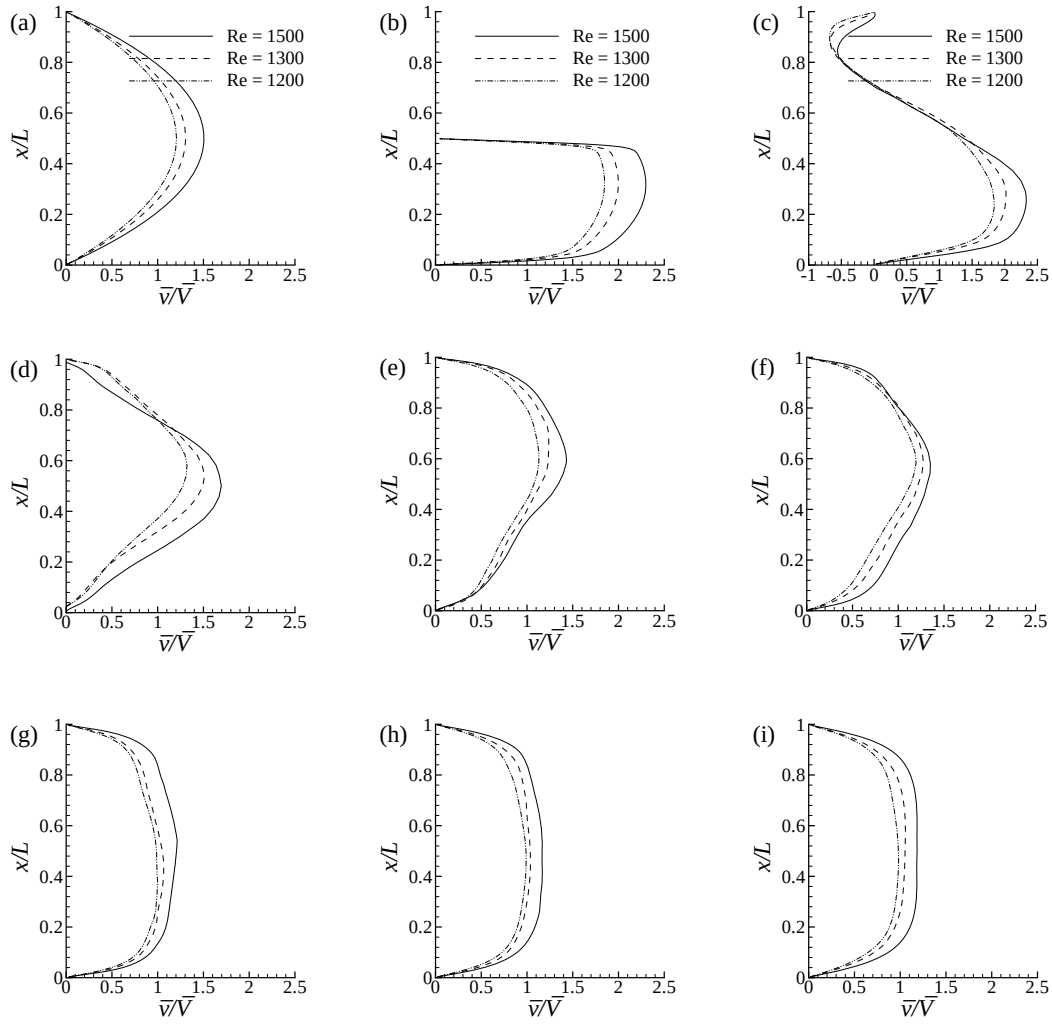

Figure 4.12: Time-mean axial velocity, $< \bar{v} > /\bar{V}$, at (a) $y/L = inlet$, (b) $y/L = 0.0$, (c) $y/L = 1.0$, (d) $y/L = 2.0$, (e) $y/L = 3$, (f) $y/L = 4.0$, (g) $y/L = 6.0$, (h) $y/L = 8.0$ and (i) $y/L = outlet$ for different Reynolds numbers.

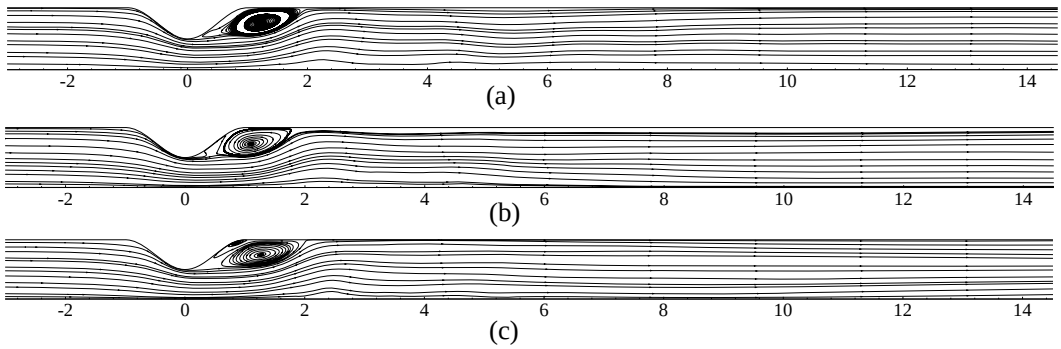

Figure 4.13: Time-mean streamlines for (a) $Re = 1200$, (b) $Re = 1300$ and (c) $Re = 1500$.

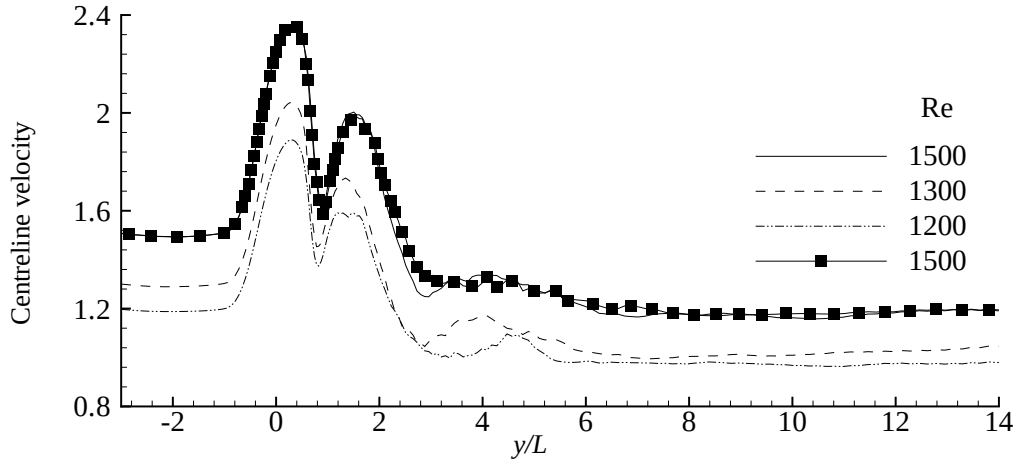

Figure 4.14: Time-mean centreline streamwise velocity, $< \bar{v} > /\bar{V}_{max}$, at the different Reynolds numbers.

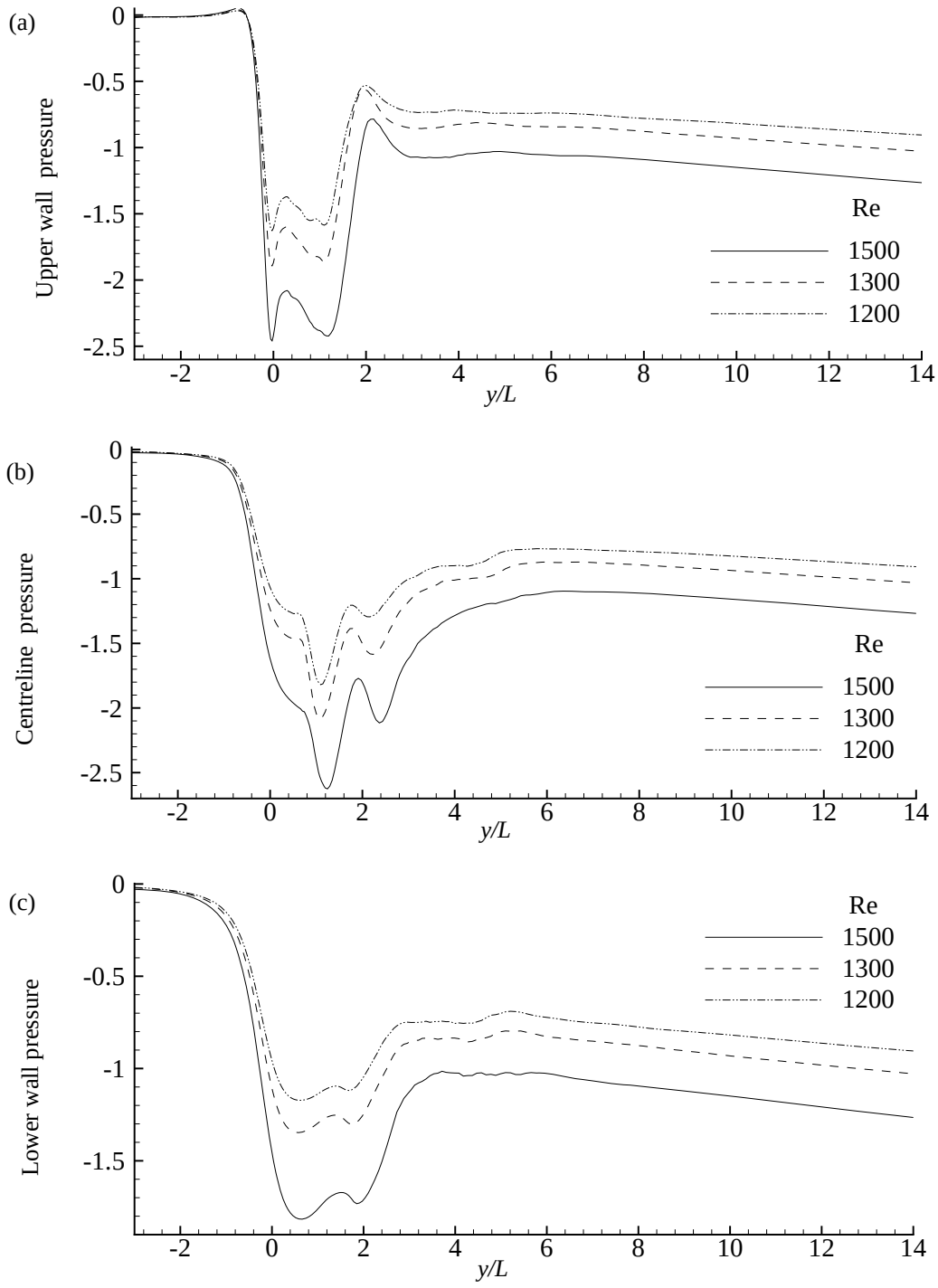

Figure 4.15: Time-mean pressure, $< \bar{P} > / \rho \bar{V}_{max}^2$, at (a) lower wall (b) centreline and (c) upper wall for the different Reynolds numbers.

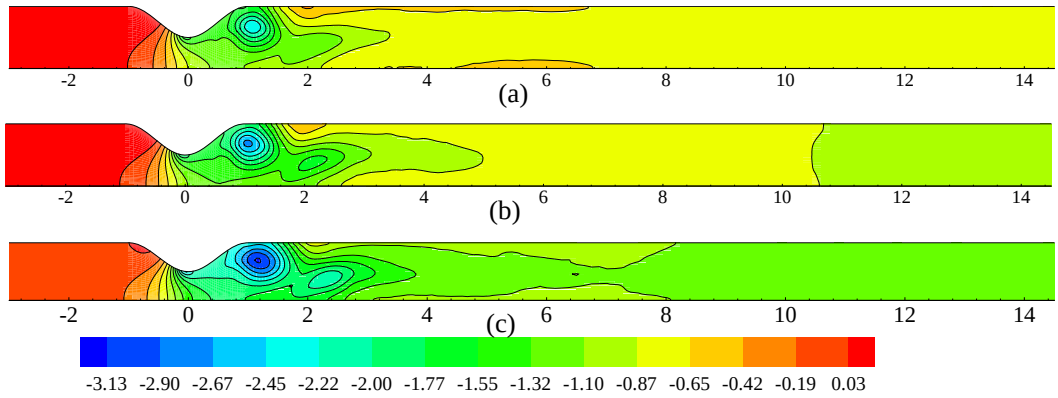

Figure 4.16: Time-mean pressure contour plot for (a) $Re = 1200$, (b) $Re = 1300$ and (c) $Re = 1500$.

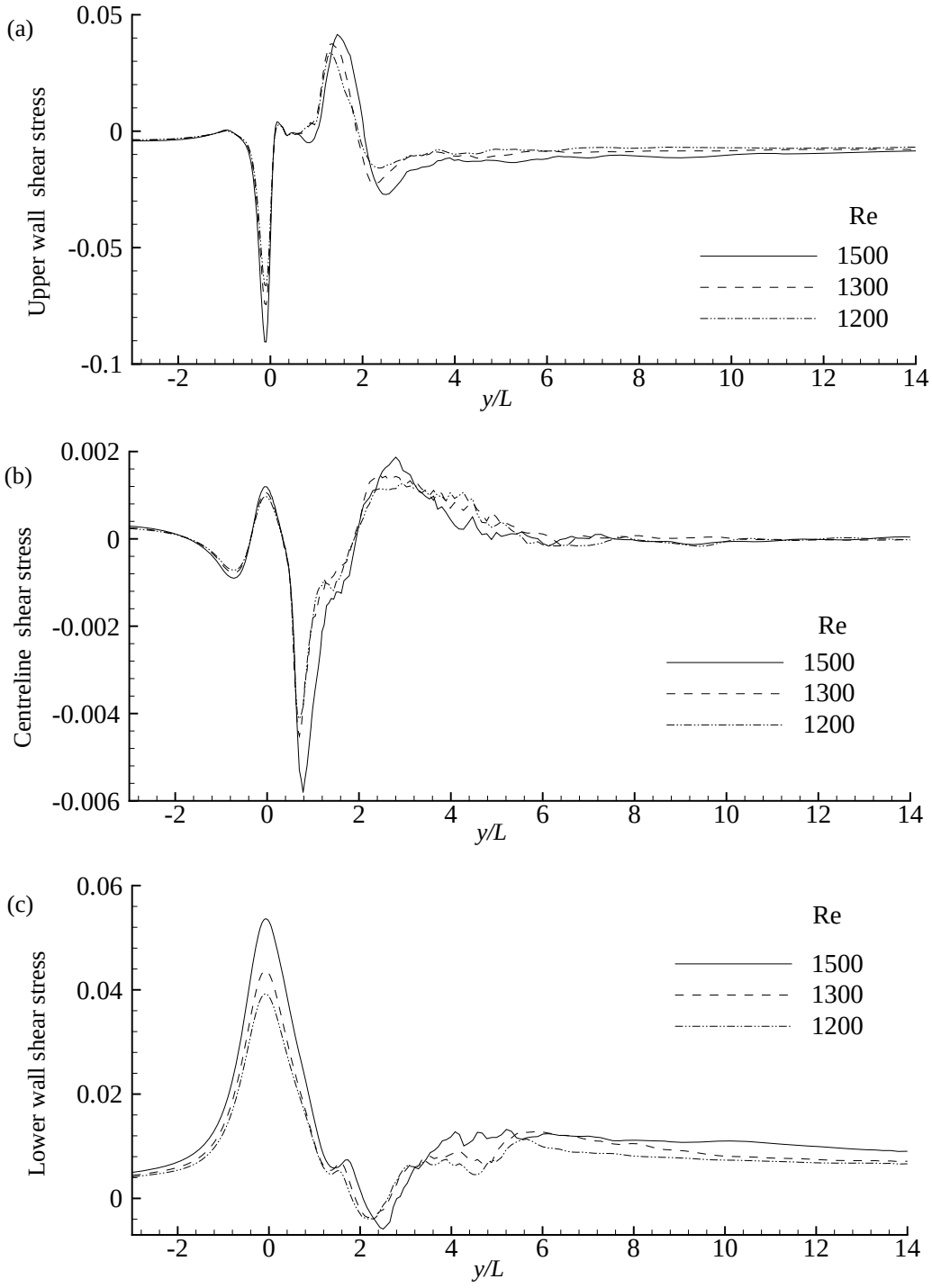

Figure 4.17: Time-mean shear stresses, $< \tau_{xy} > /\rho \bar{V}_{max}^2$, at (a) lower wall (b) centreline and (c) upper wall for the different Reynolds numbers.

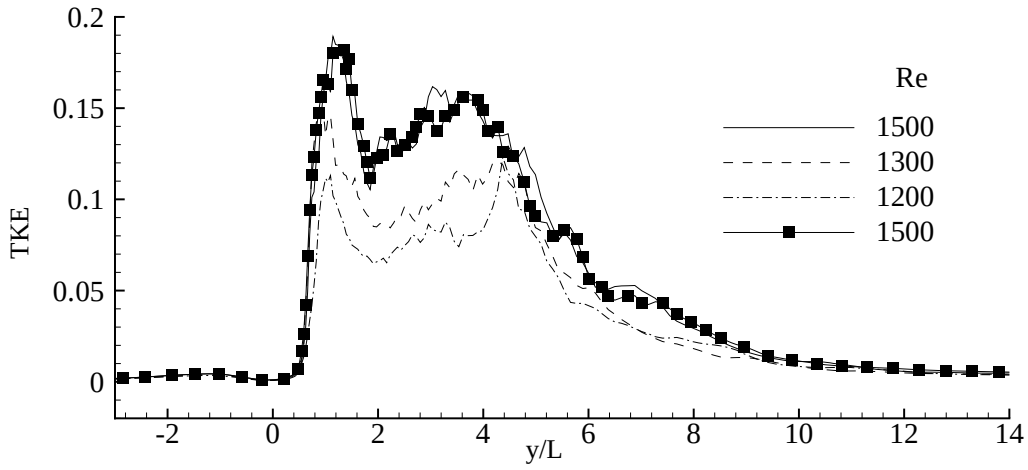

Figure 4.18: Centreline turbulent kinetic energy, $\frac{1}{2} < u_j'' u_j'' > / \bar{V}_{max}^2$, for the different Reynolds numbers.

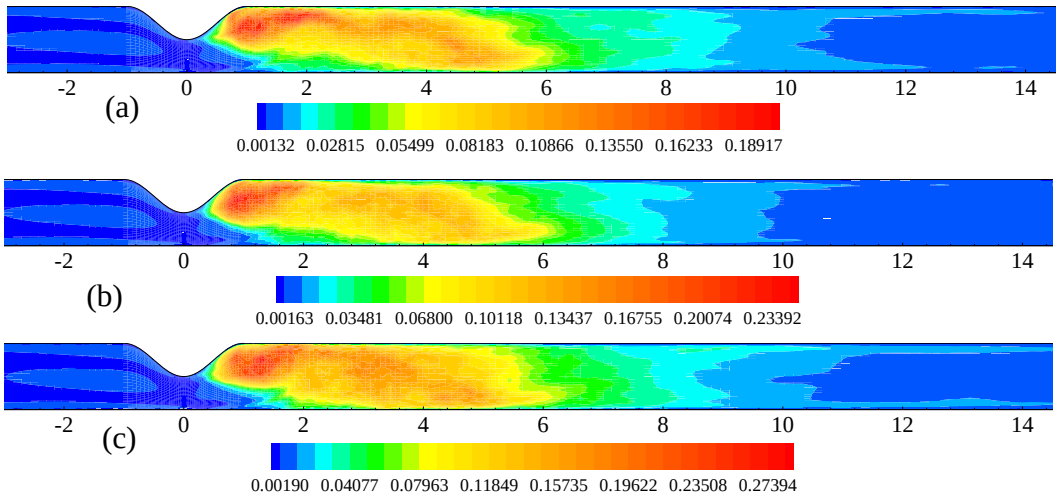

Figure 4.19: Contour plots of the turbulent kinetic energy, $\frac{1}{2} < u_j'' u_j'' > / \bar{V}_{max}^2$, for (a) $Re = 1200$, (b) $Re = 1300$ and (c) $Re = 1500$.

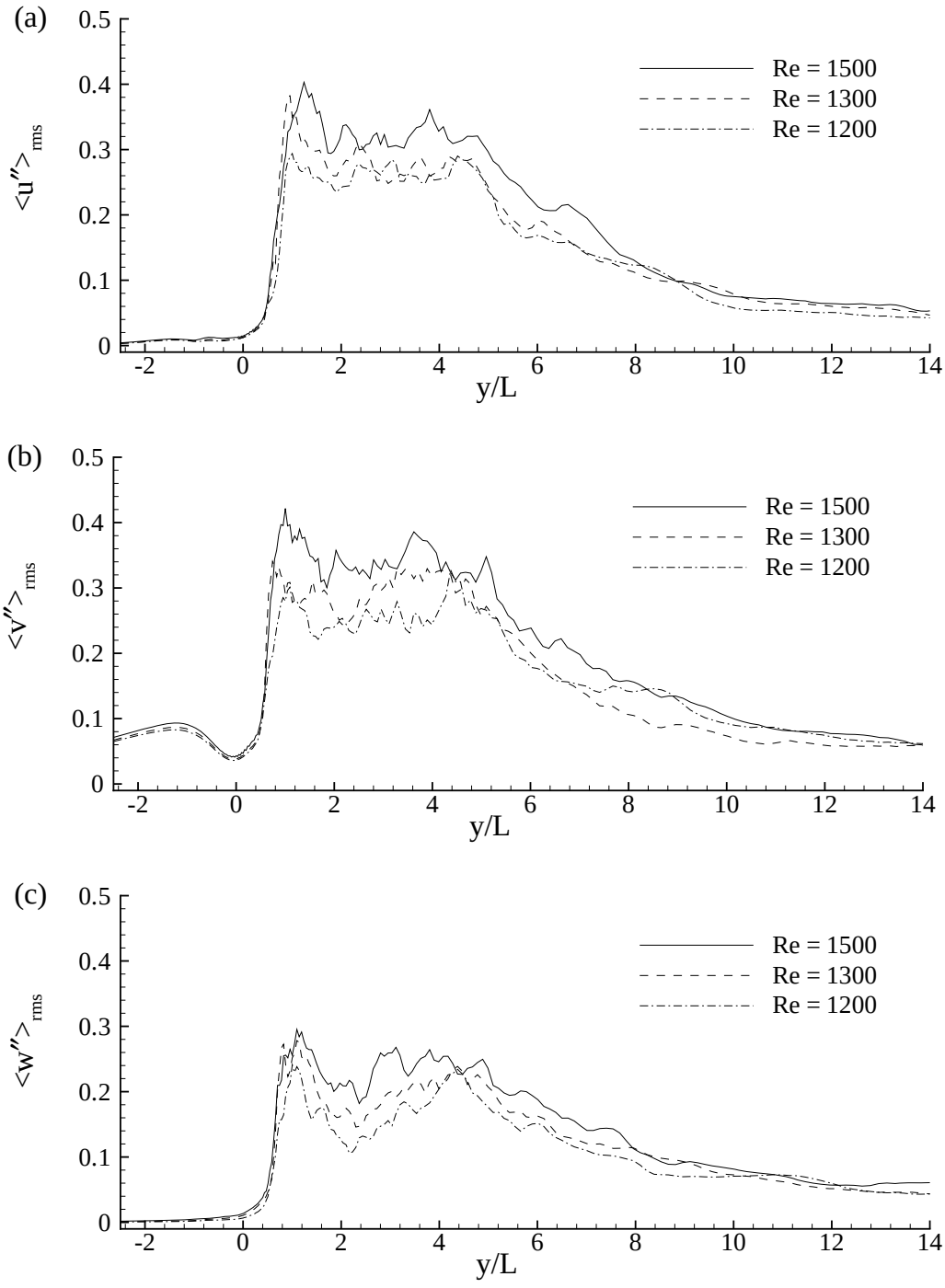

Figure 4.20: rms of the centreline velocity fluctuations (a) $< u'' >_{rms} /\bar{V}_{max}$, (b) $< v'' >_{rms} /\bar{V}_{max}$ and (c) $< w'' >_{rms} /\bar{V}_{max}$ for the different Reynolds numbers.

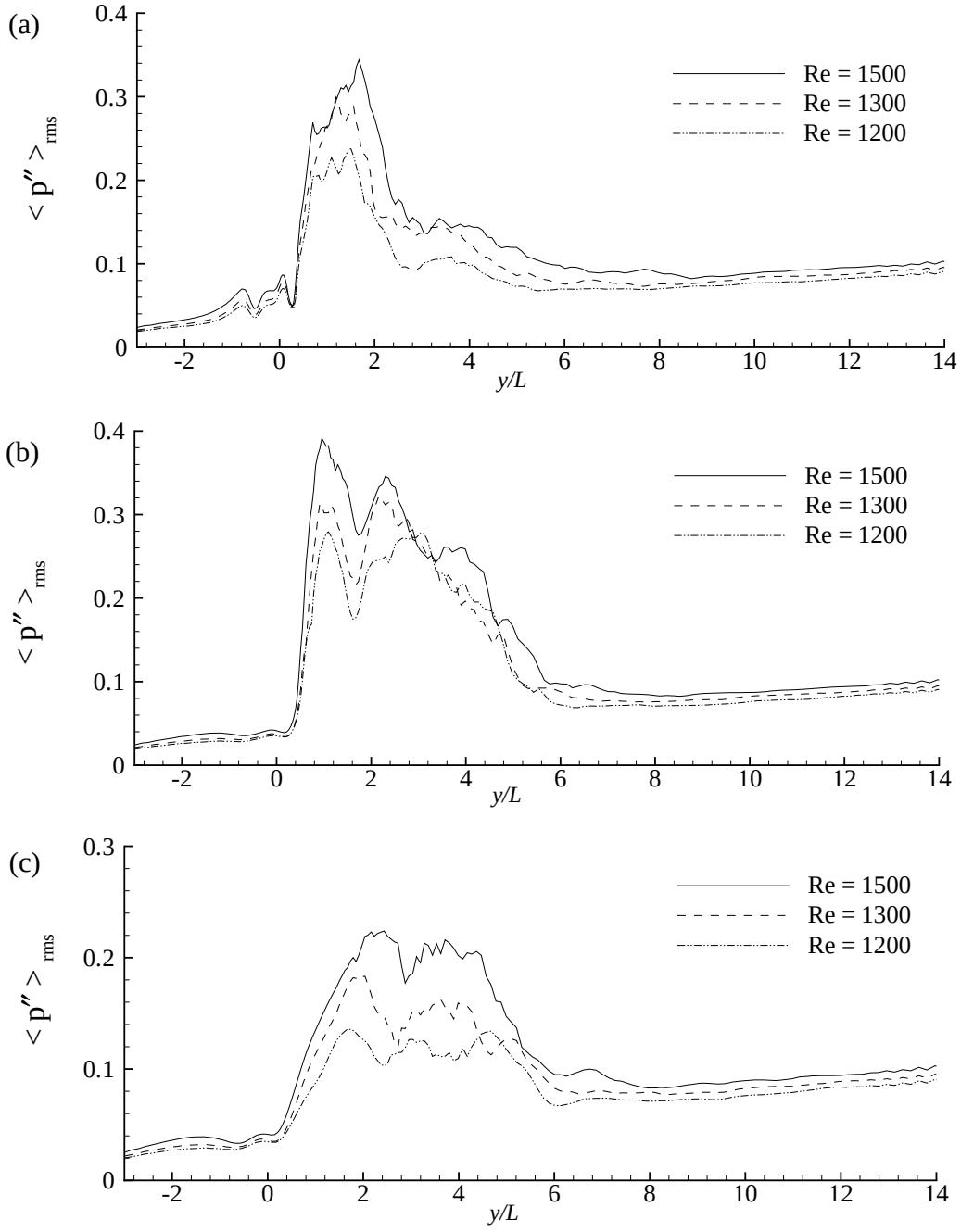

Figure 4.21: rms of the pressure fluctuations, $< p'' >_{rms} / \rho \bar{V}_{max}^2$, at (a) upper wall (b) centreline and (c) lower wall for the different Reynolds numbers.

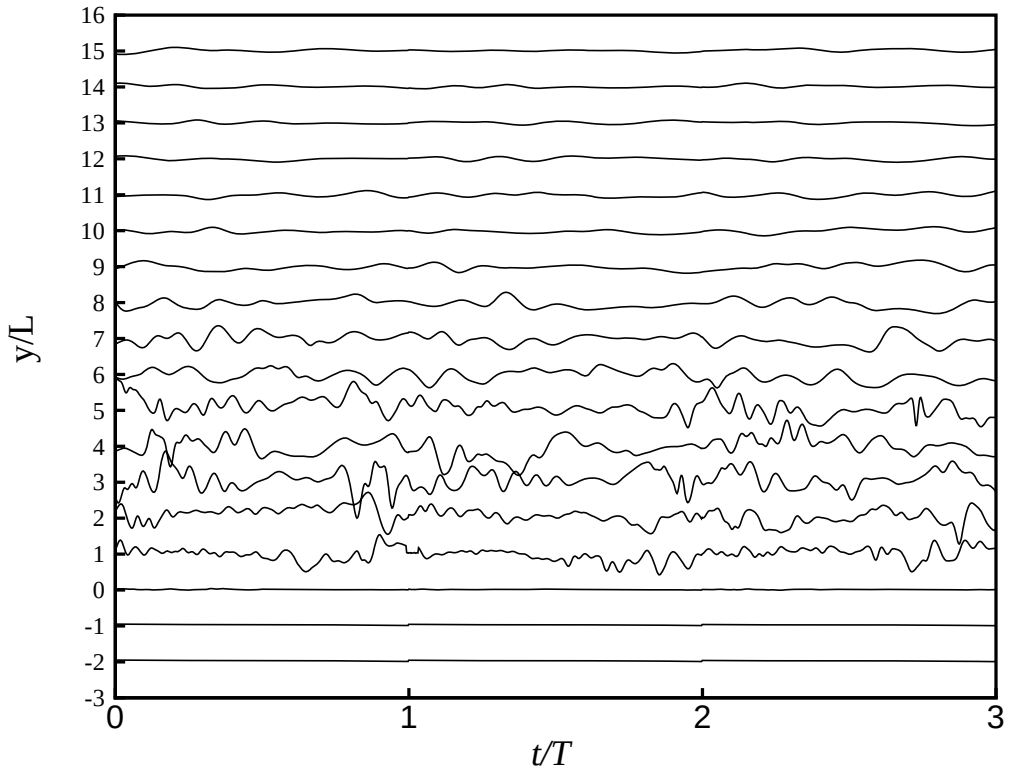

Figure 4.22: Velocity fluctuations, v''/v''_{max}, at different positions of y/L for $Re = 1500$.

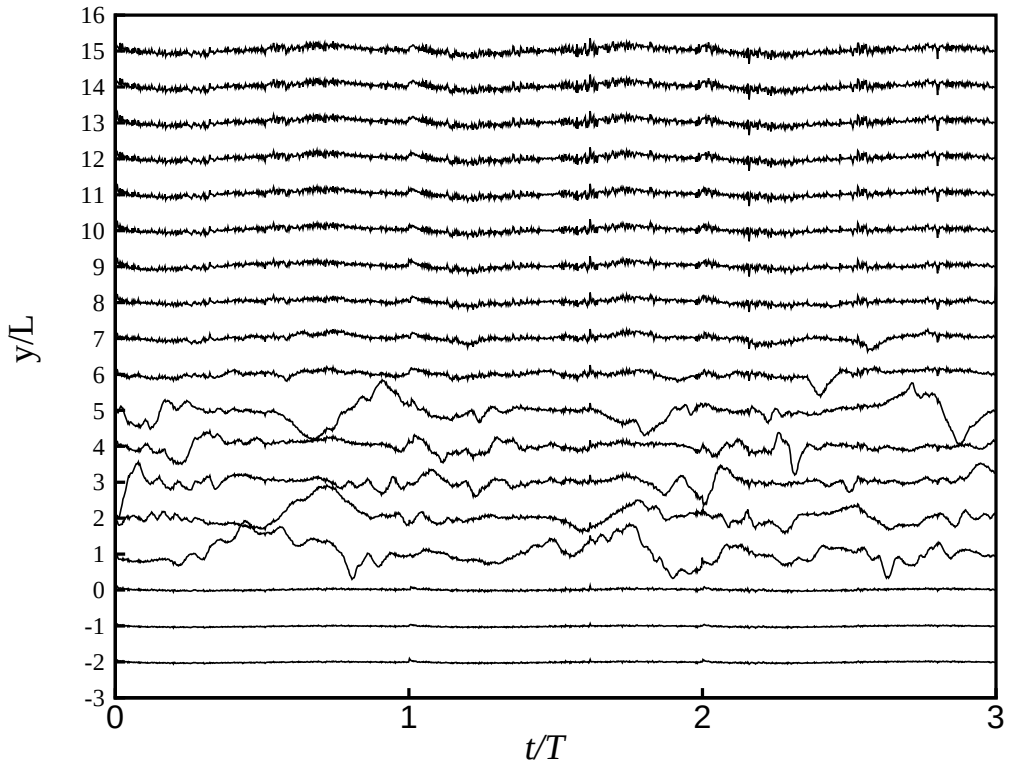

Figure 4.23: Pressure fluctuations, p''/p''_{max}, at different positions of y/L for $Re = 1500$.

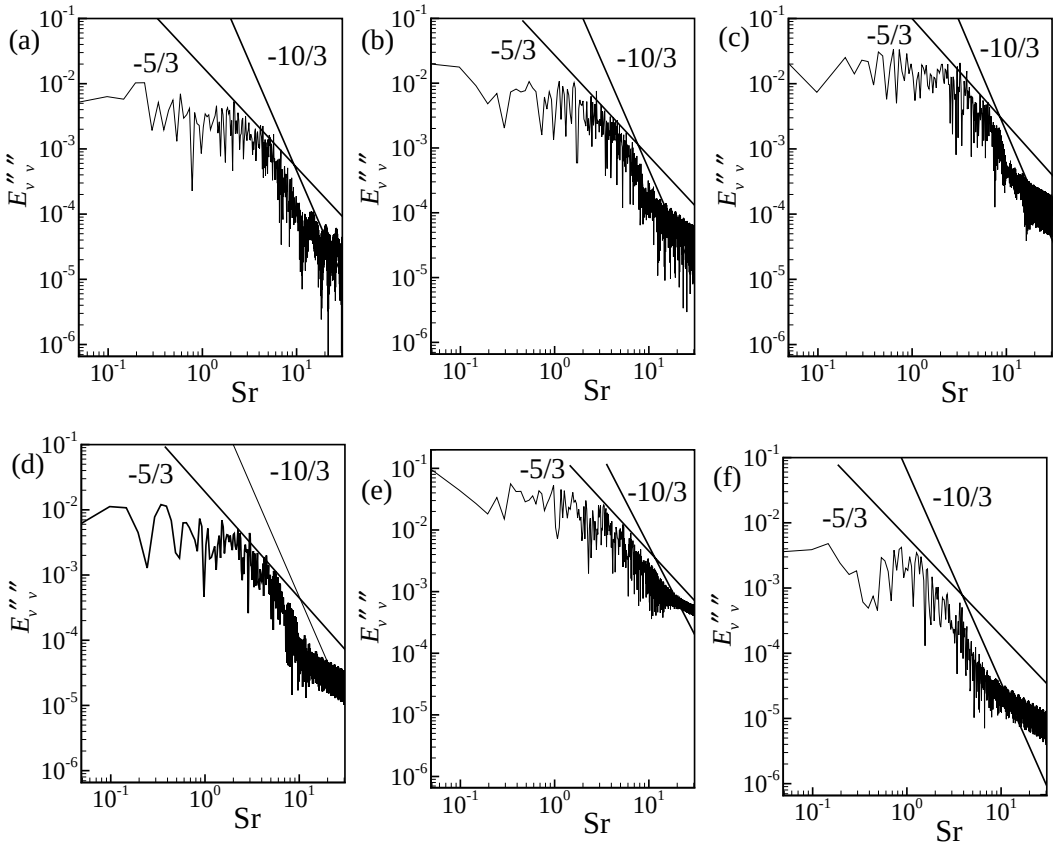

Figure 4.24: Energy spectra of the centreline velocity fluctuations, v'', at (a) $y/L = 1.0$, (b) $y/L = 2.0$, (c) $y/L = 3.0$, (d) $y/L = 4.0$, (e) $y/L = 5.0$ and (f) $y/L = 6.0$ while $Re = 1500$.

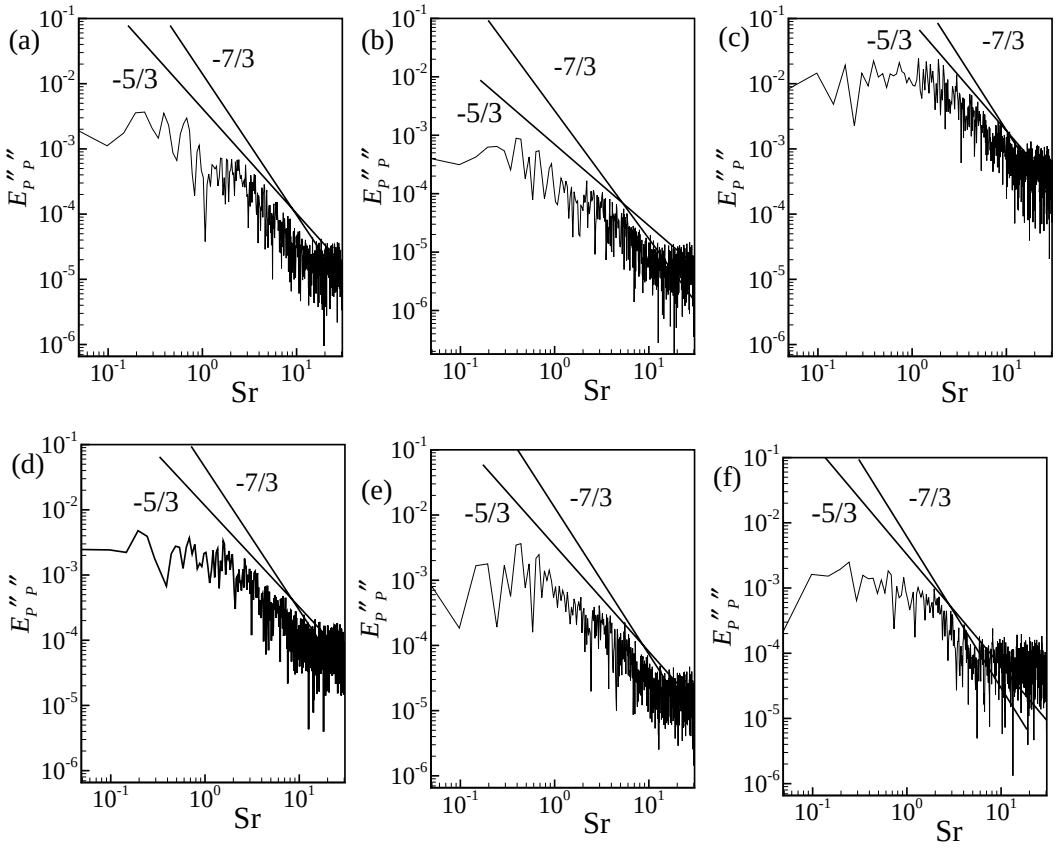

Figure 4.25: Energy spectra of the pressure fluctuations, p'', at (a) $y/L = 1.0$, (b) $y/L = 2.0$, (c) $y/L = 3.0$, (d) $y/L = 4.0$, (e) $y/L = 5.0$ and (f) $y/L = 6.0$ while $Re = 1500$.

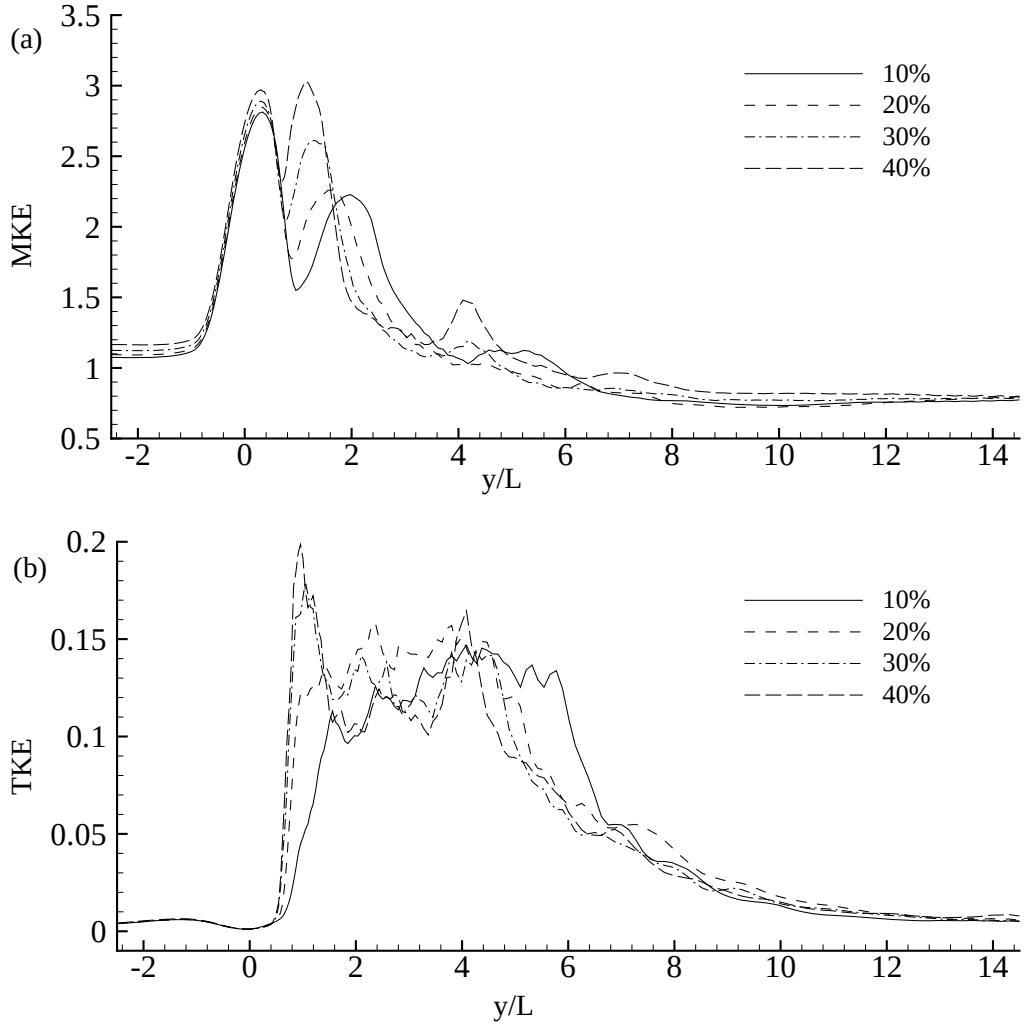

Figure 4.26: Effects of the amplitude of oscillation showing on the centreline (a) mean kinetic energy (MKE), $\frac{1}{2} < u_j u_j > /\bar{V}_{max}^2$ and (b) turbulent kinetic energy (TKE), $\frac{1}{2} < u_j'' u_j'' > /\bar{V}_{max}^2$, for $Re = 1000$.

Chapter 5

LES of Sinusoidal Pulsatile Flow in a Model Arterial Stenosis. Part 2. Additive Vs. Non-additive Oscillation

5.1 Introduction

In the previous chapter, an additive type pulsatile velocity profile was used at the inlet of the model geometry where the streamwise mean velocity is simply added to a sinusoidal oscillation. However, it was argued by Pedley [109] that a highly pulsatile flow is not believed to be additive, i.e. non-additive. Thus, the main focus of this chapter is to investigate the post-stenotic phenomena of pulsatile flow by applying a non-additive type pulsation. In the non-additive pulse, the flow rate is controlled in such a way that it becomes zero at the start and end of every pulsation.

As in Chapter 4, the large scale flows are resolved fully and the unresolved SGS motions are modelled using the Germano-Lilly [2; 3] dynamic model. A grid independence test is done for $Re = 2000$ with three different sets of grid arrangement. In addition, comparisons of the results of non-additive pulsatile case are made with those of both the additive pulsatile and steady flows and they show some distinct natures of the flow transition downstream of the stenosis.

5.2 Inlet Boundary Condition

In the case of a simple steady inflow profile, the fully developed streamwise velocity imposed at the inlet of the channel is derived as

$$\bar{v}(x) = 6\bar{V}\frac{x}{L}\left(1 - \frac{x}{L}\right), \tag{5.1}$$

where $\bar{V}$ is the average streamwise velocity.

To generate the additive pulsatile velocity profile at the inlet, the above parabolic inflow is varied with time in a way that the volumetric flow rate per unit channel width, L, varies according to

$$Q(t) = Q_{mean}\left[1 + A\sin\left(\frac{2\pi t}{T}\right)\right], \tag{5.2}$$

where T and A are the time period and the amplitude of the pulsation, respectively. Therefore, the streamwise velocity for the additive pulsation was derived as,

$$\bar{v}(x,t) = 6\bar{V}(t)\frac{x}{L}\left(1 - \frac{x}{L}\right) = 6\bar{V}_{max}\frac{x}{L}\left(1 - \frac{x}{L}\right)\left[1 + A\sin\left(\frac{2\pi t}{T}\right)\right], \tag{5.3}$$

where $\bar{V}_{max}$ is the bulk or avearge velocity, Q_{mean} is the mean flow rate and the Reynolds number is now defined as $Re = \bar{V}_{max}L/\nu$. It is clear from the above relations (5.2-5.3) that the volumetric flow rate with the additive pulsatile profile never gets to zero at any position of time when $|A| < 1$. Note that similar velocity profile was used by Lee *et al* [141] to study the effects of additive pulsatile amplitude on unsteady laminar flow in a pipe with ring-type stenosis or constriction.

In the non-additive pulsatile case, the parabolic inflow shown in Eq. (5.1) varies in a manner similar to Tutty [80], where the volumetric flow rate, $Q(t)$, per unit channel width, L, is varied in a sinusoidal manner with time as

$$Q(t) = \frac{Q_{mean}}{2}\left[1 - \cos\left(\frac{2\pi t}{T}\right)\right], \tag{5.4}$$

so that the flow rate at the start and end of every pulsation becomes zero and the maximum occurs at the mid-location of every pulse. Finally, the streamwise veloc-

Table 5.1: Mesh details for the computations.

Case	Re	N_x	N_y	N_z	T	δt
0	< 2000	50	200	50	2π	10^{-3}
1	2000	50	200	50	2π	10^{-3}
2	2000	50	250	50	2π	10^{-3}
3	2000	70	250	50	2π	10^{-3}

ity profile for the non-additive pulsation is formulated as

$$\bar{v}(x,t) = 6\bar{V}(t)\frac{x}{L}\left(1-\frac{x}{L}\right) = 3\bar{V}_{max}\frac{x}{L}\left(1-\frac{x}{L}\right)\left[1-\cos\left(\frac{2\pi t}{T}\right)\right]. \qquad (5.5)$$

In Fig. 5.1 the volumetric flow rate, $Q(t)/Q_{mean}$, for the additive and non-additive pulsatile profiles are illustrated graphically for one-cycle to show clearly the variation of the flow rates between the two pulses. Here $A = 0.5$ is used for the amplitude of the additive sine pulse. The peak-to-mean ratio for the non-additive pulsatile profile is 0.5, while the ratio for the additive pulse varies with its amplitude, A.

5.3 Results and Discussion

5.3.1 Mesh Independence Test

In order to check what would be the appropriate grid density that is required for LES to resolve the flow generated by the non-additive pulsation, simulations were run for three different grid arrangements for $Re = 2000$ as shown in Table 5.1. The results of this mesh independence test are presented in Fig. 5.2 for the mean streamwise velocity at four different axial positions (frames a, b) and for the mean kinetic energy (MKE) along the centre of the model (frame c). Note that the streamwise velocity results in frames (a-b) have been normalised by the average velocity, $\bar{V}_{max}$.

It can be seen in this figure that the comparison agrees quite well, which clearly indicates that the flow resolution is not remarkably sensitive to these grid arrangements. In addition, a comparison of the turbulent kinetic energy (TKE) is presented

in Fig. 5.3 showing a satisfactory agreement. Therefore, based on this agreement and to minimise the computational space and time, Case 1: $50 \times 200 \times 50$ grid is assumed to be sufficient for the LES at $Re = 2000$. The same grid was used for the computations of steady, additive and non-additive pulsations for other Reynolds numbers less than 2000.

5.3.2 Additive Vs. Non-additive Pulsations

In this section the development and structure of the transient flow downstream of the stenosis for the non-additive pulsations will be compared with those of the additive pulsatile and steady flows. The results of the instant spanwise-average vortices and of the mean streamlines will be compared in § 5.3.2.1, while some direct comparisons of the mean velocity, pressure and shear stresses between the non-additive and additive cases will be presented in § 5.3.2.2.

5.3.2.1 Comparisons of the Instant and Mean Flow Fields

The spanwise vortices are presented in Fig. 5.5 for (a) $Re = 1000$ and (b) $Re = 1200$ which are obtained by imposing the fully developed steady streamwise velocity in the inlet of the model. In this case, the flow structures found at the downstream of the stenosis are quite different compared to what is seen in Fig. 5.4 for the non-additive pulsation. And, as reported by Pedley [142], this 2D Poiseuille type flow can not be found anywhere in human blood vessel because blood vessels are typically short, curved, branched and elastic and the flow through a blood vessel is unsteady. Therefore, a sinusoidal pulsation adding to this steady/mean flow may misinterpret the transient flow downstream of stenosis. Pedley [142] also argued that the flow nature and the average wall shear stress in non-additive or highly oscillating flow case would not be expected to be the same as in a steady and addtive pulsatile flow. To clarify this fact fully, the spanwise vortices obtained by the additive pulsation are depicted in Fig. 5.6. Note that the amplitude of the additive pulsation is taken as $A = 0.1$ for Fig. 5.6(a-b) and 0.2 for Fig. 5.6(c). When $A = 0.1$, the peak Reynolds number of the flow attains at 1100 for $Re = 1000$, while it is 1320 for $Re = 1200$. In both cases the large vortices seen at the post-stenosis dominate the flow and roll downstream. On the other hand, when $A = 0.2$

the peak Reynolds number becomes 1440 for $Re = 1200$ and the vortex rolling in the post stenosis region remains persistent and the intensity of the turbulence grows. Again, as it can clearly be seen in Fig. 5.6 that the additive pulsations produce flow at the downstream of the stenosis whose structures are quite different from that of the non-additive pulsations (Fig. 5.4).

In Fig. 5.7 the instantaneous upper wall shear stresses between the non-additive and additive cases are compared at different phases over the last time period while $Re = 1200$. Here a 10% sinusoidal oscillation is added in the additive pulsatile case. In frame (a), at the initial phase of cycle, the shear stress drops at the throat of the stenosis and the oscillatory nature of the shear stress at the post stenotic region is found higher for the additive case than the case of non-additive. Though the shear stress for the non-additive case seen in frame (b), at $t/T = 9.1$, is almost same as in frame (a), the reduction in stress as well as the oscillation in stress for the additive case increases in the post stenotic region. However, further downstream the shear stresses are smaller in the additive case than the non-additive pulse.

Moreover, near the peak phase of the additive case (at $t/T = 9.2$), the shear stress drop achieves its extreme magnitude of -0.07487 at $y/L = -0.091$, while the corresponding reduction in stress in the non-additive case is -0.01809 located at $y/L = 0.0$. Although the stress reduction in the additive case decreases at $t/T = 9.3$, there is an increase in the non-additive with the maximum of about -0.04227 occurring at the location of its peak phase (frame (f)). After this phase, the pattern of the shear stresses gradually approaches to that observed in frame (a).

The corresponding lower wall shear stresses are presented in Fig. 5.8(a-i). The oscillating nature in the shear stresses is also present on the lower wall and the intensity is again higher for the case of additive than non-additive. The maximum shear stress for the additive case occurs at the lower wall just opposite to the throat of the stenotic region, while for the non-additive case the position of the maximum shear stress at some phases moves slightly downstream.

Significant variations are also clearly evident in the mean streamline profiles presented in Figs. 5.9 to 5.11 for the non-additive pulsatile, steady and additive pulsatile flows, respectively. In addition, the strength of the recirculation at the post-stenosis is found much higher for the additive pulsations than the non-additive cases. In the pathological context, as already mentioned in the previous chapter,

this flow recirculation usually increases the staying time of blood at the downstream region of the stenosis, which may cause heart attack or brain stroke as the flow at each cycle is reversed there for a significant time. Furthermore, these are the regions of low and adverse pressure gradient of the flow, already discussed in the previous chapter (Fig. 4.15).

5.3.2.2 Direct Comparisons of the Mean Quantites

In this section some additional physics of the mean flow at the post-stenosis will be revealed through the results of the velocity, pressure and shear stresses in Figs. 5.12 to 5.14, respectively. In addition, some direct comparisons between the non-additive and the additive pulsatile results will be made here for $Re = 1000$ and 1200 and $A = 0.1$. The mean parameters of the non-additive pulsation for different Reynolds numbers are depicted using the lines without any symbols, while the solid lines with symbols represent the additive pulsatile results. Fig. 5.12 shows that the first peaks of the mean centreline velocity for the additive pulsations occur just after the centre of the stenosis located at about $y/L = 0.2$ where the flow separation took place already observed in Figs. 5.9. These centreline velocities then drop abruptly at the position close to the post-lip of the stenosis, and their second peaks occur further downstream at the position which is close to the reattachment of the large recirculation seen in Fig. 5.10. Comparing these with the non-additive pulsatile cases, the first peaks which occur close to the centre of the stenosis create the second peaks near the post-lip of the stenosis after the initial drop. Moreover, the second peaks for the higher Reynolds numbers, e.g. when $Re \geq 1500$, become stronger than the first peaks, which contributes into producing oscillations in the velocity field further downstream. Also note that, as already shown in Fig. 5.1, the mean flow strength in the additive case for $Re = 1000$ is equivalent to $Re = 2000$ in the case of non-additive pulse.

The mean pressure distributions at the upper wall, centreline and lower wall of the stenosis are shown in Fig. 5.13(a-c), respectively. For the non-additive pulsations, the maximum pressure drop for the upper wall occurs at the centre of the stenosis, while for the centreline the extreme pressure drop takes place at the post-lip of the stenosis. In addition, the oscillations found in the pressure profiles, which are clearly seen for the higher Reynolds number cases, correspond to the oscilla-

tions in the velocity field observed in Fig. 5.12. Again, it can be seen here that the downstream mean pressure profiles for the additive pulsations are quite different compared to the non-additive pulsations.

In Fig. 5.14 the corresponding mean shear stresses are presented. For the additive pulsatile cases, the mean shear stresses found downstream of the stenosis differ significantly from those obtained by the non-additive pulsations. Medical consequences of these results have already been presented in the previous chapter (§ 4.6.3) and will not be repeated here.

5.4 Conclusion

In this chapter, it is demonstrated that the physical natures of the flow-transition and the patterns of the re-circulation zones found downstream of the stenosis for the non-additive pulsatile cases are quite different compared with those of both the steady and additive pulsatile flow cases. It is clearly seen that in the case of highly pulsatile or non-additive the length of the re-circulation region is smaller than the case of steady and additive pulse. The intensity of the centreline velocity, shear stresses and the pressure drops found are always larger in the case of additive pulsatile than those of the non-additive case. Finally, it can be concluded that the post-stenotic flow patterns and the physical quantities are strongly dependent on the flow pulsatile conditions.

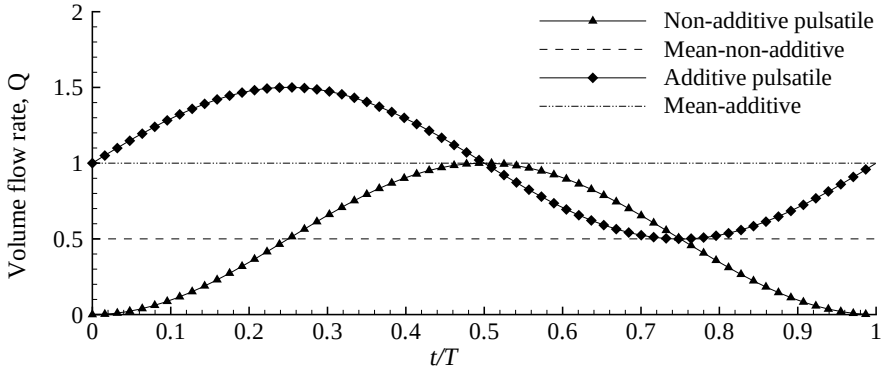

Figure 5.1: Difference between the non-additive and additive pulsatile volume flow rates, $Q(t)/Q_{max}$.

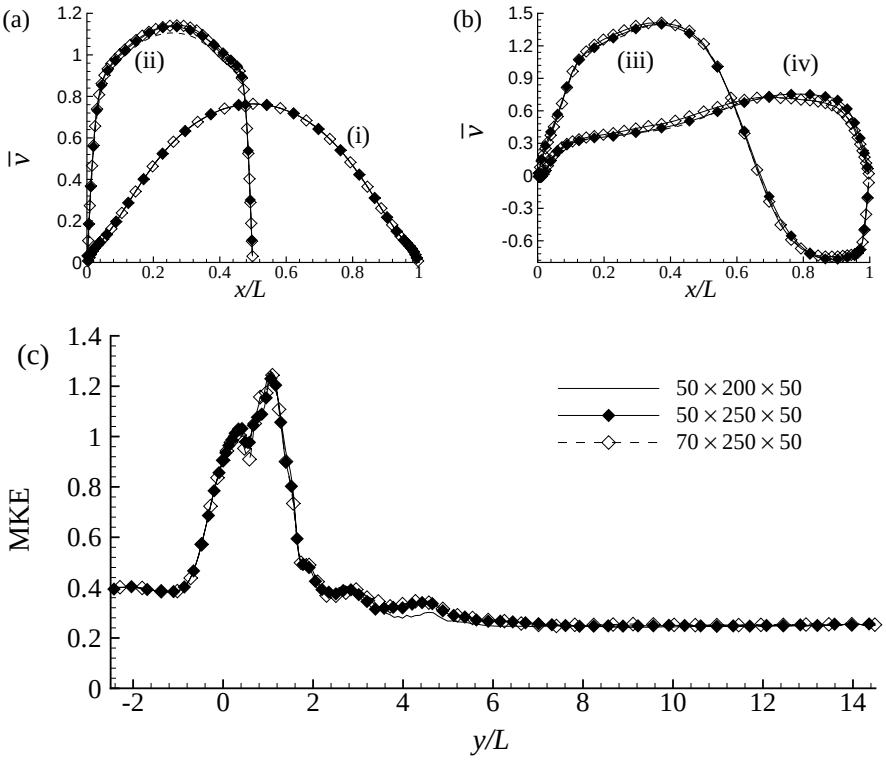

Figure 5.2: Normalised mean streamwise velocity, $\bar{v}/\bar{V}_{max}$, in frame (a) at (i) $y/L = -0.2$ (ii) $y/L = 0.0$, in frame(b) at (iii) $y/L = 1.0$ and (iv) $y/L = 2.0$ and the centreline mean kinetic energy (MKE), $\frac{1}{2} < \bar{u}_j\bar{u}_j > /\bar{V}^2_{max}$, in frame (c) for the three different mesh arrangements while $Re = 2000$.

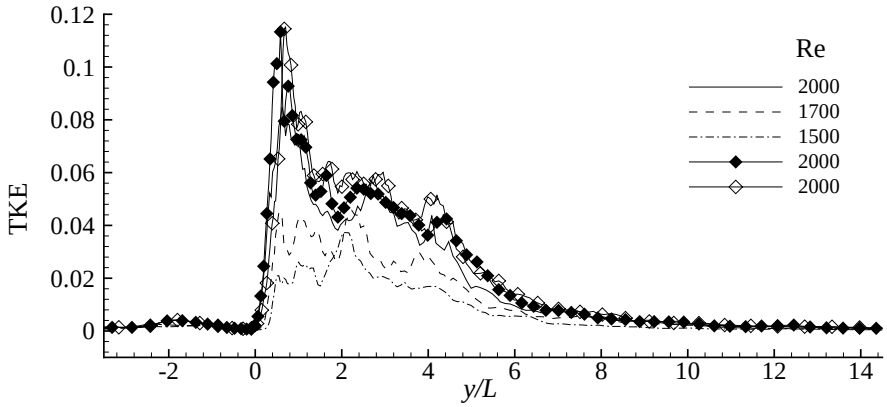

Figure 5.3: Centreline turbulent kinetic energy (TKE), $\frac{1}{2} < u_j'' u_j'' > / \bar{V}_{max}^2$, for the three different Reynolds numbers.

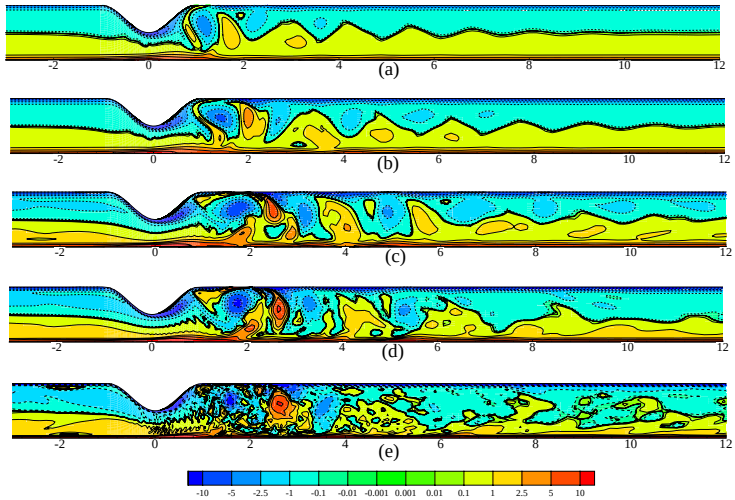

Figure 5.4: Spanwise average vorticity, $< \omega_z >_s$, for (a) $Re = 1000$, (b) $Re = 1200$, (c) $Re = 1500$, (d) $Re = 1700$ and (e) $Re = 2000$ at $t/T = 10.5$.

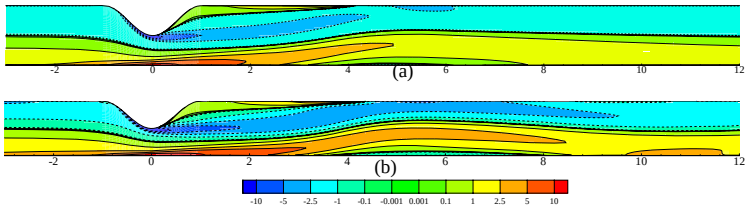

Figure 5.5: Spanwise average vorticity, $< \omega_z >_s$, for the steady inlet flow at (a) $Re = 1000$ and (b) $Re = 1200$.

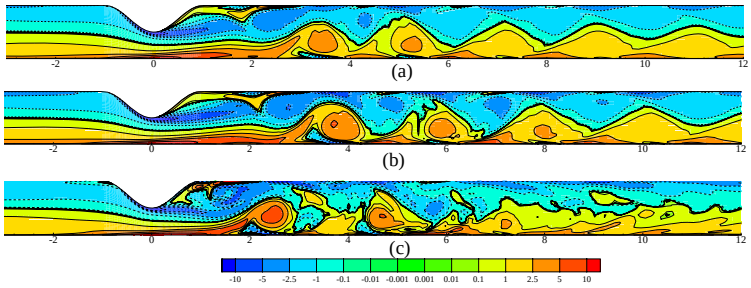

Figure 5.6: Spanwise average vorticity, $< \omega_z >_s$, (a) $Re = 1000$ and (b) $Re = 1200$ with 10% additive oscillation, and (c) $Re = 1200$ with 20% additive oscillation at $t/T = 10.25$.

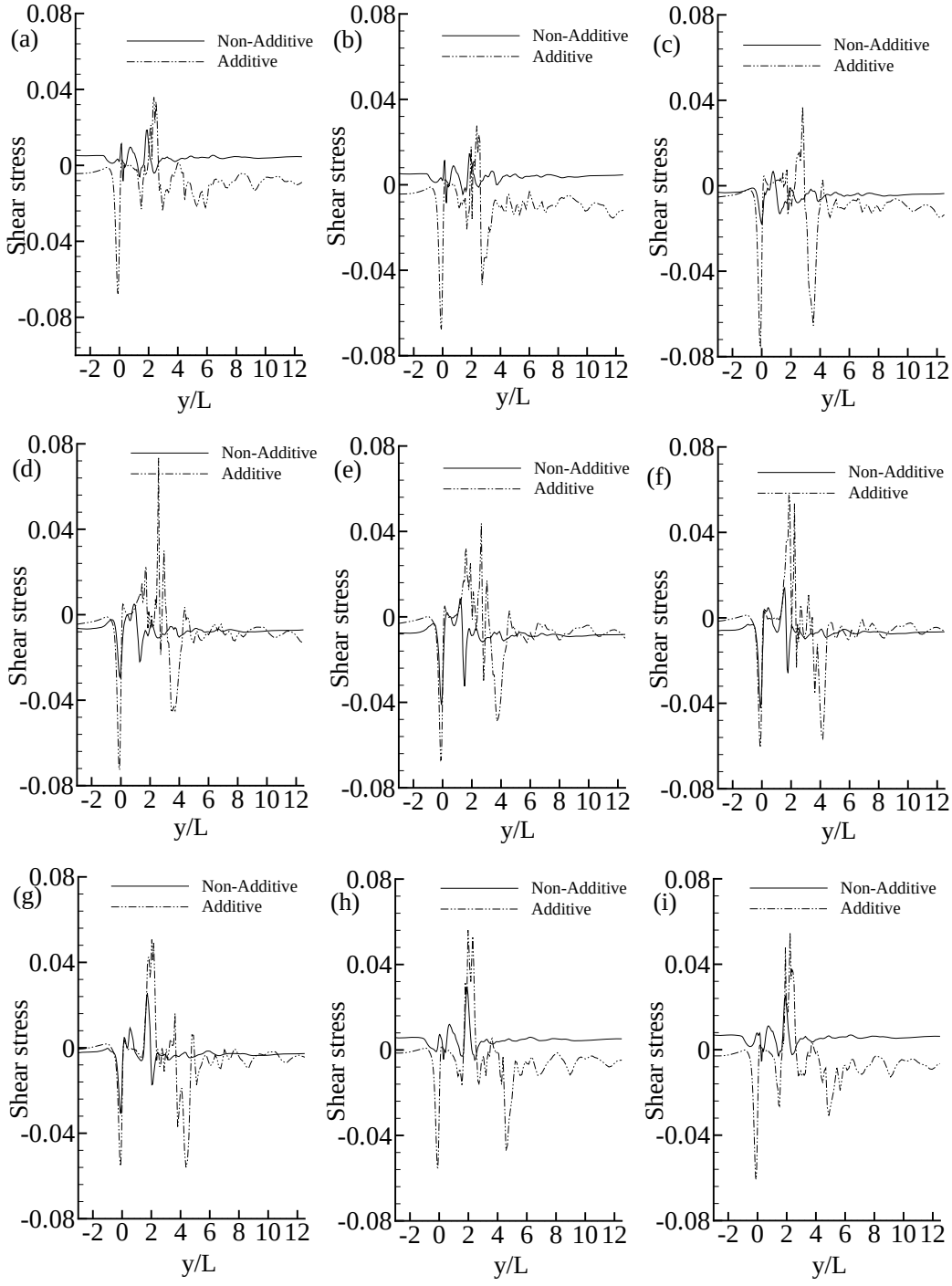

Figure 5.7: Instantaneous upper wall shear stress, $\tau_{xy}/\rho\bar{V}_{max}^2$, at the different phases over the last time period; (a) $t/T = 9.0$, (b) $t/T = 9.1$, (c) $t/T = 9.2$, (d) $t/T = 9.3$, (e) $t/T = 9.4$, (f) $t/T = 9.5$, (g) $t/T = 9.6$, (h) $t/T = 9.7$ and (i) $t/T = 9.9$ while $Re = 1200$.

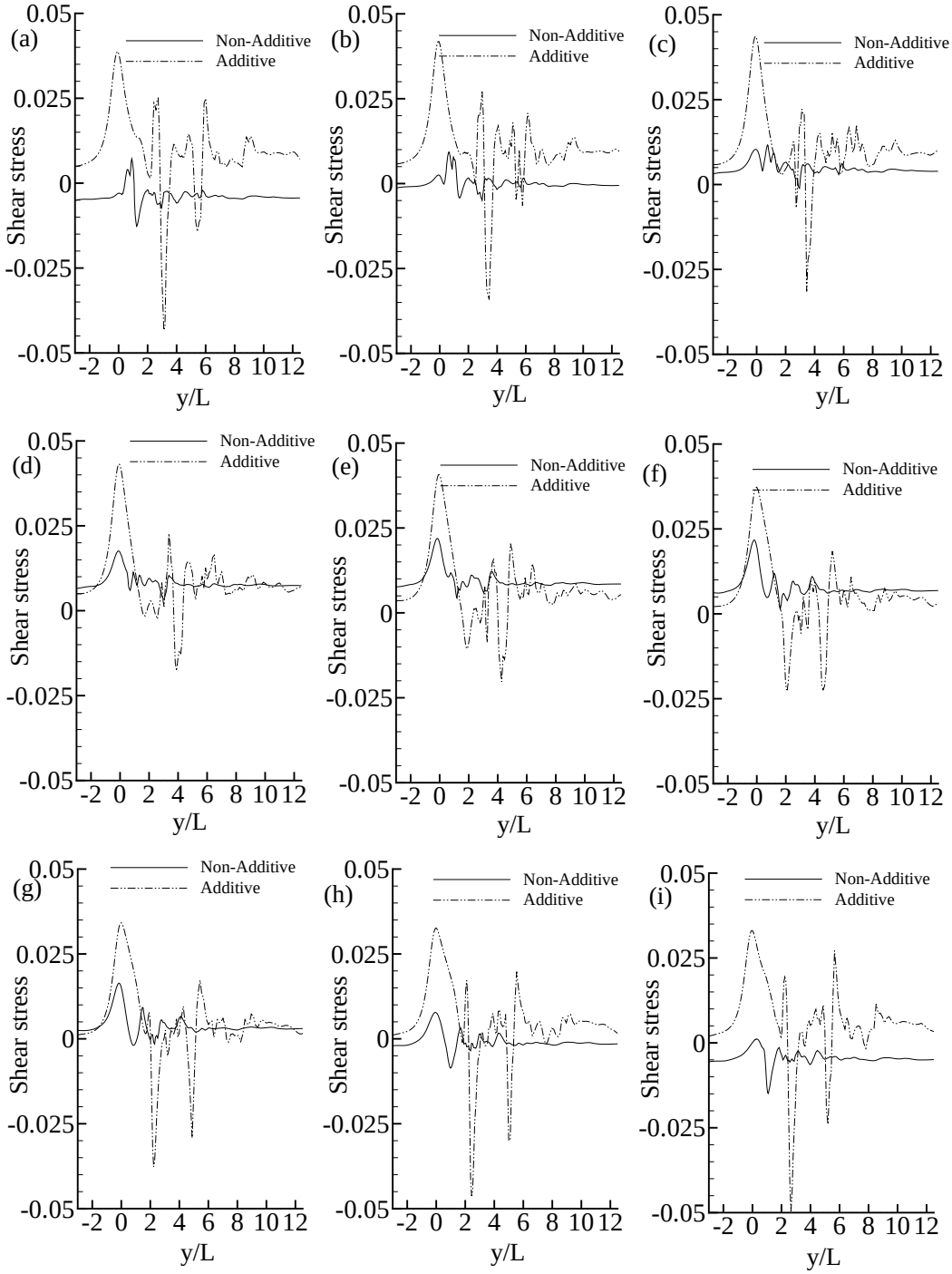

Figure 5.8: Instantaneous lower wall shear stress, $\tau_{xy}/\rho\bar{V}_{max}^2$, at the different phases over the last time period; (a) $t/T = 9.0$, (b) $t/T = 9.1$, (c) $t/T = 9.2$, (d) $t/T = 9.3$, (e) $t/T = 9.4$, (f) $t/T = 9.5$, (g) $t/T = 9.6$, (h) $t/T = 9.7$ and (i) $t/T = 9.9$ while $Re = 1200$.

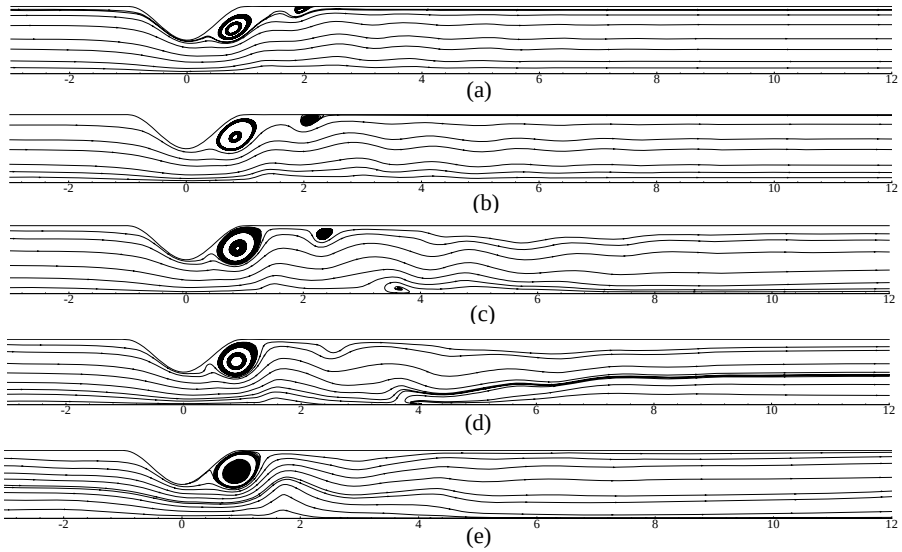

Figure 5.9: Mean streamlines for non-additive pulsation for (a) $Re = 1000$, (b) $Re = 1200$, (c) $Re = 1500$, (d) $Re = 1700$ and (e) $Re = 2000$.

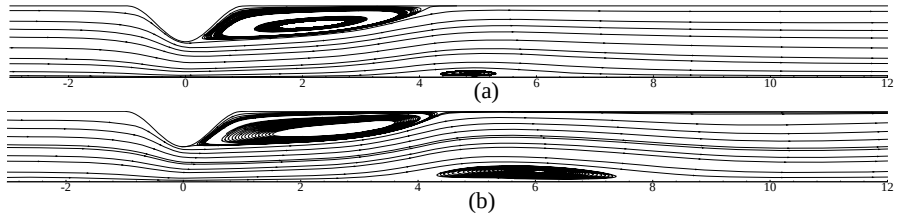

Figure 5.10: Streamlines for steady flow for (a) $Re = 1000$ and (b) $Re = 1200$.

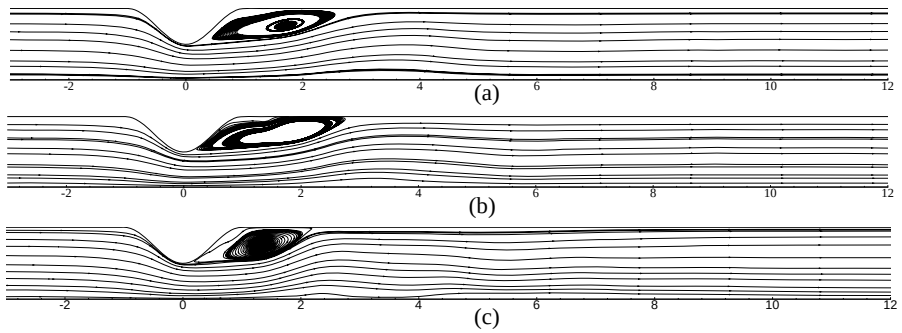

Figure 5.11: Mean streamlines for additive pulsation for (a) $Re = 1000$ and (b) $Re = 1200$ with 10% additive oscillation, and (c) $Re = 1200$ with 20% additive oscillation.

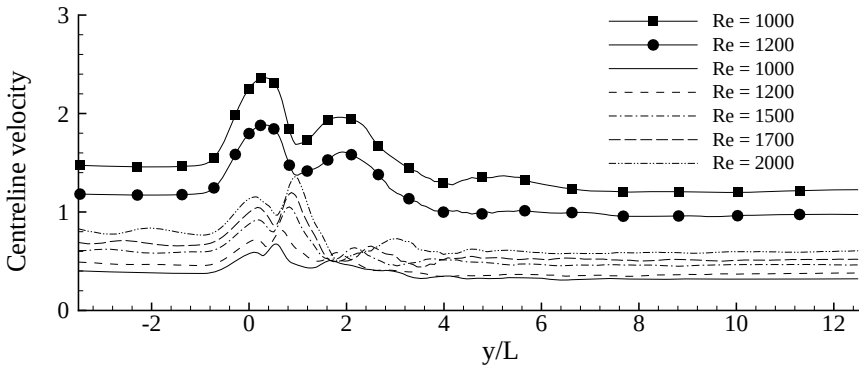

Figure 5.12: Mean centreline sreamwise velocity, $< \bar{v} > /\bar{V}_{max}$, for the different Reynolds numbers.

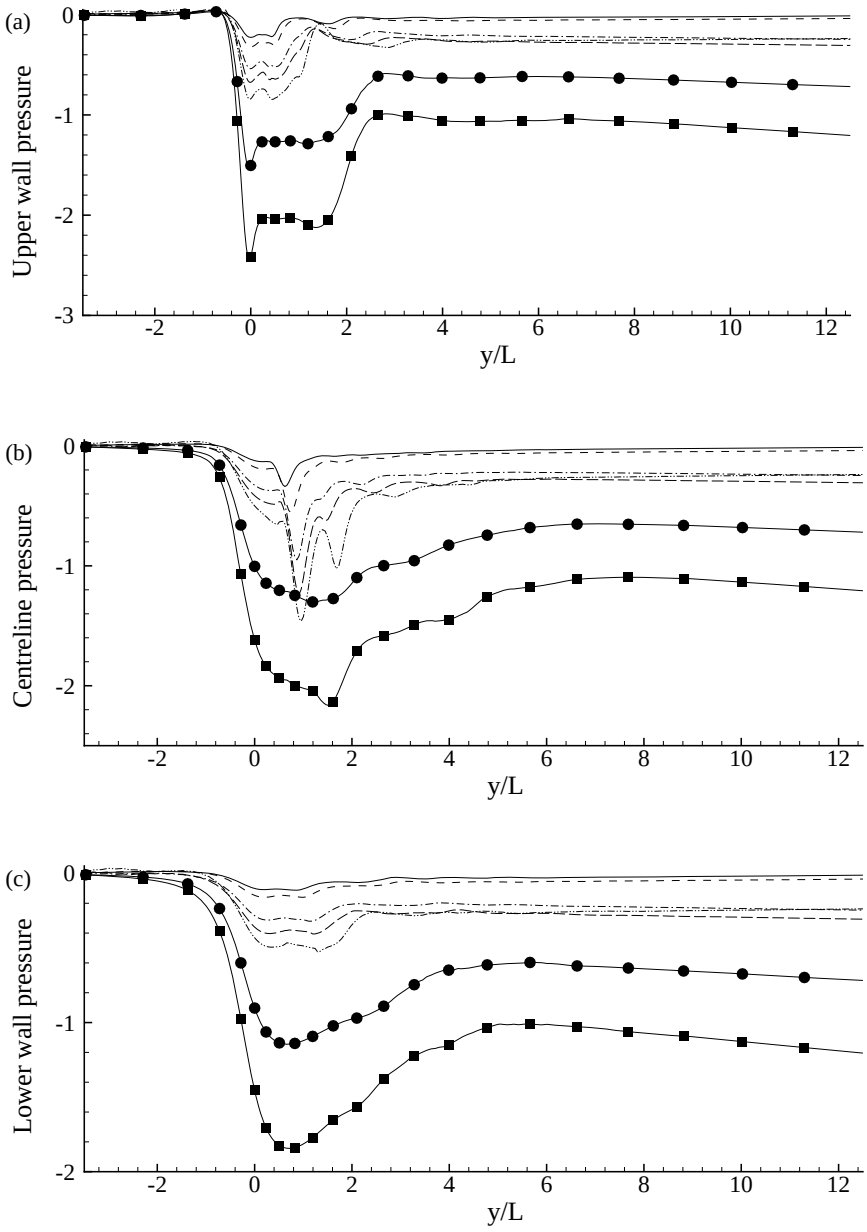

Figure 5.13: Mean pressure, $< \bar{p} > /\rho \bar{V}_{max}^2$, at the (a) upper wall, (b) centreline and (c) lower wall for the different Reynolds numbers (figure legend is the same as in Fig. 5.12).

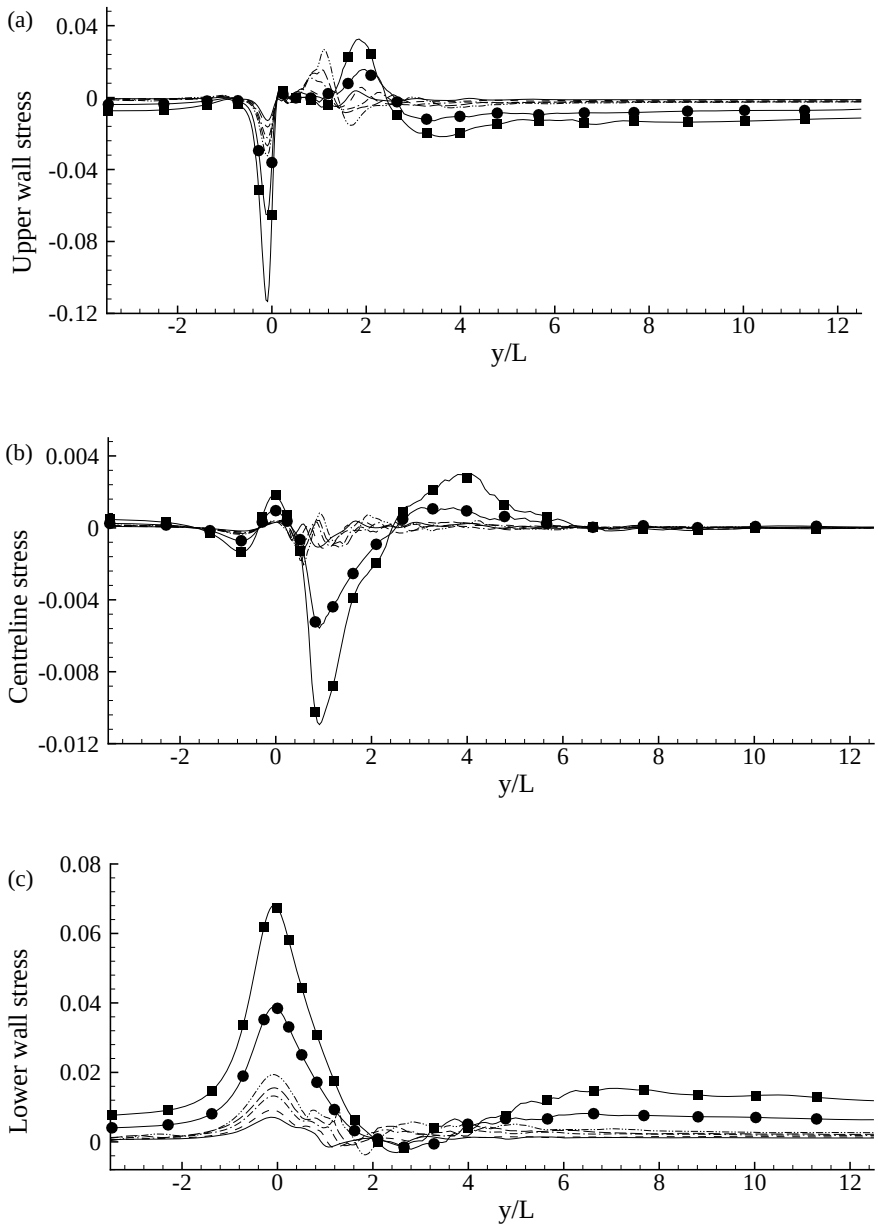

Figure 5.14: Mean shear stresses, $< \tau_{xy} > / \rho \bar{V}_{max}^2$, for the different Reynolds numbers at the (a) upper wall, (b) centreline and (c) lower wall (figure legend is the same as in Fig. 5.12).

Chapter 6

Simulation of Physiological Pulsatile Flow. Part 1. Results of the First Harmonic Pressure Pulse

6.1 Introduction

In the previous chapters, simple sinusoidal oscillations were imposed at the inlet of the model stenosed artery to investigate the transition-to-turbulent process of both additive (Chapter 4) and non-additive (Chapter 5) types of pulsations downstream of the stenosis. The objective of this chapter is to consider a biologically realistic pulsatile flow, i.e. physiological flow, at the inlet of the same model and further investigate the transient flow through the stenosis. The physiological pulsation is generated using the first harmonic of the Fourier series of the pressure pulse according to Womersley [6]. The results of the effects of various harmonics of the Fourier series of the pressure pulsations will be presented in the next chapter.

In the Fourier series of the pressure pulse, all the harmonic terms are sine waves and they have a mean value of zero. So, the summation of all the harmonic terms leads to zero over a complete cycle. But the flow through an artery must have a positive mean value because its function is to transport blood from the heart to the tissues of the body (Nichols and O'Rourke [10], pp. 130). The first term in the pressure gradient (Eq. 6.7) gives the positive mean flow and this is the simplest way of representing physiological pulsatile flow in artery (Womersley [6]).

We have applied LES technique in this Chapter to solve the filtered governing equations of flow using a different model for the SGS, which is known as the

Piomelli-Liu [4] localized dynamic model. Note that the Germano-Lilly ([2], [3]) dynamic model was used in the previous chapters. The benefit of the new SGS model over the Germano-Lilly will be highlighted in § 6.2.1 and a comparison between the results of the two SGS dynamic models will be given in the next chapter.

Transition-to-turbulent pulsatile flow in the post stenosis is examined through various numerical quantities such as velocity, streamlines, velocity vectors vortices, wall pressure and shear stresses, turbulent kinetic energy, pressure gradient, velocity and pressure fluctuations and their energy spectra etc, and these results are explained physically. A comparison of the LES results with those obtained by the coarse Direct Numerical Simulation (DNS) is made and the agreement found between them is quite acceptable. Another comparison is drawn between the results obtained by using the additive sinusoidal and physiological pulsatile flow at the inlet.

6.2 Formation of the Problem

The governing equations and the model geometry for the present chapter are the same as those described in Chapters 3 and 4 respectively. But the sub-grid model and the inlet boundary condition used in this chapter are different and presented in the following sub-sections.

6.2.1 Piomelli-Liu Localized Dynamic Model for SGS

The Germano-Lilly ([2], [3]) dynamic model which was described in Chapter 3 (§ 3.5.1) yields the model constant C_s as a function of both space and time. But two difficulties may arise in the determination of C_s: (i) the model is ill-conditioned when the denominator of the expression for C_s (in Chapter 3, Eq. 3.45) becomes very small in the flow domain, and (ii) the procedure described in Chapter 3 (§ 3.5.1) is not mathematically self-consistent, that is, the values of C_s can become negative, which is known as "backscattering".

Piomelli-Liu [4] described a localized dynamic model in which the mathematical inconsistency is removed and the backscattering is reduced. To explain the Piomelli-Liu [4] localized dynamic model, the expression (3.43) in Chapter 3 is re-written here

$$L_{ij}^a = L_{ij} - \frac{1}{3}\delta_{ij}L_{kk} = -2C_s^2 M_{ij} = -2C_s^2(\alpha_{ij} - \beta_{ij}), \tag{6.1}$$

where $\beta_{ij} = (\triangle)^2|\bar{S}|\bar{S_{ij}}$ and $\alpha_{ij} = (\tilde{\triangle})^2|\tilde{\bar{S}}|\tilde{\bar{S}}_{ij}$.

Lilly [3] applied a least square approach for defining the square of the residuals of Eq.(6.1) as

$$E = (L_{ij} - \frac{1}{3}\delta_{ij}L_{kk} + 2C_s^2 M_{ij})^2, \tag{6.2}$$

and set $\frac{\partial E}{\partial C_s} = 0$ for evaluating C_s as

$$C_s^2 = \frac{1}{2}\frac{L_{ij}^a(\alpha_{ij} - \beta_{ij})}{(\alpha_{ij} - \beta_{ij})(\alpha_{ij} - \beta_{ij})} \tag{6.3}$$

This was the original dynamic model of Germano-Lilly ([2], [3]), and using the expression (6.3) the constant C_s was calculated. However, in the Piomelli-Liu [4] localized dynamic model, the expression (6.1) is slightly re-arranged in the following form

$$2C_s^2\alpha_{ij} = (L_{ij} - \frac{1}{3}\delta_{ij}L_{kk}) + 2C_s^{*2}\beta_{ij}, \tag{6.4}$$

where the values of C_s^{*2} are known from the previous time step. Since C_s^{*2} is known, the sum of the squares of the residuals can be minimised locally. The contraction that minimises it is:

$$C_s^2 = \frac{1}{2}\frac{(L_{ij} - \frac{1}{3}\delta_{ij}L_{kk} + 2C_s^{*2}\beta_{ij})\alpha_{ij}}{\alpha_{mn}\alpha_{mn}}. \tag{6.5}$$

The denominator of (6.5) is positive definite, but has the advantage that it does not involve a difference between two terms of the same order of magnitudes in (6.3).

6.2.2 Physiological Inlet Condition and Computational Parameters

The physiological velocity profile, which is used to generate the time-dependent pulsatile flow at the inlet of the channel, is obtained via the analytic solution of the one-dimensional form of the Navier-Stokes equation in the streamwise direction by taking the pressure gradient as a Fourier series in time (Womersley [6], Chan-

dran [143], Nichols and O'Rourke [10] and Loudon and Tordesillas [144]).

The Navier-Stokes equation in the streamwise direction can easily be written as

$$\frac{\partial^2 \bar{v}}{\partial x^2} - \frac{\rho}{\mu}\frac{\partial \bar{v}}{\partial t} = \frac{1}{\mu}\frac{\partial \bar{p}}{\partial y}, \quad 0 \leq x \leq L \tag{6.6}$$

where the pressure gradient for the physiological pulsation is defined as

$$\frac{\partial \bar{p}}{\partial y} = \frac{2}{3}A_0 + A\sum_{n=1}^{NH} M_n e^{i(n\omega t + \phi_n)}. \tag{6.7}$$

The constants A_0 and A appearing in (6.7) correspond to the steady and oscillatory parts of the pressure gradient, respectively. M_n and ϕ_n are the respective coefficients and the phase angle, and NH gives the number of harmonics of the physiological flow. The frequency (ω) of the unsteady flow is defined as $\omega = \frac{2\pi}{T}$.

The solution of Eq. (6.6) takes the following form:

$$\bar{v}(x,t) = 4\bar{V}_{max}\frac{x}{L}\left(1 - \frac{x}{L}\right) + A\sum_{n=1}^{NH}\frac{iM_nL^2}{\mu\alpha^2 n}$$
$$\left[\cosh(\alpha\sqrt{in}\frac{x}{L}) - \frac{\cosh(\alpha\sqrt{in}) - 1}{\sinh(\alpha\sqrt{in})}\sinh(\alpha\sqrt{in}\frac{x}{L}) - 1\right] e^{i(n\omega t + \phi_n)}. \tag{6.8}$$

In the solution, the bulk velocity, $\bar{V}_{max}$, depends on the flow Reynolds number which is defined as $Re = \frac{\bar{V}_{max}L}{\nu}$; and $\alpha = L\sqrt{\frac{\rho\omega}{\mu}}$ is the unsteady Reynolds number or the Womersley number which gives the ratio of the unsteady to viscous forces. When the Womersley number is relatively small, the viscous forces usually dominate flow. On the other hand, the unsteady inertia forces take an important role in the physiological flow when $\alpha > 10$, see Ku [9]. In our simulation the real part of this solution (6.8) is used as an inlet boundary condition to generate the physiological flow through the channel and we have used $\alpha = 10.5$ for controlling the maximum flow rate. As the objective of this chapter is to concentrate only on the first harmonic of the pressure pulse, we have used $NH = 1$ in Eq. (6.8). A detailed description of the derivation of the real part of (6.8) is given in Appendix B.

The amplitude of oscillation, A, is varied with the Reynolds number to maintain the maximum flow rate at the inlet. For example, for $Re = 1000$, 1400, 1700 and

2000 the values of A are taken as 0.25, 0.3, 0.35 and 0.4 respectively. In addition, the pulsatile coefficient, M_n, takes a value of 0.78 and the phase angle, ϕ_n, of 0.0113446 when $NH = 1$. These values are taken from the paper of Womersley [6].

The inlet pulsatile velocity profile derived from the above relation (6.8) is presented in Fig. 6.1 for the Reynolds number of 2000. In frame (a) the velocity recorded in the centre of the inlet plane is shown at a full pulsation, while the variation of this between the top and bottom planes at different phases during the same pulsation is shown in frame (b). It is interesting to observe that the oscillating part of the pressure pulse has created the negative velocity (back flow) close to the walls of the channel during the diastolic phase (e.g. at $t/T = 0.5$, 0.625 and 0.75).

6.3 Results and Discussion

In the present Chapter Reynolds numbers ranging from 1000 to 2000 are considered and the area reduction of the channel due to the stenosis remains fixed at 50%. Various simulations with LES and DNS have been performed using various grid arrangements and timesteps, Table 6.1 shows a list of the simulation details.

Initially, the results of the grid and timestep independence tests are presented in § 6.3.1. Then the results of the contribution of the SGS model constant C_s and eddy viscosity are presented in § 6.3.2. In § 6.3.3 and § 6.3.4, the results of the instant and mean flow physics are presented, respectively. The results of the in-depth investigations of the turbulent flow downstream of the stenosis are summarised in § 6.3.5 and § 6.3.6. A comparison between the results of additive sinusoidal and the physiological pulsatile flow is given in § 6.3.7.

6.3.1 Grid and Timestep Independence Tests

The grid and timestep independence tests have been carried out to establish a suitable combination of grid configuration and timestep that are required for the LES to adequately resolve the physiological flow in the stenosis. Initially, fixing Reynolds number (Re) at (2000) and the timestep (δt) at 10^{-3}, four computations have been performed with LES by using the four different grid setups: $50 \times 200 \times 50$ (Case 1), $50 \times 250 \times 50$ (Case 2), $50 \times 300 \times 50$ (Case 3) and $70 \times 250 \times 50$ (Case 4).

Table 6.1: Grid details for the LES and DNS approaches.

Case	Re	Approach	N_x	N_y	N_z	δt
0	< 2000	LES	50	200	50	1.0×10^{-3}
1	2000	LES	50	200	50	1.0×10^{-3}
2	2000	LES	50	250	50	1.0×10^{-3}
3	2000	LES	50	300	50	1.0×10^{-3}
4	2000	LES	70	250	50	1.0×10^{-3}
5	2000	DNS	50	350	50	1.0×10^{-3}
6	2000	DNS	70	350	50	1.0×10^{-3}
7	2000	LES	50	200	50	1.5×10^{-3}
8	2000	LES	50	200	50	2.0×10^{-3}

The results of these four cases are compared in Figs. 6.2 and 6.3 in terms of the mean streamwise velocity, $< \bar{v} > /\bar{V}_{max}$, and the turbulent kinetic energy (TKE), $\frac{1}{2} < u_j'' u_j'' > /\bar{V}_{max}^2$, respectively, at the different axial positions along the flow. As can be seen in Fig. 6.2, the grid configurations used in the LES (Cases 1-4) are sufficient to resolve the mean streamwise velocity, and their comparisons with the two coarse DNS results (Cases 5,6) also show excellent agreement. However, Fig. 6.3 shows that the results of the turbulent kinetic energy at the immediate post stenotic region, $1 < y/L < 6$ (frames c-j), are sensitive slightly to the choice of grids in LES since only the resolved scale flows are computed in LES by the grid resolution. Thus, total grid independence of the computed turbulent random fluctuations is not expected in LES and it is adequate to prove in LES that the primary flow features (mean velocities) do not vary significantly with the grid. Moreover, this dependence is apparent until the grid resolution becomes fine enough that the LES starts to qualify as DNS.

The timestep δt in Case 1 is now varied from 10^{-3} to 1.5×10^{-3} (Case 7) and 2.0×10^{-3} (Case 8) and the results are compared in Fig. 6.4 in terms of the centreline mean kinetic energy $\frac{1}{2} < \bar{u}_j \bar{u}_j > /\bar{V}_{max}^2$ (frame a) and the turbulent kinetic energy $\frac{1}{2} < u_j'' u_j'' > /\bar{V}_{max}^2$ (frame b). From this figure it is seen that the results before the stenosis are quite independent of the timesteps used, however, at the post stenotic region, where the flow is turbulent, the results are sensitive slightly. In the simulation of turbulent flow the timestep usually depends on the grid size, therefore,

fixing one grid arrangement it is reasonable to get some sensitivities in the turbulent results for the different timesteps (Choi and Moin [132]). To avoid any unstable solutions for the different types of grid arrangement, the smallest timestep of 10^{-3}, was chosen in the computation, by ensuring that the maximum Courant number lies between 0.1 and 0.2. Also based on the above satisfactory grid independent test in Figs. 6.2 and 6.3 for $Re = 2000$, the simulations for other Reynolds numbers less than 2000 have been performed with $50 \times 200 \times 50$ (Case 1).

As in Chapters 4 and 5 the non-uniform dense meshes have been used close to both the top and bottom walls of the model to capture the thin shear layer at the vicinity of the wall. And the mesh lines are concentrated at the centre and immediate downstream of the stenosis. Moreover, for Cases 1-6, when the number of grid points along the streamwise direction (N_y) is increased, particular attention is paid to the accurate capturing of the small scale turbulent eddies at the post-stenosis regime. For that, the number of streamwise grid points before the stenosis is always kept fixed at 50 while the rest of the total grid points of N_y is distributed in the post stenosis region.

6.3.2 Contribution of the SGS Model

Fig. 6.5 represents the contour plots of the sub-grid scale (SGS) model parameter C_s in the $x-y$ mid plane for the different Reynolds numbers. This figure shows that the maximum value of the dynamic Smagorinsky constant, C_s, clearly depends on the flow Reynolds number and increases as the Reynolds number is increased. For example, the maximum value of C_s for $Re = 1000$ is found approximately 0.053, while for the other Reynolds numbers, $Re = 1400$, 1700 and 2000, the respective maximum values of C_s are about 0.071, 0.098 and 0.106. It is important to note that the maximum value of C_s occurs at the post stenotic region where the nature of the flow is predicted to be turbulent. On the ot0her hand, the values of C_s before the stenosis are very small due to the laminar nature of the flow. Therefore, it is quite clear from this finding that the dynamic procedure is well capable of calculating the SGS stresses properly in the model. Note that similar results were found in Chapter 4 where the sinusoidal pulse was imposed at the inlet.

The corresponding eddy viscosity, μ_{sgs}, normalized by the molecular viscosity,

μ, is depicted in Fig. 6.6. The maximum eddy viscosity for $Re = 1000$ is 0.069, that means, the contribution of the SGS model in the LES is approximately 6.9% which indicates that when $Re < 1000$, the flow in this model may be resolved properly by using the DNS technique, whereas for $Re \leq 1200$ a DNS could be used for the sinusoidal pulse which is mentioned in the Chapter 4 (§ 4.6.1). On the other hand, the maximum of 18.2%, 29.2% and 37.4% contribution is received for $Re = 1400$, 1700 and 2000 respectively and in line with the Smagorinsky constant this maximum SGS dissipation occurs at the post stenotic region.

6.3.3 Instantaneous Flow Field

To show the cycle-to-cycle development of the streamwise flow at the downstream of the stenosis, the streamwise velocity recorded at the end of every cycle for $Re = 2000$ is presented in Fig. 6.7. In frame (a) a small re-circulation region or a primary shear layer which is initially created between the centre and post-lip of the stenosis elongates the downstream at the end of cycle two. The creation of a secondary shear layer is also observed near the lower wall at this phase. As the flow progresses with time, these two shear layers interact with each other and break down into vortices which then move the downstream, shown clearly in frames (c-g). As a result, the nature of the transient/separated flow downstream of the stenosis is observed turbulent. Note that the simulation has been carried out up to the end of eleventh cycle, as it has been shown that the solutions eventually reach a stationary state after the eighth cycle and the mean results did not vary significantly between the eighth and eleventh cycles. Moreover, the instant flow pattern at the downstream of stenosis did not show any significant change at the end of eighth time period.

While in Fig. 6.7 the development of the instant flow at the end of various cycles is presented in the mid-horizontal plane, Fig. 6.8 shows the cross-sectional flow streamlines of Fig. 6.7(h) in the different streamwise locations. The streamlines at the inlet of the channel indicate that the flow pattern is laminar (frame a) since there is no intersection among the streamlines. The flow at the centre of the stenosis is still laminar but about to transient close to the lower wall. At the post lip of the stenosis, at $y/L = 1$ (frame c), the transitional behaviour of the flow is evident near the upper wall and the flow patterns in the subsequent frames plotted at $y/L = 2$ to 10 are

very chaotic. Here, it is mentioned that the transitional flow view is not similar to that in Chapter 4 (Fig. 4.8a) Frydrychowicz *et al* . [12] in their investigation using the 4D MRI technique on aortic vascular hemodynamics with stenosis termed the formation of these complex vortices or flow features as "corkscrew". The intensity of the turbulent nature of this flow will be examined later in § 6.3.5.

The effects of Reynolds number on the development of the flow along the streamwise direction are presented in Fig. 6.9 at $t/T = 10.25$ with the streamwise velocity vectors which are appended on the contours of the streamwise velocity $\bar{v}/\bar{V}_{max}$ for all the Reynolds numbers under consideration. The large primary re-circulation region near the post lip of the stenosis extends to the streamwise direction as the Reynolds number is increased. This re-circulation zone is permanent and has some important medical consequences, as it increases the time that the blood remains in the post stenosis region. This increased time of residence is dangerous for a patient.

The separation of the secondary shear layer from the lower wall is also affected by the Reynolds number. It is found that the separation for $Re = 1000$ happens close to the centre, while the separation point for other Reynolds numbers moves slightly downstream. Though the scenario is quite common for all the cases, the vortex cells move further downstream when the Reynolds number increases. More information is revealed through the spanwise-averaged vorticity, $< \omega_z >_s$, contours in Fig. 6.10. The anti-clockwise vortex is shown by dashed lines and the clockwise vortex by solid lines. It is evident from the colour legend that the maximum magnitude of the clockwise vortices for $Re = 1000$ and 1400 lies within the region of $2.0 < y/L < 4.0$, while for $Re = 1700$ and 2000 it occurs after $y/L > 4.0$, which is plausible for the higher Reynolds number as the intensity of the streamwise velocity is larger in these cases.

Fig. 6.11 illustrates results of another important physical quantity, namely the shear stress, $\tau_{xy} = \mu(\frac{\partial \bar{v}}{\partial x} + \frac{\partial \bar{u}}{\partial y})/\rho \bar{V}^2_{max}$, which are plotted at the centreline along the streamwise direction in the upper and lower walls for the different Reynolds numbers. The acute shear stress drop found just prior to the centre of the stenosis in the upper wall has some important pathological issues, as this could usually induce an accelerated amount of intimal thickening of a blood vessel (Salam *et al* . [37]). However, from the throat of the stenosis the shear stresses rise up and attain a peak value in the region $1.0 < y/L < 2.0$. Afterwards they decay but oscillate

in $1.0 < y/L < 5.0$, and further downstream their magnitudes drop gradually. On the other hand, the extreme rise of the shear stresses at the centre of the stenosis on the lower wall together with the abnormal oscillating form at the downstream are quite harmful in the sense that they cause damage to the blood cells and the inner lining of an arterial vessel. Moreover, this high shear stress may also overstimulate platelet thrombosis and cause a total occlusion in blood vessel (Folts *et al* . [33]).

6.3.4 Mean Flow Characteristics

The mean streamwise velocity recorded at the different axial locations is presented in Fig. 6.12(a-n) for defferent Reynolds numbers. The mean velocity whose patterns in the inlet correspond to a fully developed laminar Poiseuille flow increase rapidly in the post-stenotic region for all the Reynolds numbers, and the negative values in the velocity occurring near the upper wall correspond to the presence of the permanent re-circulation region seen in Figs. 6.7 and 6.13. However, further downstream the velocity does not change significantly as the flow settles down there after the transient. Again we see in Fig. 6.13 that the length of the re-circulation region increases with the Reynolds number since the intensity of the adverse pressure increases in the post-lip region (see Fig. 6.14a). Moreover, the acute pressure drop seen in Fig. 6.14 within the immediate post stenosis region can cause a stroke as the blood in this region flows in the opposite direction owing to the reversal of the pressure gradients. Note that similar results have been found in Chapter 4 (Fig. 4.15). The DNS (Case 6) results for $Re = 2000$ have been compared with those of the LES and the agreement found is quite good indeed.

The instantaneous results of the shear stress were presented in Fig. 6.11 and discussed. However, it would be interesting to see how their mean results vary in the post stenosis region. In this regard, the mean shear stresses for the various Reynolds numbers are plotted in Fig. 6.15 at the (a) upper wall, (b) centreline, and (c) lower wall. The mean stresses at the upper wall show an abrupt drop just prior to the centre of the stenosis but rises up after the immediate region of the post lip, which is similar to that shown in Chapter 4 (Fig. 4.18a). Though the extreme rise of the mean shear stress at the lower wall coincides with the instantaneous results (Fig. 6.11b), the highly oscillatory nature that was found in the instant shear stresses

is clearly absent here. The medical consequences of the instantaneous shear stresses have been pointed out in the previous section, in addition to those, the blood cells and the endothelial side of the blood vessels can experience the sharp rise and fall of the mean shear stresses in the post stenosis. Again the DNS results for $Re = 2000$ show an excellent agreement with those of the LES.

6.3.5 Turbulent Characteristics

The root mean square (rms) of the streamwise velocity fluctuation, v''_{rms}, normalised by $\bar{V}_{max}$, is recorded at different axial positions and depicted in Fig. 6.16 for $Re = 1000, 1400, 1700$ and 2000. The zero values of v''_{rms} at the inlet correspond to the presence of laminar pulsatile flow, while their slight growth at the centre of the stenosis correspond to the transition stage. The effect of Reynolds number on v''_{rms} upstream of the stenosis is indistinctive but clearly distinctive at the post-stenosis. The maximum rise in the magnitude of v''_{rms} which takes place near the upper wall of the post stenosis reduces gradually far downstream as the intensity of turbulent velocity fluctuations v'' drops there, Fig. 6.17.

The total turbulent intensity is simulated in terms of the turbulent kinetic energy (TKE), $\frac{1}{2}[< u''u'' > + < v''v'' > + < w''w'' >]/\bar{V}^2_{max}$, which is presented in Fig. 6.18 along the mid-centreline and in Fig. 6.19 at the different axial positions. From these figures it is again found that the turbulent kinetic energy is negligible upstream, but it increases from the centre of the stenosis and becomes extreme in the post stenosis region of $0.0 < y/L < 6.0$. In a pathological sense, this extreme rise of the TKE is responsible for damaging the blood cells and the tissues inside of a blood vessel, as already discussed in Chapter 4. Also the effect of the Reynolds number on the magnitude of the TKE is clearly visible here. The TKE grows with the Reynolds number, but at the far downstream region the turbulent characteristic is more universal and independent to the Reynolds number. And the coarse DNS (Case 6) results of the TKE for $Re = 2000$ show reasonable agreement with those of the LES.

6.3.5.1 Cycle-to-cycle variations

To demonstrate clearly where, when and how the physiological flow becomes disturbed, cycle-to-cycle variations of the important flow quantities are presented in this section. Fig 6.20 shows that the velocity at the centre of the stenosis remains undisturbed at every cycle, but due to the presence of the stenosis the flow downstream of it is completely disturbed. The magnitude of the velocity of this disturbed flow is different at different cycle and streamwise location, and its cycle-to-cycle variation is not periodic. Moreover, the flow velocity is increased immediately downstream of the stenosis where the level of turbulence is high and it drops gradually further downstream because of the decaying of the turbulence.

The cycle-to-cycle variation of the upper wall pressure gradient in Fig. 6.21 reveals some additional and important information of the disturbed flow observed downstream of the stenosis. In the pathological context, the severely oscillating pressure gradient that occurs at the immediate post stenotic region has a close link with arterial murmur sound that was discussed in Chapter 4 in more details by means of the energy spectra of the pressure fluctuations.

Cycle-to-cycle variations of the three turbulent velocity fluctuations, u''/u''_{max}, v''/v''_{max} and w''/w''_{max}, are presented in Fig. 6.22 at the different axial positions while $Re = 2000$. The fluctuating quantities found upstream and at the centre of the stenosis are almost flat because of the laminar nature of the oscillation, but they grow and become severe at the immediate post stenotic region, clearly it can be framed within $1.0 \leq y/L \leq 6.0$. However, after the region $y/L = 6.0$, the magnitude of the velocity fluctuations decrease since the effect of the stenosis vanishes there. In addition, the extreme upper wall pressure fluctuations p'' in Fig. 6.23 are again directly responsible for creating arterial murmur sounds in the presence of an arterial stenosis.

6.3.6 Turbulent Energy Spectra

The energy spectra, $E_{\alpha''\alpha''}$, (here α represents a generic variable either fluctuating velocity or pressure) of the three velocity fluctuations, $(u''/\bar{V}_{max})^2$, $(v''/\bar{V}_{max})^2$ and $(w''/\bar{V}_{max})^2$, and the pressure fluctuation, $(p''/\rho\bar{V}^2_{max})^2$, for $Re = 2000$ are presented in Figs. 6.24 -6.27, respectively, at the different axial positions in the post

stenosis region. The methods of calculation of $E_{\alpha''\alpha''}$, have already been discussed in § 4.6.5 in Chapter 4 and will not be repeated here.

The two stage decay in the slope of the turbulent flow spectra in Fig. 6.24 from the inertial sub range of slope $-5/3$ to the sub range of $-10/3$ agrees quite well with the experimental results of Gross et al. [145] and Lu *et al* . [42]. However, the region of the power spectra with the slope of $-7/1$ in the viscous dissipation range, which was also predicted by the classical theory of turbulence by Heisenberg [146], is found very small in our results and that is why it is included only in frame (a). Here it is mentioned that in Chapter 4, the region of the power spectra with the slope of $-7/1$ was also very small, but it was not shown in the figure. Furthermore, the range of the inertia sub-range region found in frames 6.24(a-e) is approximately same, while it is very small in frames 6.24(f-i) due to the small intensity of the turbulence found at the far downstream region.

The energy spectra of the two other velocity components, $(v''/\bar{V}_{max})^2$ in Fig. 6.25 and $(w''/\bar{V}_{max})^2$ in Fig. 6.26 respectively show a similar break frequency as shown in Fig. 6.24. Also, it is observed that the region of the inertia sub-range downstream is very small or totally absent (frames 6.26(h-i)). As with the velocity spectra, the broadband frequency found for the pressure fluctuations shown in frames (a-e) of Fig. 6.27. For the pressure fluctuations the inertia sub-range region is larger than that of the spectra of the break frequency region with slope $-7/3$, and it is very small in frame (f) where the turbulent intensity is relatively low. As discussed in Chapter 4, the potential source of murmurs of the arterial stenosis is caused by the change of slope from $-5/3$ to $-7/3$ where the energy from the pressure fluctuations spectra transfers to the sound spectra.

6.3.7 Comparison Between Additive Sinusoidal and Physiological Pulsatile Flow

A comparison has been drawn between the additive sinusoidal and physiological pulsatile flow cases in Figs. 6.28(a-b) in terms of the upper wall mean shear stress and turbulent kinetic energy (TKE), respectively, while $Re = 2000$. From Fig. 6.28(a), it is seen that in the sinusoidal case the stress drop and rise at the post stenosis region are larger than the physiological case. In the sinusoidal case, the

turbulent kinetic energy is also higher than that of the physiological pulsatile case. This might happen for the following reasons:

in the additive sinusoidal case, the steady part of the inlet condition dominates the whole flow and the streamwise velocity is always directed to the streamwise direction for some part of the time cycle

in the physiological case, the oscillating part of the inlet condition dominates the whole flow and the streamwise velocity is not always directed to the streamwise direction within the whole time cycle. In the diastolic phase the streamwise velocity is directed to the backward direction near the wall, owing to the effect of the Womerseley number.

6.4 Conclusion

Large Eddy Simulation with a localised dynamic sub-grid model of Piomelli-Liu [4] has been applied to investigate the physiological pulsatile flow through the model of an arterial stenosis. The justification of using LES in the study of physiological pulsatile flow in the model is made through the contribution of the SGS model. It is found that a maximum 37.4% contribution is received from the SGS model while $Re = 2000$.

A comparison of the results obtained from the LES and coarse DNS is made and excellent agreement is found in the mean pressure and shear distributions. But the results show some variations in the turbulent characteristics, which is quite reasonable due to the effects of the sub-grid model.

For the different grid arrangements and timesteps, the turbulent intensities vary slightly since the instantaneous flow field at the post stenosis region is highly oscillating due to the physiological pulse. In this chapter, it is also found that the upper wall shear stress drops just prior to the centre of the stenosis which is completely opposite to the results of Mittal *et al* . [79], as already noticed in Chapter 4.

The maximum turbulent kinetic energy occurs not in the centre of the channel but near the upper wall where the stenosis appeared. In addition, the high level of turbulent fluctuations found downstream ($0 < y/L < 6$ as in Chapter 4) of the stenosis is harmful in the pathological point of view.

The break frequency of the energy spectra from $-5/3$ to $-10/3$ for the velocity

fluctuations are clearly observed in the immediate downstream region of the stenosis. The break frequency for the pressure fluctuations spectra from $-5/3$ to $-7/3$ instead of $-10/3$ as in the velocity fluctuations. Similar results have been found in the case of sinusoidal pulse which is mentioned in Chapter 4.

A comparison is drawn between the results of the additive sinusoidal and physiological pulsatile flows and we have found that the shear stress and the TKE are higher in case of the sinusoidal than the physiological.

In the physiological pulsatile velocity profile, only the first harmonic ($NH = 1$) pressure oscillation was considered. In Chapter 7, we will investigate the effects of the various harmonics of the pressure pulse.

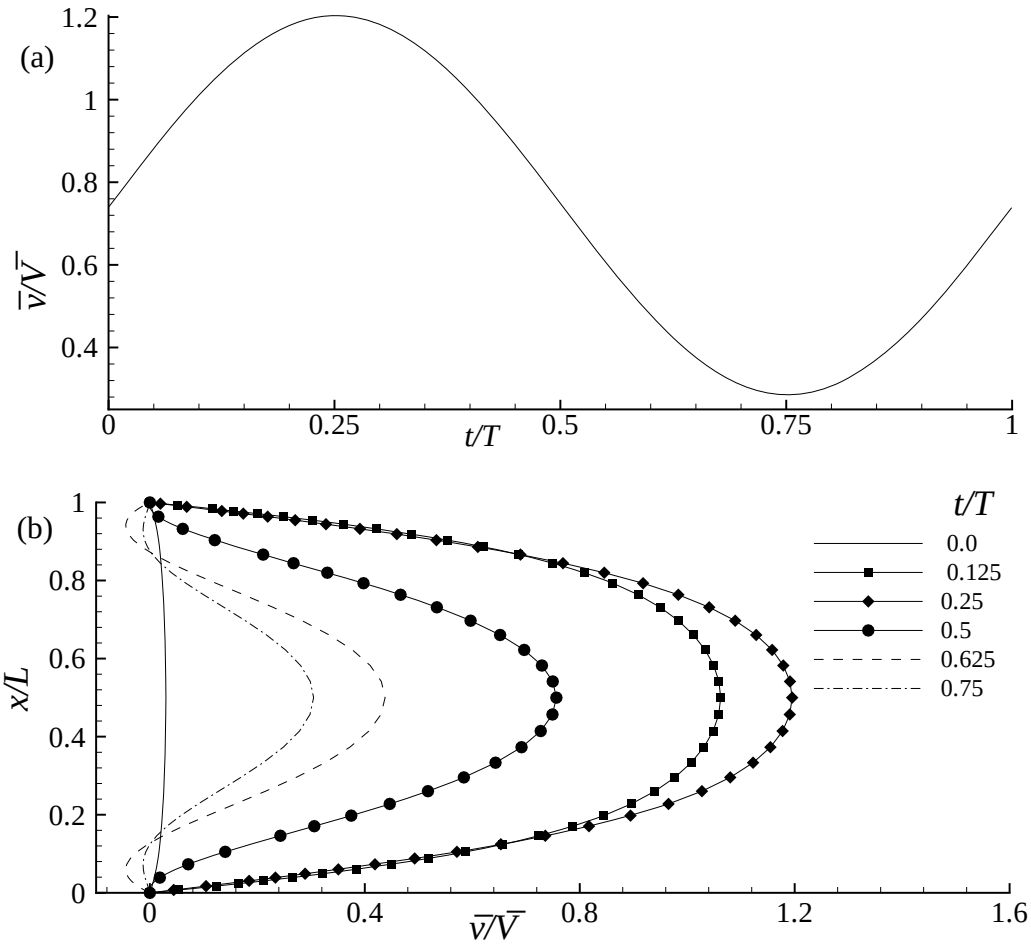

Figure 6.1: Inlet velocity profile, $\bar{v}/\bar{V}_{max}$, while $Re = 2000$ and the Womersely number $\alpha = 10.5$.

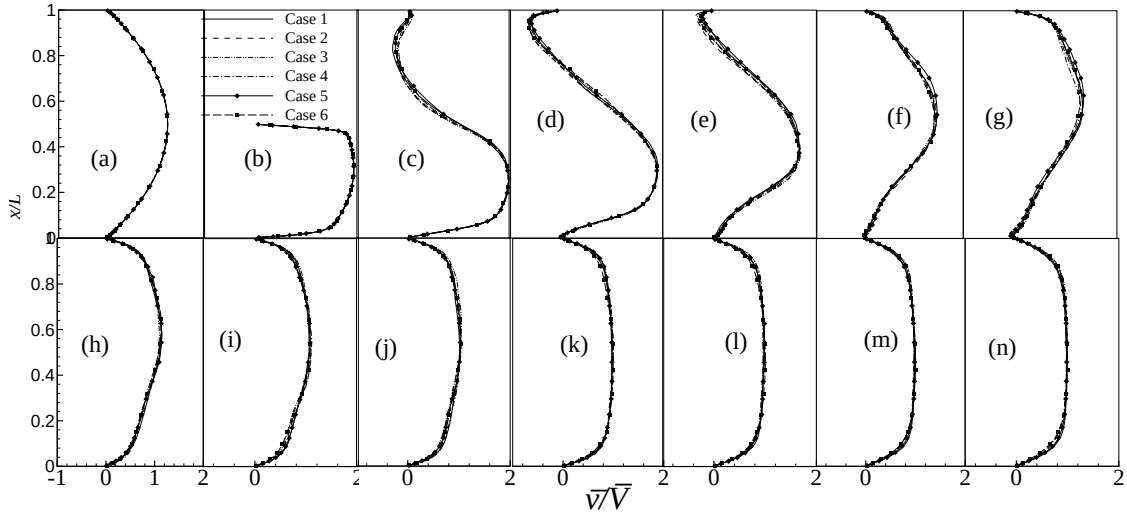

Figure 6.2: Grid independence test for the mean streamwise velocity, $< \bar{v} > /\bar{V}$ at (a) $y/L =$ inlet, (b) $y/L = 0.0$, (c) $y/L = 1.0$, (d) $y/L = 1.5$, (e) $y/L = 2.0$, (f) $y/L = 2.5$, (g) $y/L = 3.0$, (h) $y/L = 4.0$, (i) $y/L = 5.0$, (j) $y/L = 6.0$, (k) $y/L = 8.0$, (l) $y/L = 10.0$, (m) $y/L = 12.0$ and (n) $y/L =$ outlet, while $Re = 2000$.

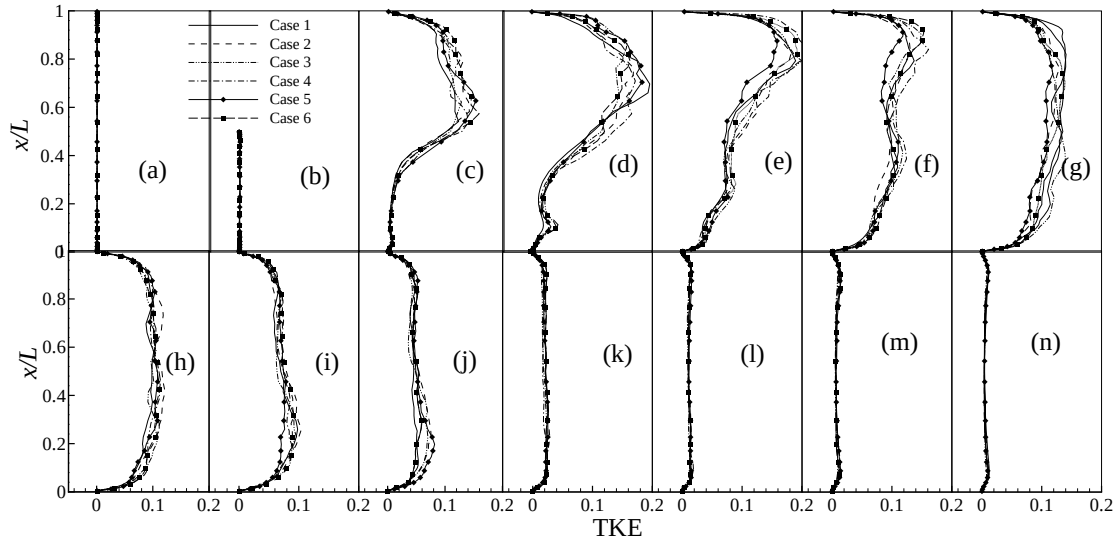

Figure 6.3: Grid independence test for the turbulent kinetic energy (TKE), $\frac{1}{2} < u_j'' u_j'' > /\bar{V}_{max}^2$, at (a) $y/L =$ inlet, (b) $y/L = 0.0$, (c) $y/L = 1.0$, (d) $y/L = 1.5$, (e) $y/L = 2.0$, (f) $y/L = 2.5$, (g) $y/L = 3.0$, (h) $y/L = 4.0$, (i) $y/L = 5.0$, (j) $y/L = 6.0$, (k) $y/L = 8.0$, (l) $y/L = 10.0$, (m) $y/L = 12.0$ and (n) $y/L =$ outlet, while $Re = 2000$.

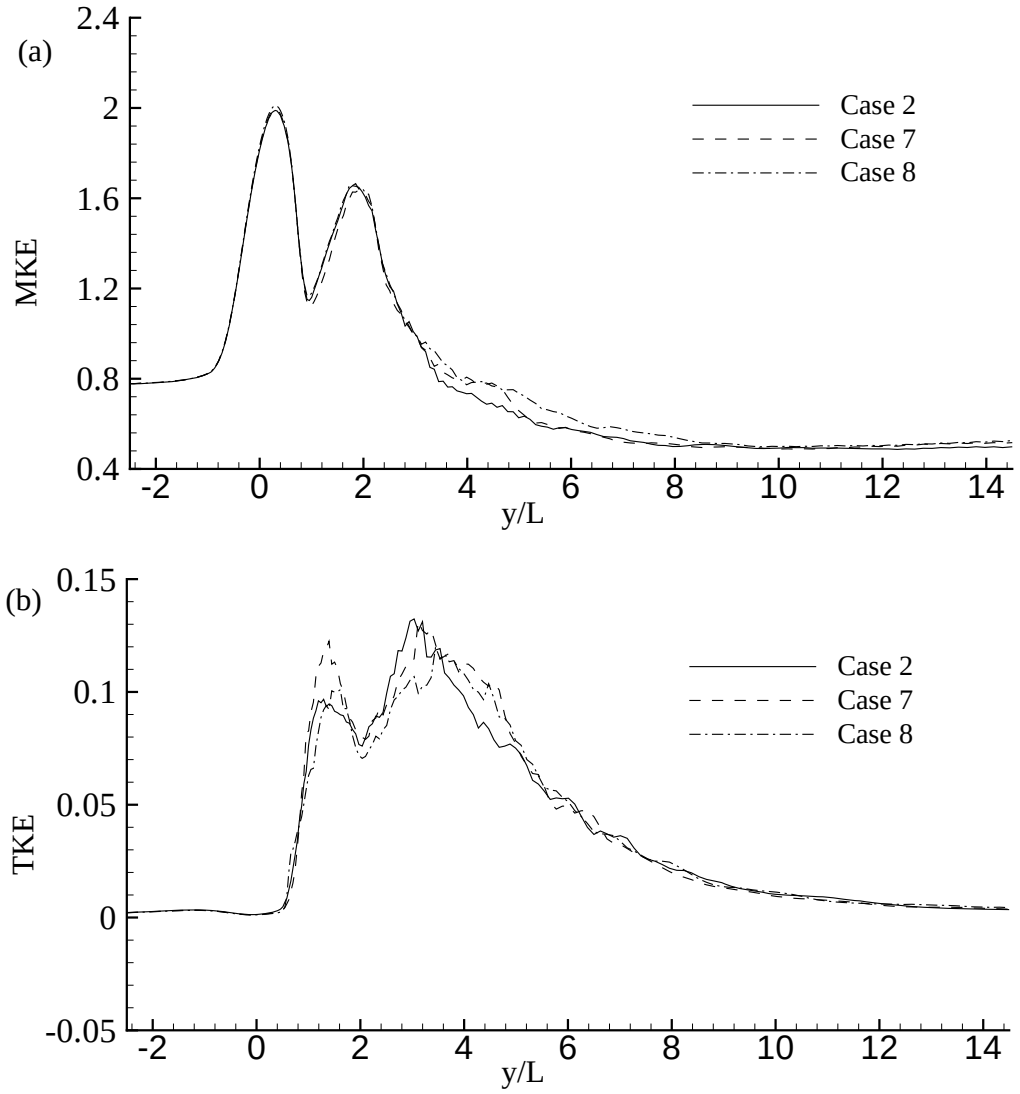

Figure 6.4: Timestep independence test for the (a) mean kinetic energy (MKE), $\frac{1}{2} < u_j u_j > /\bar{V}^2_{max}$, and (b) turbulent kinetic energy (TKE), $\frac{1}{2} < u''_j u''_j > /\bar{V}^2_{max}$, while $Re = 2000$.

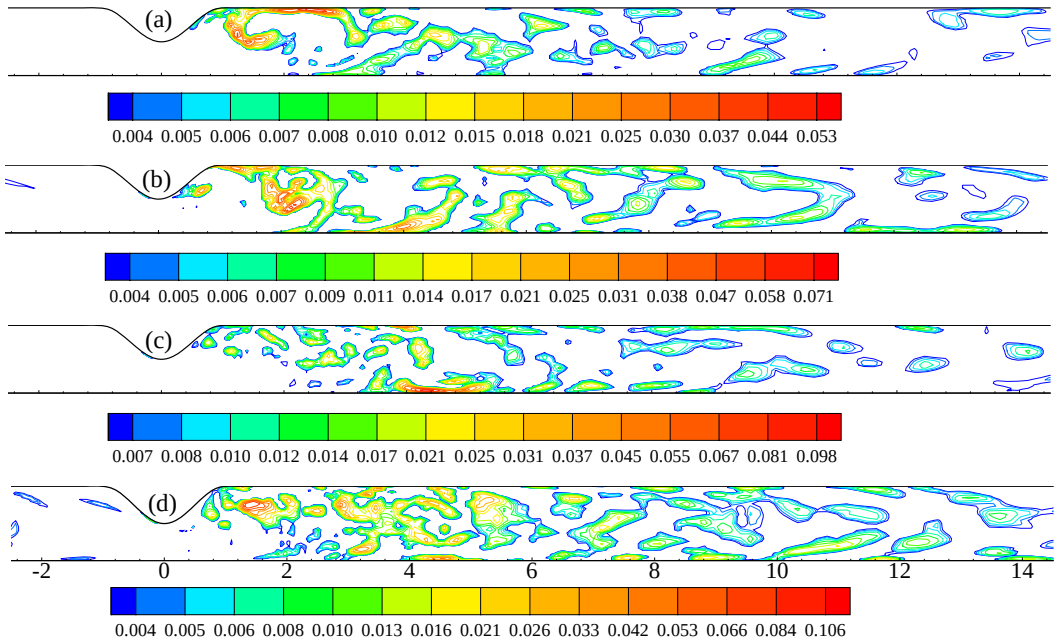

Figure 6.5: Dynamic Smagorinsky constant, C_s, for (a) $Re = 1000$, (b) $Re = 1400$, (c) $Re = 1700$ and (d) $Re = 2000$.

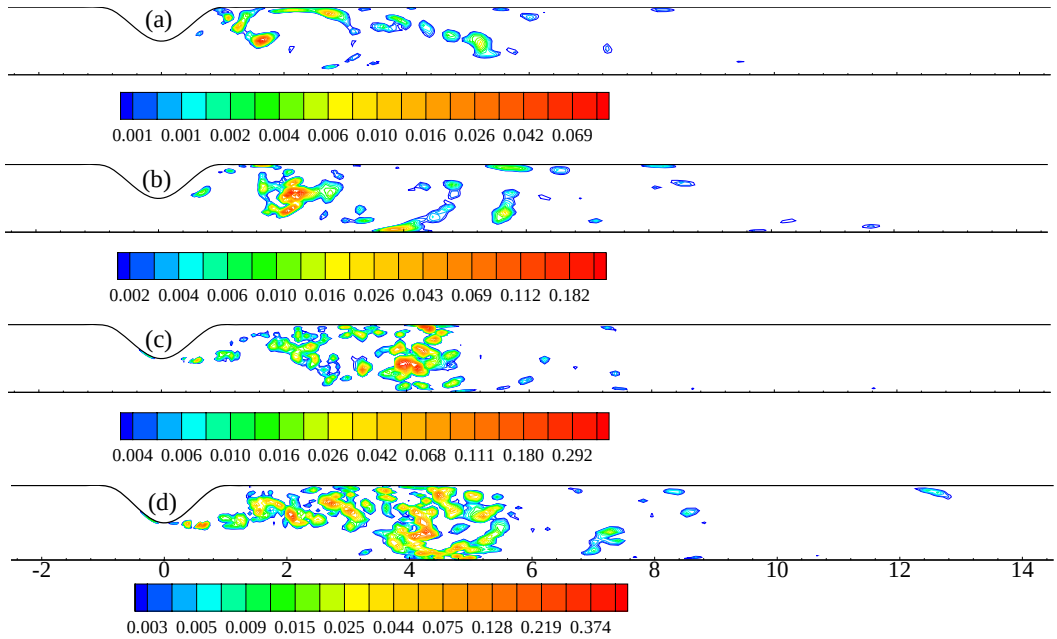

Figure 6.6: Normalised SGS eddy viscosity, μ_{sgs}/μ, for (a) $Re = 1000$, (b) $Re = 1400$, (c) $Re = 1700$ and (d) $Re = 2000$.

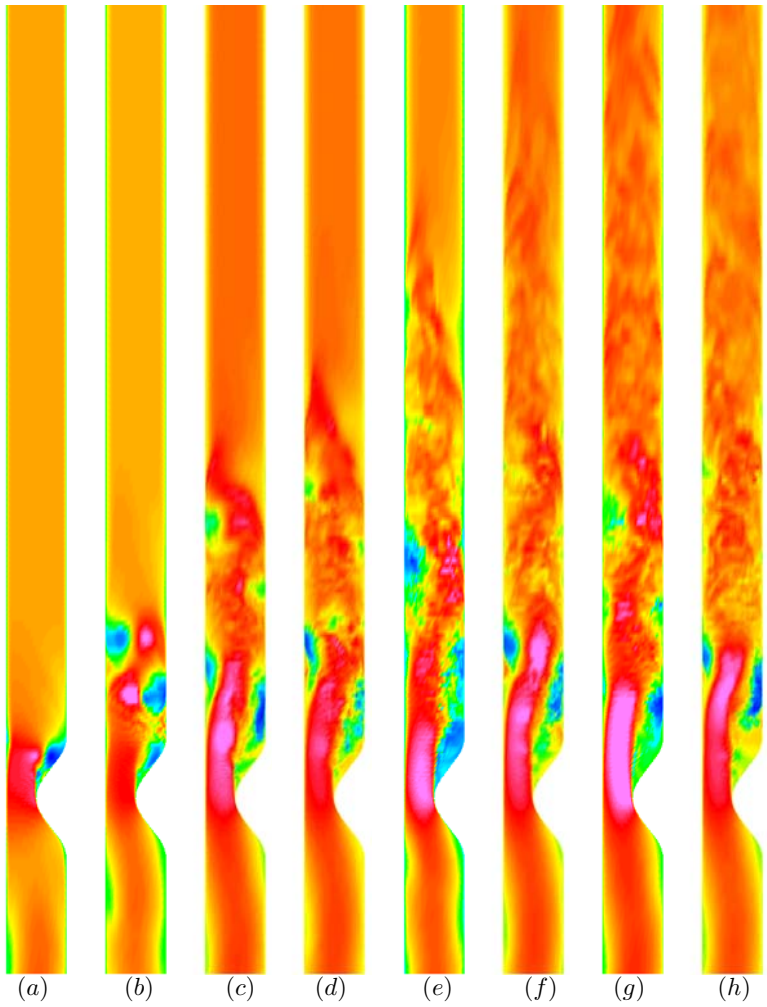

Figure 6.7: Streamwise velocity, $\bar{v}$, at (a) $t/T = 1.0$, (b) $t/T = 2.0$, (c) $t/T = 3.0$, (d) $t/T = 4.0$, (e) $t/T = 5.0$, (f) $t/T = 6.0$, (g) $t/T = 7.0$ and (h) $t/T = 8.0$ while $Re = 2000$.

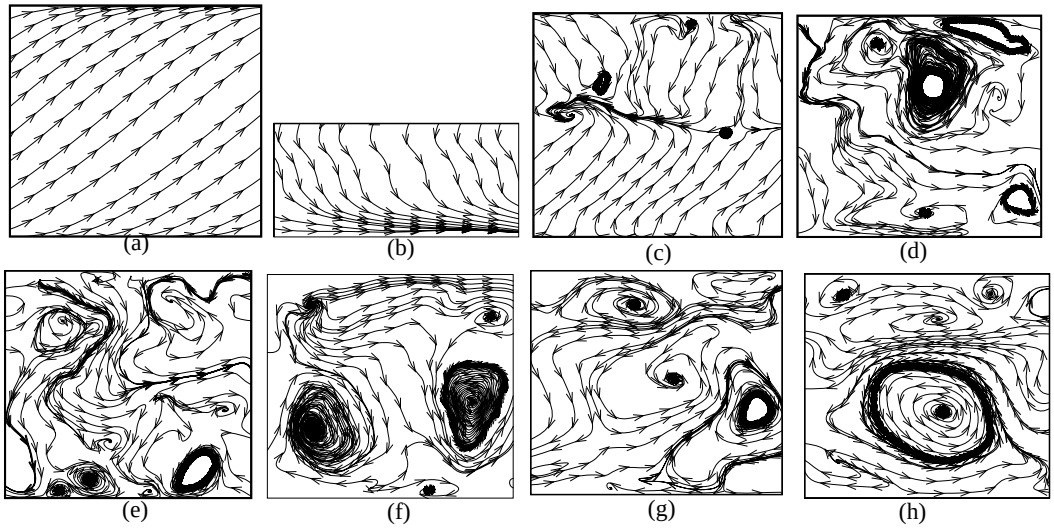

Figure 6.8: Instantaneous cross-sectional streamlines plotted at (a) $y/L = inlet$, (b) $y/L = 0$, (c) $y/L = 1$, (d) $y/L = 2$, (e) $y/L = 4$, (f) $y/L = 6$, (g) $y/L = 10$, and (h) $y/L = outlet$ while $Re = 2000$ and $t/T = 10.25$.

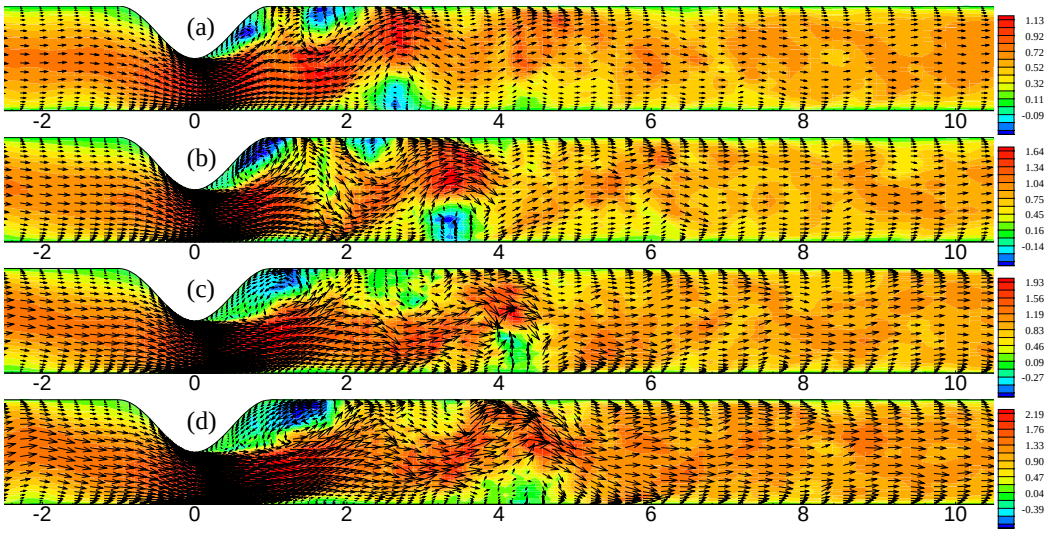

Figure 6.9: Instantaneous streamwise vectors appended on the streamwise velocity, $\bar{v}/\bar{V}_{max}$, at $t/T = 10.25$ for (a) $Re = 1000$, (b) $Re = 1400$, (c) $Re = 1700$, and (d) $Re = 2000$.

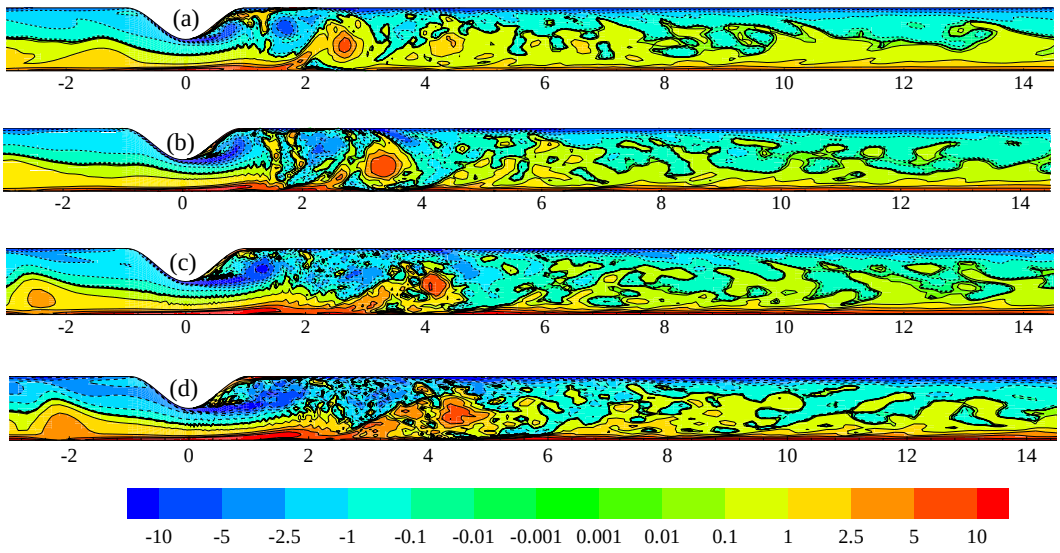

Figure 6.10: Spanwise average vorticity, $< \omega_z >_s$, for (a) $Re = 1000$, (b) $Re = 1400$, (c) $Re = 1700$, and (d) $Re = 2000$ at $t/T = 10.25$.

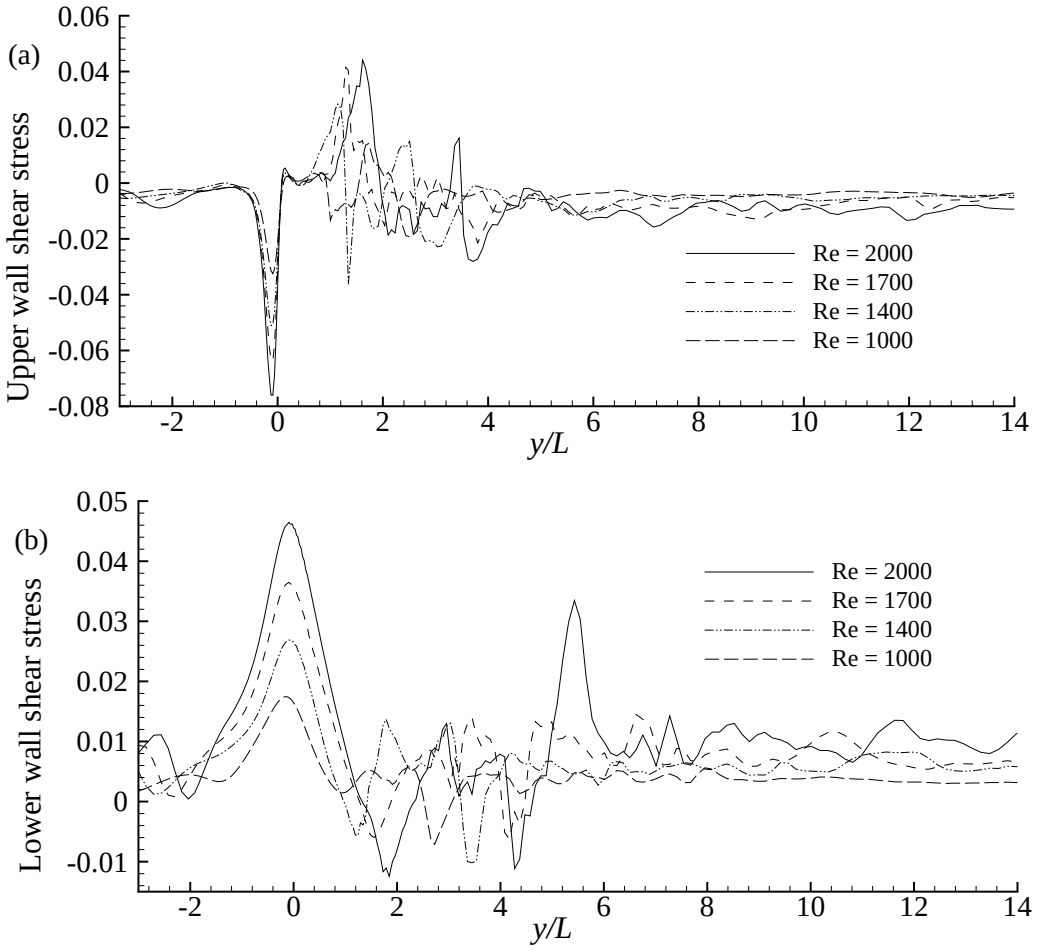

Figure 6.11: Instantaneous wall shearing stress,$\tau_{xy}/\rho\bar{V}_{max}^2$, at the (a) upper wall and (b) lower wall for the different Reynolds numbers while $t/T = 10.25$.

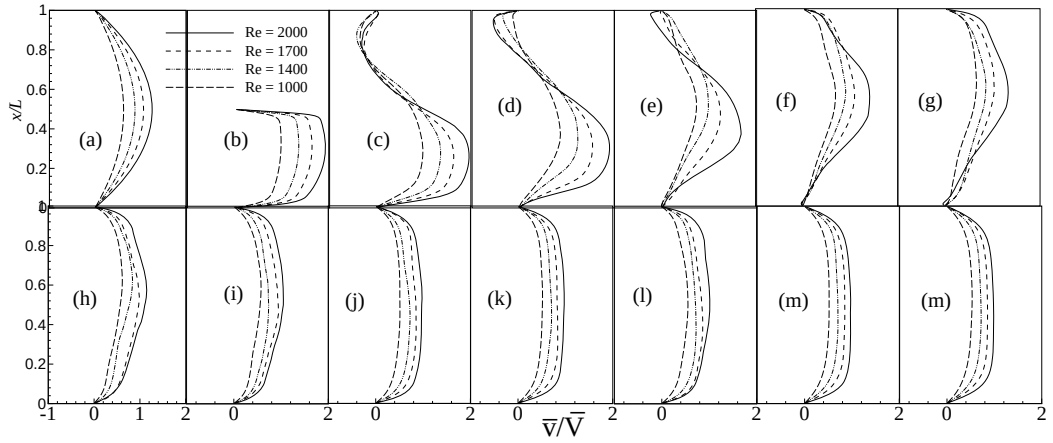

Figure 6.12: Time-mean streamwise velocity, $< \bar{v} > /\bar{V}_{max}$, at (a) $y/L =$ inlet, (b) $y/L = 0.0$, (c) $y/L = 1.0$, (d) $y/L = 1.5$, (e) $y/L = 2.0$, (f) $y/L = 2.5$, (g) $y/L = 3.0$, (h) $y/L = 4.0$, (i) $y/L = 5.0$, (j) $y/L = 6.0$, (k) $y/L = 8.0$, (l) $y/L = 10.0$, (m) $y/L = 12.0$ and (n) $y/L =$ outlet for the different Reynolds numbers.

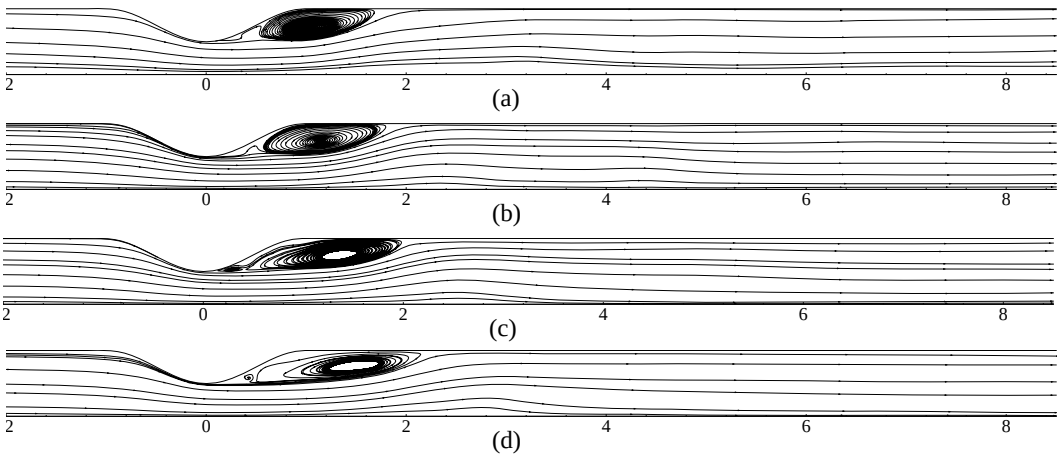

Figure 6.13: Time-mean streamlines for (a) $Re = 1000$, (b) $Re = 1400$, (c) $Re = 1700$, and (d) $Re = 2000$.

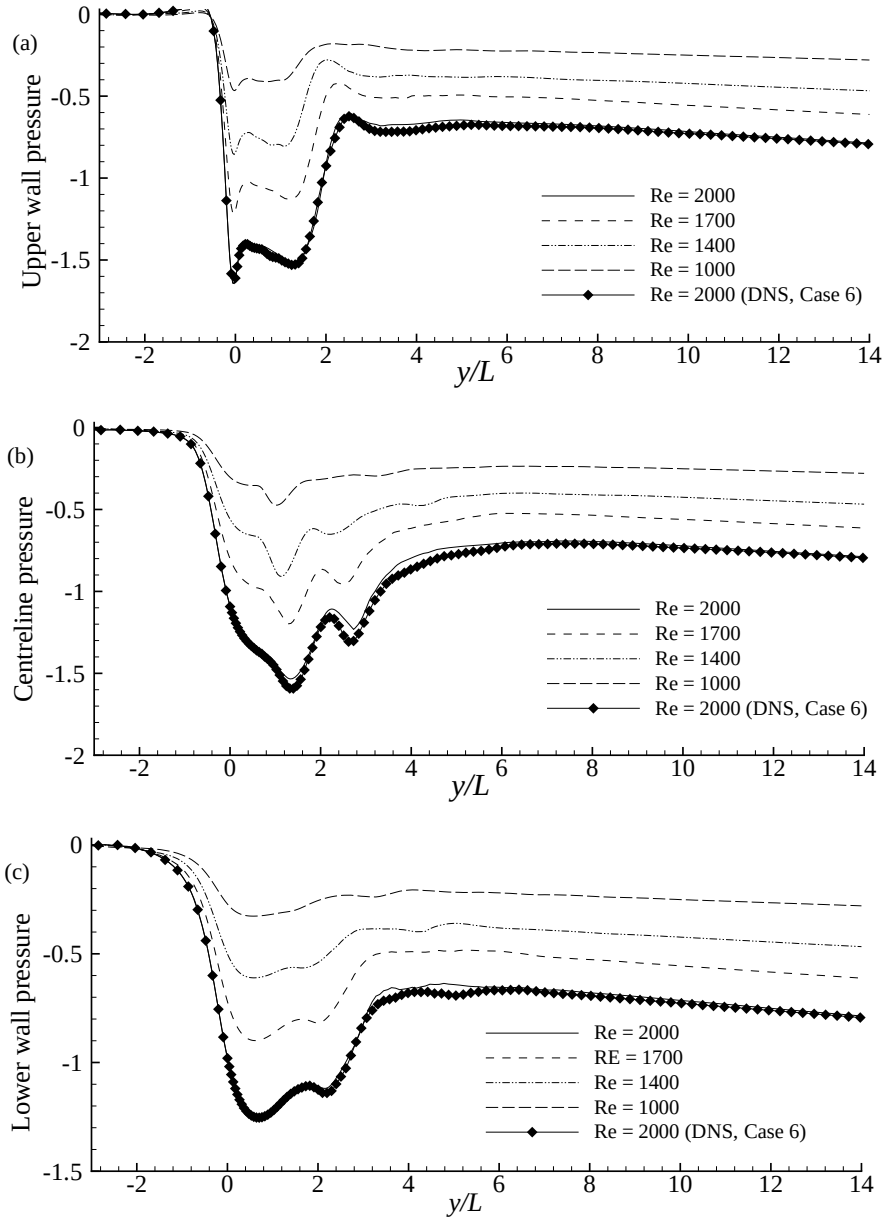

Figure 6.14: Time-mean pressure, $< \bar{p} > /\rho \bar{V}^2_{max}$, at (a) upper wall (b) centreline and (c) lower wall for the different Reynolds numbers.

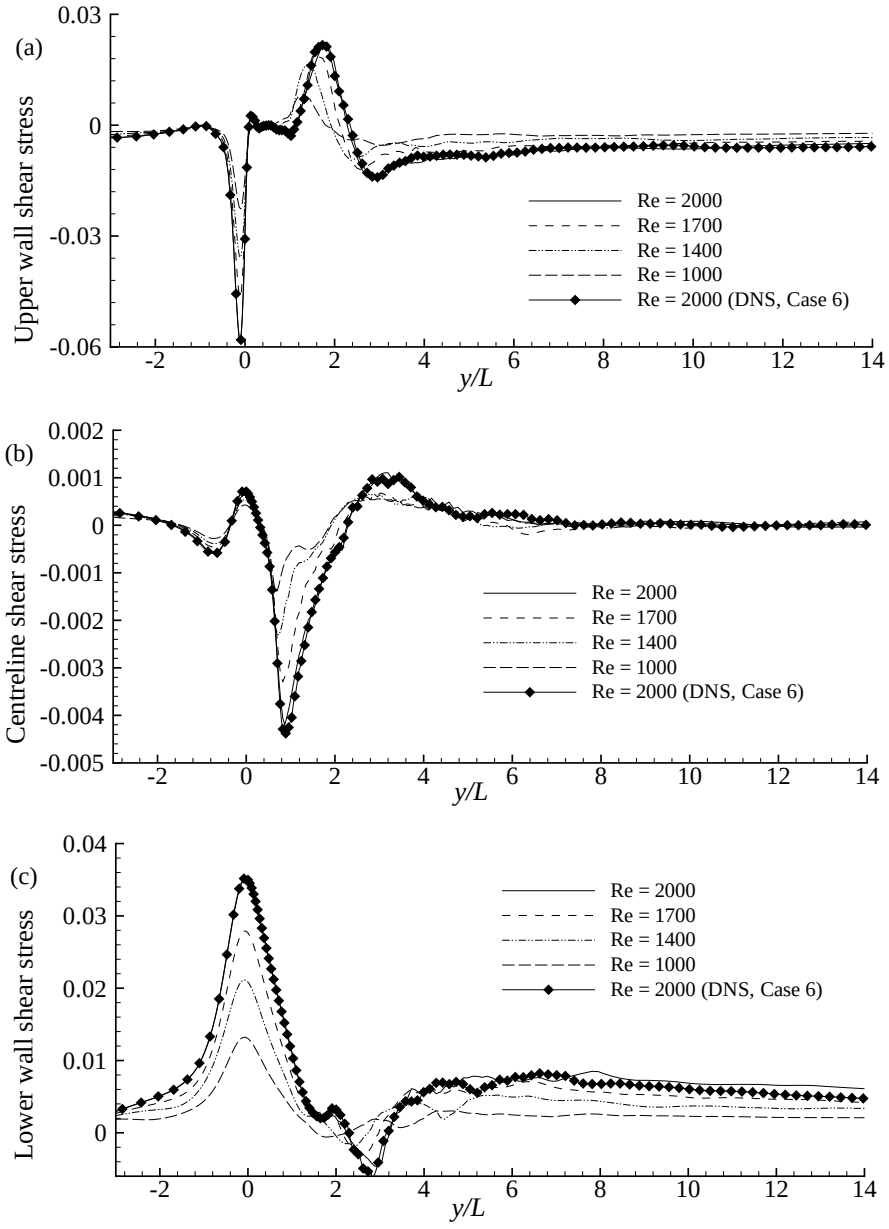

Figure 6.15: Time-mean shear stresses, $< \tau_{xy} > /\rho \bar{V}_{max}^2$, at (a) upper wall (b) centreline and (c) lower wall for the different Reynolds numbers.

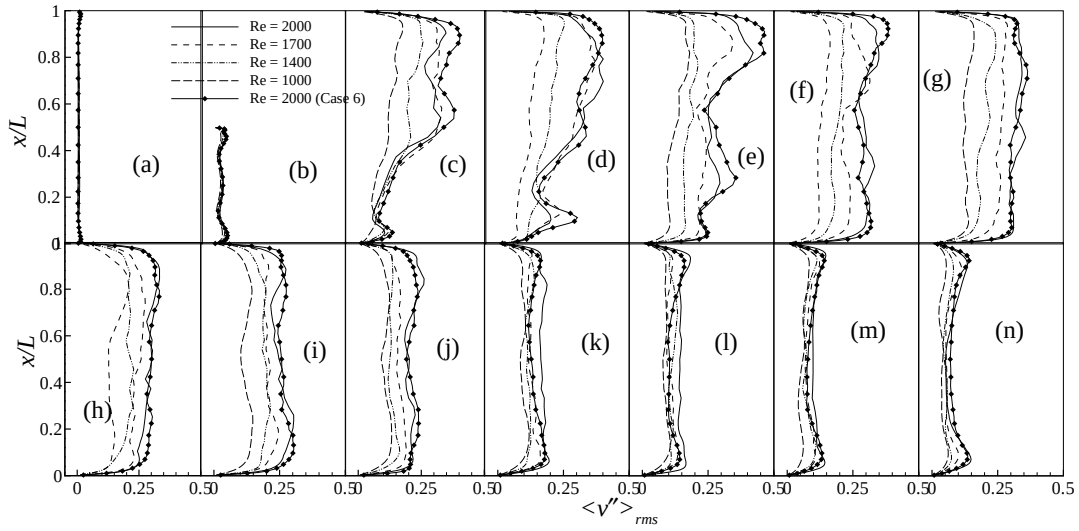

Figure 6.16: rms of the streamwise velocity fluctuations, $< v'' >_{rms} /\bar{V}_{max}$, at the different axial location, (a) $y/L =$ inlet, (b) $y/L = 0.0$, (c) $y/L = 1.0$, (d) $y/L = 1.5$, (e) $y/L = 2$, (f) $y/L = 2.5$, (g) $y/L = 3.0$, (h) $y/L = 4.0$, (i) $y/L = 5.0$, (j) $y/L = 6.0$, (k) $y/L = 8.0$ (l) $y/L = 10.0$, (m) $y/L = 12.0$ and (n) $y/L =$ outlet, for the different Reynolds numbers.

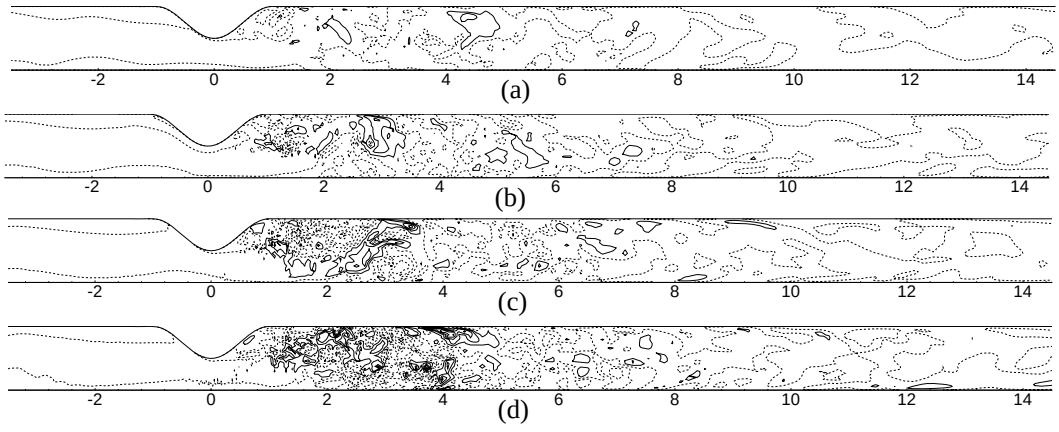

Figure 6.17: Contour plot of the streamwise velocity fluctuations, v'', for the different Reynolds numbers.

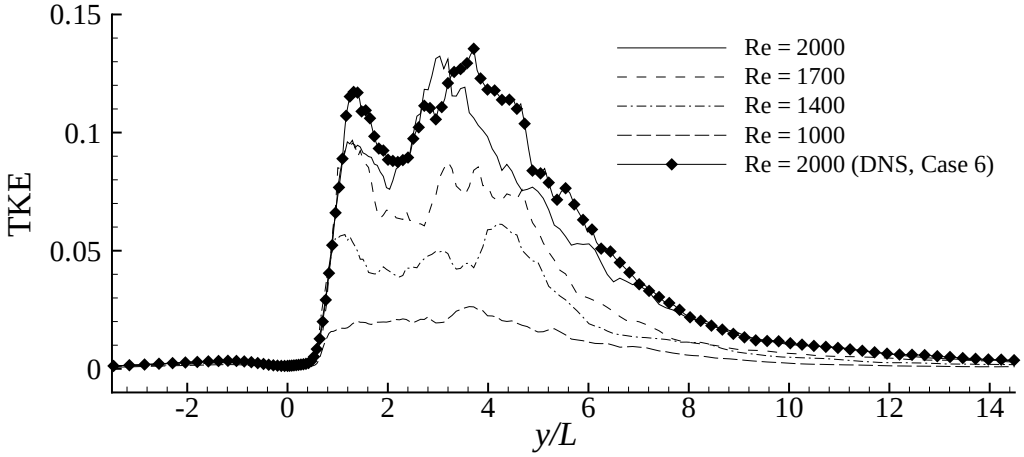

Figure 6.18: Centreline turbulent kinetic energy, $\frac{1}{2} < u_j'' u_j'' > / \bar{V}_{max}^2$, for the different Reynolds numbers.

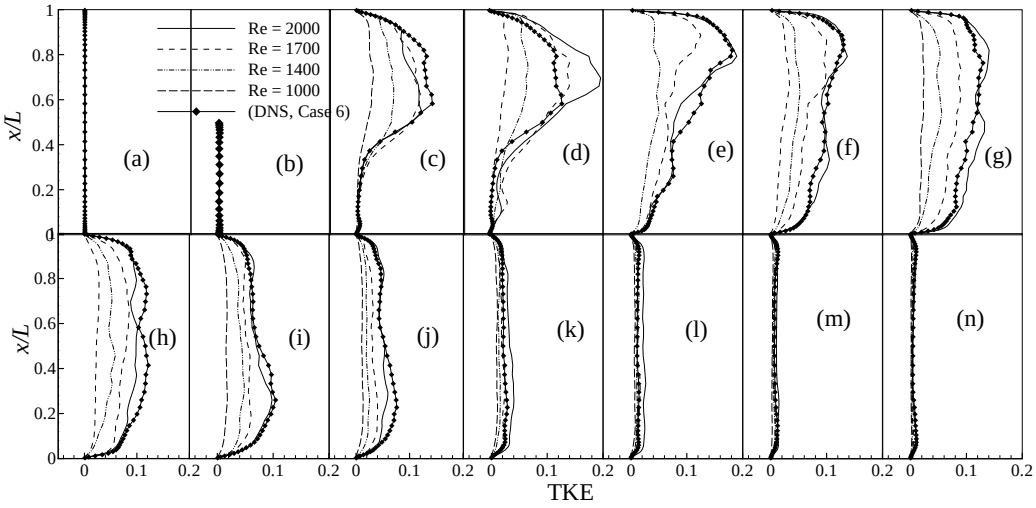

Figure 6.19: Turbulent kinetic energy, $\frac{1}{2} < u_j'' u_j'' > / \bar{V}_{max}^2$, at the different axial locations, (a) $y/L =$ inlet, (b) $y/L = 0.0$, (c) $y/L = 1.0$, (d) $y/L = 1.5$, (e) $y/L = 2$, (f) $y/L = 2.5$, (g) $y/L = 3.0$, (h) $y/L = 4.0$, (i) $y/L = 5.0$, (j) $y/L = 6.0$, (k) $y/L = 8.0$ (l) $y/L = 10.0$, (m) $y/L = 12.0$ and (n) $y/L =$ outlet, for the different Reynolds numbers.

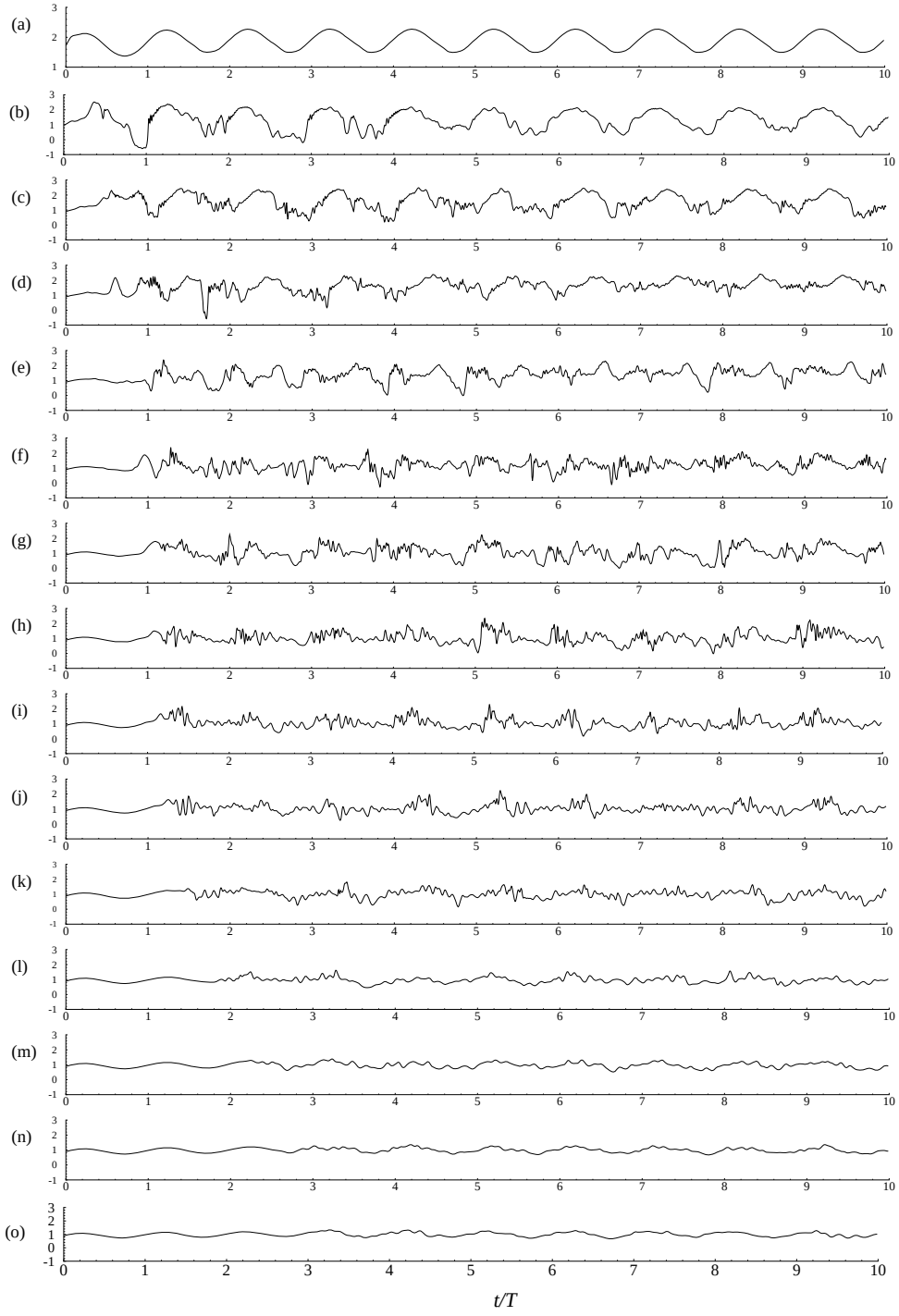

Figure 6.20: Time history of the streamwise centreline velocity, $\bar{v}/\bar{V}_{max}$, at (a) $y/L = 0.0$, (b) $y/L = 1.0$, (c) $y/L = 1.5$, (d) $y/L = 2.0$, (e) $y/L = 2.5$, (f) $y/L = 3.0$, (g) $y/L = 3.5$, (h) $y/L = 4.0$, (i) $y/L = 4.5$, (j) $y/L = 5.0$, (k) $y/L = 6.0$, (l) $y/L = 7.0$, (m) $y/L = 8.0$, (n) $y/L = 10.0$, and (o) $y/L =$outlet, while $Re = 2000$.

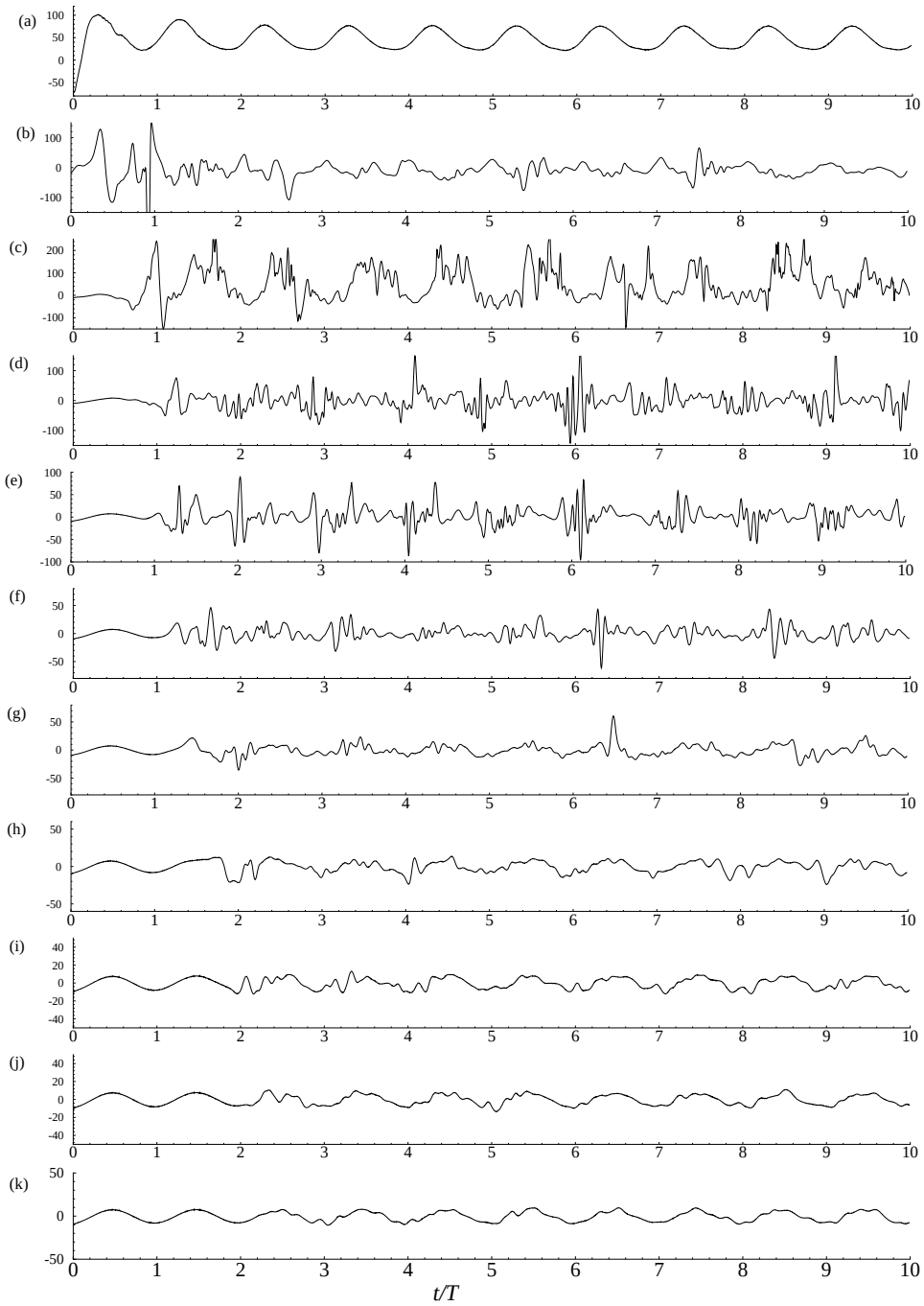

Figure 6.21: Time history of the upper wall pressure gradient, $\frac{\partial p}{\partial y}$, at (a) $y/L = 0.0$, (b) $y/L = 1.0$, (c) $y/L = 2.0$, (d) $y/L = 3.0$, (e) $y/L = 4.0$, (f) $y/L = 5.0$, (g) $y/L = 6.0$, (h) $y/L = 7.0$, (i) $y/L = 8.0$, (j) $y/L = 9.0$, and (k) $y/L = 10.0$ while $Re = 2000$.

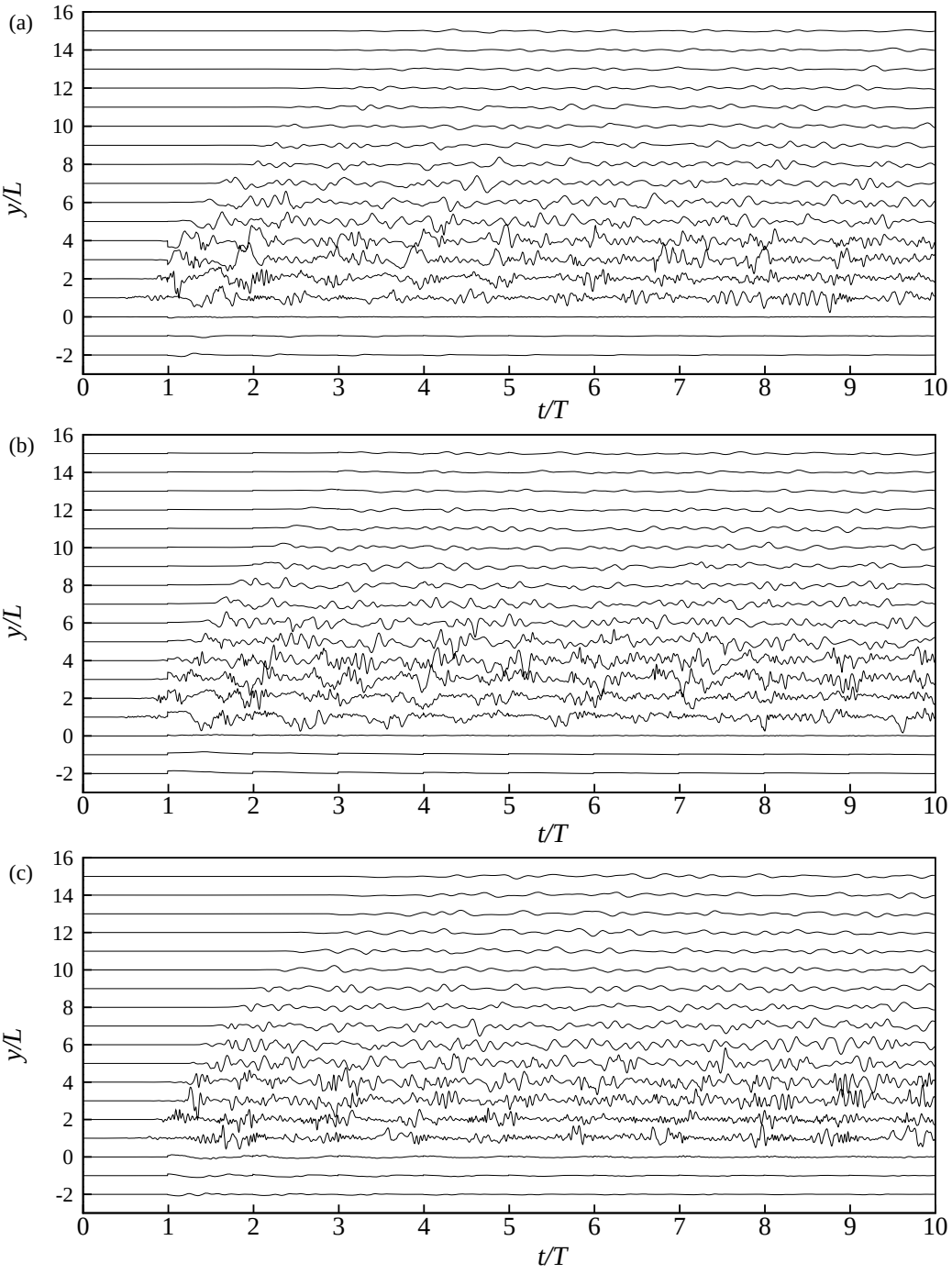

Figure 6.22: Time history of the centreline velocity fluctuations, (a) u''/u''_{max}, (b) v''/v''_{max} and (c) w''/w''_{max} at different axial locations while $Re = 2000$.

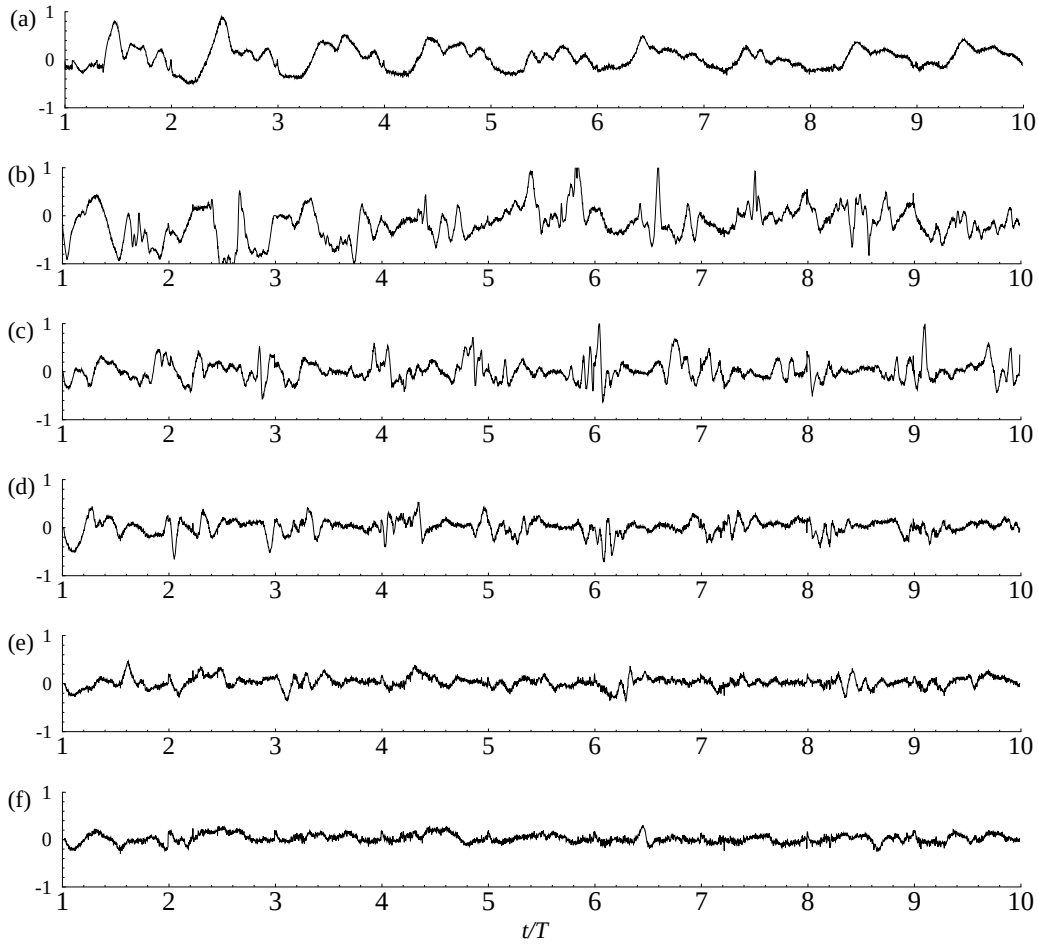

Figure 6.23: Time history of the upperwall pressure fluctuations, $p''/\rho\bar{V}_{max}^2$, at (a) $y/L = 1.0$, (b) $y/L = 2.0$, (c) $y/L = 3.0$, (d) $y/L = 4.0$, (e) $y/L = 5.0$ and (f) $y/L = 6.0$ while $Re = 2000$.

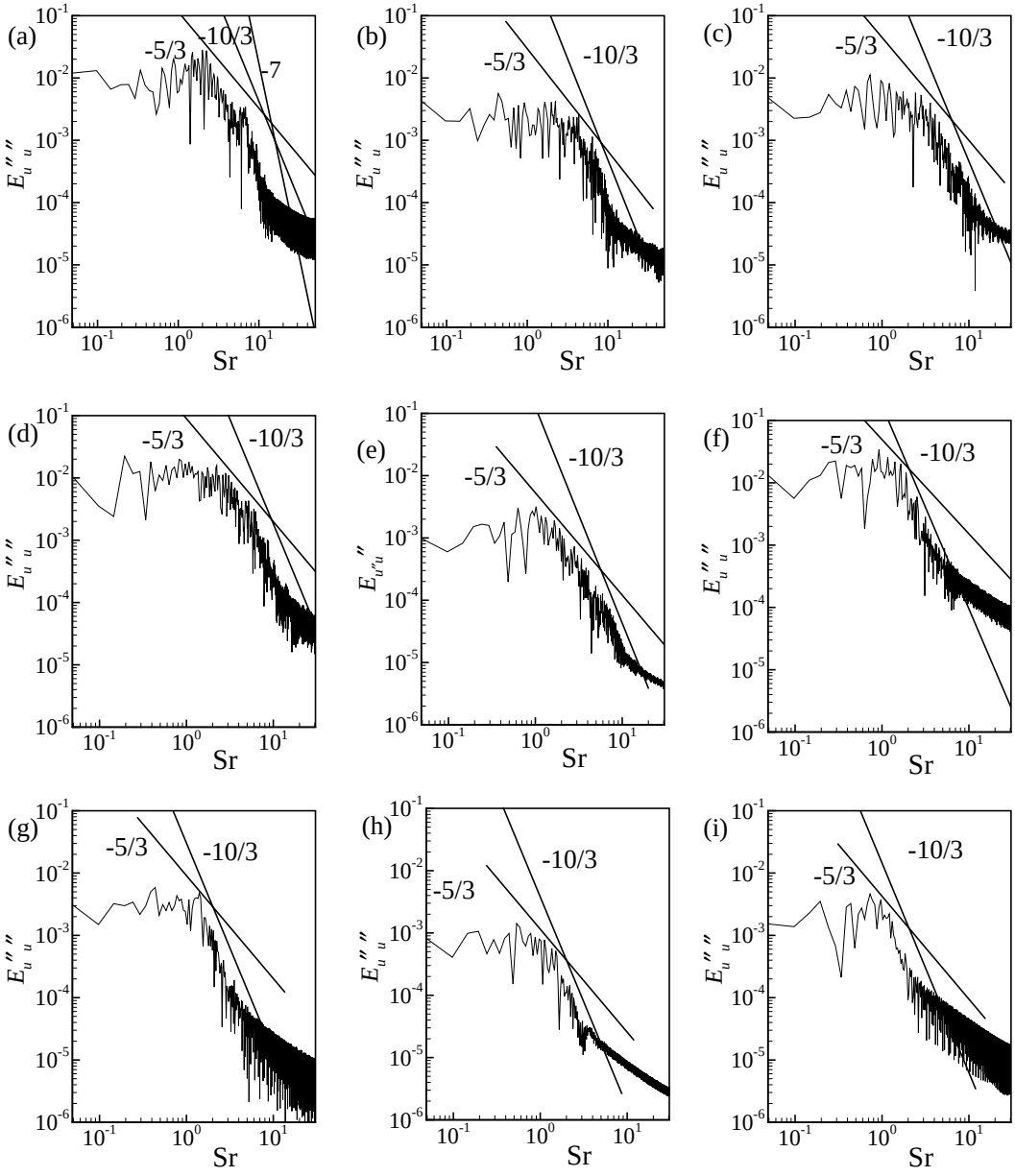

Figure 6.24: Energy spectrum of, u'', at (a) $y/L = 1.0$, (b) $y/L = 2.0$, (c) $y/L = 3.0$, (d) $y/L = 4.0$, (e) $y/L = 5.0$, (f) $y/L = 6.0$, (g) $y/L = 8.0$, (h) $y/L = 10.0$ and (i) $y/L = 12.0$ while $Re = 2000$.

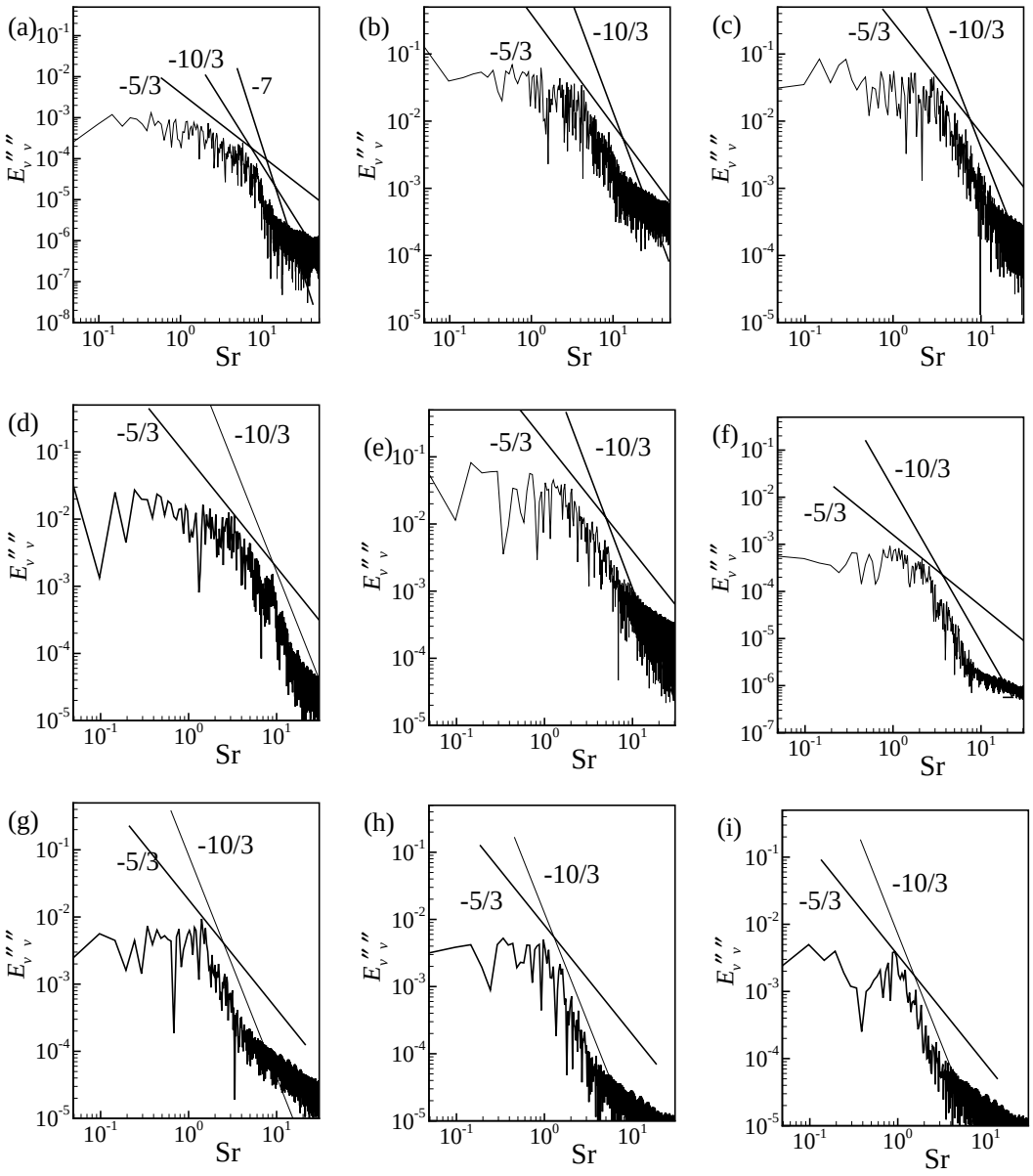

Figure 6.25: Energy spectrum of, v'', at (a) $y/L = 1.0$, (b) $y/L = 2.0$, (c) $y/L = 3.0$, (d) $y/L = 4.0$, (e) $y/L = 5.0$, (f) $y/L = 6.0$, (g) $y/L = 8.0$, (h) $y/L = 10.0$ and (i) $y/L = 12.0$ while $Re = 2000$.

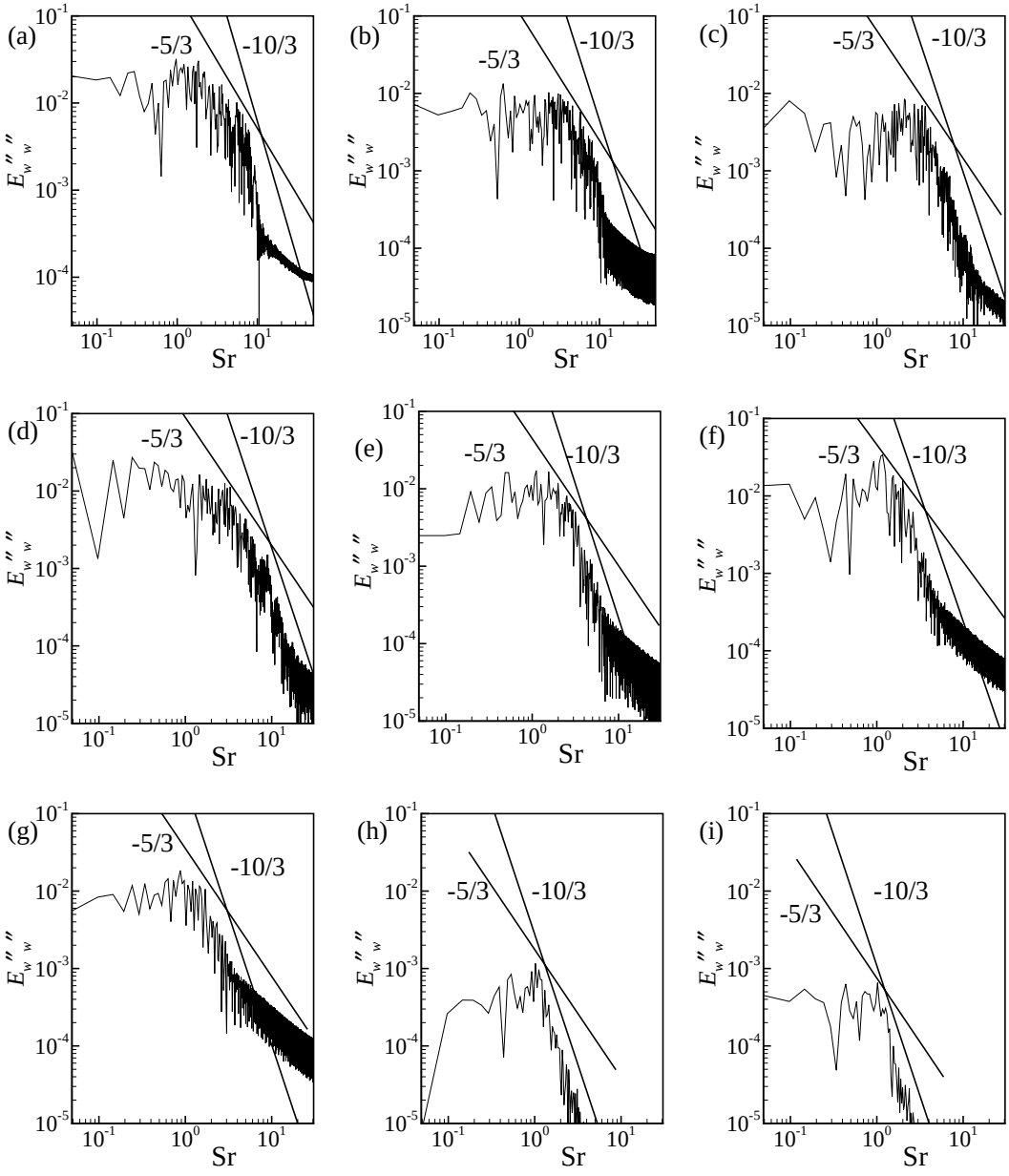

Figure 6.26: Energy spectrum of, w'', at (a) $y/L = 1.0$, (b) $y/L = 2.0$, (c) $y/L = 3.0$, (d) $y/L = 4.0$, (e) $y/L = 5.0$, (f) $y/L = 6.0$, (g) $y/L = 8.0$, (h) $y/L = 10.0$ and (i) $y/L = 12.0$ while $Re = 2000$.

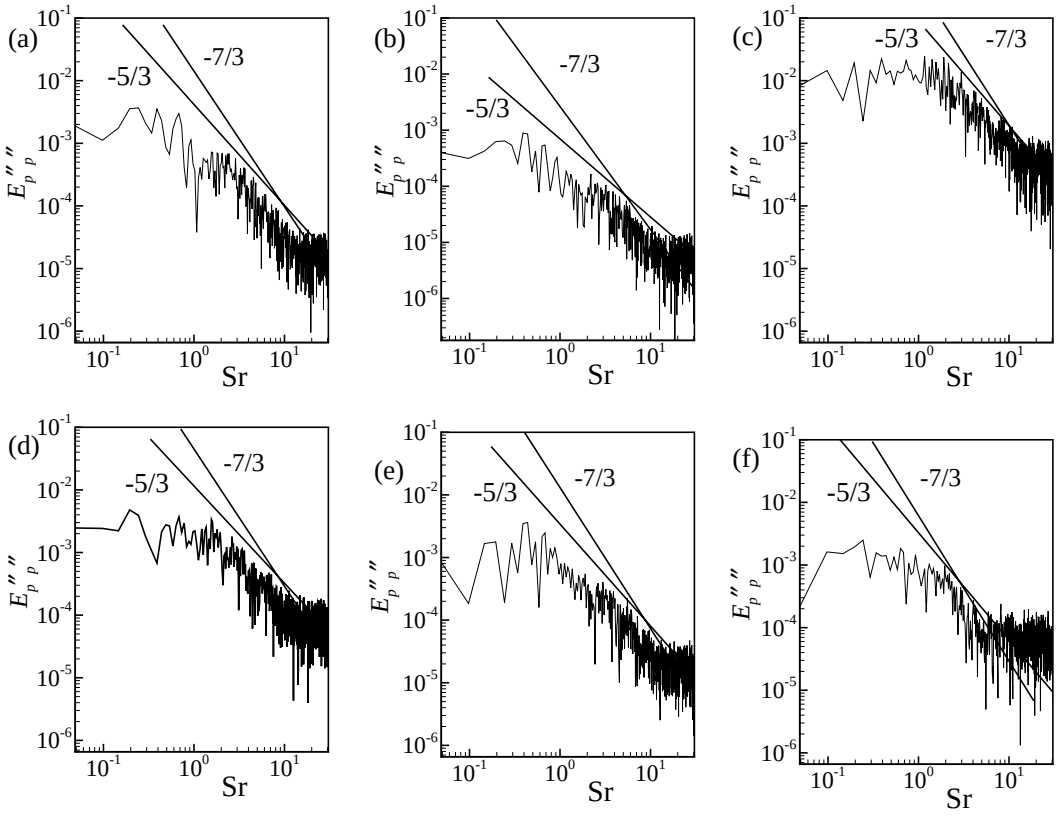

Figure 6.27: Energy spectrum of, p'', at (a) $y/L = 1.0$, (b) $y/L = 2.0$, (c) $y/L = 3.0$, (d) $y/L = 4.0$, (e) $y/L = 5.0$ and (f) $y/L = 6.0$ while $Re = 2000$.

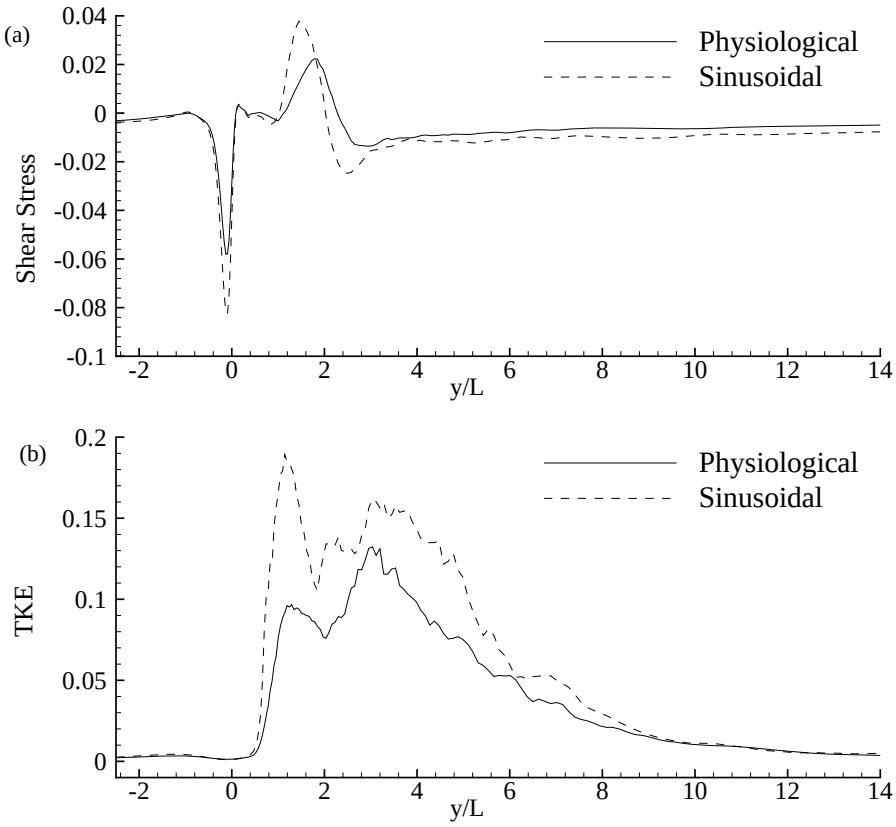

Figure 6.28: Comparison between the results of the physiological and sinusoidal pulsatile flows, here (a) upper wall shear stress, $< \tau_{xy} > /\rho \bar{V}^2_{max}$ and (b) centreline turbulent kinetic energy (TKE), $\frac{1}{2} < u''_j u''_j > /\bar{V}^2_{max}$.

Chapter 7

Simulation of Physiological Pulsatile Flow. Part 2. Effects of Various Harmonics, Percentage and Length of Stenosis

7.1 Introduction

In Chapter 6, physiological pulsatile flow in a model arterial stenosis using the first harmonic of the Fourier series of pressure pulse is investigated. In this Chapter, it would be studied the effects of the various harmonics of the pressure pulse in the same model.

LES technique is applied here with two SGS models: Germano-Lilly [2; 3] dynamic model (§ 3.5.1 in Chapter 3) and Piomelli-Liu [4] localized dynamic model (§ 6.2.1 in Chapter 6). A comparison between the two SGS models is made in terms of the results of the Smagorinsky constant and the normalised SGS viscosity. The LES results for the different grid arrangements are compared with a coarse DNS results in the case of fourth harmonic physiological pressure pulse.

A comparison of various harmonics is also made by means of the upper wall shear stress and turbulent kinetic energy while $Re = 2000$. Using the fourth harmonic of pressure pulse, the effects of different percentage and length of the stenosis are studied in this Chapter.

Table 7.1: Values of M_n and ϕ_n for different harmonics according to Womersley [6].

Number of harmonic, NH	M_n	ϕ_n
$1 = 1^{st}$ Harmonic	0.78	0.0113446
$2 = 2^{nd}$ Harmonic	1.32	-1.4442599
$3 = 3^{rd}$ Harmonic	-0.74	0.4625122
$4 = 4^{th}$ Harmonic	-0.41	-0.2879793

7.2 Physiological Inlet Profile

In Chapter 6, we obtained the following solution for generating the physiological flow at the inlet of the stenosis,

$$\bar{v}(x,t) = 4\bar{V}_{max}\frac{x}{L}\left(1-\frac{x}{L}\right) + A\sum_{n=1}^{NH}\frac{iM_nL^2}{\mu\alpha^2 n} \left[\cosh(\alpha\sqrt{in}\frac{x}{L}) - \frac{\cosh(\alpha\sqrt{in})-1}{\sinh(\alpha\sqrt{in})}\sinh(\alpha\sqrt{in}\frac{x}{L}) - 1\right] e^{i(n\omega t+\phi_n)}, \quad (7.1)$$

and $NH = 1$ was used to study the first harmonic of physiological flow. In this chapter, we will extend the number of harmonics to four for which we use $NH = 4$ and investigate further the transition of physiological flow through the stenosis with all these harmonics. For different harmonics, the values of M_n and ϕ_n are given in Table 7.1, and the values of the A and α (Womersley number) remain the same as in Chapter 6.

The real parts of the inlet velocity profile for the first four harmonics are shown in Figs. 7.1 - 7.4, respectively, while $Re = 2000$, $A = 0.4$ and $\alpha = 10.5$. In the first harmonic, the velocity profile is similar to a sin curve and seen in Fig. 7.1(a-b) where at (a) near the wall (b) centre of the channel. At the different phases, the velocity profiles are parabolic along the streamwise direction with the maximum occurring at the systolic phase ($t/T = 0.25$), but during the diastolic phase (after $t/T = 0.25$) the velocity decreases and gets the negative value near the top and bottom walls as seen in frame 7.1(c).

For the second to fourth harmonics, the velocity profiles are completely different

Table 7.2: Mesh details for the LES and DNS approaches.

Case	Re	approach	N_x	N_y	N_z	δt
0	< 2000	LES	50	200	50	10^{-3}
1	2000	LES	50	200	50	10^{-3}
2	2000	LES	50	250	50	10^{-3}
3	2000	LES	70	250	50	10^{-3}
4	2000	DNS	70	350	50	10^{-3}

from the first harmonic case. Moreover, the intensity of the streamwise velocity at the systolic phase and the backward directed velocity near the walls during the diastolic phases are larger in the cases from second to fourth harmonics than the first harmonic.

7.3 Results and Discussion

First, using the first four harmonics pressure pulse, the results of the grid independent test are presented in § 7.3.1. This is followed by the comparison between the SGS contributions in § 7.3.2 of the Germano-Lilly and Piomelli-Liu dynamic models. An overview of the time evolution of the turbulent flow quantity for the first four harmonics is given in § 7.3.3. The results of the various harmonics are compared in § 7.3.4 and § 7.3.5. The effects of the different percentages and length of the stenosis are presented in § 7.3.6 and § 7.3.7 respectively, followed by the conclusion of this chapter in § 8.4.

7.3.1 Grid Independence Test

In Chapter 6, a detailed grid and timestep independence test was carried out for the first harmonic case, and we have found that the primary flow features (especially the mean velocity) do not vary significantly with the different grid sizes and timesteps used in the simulation. In this Chapter, a grid independence test is conducted only for the first four harmonics case by taking four sets of different grid arrangements (see Table 7.2), and the results are compared in Figs. 7.5 and 7.6 in terms of the time mean streamwise velocity, $< \bar{v} > /\bar{V}_{max}$, and turbulent kinetic energy, $\frac{1}{2} <$

$u_j'' u_j'' > /\bar{V}_{max}^2$. The agreement is quite good indeed as shown in the previous Chapter 6. In particular, the mean flow is well resolved in the grids used, but some sensitivities exist in the turbulent results. Based on this grid independent test, a grid arrangement of $50 \times 200 \times 50$ is chosen for all the computations when the percentage of the stenosis is 50%. The grid details used in the higher percentage of stenosis are discussed in § 7.3.6.

7.3.2 SGS Contributions between the Germano-Lilly and Piomelli-Liu Dynamic Models

Figs. 7.7 and 7.8 show the contour plots of the dynamics Smagorinsky constant C_s obtained by using the Germano-Lilly [119; 3] and Piomelli-Liu [4] localized dynamic models, respectively. The results show that the dynamic values of C_s obtained by the Piomelli-Liu model are slightly larger than those of the Germano-Lilly model, since the back-scatter problem is reduced by using the Piomelli-Liu [4] localized dynamic model but not completely removed for the SGS scale. The corresponding results of the normalised SGS eddy viscosity, μ_{sgs}/μ, are presented in Figs. 7.9 and 7.10 respectively. Here it is also seen that the Piomelli-Liu SGS model's contribution is slightly greater than the Germano-Lilly. In addition to those, it is also observed that the less computational time was required for the Piomelli-Liu SGS model than the Germano-Lilly. So, due to less back-scatter effects and less CPU time, the Piomelli-Liu model is chosen for the rest of the computations.

7.3.3 Time Evolution of the Turbulent Flow Quantity

In this section, the results are presented only for the first four harmonics case. Figs. 7.11-7.13 illustrate the turbulent velocity fluctuations, $u''/\bar{V}_{max}$, $v''/\bar{V}_{max}$ and $w''/\bar{V}_{max}$, respectively, at the different axial positions while $Re = 1000$ and 2000. The solid lines are the results of $Re = 2000$ while the dashed lines are of $Re = 1000$. At the centre of the stenosis, the flow is quite laminar when $Re = 1000$, but it is slightly disturbed after the six cycles of pulsation when $Re = 2000$ and creating some small random oscillations. For $Re = 1000$ the random fluctuations are not very high, but for $Re = 2000$ they are significantly higher in the region between $y/L = 1.0$ and $y/L = 6.0$.

The corresponding upper wall pressure, $\bar{p}/\rho\bar{V}_{max}^2$, and its fluctuations, $p''/\rho\bar{V}_{max}^2$, are shown in Figs. 7.14 and 7.15, respectively. From Fig. 7.14, it is seen that the upper wall pressure is very small before the centre of the stenosis, but at the centre of the stenosis it is always less than or equal to zero due to the pressure drop. Moreover, after the stenosis the flow pressure increases gradually at the upper wall in which the stenosis appeared. The upper wall pressure fluctuations in Fig. 7.15 are quite high at the region where the velocity fluctuations are high, specifically in the region between $y/L = 1.0$ and $y/L = 4.0$.

The upper wall shear stresses, recorded at the different axial positions against the time cycle of the pulsation, are shown in Fig. 7.16. In frame (a), the wall shear stresses before the stenosis are very small with some regular pulsations. But in frame (b), the pulsatile shear stresses at all time steps are negative, which proves the fact of the permanent stress drop at the centre of the stenosis. After the stenosis, from $y/L = 1.0$ to $y/L = 3.0$, the shear stress takes the random oscillatory forms while $Re = 2000$, and gradually decreases downstream . The intensity of the oscillation is low while $Re = 1000$.

7.3.4 Comparison of the Results of the First Four Harmonics

The comparison of the results of the first four harmonics are made in Fig. 7.17(a-b) in terms of the normalised instantaneous upper wall shear stress, $\tau_{xy}/\rho\bar{V}_{max}^2$ and the turbulent kinetic energy (TKE), $\frac{1}{2} < u_j''u_j'' > /\bar{V}_{max}^2$, respectively, while $Re = 2000$. Just prior to the centre of the stenosis, the stress drop at the upper wall for the harmonic cases from second to fourth remains almost the same, while for the first harmonic case this drop is smaller than the other cases. After the stenosis, the results show that the stresses oscillate randomly, but the oscillation for the first harmonic case is different from the other cases. In Fig. 7.17(b), it is seen that the maximum TKE occurs between $y/L = 2$ and $y/L = 3$ for the first harmonic case, while for the other harmonic cases the maximum is attained between $y/L = 0$ and $y/L = 2$ and the magnitudes of TKE are very close to each other.

7.3.5 Comparison between the First and First Four Harmonics

It has been reported in the previous section (§ 7.3.4) that the effects of the last three harmonics (i.e. second to fourth) on the results of the shear stress and turbulent kinetic energy are small. Therefore, in this section we will concentrate on how the results of the first and first four harmonics compares with each other, and in particular we investigate their effects on the turbulent flow quantities only.

Figs. 7.18-7.20 demonstrate the turbulent intensity in terms of the normalised root mean square (rms) of the velocity fluctuations $< u'' >_{rms}$, $< v'' >_{rms}$ and $< w'' >_{rms}$, respectively, for the different Reynolds numbers along with the comparison of the first harmonic results for $Re = 2000$. From the comparison between the first and first four harmonics cases for $Re = 2000$, it is clearly seen that the turbulent intensity at the post stenosis region, after $y/L = 2.5$, is always bit larger for the first harmonic case than the first four harmonics. This happens, since for the first harmonic case the contribution of the oscillating part is smaller than that of the first four harmonics case. Thus, the magnitude of the additive oscillation becomes smaller in the first harmonic than the first four, as a result, the maximum turbulent intensity for the first harmonic case occurs a bit further downstream, which was also seen in Fig. 7.17(a). Similar results were found in § 4.6.6.

The normalised root mean square of the pressure fluctuations, $< p'' >_{rms}$, for the upper and lower wall are plotted in Fig. 7.21(a-b) respectively, along with the results of the first harmonic case. At the upper wall, the maximum of the pressure fluctuations occurs between $y/L = 1.0$ and $y/L = 3.0$ for all the Reynolds numbers but for the lower wall it occurs between $y/L = 2.0$ and $y/L = 3.0$. Moreover, the magnitude of the pressure fluctuations at the upper wall is higher than the lower wall. Again, it is seen here that the rms of the pressure fluctuations for the first harmonic case is larger at the post-lip of the stenosis than that of the first four harmonics case, but is smaller in the further downstream.

Figs. 7.22(a-c) show the normalised Reynolds stresses $< u''v'' >$, $< u''w'' >$ and $< v''w'' >$, respectively, for the different Reynolds numbers along with the comparison of the first harmonic case at $Re = 2000$. Between the inlet and the post-lip of the stenosis i.e. before $y/L = 1.0$, the Reynolds stresses are zero since the flow is fully laminar there. From the post-lip the Reynolds stresses take the oscillating form due to the effects of the stenosis and they gradually decrease further

downstream. The differences between the first and first four harmonics cases are also observed here and the intensity of the first Reynolds stress, $< u''v'' >$ is higher than the two other Reynolds stresses.

The normalised instantaneous wall shear stresses are plotted in Fig. 7.23 for the different Reynolds numbers along with the shear stress of the first harmonic case while $Re = 2000$. At the upper, it is seen that the shear stress drop for $Re = 2000$ is higher for the first four harmonics case than the first harmonic, but at the immediate post stenosis region the shear stress is higher for the first harmonic case. For the lower wall, at the centre of the stenosis, the maximum shear stress in the case of first four harmonics is larger than the first harmonic.

7.3.6 Effects of the Different Area reduction of the Stenosis

Fig. 7.24(a-b) depict the instantaneous upper and lower wall shear stresses for the three different area reduction, 50%, 65% and 75% of the stenosis while $Re = 1000$. These results are obtained by using the first four harmonics pulsation. The stress drop at the upper wall for the 75% stenosis is more than three times higher than that of the case of 50% stenosis. On the other hand, at the lower wall the maximum shear stress for the 75% of stenosis is approximately five times higher than that of the 50% stenosis. So, the higher area reduction of the arterial stenosis would be more dangerous to the arterial inner vessels and the blood cells as the damage on them will be higher. Moreover, it was already reported that the higher stress drop stimulates the atherogenic phenotype, as a result, the inner vessel remodeles itself at the stenosis and increases the area reduction of the stenosis, which could be the reason for the arterial blockage.

The effects of the percentage of the stenosis on the turbulent kinetic energy are presented in Figs. 7.25(a-c) respectively for $Re = 1000$, 1400 and 2000. All three frames reveal the fact that the turbulent flow for the arterial stenosis is highly dependent on the percentage of the arterial area reduction. At the 75% stenosis the TKE is again more than four times larger than the case of 50% stenosis while $Re = 1000$, and it is even larger than the 50% stenosis for $Re = 2000$. At the 65% stenosis the maximum TKE is approximately four times larger than that of the 50% stenosis while $Re = 1400$.

Here it should be mentioned that the minimum grid size of $(N_x \times N_y \times N_z) \sim (50 \times 300 \times 50)$ is required in the LES to resolve the flow at the 75% stenosis for $Re = 1000$ and at the 65% stenosis for $Re = 1400$. But for $Re = 2000$ the grid size at the 60% stenosis is increased to $70 \times 350 \times 50$. To obtain the results in the stenosis which is greater than 60% when $Re = 2000$, one needs to increase further the grid density to resolve adequately the turbulent flow downstream of the stenosis. Because of the limitation of computing resources, the cases higher than 60% for $Re = 2000$ remain unsolved here. However, from the results of $Re = 1000$ and 1400 in frames (a-b), we can roughly understand the level of turbulence that may occur at the stenosis greater than 60% when $Re = 2000$.

7.3.7 Effects of the Length of the Stenosis

The effects of the length of the stenosis on the results of the wall shear stresses, $\tau_{xy}/\rho\bar{V}^2_{max}$, and the turbulent kinetic energy, $\frac{1}{2} < u''_j u''_j > /\bar{V}^2_{max}$, are shown in Fig. 7.26. It is observed that the stress drop at the upper wall and the maximum shear stress at the lower wall are reduced when the length of the stenosis is increased. The turbulent kinetic energy is also decreased because the sharpness of the stenosis decreases when we increase the length of the stenosis fixing its percentage, as a result, the turbulent intensity is reduced.

7.4 Conclusion

In this chapter, we have investigated the effects of the various harmonics of the physiological pressure pulse in the model arterial stenosis by using the LES technique with the two SGS models, namely, the Germano-Lilly [2; 3] dynamic model and the Piomelli-Liu [4] localized dynamic model. We have found that the Piomelli-Liu localised dynamic model is better to model the subgrid scale. For example, when $Re = 2000$ and the stenosis case is 50%, the SGS contributions found between the Germano-Lilly and the Piomelli-Liu localized dynamic models are 74% and 97%, respectively, because the Piomelli-Liu localized dynamic model is less suffered by the problem of backscattering.

The effects of the second to fourth harmonics on the results are found very small,

however, in the first harmonic case the results are slightly different compared to the other three harmonics, since in the first harmonic case, the intensity of the streamwise velocity at the systolic phase and the backward flow near the walls during the diastolic phase are smaller than that of the other harmonics.

The upper wall stress reduction is found significantly higher for the fourth harmonic case than the first harmonic. The maximum turbulence intensity occurred at the immediate downstream region for the harmonic cases from second to fourth but for the first harmonic case it is found further downstream and is larger than that of the case of first four harmonics.

For the higher area reduction of the stenosis, both the stress drop at the upper wall and the maximum stress at the lower wall increase. The turbulent kinetic energy also increases rapidly at the immediate post stenotic region. Larger mesh arrangement was required for the highly reduced arterial stenosis for capturing the high vortices and resolving the large scale motions properly. The intensity of the wall shear stress and the turbulence decrease for the larger length of the stenosis.

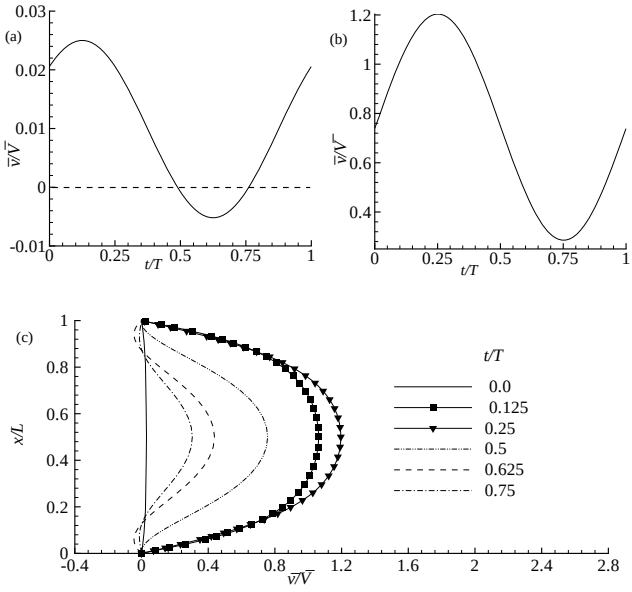

Figure 7.1: Inlet velocity profile of the 1^{st} harmonic pulsatile, for a time cycle at (a) near the wall (b) centre of the channel and (c) for the different phases of a time cycle while $Re = 2000$.

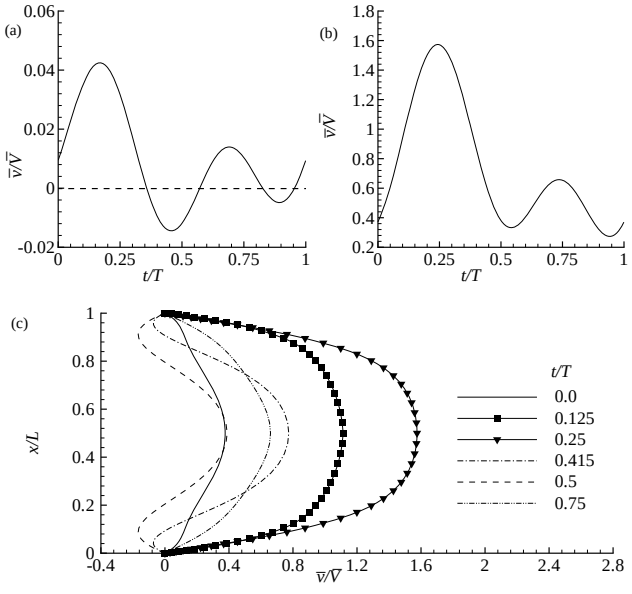

Figure 7.2: Inlet velocity profile of the 2^{nd} harmonic pulsatile, for a time cycle at (a) near the wall (b) centre of the channel and (c) for the different phases of a time cycle while $Re = 2000$.

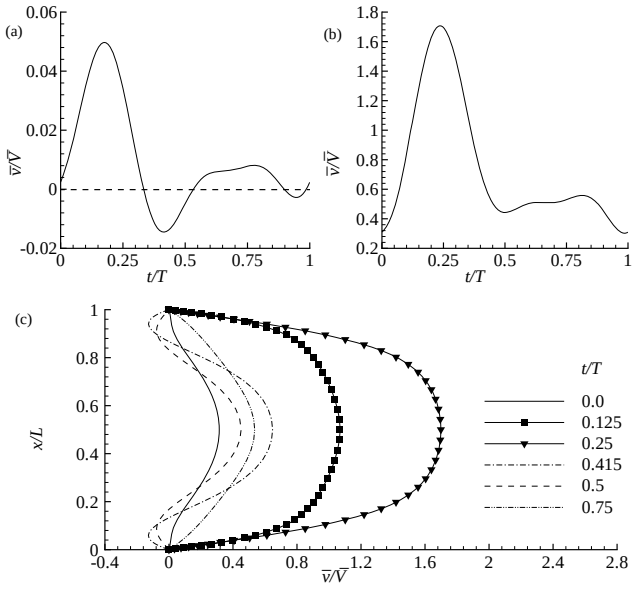

Figure 7.3: Inlet velocity profile of the 3^{rd} harmonic pulsatile, for a time cycle at (a) near the wall (b) centre of the channel and (c) for the different phases of a time cycle while $Re = 2000$.

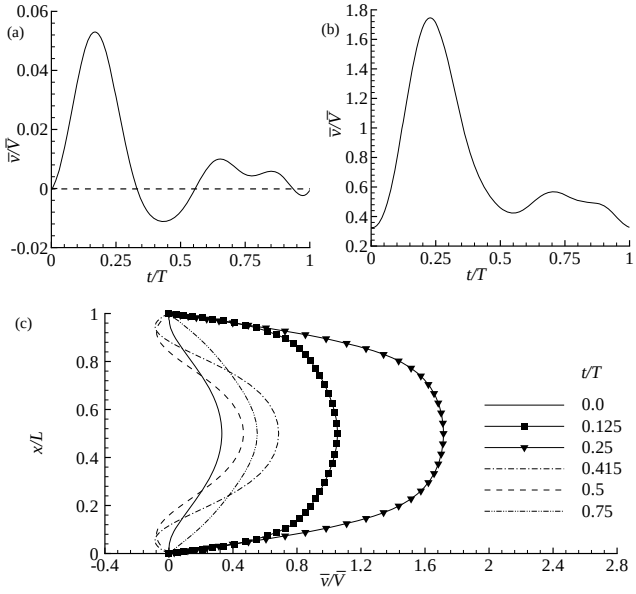

Figure 7.4: Inlet velocity profile of the 4^{th} harmonic pulsatile, for a time cycle at (a) near the wall (b) centre of the channel and (c) for the different phases of a time cycle while $Re = 2000$.

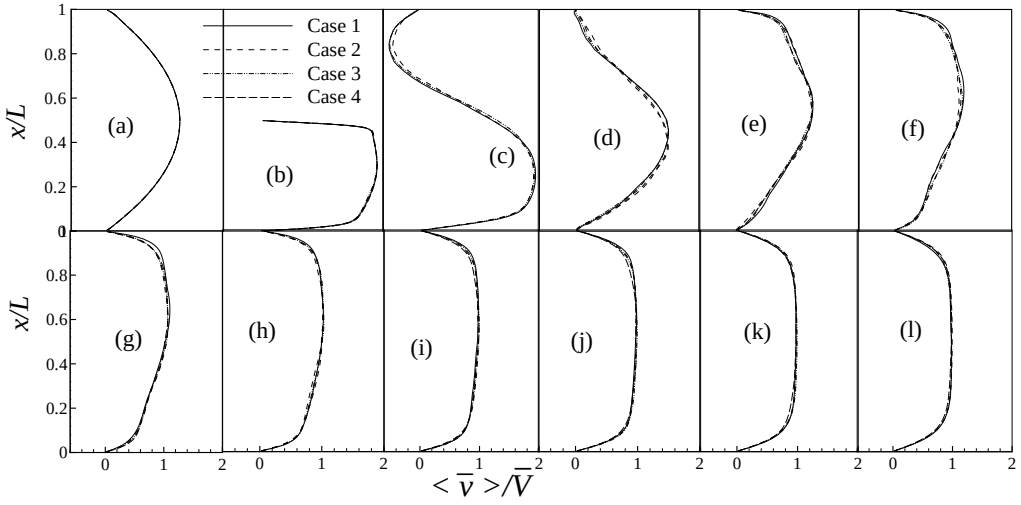

Figure 7.5: Grid independence test for the time-mean streamwise velocity, $< \bar{v} > /\bar{V}$, at (a) $y/L =$ inlet, (b) $y/L = 0.0$, (c) $y/L = 1.0$, (d) $y/L = 2.0$,(e) $y/L = 3.0$, (f) $y/L = 4.0$, (g) $y/L = 5.0$, (h) $y/L = 6.0$, (i) $y/L = 8.0$, (j) $y/L = 10.0$, (k) $y/L = 12.0$ and (l) $y/L =$ outlet while $Re = 2000$.

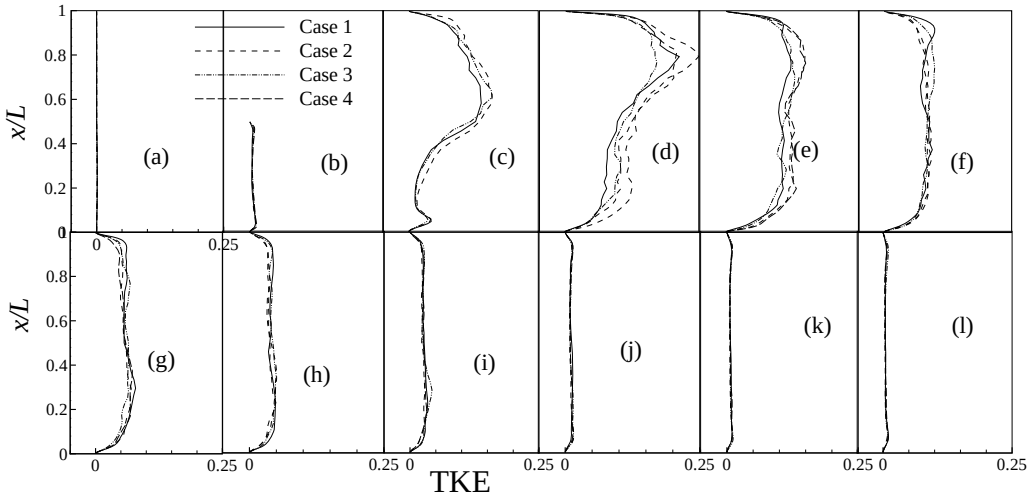

Figure 7.6: Grid independence test for the turbulent kinetic energy (TKE), $\frac{1}{2} < u_j'' u_j'' > /\bar{V}^2$, at (a) $y/L =$ inlet, (b) $y/L = 0.0$, (c) $y/L = 1.0$, (d) $y/L = 2.0$, (e) $y/L = 3.0$, (f) $y/L = 4.0$, (g) $y/L = 5.0$, (h) $y/L = 5.0$, (i) $y/L = 8.0$, (j) $y/L = 10.0$, (k) $y/L = 12.0$ and (l) $y/L =$ outlet while $Re = 2000$.

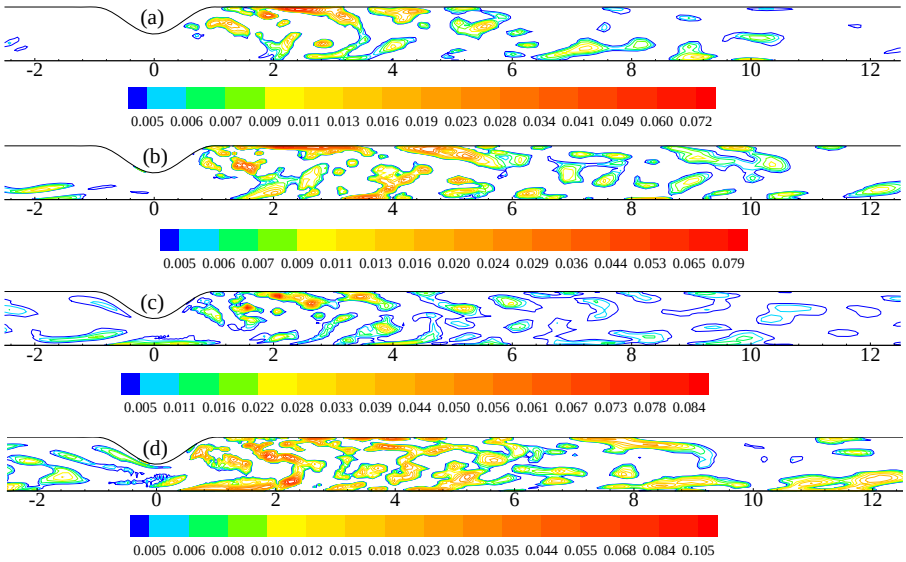

Figure 7.7: Dynamic Smagorinsky constant, C_s, obtained by the Germano-Lilly [2; 3] model for (a) $Re = 1000$, (b) $Re = 1400$, (c) $Re = 1700$ and (d) $Re = 2000$.

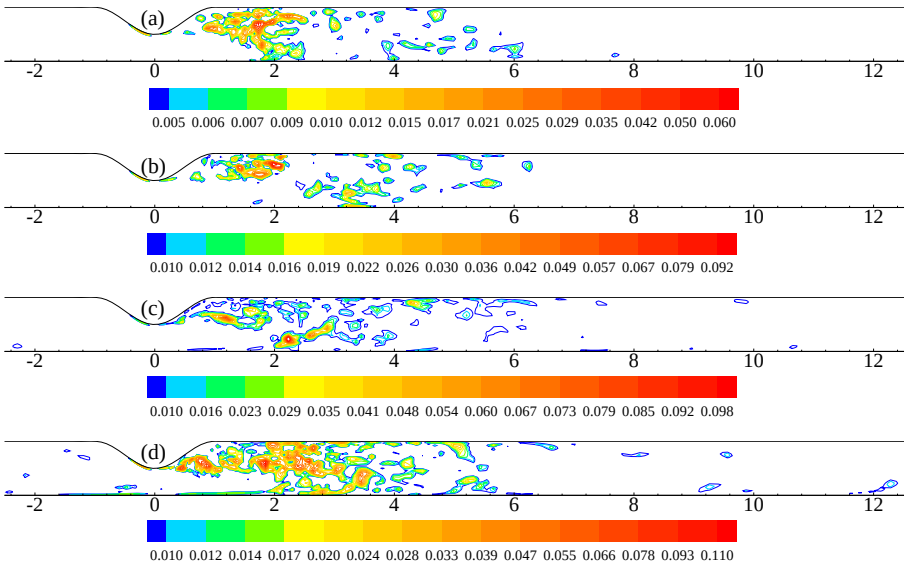

Figure 7.8: Dynamic Smagorinsky constant, C_s, obtained by the Piomelli-Liu [4] model for (a) $Re = 1000$, (b) $Re = 1400$, (c) $Re = 1700$ and (d) $Re = 2000$.

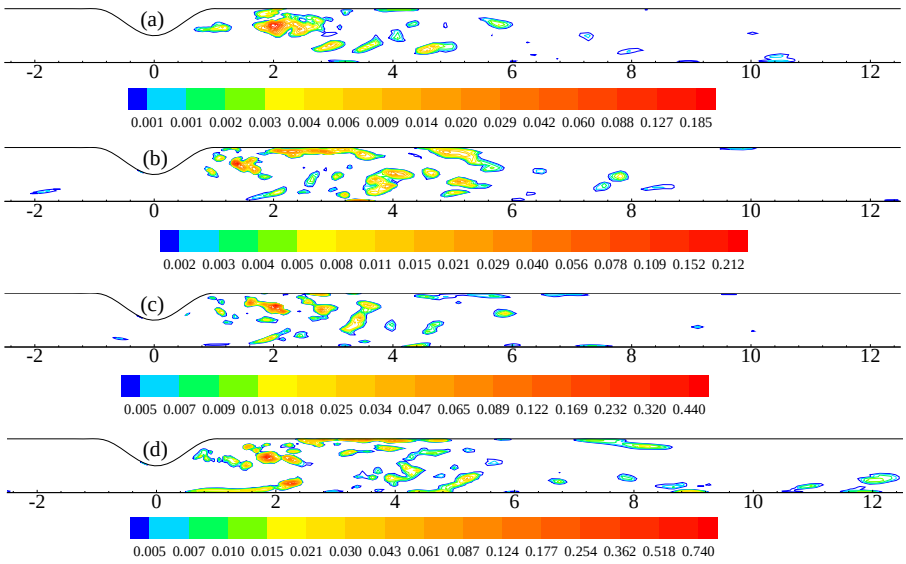

Figure 7.9: Normalised SGS eddy viscosity, μ_{sgs}/μ, obtained by the Germano-Lilly [2; 3] model for (a) $Re = 1000$, (b) $Re = 1400$, (c) $Re = 1700$ and (d) $Re = 2000$.

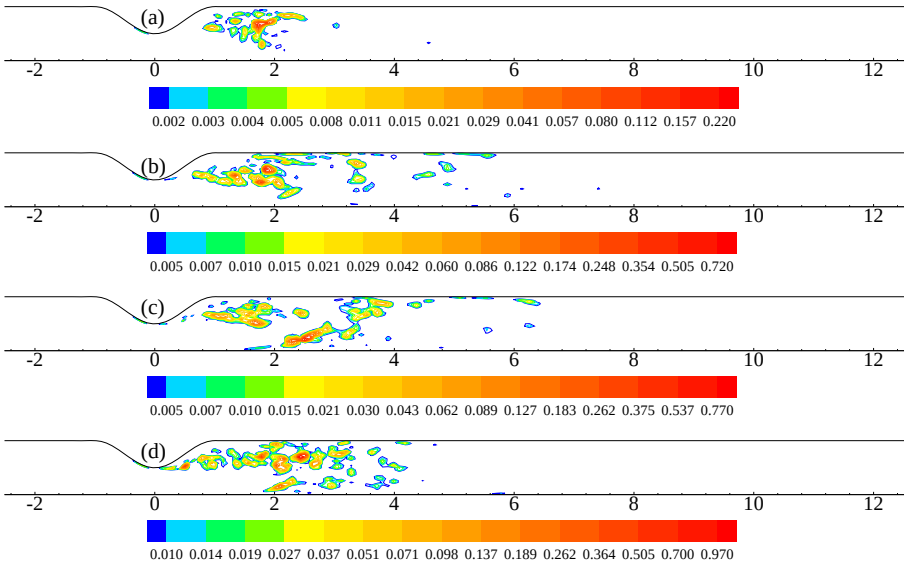

Figure 7.10: Normalised SGS eddy viscosity, μ_{sgs}/μ, obtained by the Piomelli-Liu [4] model for (a) $Re = 1000$, (b) $Re = 1400$, (c) $Re = 1700$ and (d) $Re = 2000$.

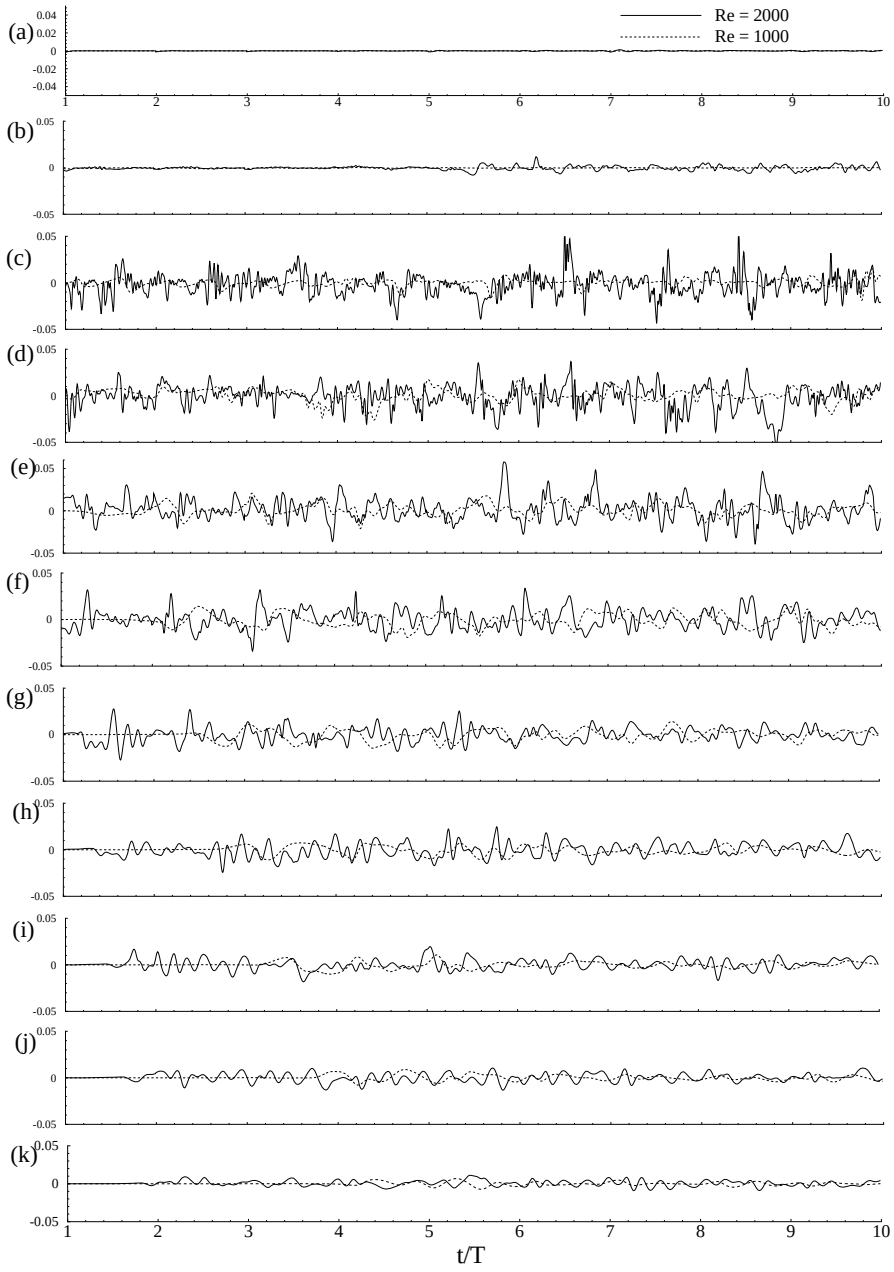

Figure 7.11: Time history of the centreline cross-stream velocity fluctuations $u''/\bar{V}_{max}$ at (a) $y/L = -2.0$, (b) $y/L = 0.0$, (c) $y/L = 1.0$, (d) $y/L = 2.0$, (e) $y/L = 3.0$, (f) $y/L = 4.0$, (g) $y/L = 5.0$, (h) $y/L = 6.0$, (i) $y/L = 8.0$, (j) $y/L = 10.0$ and (k) $y/L = 12.0$.

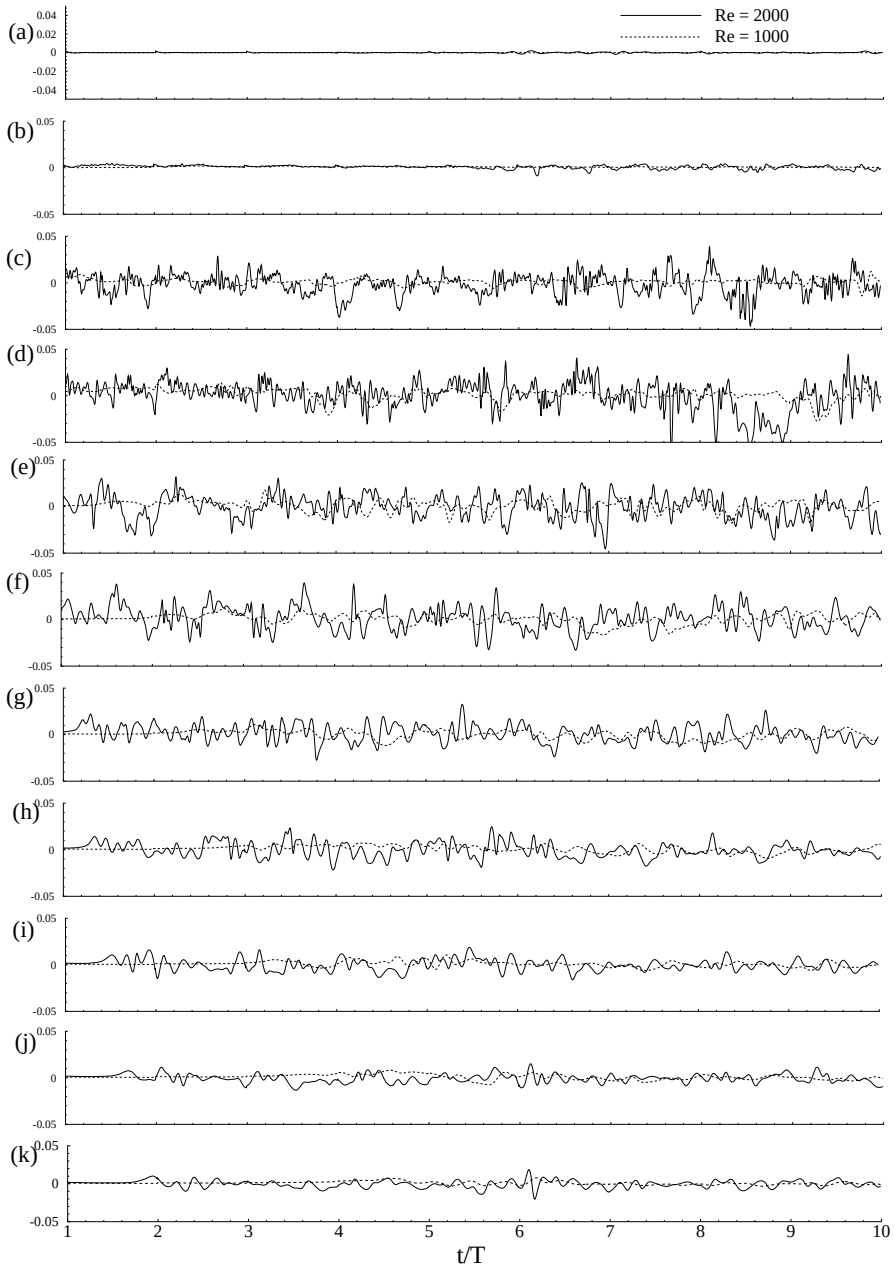

Figure 7.12: Time history of the centreline streamwise velocity fluctuations $v''/\bar{V}_{max}$ at (a) $y/L = -2.0$, (b) $y/L = 0.0$, (c) $y/L = 1.0$, (d) $y/L = 2.0$, (e) $y/L = 3.0$, (f) $y/L = 4.0$, (g) $y/L = 5.0$, (h) $y/L = 6.0$, (i) $y/L = 8.0$, (j) $y/L = 10.0$ and (k) $y/L = 12.0$.

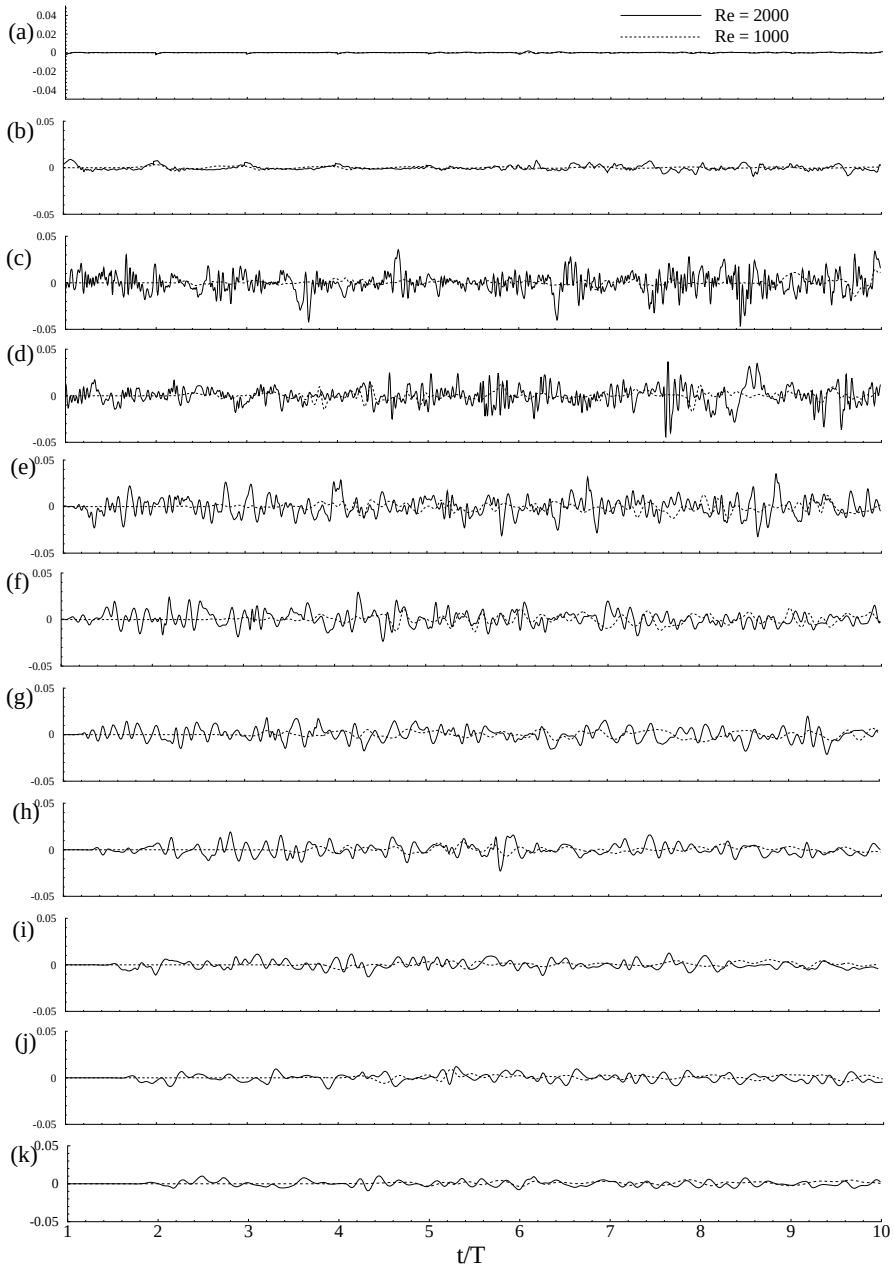

Figure 7.13: Time history of the centreline spanwise velocity fluctuations, $w''/\bar{V}_{max}$, at (a) $y/L = -2.0$, (b) $y/L = 0.0$, (c) $y/L = 1.0$, (d) $y/L = 2.0$, (e) $y/L = 3.0$, (f) $y/L = 4.0$, (g) $y/L = 5.0$, (h) $y/L = 6.0$, (i) $y/L = 8.0$, (j) $y/L = 10.0$ and (k) $y/L = 12.0$.

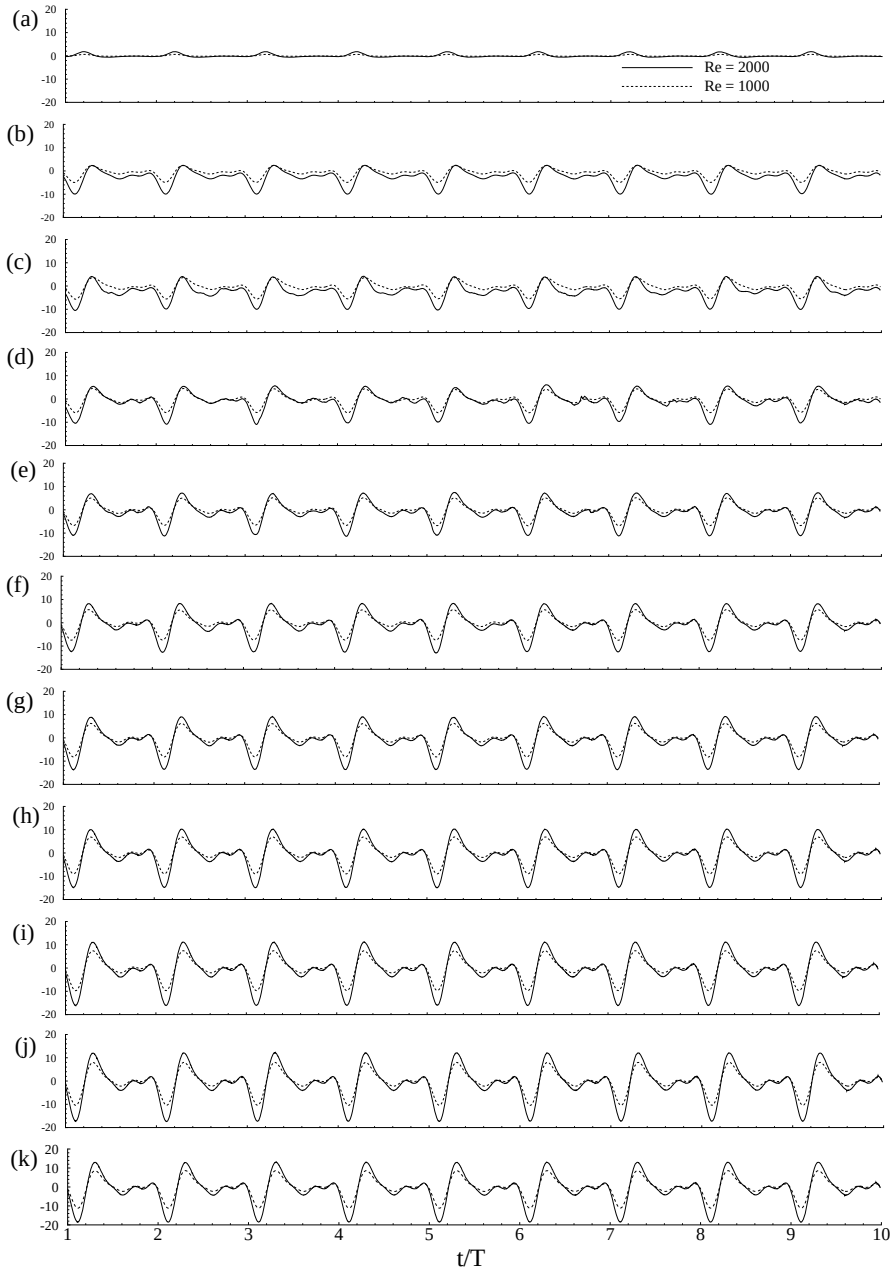

Figure 7.14: Time history of the upper wall pressure, $\bar{p}/\rho\bar{V}_{max}^2$, at (a) $y/L = -2.0$, (b) $y/L = 0.0$, (c) $y/L = 1.0$, (d) $y/L = 2.0$, (e) $y/L = 3.0$, (f) $y/L = 4.0$, (g) $y/L = 5.0$, (h) $y/L = 6.0$, (i) $y/L = 8.0$, (j) $y/L = 10.0$ and (k) $y/L = 12.0$.

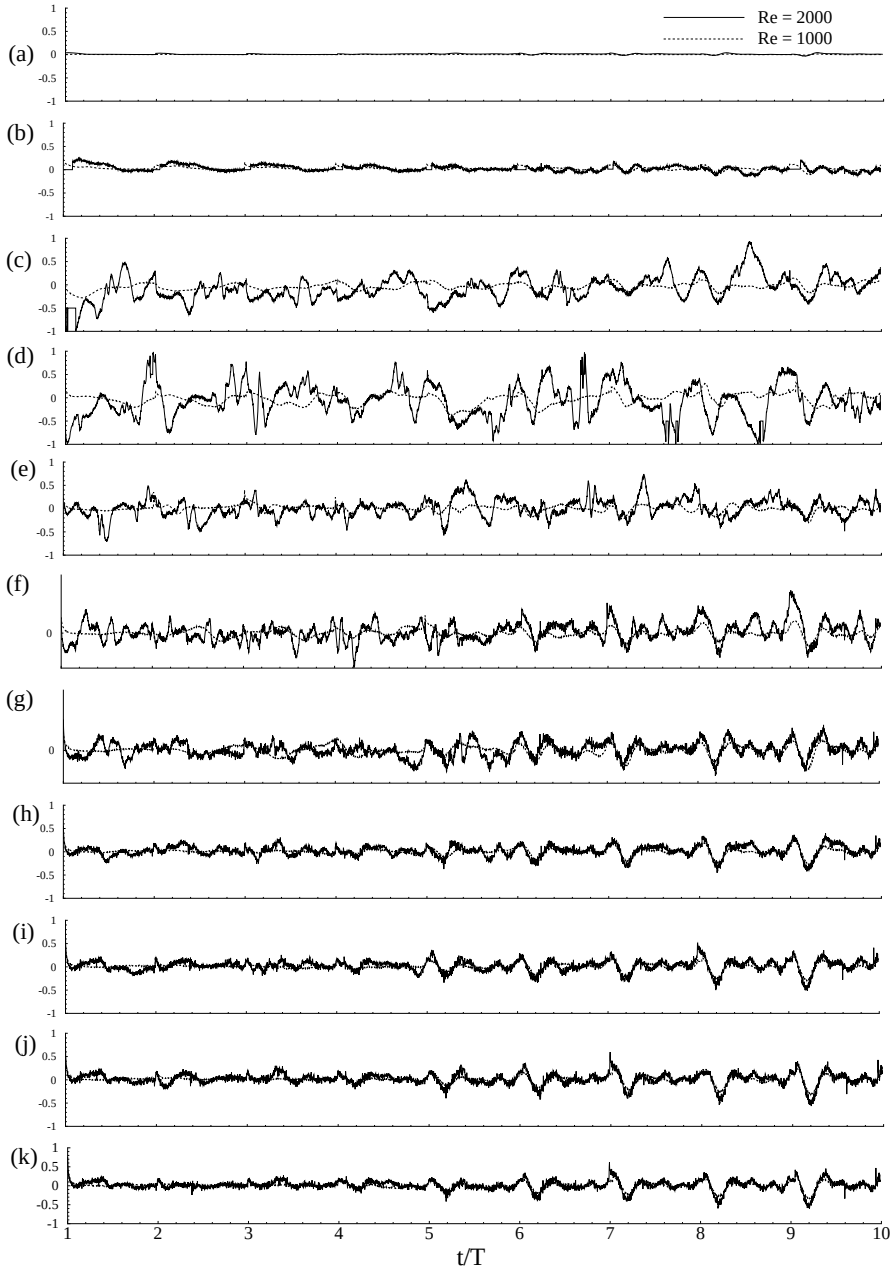

Figure 7.15: Time history of the upper wall pressure fluctuations, $p''/\rho\bar{V}_{max}^2$, at (a) $y/L = -2.0$, (b) $y/L = 0.0$, (c) $y/L = 1.0$, (d) $y/L = 2.0$, (e) $y/L = 3.0$, (f) $y/L = 4.0$, (g) $y/L = 5.0$, (h) $y/L = 6.0$, (i) $y/L = 8.0$, (j) $y/L = 10.0$ and (k) $y/L = 12.0$.

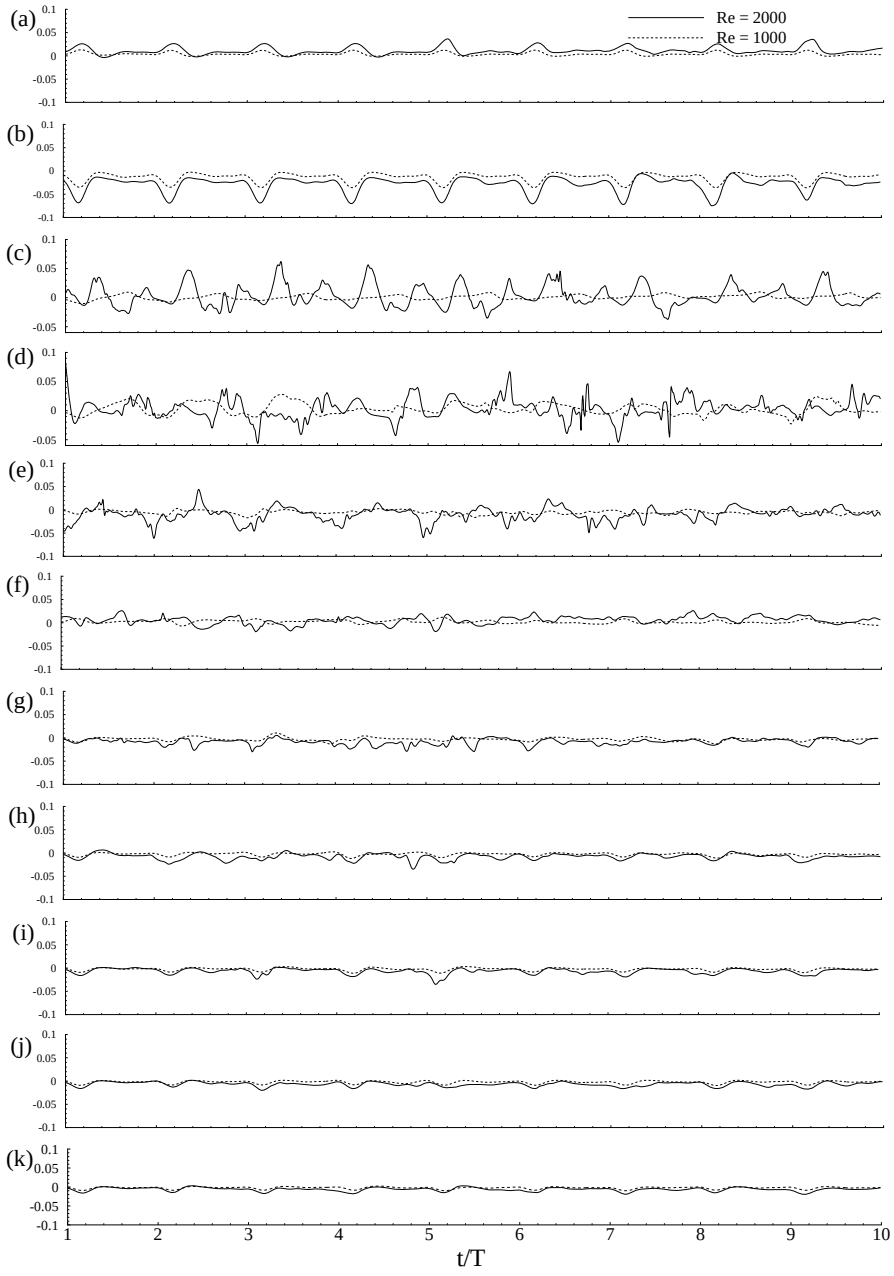

Figure 7.16: Time history of the upper wall shear stress, $\tau_{xy}/\rho\bar{V}^2_{max}$ at (a) $y/L = -2.0$, (b) $y/L = 0.0$, (c) $y/L = 1.0$, (d) $y/L = 2.0$, (e) $y/L = 3.0$, (f) $y/L = 4.0$, (g) $y/L = 5.0$, (h) $y/L = 6.0$, (i) $y/L = 8.0$, (j) $y/L = 10.0$ and (k) $y/L = 12.0$.

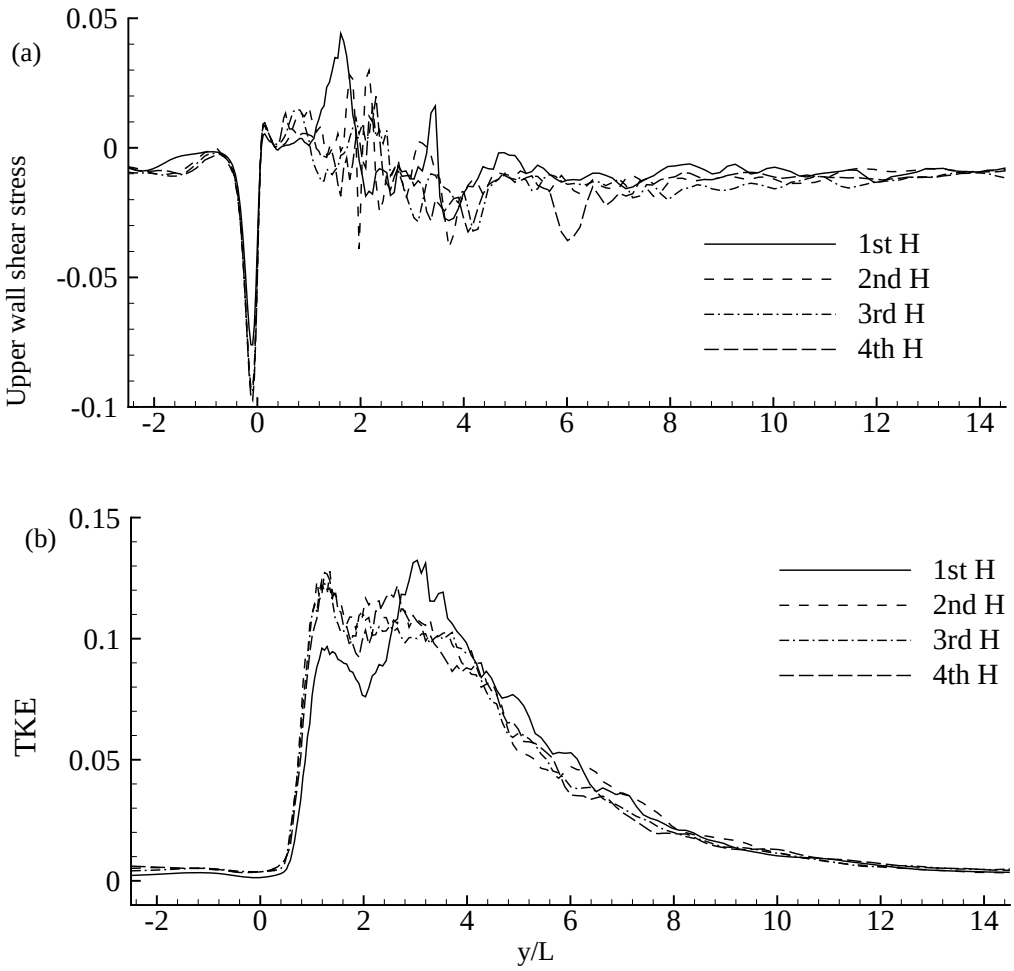

Figure 7.17: (a) Instantaneous upper wall shear stress, $\tau_{xy}/\rho\bar{V}^2$ and (b) Centreline turbulent kinetic energy (TKE) , $\frac{1}{2} < u_j'' u_j'' > /\bar{V}^2$, while $Re = 2000$.

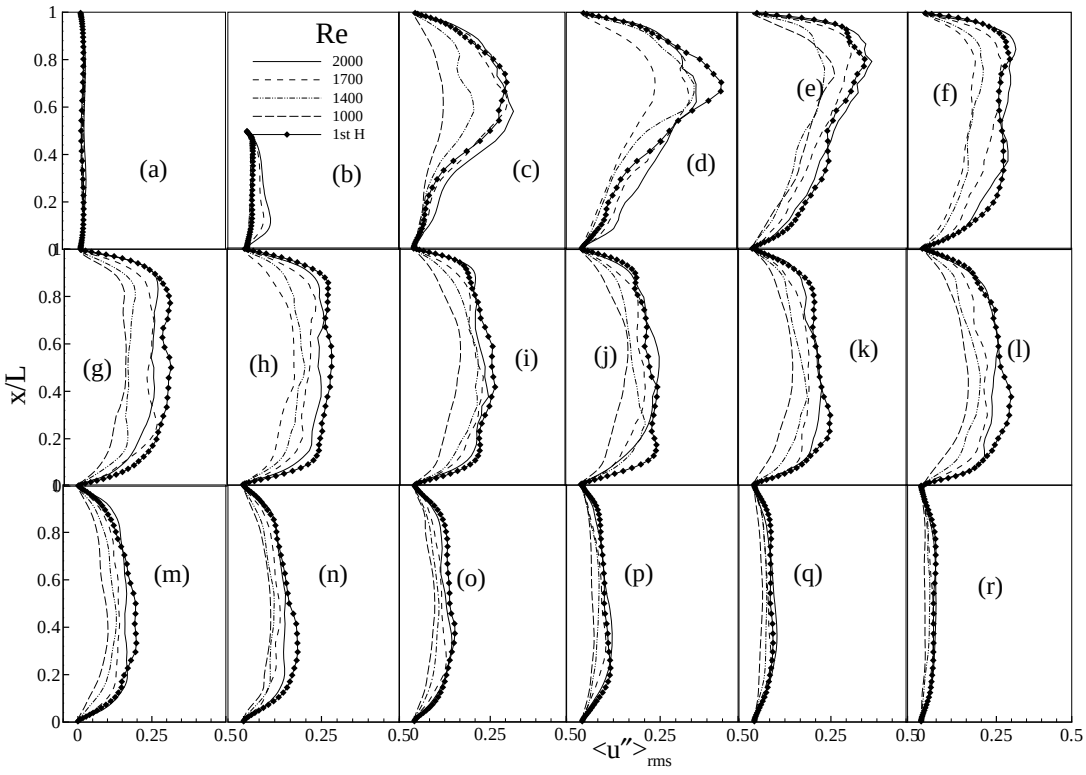

Figure 7.18: rms of the cross-stream velocity fluctuations, $< u'' >_{rms} /\bar{V}$, at different axial (a) $y/L =$ inlet, (b) $y/L = 0.0$, (c) $y/L = 1.0$, (d) $y/L = 1.5$, (e) $y/L = 2.0$, (f) $y/L = 2.5$, (g) $y/L = 3.0$, (h) $y/L = 3.5$, (i) $y/L = 4.0$, (j) $y/L = 4.5$, (k) $y/L = 5.0$ (l) $y/L = 5.5$, (m) $y/L = 6.0$, (n) $y/L = 7.0$, (o) $y/L = 8.0$, (p) $y/L = 10.0$, (q) $y/L = 12.0$ and (r) $y/L =$ outlet, for the different Reynolds number.

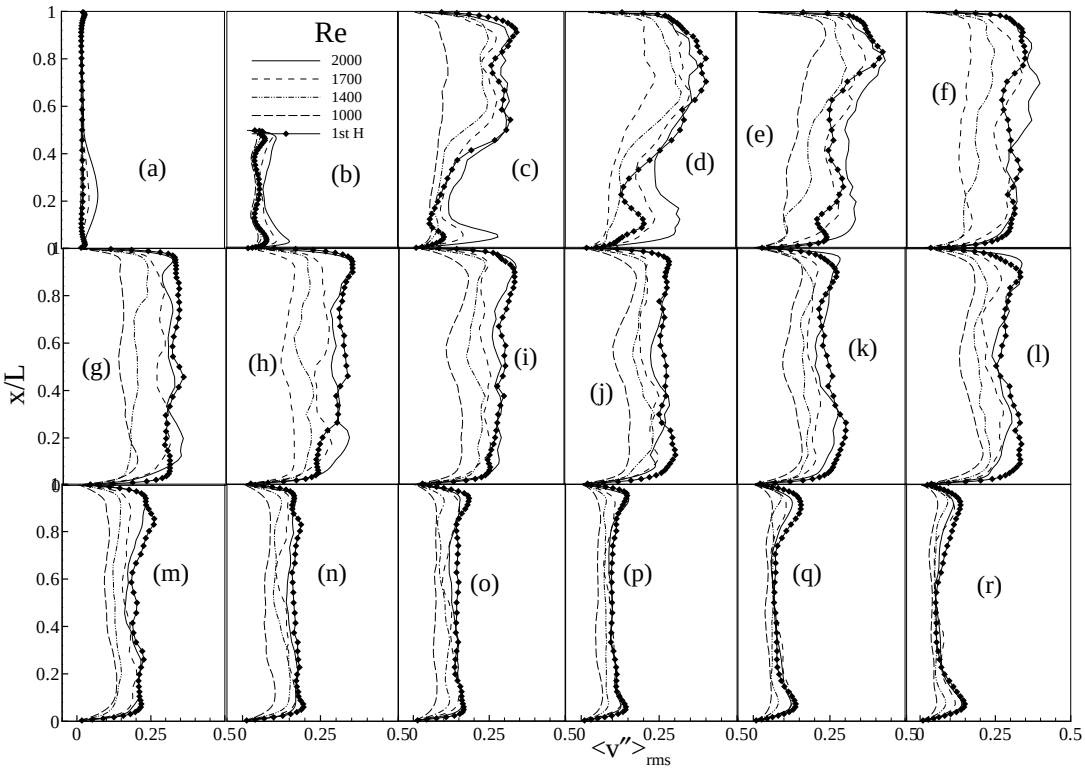

Figure 7.19: rms of the streamwise velocity fluctuations, $< v'' >_{rms} /\bar{V}$, at different axial (a) $y/L =$ inlet, (b) $y/L = 0.0$, (c) $y/L = 1.0$, (d) $y/L = 1.5$, (e) $y/L = 2.0$, (f) $y/L = 2.5$, (g) $y/L = 3.0$, (h) $y/L = 3.5$, (i) $y/L = 4.0$, (j) $y/L = 4.5$, (k) $y/L = 5.0$ (l) $y/L = 5.5$, (m) $y/L = 6.0$, (n) $y/L = 7.0$, (o) $y/L = 8.0$, (p) $y/L = 10.0$, (q) $y/L = 12.0$ and (r) $y/L =$ outlet, for the different Reynolds number.

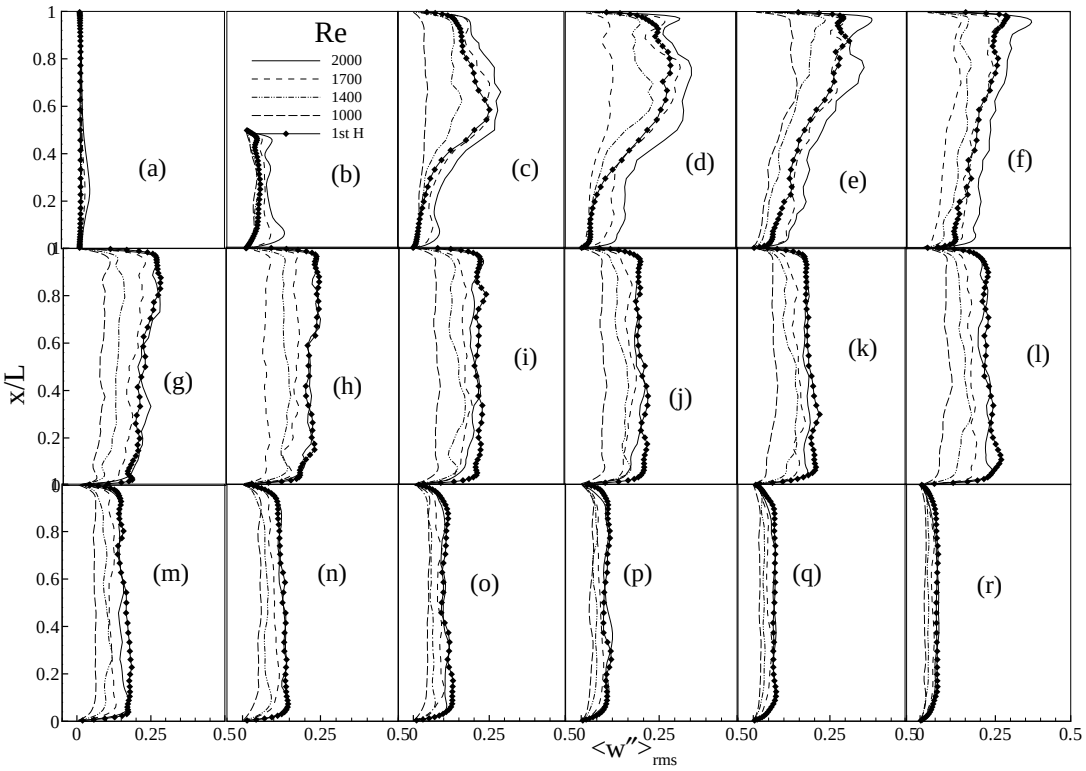

Figure 7.20: rms of the spanwise velocity fluctuations, $< w'' >_{rms} /\bar{V}$, at different axial (a) $y/L =$ inlet, (b) $y/L = 0.0$, (c) $y/L = 1.0$, (d) $y/L = 1.5$, (e) $y/L = 2.0$, (f) $y/L = 2.5$, (g) $y/L = 3.0$, (h) $y/L = 3.5$, (i) $y/L = 4.0$, (j) $y/L = 4.5$, (k) $y/L = 5.0$ (l) $y/L = 5.5$, (m) $y/L = 6.0$, (n) $y/L = 7.0$, (o) $y/L = 8.0$, (p) $y/L = 10.0$, (q) $y/L = 12.0$ and (r) $y/L =$ outlet, for the different Reynolds number.

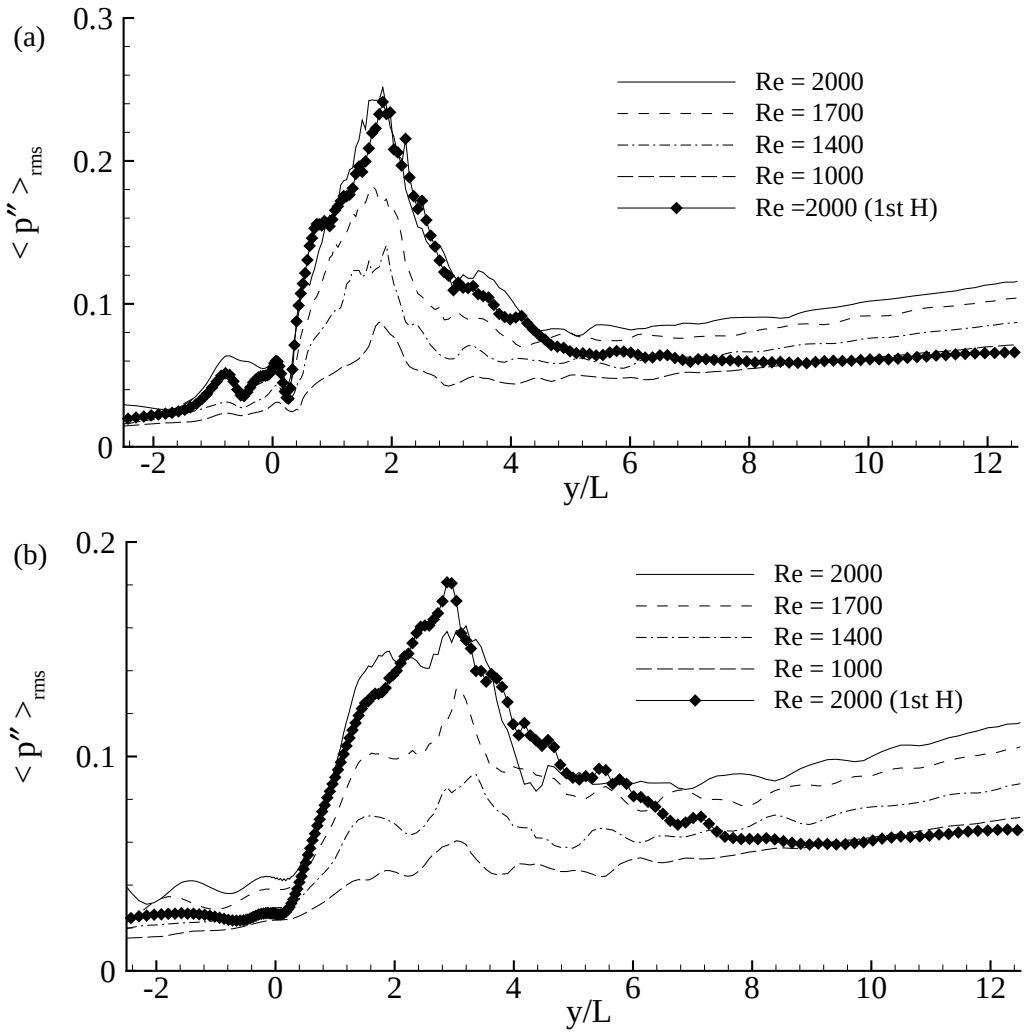

Figure 7.21: rms of the pressure fluctuations, $< p'' >_{rms} / \rho \bar{V}^2$ at the (a) upper wall and (b) lower wall for the different Reynolds number.

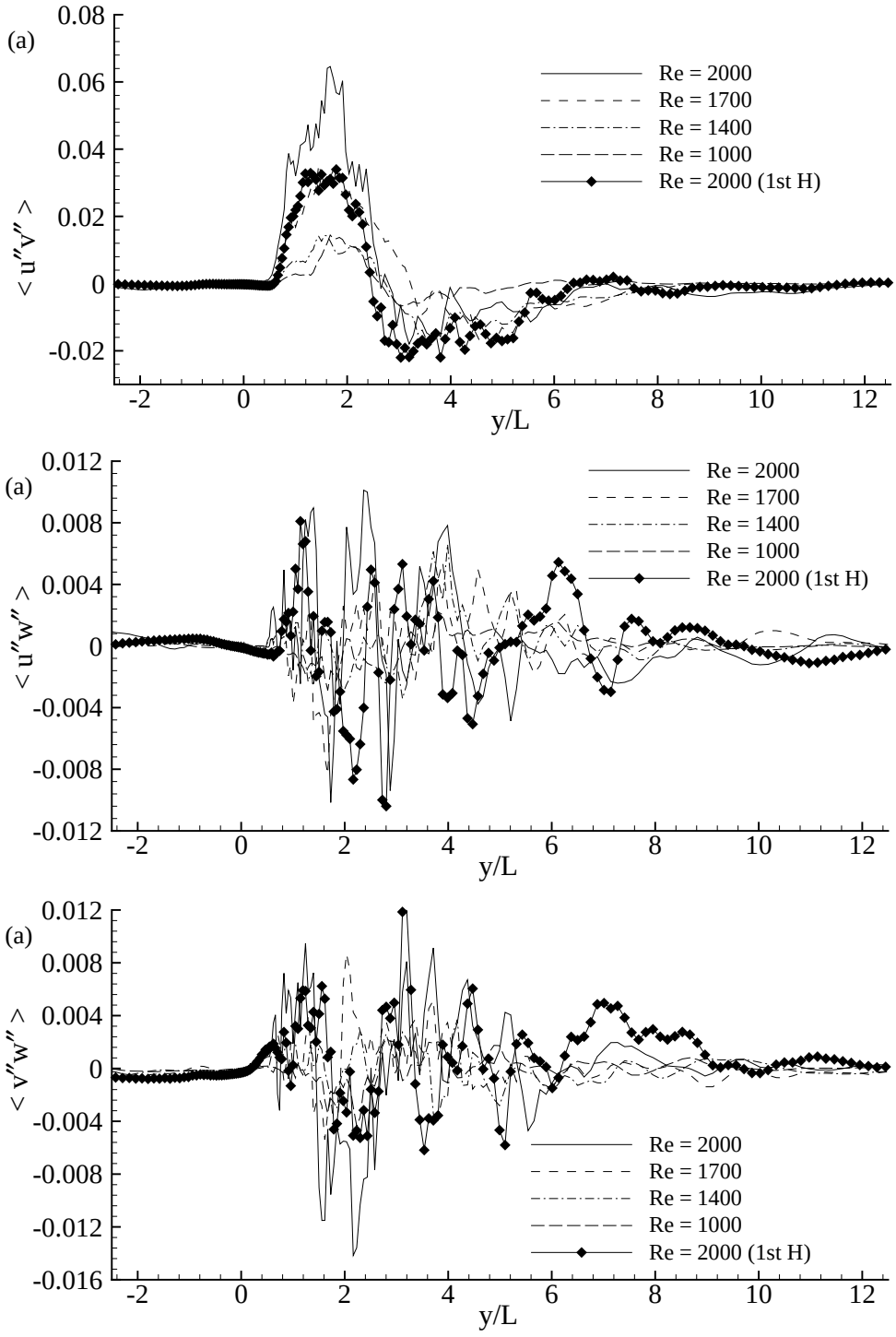

Figure 7.22: Centreline Reynolds stress (a) $< u''v'' > /\bar{V}^2$ (b)$< u''w'' > /\bar{V}^2$ and (c) $< v''w'' > /\bar{V}^2$ for the different Reynolds number.

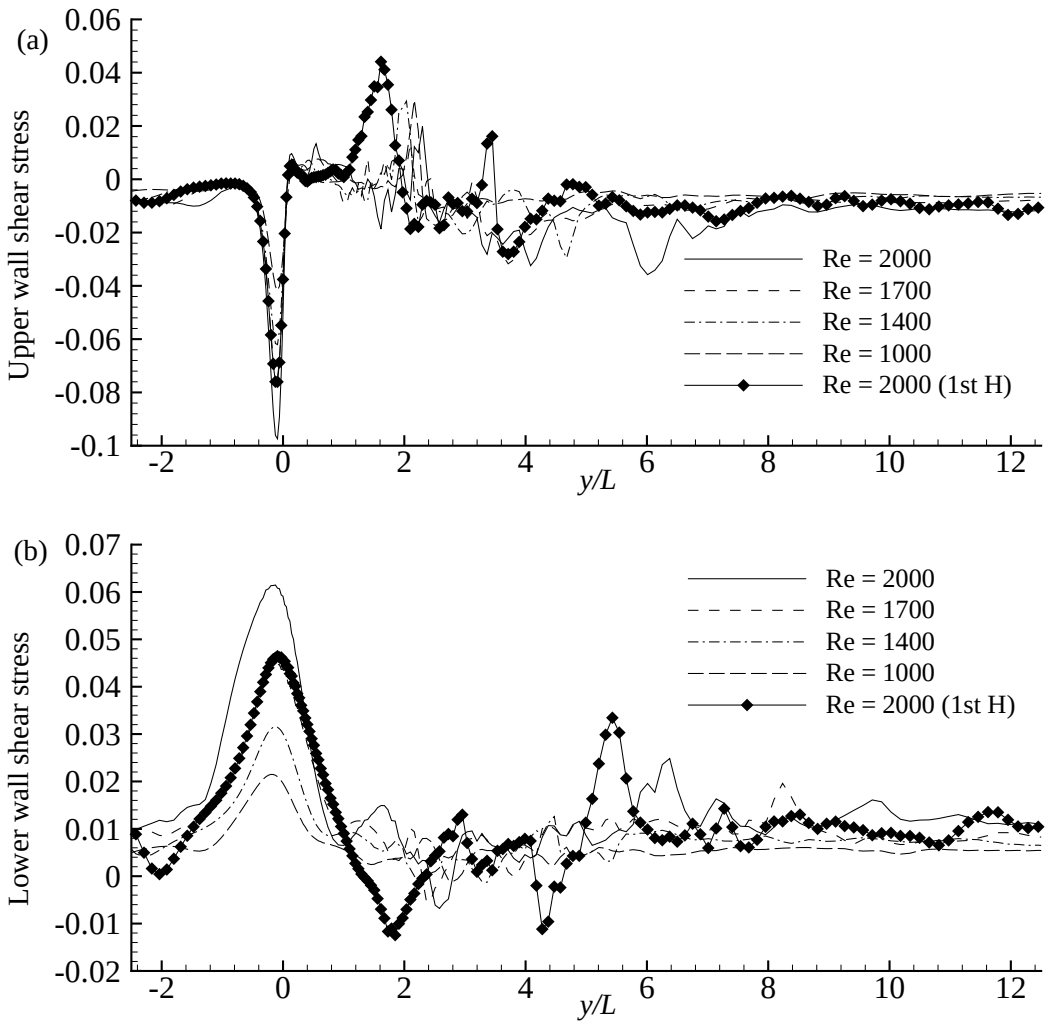

Figure 7.23: Instantaneous wall shear stress,$\tau_{xy}/\rho\bar{V}^2$, at (a) Upper wall and (b) Lower wall, for the different Reynolds number.

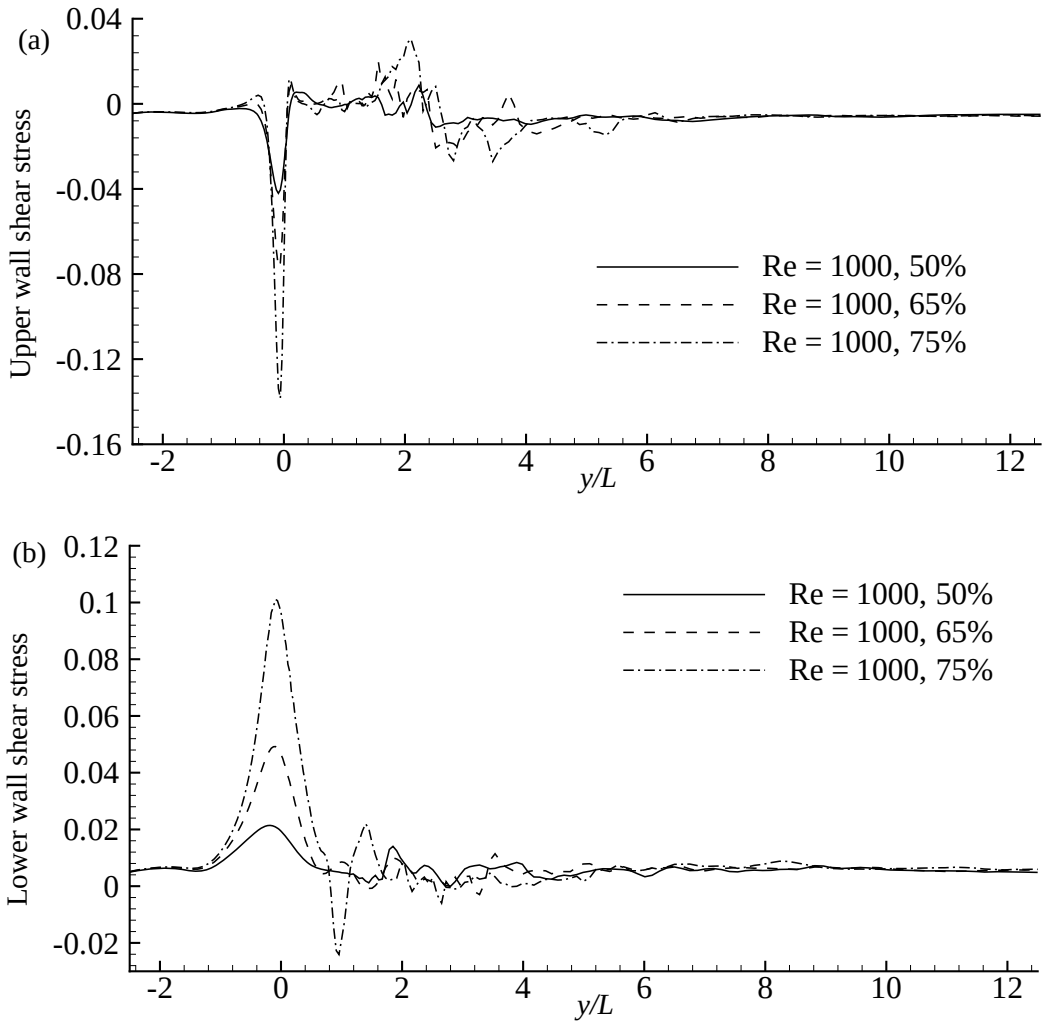

Figure 7.24: Instantaneous wall shear stress, $\tau_{xy}/\rho\bar{V}^2$, at (a) Upper wall and (b) Lower wall, for two different percentage of the stenosis.

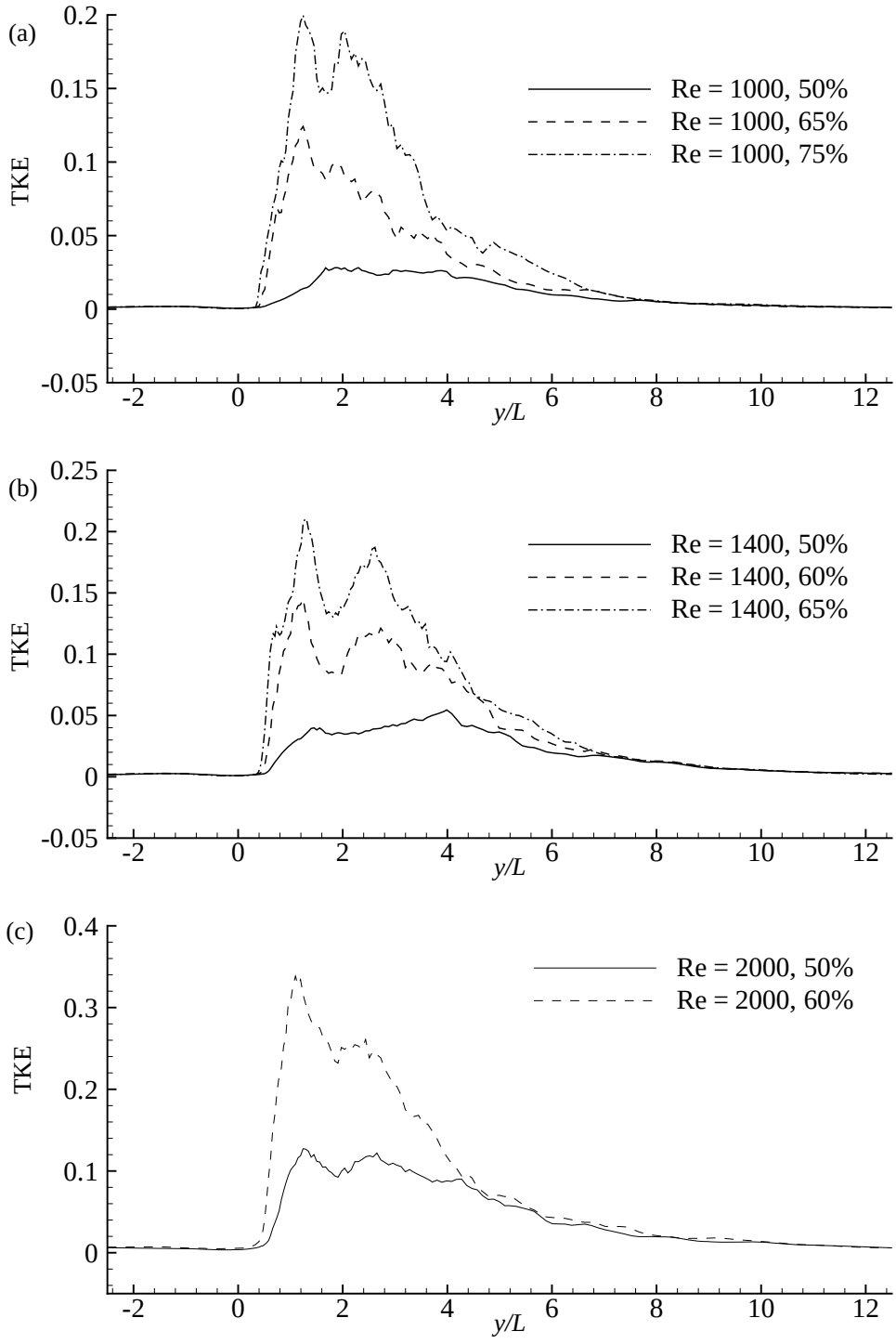

Figure 7.25: Centreline turbulent kinetic energy (TKE) , $\frac{1}{2} < u_j'' u_j'' > /\bar{V}^2$, at (a) $Re = 1000$, (b) $Re = 1000$ and (c) $Re = 2000$ for two different percentage of the stenosis .

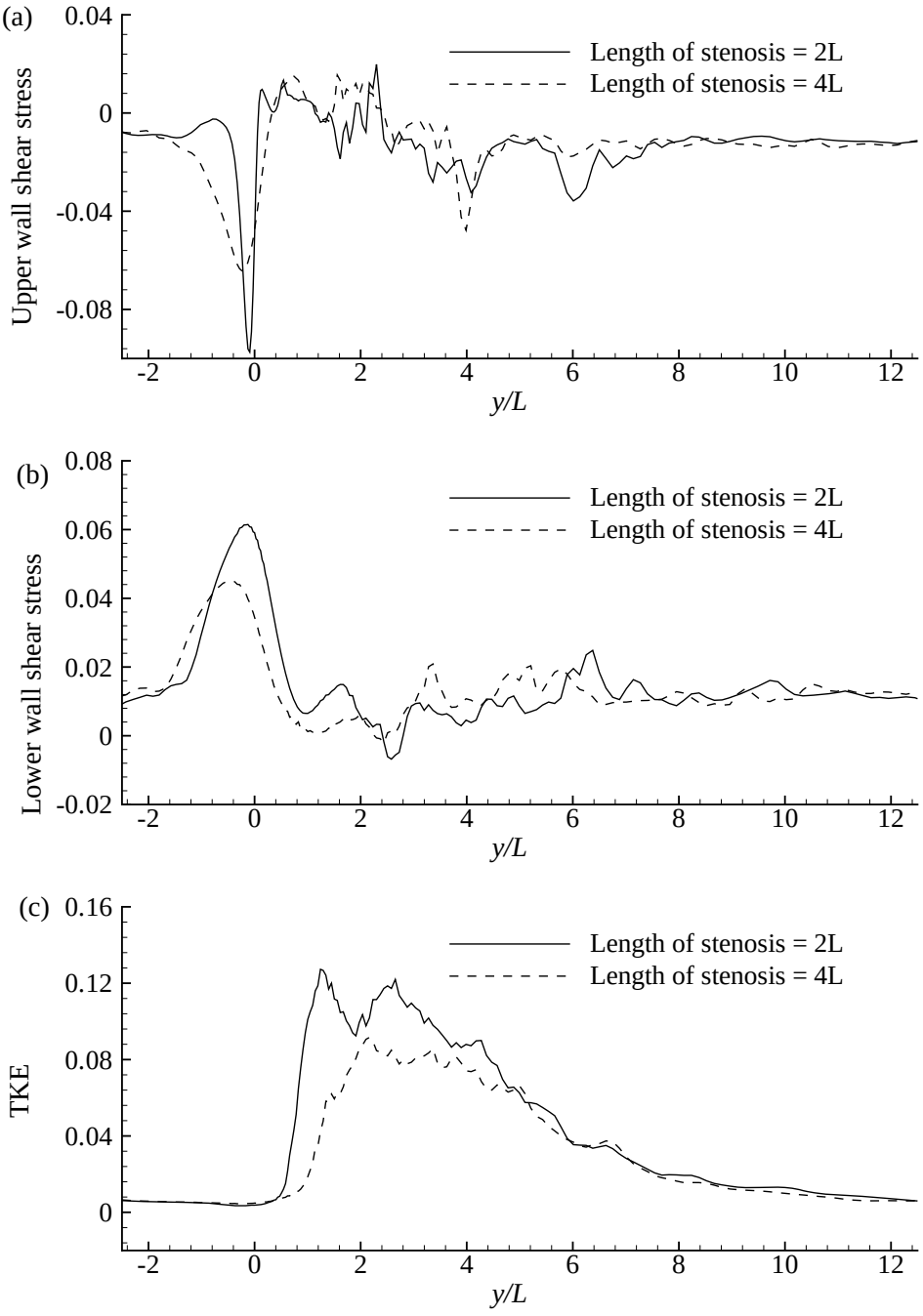

Figure 7.26: Instantaneous wall shear stress, $\tau_{xy}/\rho\bar{V}^2$ at (a) Upper wall, (b) Lower wall and (c) Centreline turbulent kinetic energy (TKE) , $\frac{1}{2} < u_j'' u_j'' > /\bar{V}^2$, for two different length of the stenosis while $Re = 2000$.

Chapter 8

Physiological Pulsatile Flow Through a Double Stenosis

8.1 Introduction

From the studies in previous chapters, it is now clear that due to the arterial stenosis the flow becomes turbulent at the post stenotic region. Relevant pathological consequences of the flow turbulence have also been illustrated in the previous chapters. However, if there are double stenoses present in a diseased artery, the transient flow physics and the severity of the turbulence downstream of both the stenoses, especially at the second stenosis, are not known.

There are very few studies related to double or multiple arterial stenoses in the literature. One experimental investigation was done by Talukder *et al* . [147] to study the effects of multiple stenoses on the pressure drop for various Reynolds number ranging from 30 to 280. They reported that the intensity of pressure drop increases owing to the presence of multiple stenoses. A numerical study of steady laminar flow through a tube with multiple constrictions was done by Damodaran *et al* . [60] for Reynolds number between 50 and 250. They also reported a significant change in pressure drop and wall shear stress due to the effects of multiple constrictions.

Lee [61] and Huang *et al* . [148] investigated steady laminar fluid flow through a double constriction in a tube taking a maximum Reynolds number of 400. In addition, Lee *et al* . [65; 66] have investigated steady and physiological 2D turbulent flows through double arterial stenoses using the RANS (k-ω) method. However, in Chapter 2, we have mentioned clearly that RANS is not capable of calculating

properly pulsatile turbulent flow, and the above mentioned numerical studies are confined to the two-dimensional case.

In this Chapter, we investigate three-dimensional physiological pulsatile flow through double stenoses by using the Large Eddy Simulation technique. A simple channel with two cosine shaped stenoses on the top wall is chosen as the computational domain. The first four harmonics of the physiological pulsatile flow, already described in Chapter 7, is used at the inlet for generating the oscillating flow. The effects of the double stenoses on the pressure drop, the stress drop and the turbulent intensity are examined.

In LES, the Piomelli-Liu [4] localized dynamic model has been used for modelling the subgrid-scale motions, and the maximum contribution of the SGS model is also assessed. The numerical results are presented in terms of the time-mean streamwise velocity, streamlines and wall pressure distribution, contour plots of instantaneous streamwise velocity, instantaneous wall shear stresses, root mean square velocity and pressure fluctuations as well as the energy spectra of the streamwise velocity turbulent fluctuations.

8.2 Formation of the Problem

8.2.1 Model Geometry and Mesh Arrangement

The geometry shown in Fig. 8.1 consists of a 3D channel with two cosine shape stenoses formed on the upper wall. The first stenosis is centred at $y/L = 0.0$ while the second stenosis at $y/L = 3.0$ with a 50% cross-sectional area reduction at the centre of both the stenoses. Here y is the horizontal distance or the distance along the flow and L is the height of the channel. In the model the height (x) and its width (z) are kept the same as in the previous chapters. The length of each of the stenosis is equal to twice the channel height. The formation of the stenoses is done by using the following relation:

$$\frac{x}{L} = \begin{cases} 1 - \frac{\delta_c^1}{2}\left(1 + \cos\frac{y\pi}{L}\right) & \text{if} \quad -L \leq y \leq L \\ 1 - \frac{\delta_c^2}{2}\left(1 - \cos\frac{y\pi}{L}\right) & \text{if} \quad 2L \leq y \leq 4L \\ 1 & \text{otherwise} \end{cases} \tag{8.1}$$

Table 8.1: Mesh details used in the computations.

Case	Re	approach	N_x	N_y	N_z	δt
0	< 2000	LES	50	300	50	10^{-3}
1	2000	LES	50	300	50	10^{-3}
2	2000	LES	50	350	50	10^{-3}
3	2000	LES	70	350	50	10^{-3}

where δ_c^1 and δ_c^2 are the parameters that control the percentage of the first and second stenoses, respectively, which are fixed to $\frac{1}{2}$ to keep a 50% reduction of the cross-sectional area at the centre of the stenoses. As in previous chapters, we have used a fine mesh near the top and bottom walls as well as in the immediate vicinity of the both stenoses (see Fig. 8.2).

8.2.2 Governing Equations and Boundary Conditions

The filtered Navier-Stokes equations have been solved assuming that the fluid through the arterial double stenoses is homogeneous and incompressible. The details are described in Chapter 3. The physiological pulsatile flow at the inlet and the rest of the boundary conditions remain same as in Chapter 7.

8.3 Results and Discussion

The simulations are carried out with Reynolds numbers, $Re = 1000$, 1400, 1700 and 2000, fixing the Womersley number α to 10.5. The grid independence test for $Re = 2000$ is performed with various grid arrangements, the details are in Table 8.1. For all the computations the timestep δt is fixed to 10^{-3} following the results in the previous chapters. The flow simulation is carried out up to the peak phase of the 11th cycle of pulsation.

This section is structured in the following order: a description of grid independence test is in § 8.3.1, the contribution of the subgrid model to the large scale motion is in § 8.3.2. The mean and instantaneous flow characteristics are presented in § 8.3.3 while the turbulent flow characteristics are in § 8.3.4. Finally, a conclusion based on the findings is drawn in § 8.4.

8.3.1 Grid Independence Test

Figs. 8.3 and 8.4 show the grid independent test in terms of the mean streamwise velocity, $< \bar{v} > /\bar{V}_{max}$, and the turbulent kinetic energy (TKE), $\frac{1}{2} < u_j'' u_j'' > /\bar{V}_{max}^2$, at the different streamwise axial positions, while $Re = 2000$. Three different grid arrangements used in the test are Case 1: $50 \times 300 \times 50$, Case 2: $50 \times 350 \times 50$ and Case 3: $70 \times 350 \times 50$.

The mean streamwise velocity at the inlet of the channel (Fig. 8.3a) where the flow is laminar, and at the centre of the stenosis (Fig. 8.3b) from where the flow is going to be transitional is exactly the same for the different grid arrangements. However, the velocity slightly deviated at the position of post lip of the first stenosis (frames c and d) where the permanent re-circulation region takes place. The velocity decreases slightly at $y/L = 2.0$, but due to the presence of the second stenosis velocity increases at the centre and post-lip of the second stenosis. The negative velocity seen in frame (f), indicates the presence of another re-circulation region at the post-lip of the second stenosis. After the second stenosis, the agreement of the velocity for the different grid arrangements is excellent. The turbulent kinetic energy in Fig. 8.4 shows some variations after the stenoses, which are acceptable. As already explained in Chapter 6, in LES only the resolved scale flows are computed by the grid resolution and the strict grid independence of the computed solution is not expected in LES. So, the grid arrangement of $50 \times 300 \times 50$ seems fine to resolve the transient flow adequately in the double stenosis. In frames (a-b), the turbulent kinetic energy (TKE) is almost zero as the flow is laminar upstream of the first stenosis, this result is exactly same as it was seen in the one-stenosis compared in Chapter 7. However, the effects of the second stenosis are clearly seen in frames (d-h). In the one-stenosis case, the maximum rise in TKE was observed in the post-lip region, i.e. at $y/L = 1.0$, but in the multiple stenoses case it is seen that there is a sharp rise of TKE upstream and immediate down stream of the stenosis. Finally, the TKE gradually decreases and approaches zero further downstream because of the re-laminarisation process, also seen at the one-stenosis model.

8.3.2 Contribution of the SGS Model

The dynamic values of the Smagorinsky constant C_s, are presented in Fig. 8.5(a-d) for the different Reynolds numbers. The maximum values of C_s, found near the throat and downstream of the second stenosis, are 0.088, 0.13, 0.14 and 0.19 respectively, for $Re = 1000$, 1400, 1700 and 2000. Due to the effects of the two stenoses, the values of the C_s are almost doubled compared to those of the single stenosis in Chapter 7 (Fig. 7.8) while $Re = 1400$, 1700 and 2000, and the contribution from the SGS model, which are presented in Fig. 8.6(a-d) in terms of the normalised SGS viscosity, increases in the second stenosis. Furthermore, the maximum SGS viscosity, μ_{sgs}/μ, of 0.26, 0.83, 1.64 and 3.69, obtained respectively for the Reynolds numbers above, corresponds to the large dissipation of the SGS model in the region of the second stenosis.

8.3.3 Mean and Instantaneous Flow Characteristics

The mean streamwise streamlines appended on the mean streamwise velocity contours are presented in Fig. 8.7(a-d) for the different Reynolds numbers. It is now clearly seen in this figure that there are two permanent re-circulation regions: the first one lies near the upper wall between the first and second stenoses, while the second re-circulation region lies at the post-lip of the second stenosis. The length of these re-circulation regions also depends on the Reynolds number. For example, when $Re = 1000$ and 1400 the length of the first re-circulation region is larger than the second re-circulation region. Whereas, the length of the second re-circulation region is larger than the first re-circulation region when $Re = 1700$ and 2000.

In order to understand more clearly the process of the flow separation from the nose of the both stenoses and the region of the flow transition from laminar to turbulent, the instantaneous streamwise velocity $\bar{v}/\bar{V}_{max}$ is presented in Fig. 8.8 for the different Reynolds numbers. The results show that the shear layer separates from the nose of the first stenosis is affected by the second stenosis and causes the stagnation of flow (i.e. re-circulation) near the upper wall between the two stenoses. The highly disturbed flow downstream of the second stenosis is caused by the separation of the shear layer from the second nose. The intensity of the flow will be analysed in § 8.3.4.

The instantaneous shear stress, $\tau_{xy}/\rho\bar{V}^2_{max}$, at the upper and lower walls are depicted in Figs. 8.9 (a-b), respectively for the different Reynolds numbers. At the upper wall there are two levels of stress reduction: one takes place just prior to the centre of the first stenosis where flow is transitional and the second one occurs just prior to the centre of the second stenosis where the flow is turbulent. The higher level of stress drop at the turbulent region can increase the tissue proliferation inside the arterial vessel, and consequently, increase the percentage of the stenosis. So, the presence of multiple stenoses in an artery is more dangerous for a patient. In addition, the highly oscillating forms of the wall shear stress that occur at the second stenosis are more harmful to the blood cells and blood vessels.

The effects of the multiple stenoses on the mean pressure, $< \bar{p} > /\rho\bar{V}^2_{max}$, at the upper and lower walls are illustrated respectively in Figs. 8.10 (a-b). In the upper wall the pressure drops at the centre of the stenoses are very acute due to the direct effect of the stenosis while they are blunt in the lower wall. Moreover, the effect is prominent in the second stenosis. The pressure drop in the second stenosis is larger than the first one, which again indicates the fact that the flow separated from the nose of the second stenosis re-circulates for a longer time than with the single stenosis, consequently, increasing the risk of the thrombosis or stroke.

8.3.4 Turbulent Flow Characteristics

The effects of the second stenosis on the turbulent flows are presented in this section in terms of the root mean square (rms) of the velocity and pressure fluctuations as well as the energy spectra of the streamwise velocity fluctuations.

Fig. 8.11 depicts the rms of the cross-stream velocity fluctuations, $< u'' >_{rms} /\bar{V}_{max}$, at the different axial locations for the different Reynolds numbers. The results show that at the centre of the first stenosis, $y/L = 0.0$, the flow is transitional for $Re = 1700$ and 2000. The intensity of the cross-stream velocity fluctuations increases at the downstream of the first stenosis for all the Reynolds numbers and the maximum occurs at $y/L = 1.5$. Although, the intensity of the fluctuations reduces slightly at the pre-lip of the second stenosis, $y/L = 2.0$, due to the effects of the second stenosis the fluctuations grow again downstream of the second stenosis near the upper wall. Further downstream the turbulent fluctuations diminish in a similar

manner as found in the single stenosis where the flow re-laminarises, which is also known as a recovery zone. The contour plots of $< u'' >_{rms} /\bar{V}_{max}$ in Fig. 8.12 give additional information about the turbulent region and the magnitude of the cross-stream turbulent intensity.

The corresponding rms values of the stream-wise and spanwise velocity turbulent fluctuations $< v'' >_{rms} /\bar{V}_{max}$ and $< w'' >_{rms} /\bar{V}_{max}$, at the different axial locations are plotted in Figs. 8.13 - 8.11 respectively. The maximum value of $< v'' >_{rms} /\bar{V}_{max}$ is found after the centre of the second stenosis at $y/L = 3.5$ while the maximum value of $< w'' >_{rms} /\bar{V}_{max}$ occurs before the centre of the second stenosis at $y/L = 2.5$. So, the presence of the second stenosis is pathologically important since it increases the turbulent intensity. The contour plots of $< v'' >_{rms} /\bar{V}_{max}$ and $< w'' >_{rms} /\bar{V}_{max}$, plotted in Figs. 8.14 and 8.16 respectively, show their variations in the whole plane.

Another important turbulent quantity is the rms of the pressure fluctuations presented in Figs. 8.17 and 8.16. The pressure fluctuations after the immediate downstream region of the first stenosis are higher near the upper wall but they mitigate slightly at the centre of the second stenosis. The magnitude of the fluctuations then increases rapidly up to the position of $y/L = 4.5$, followed by a gradual decrease far downstream. In Chapters 4 to 7, it was discussed that the pressure fluctuations are the main source of the arterial murmur sounds, which are detected by using a non-invasive device. Since the presence of the double stenosis increases the magnitude of the pressure fluctuations, the intensity of the murmur sound from a double stenosed artery would be higher than the single stenosis.

Fig.8.19 shows the energy spectra of the streamwise velocity fluctuations $v''^2/\bar{V}^2_{max}$ along with the straight lines of $Sr^{-5/3}$ and $Sr^{-10/3}$ at the different post-stenotic positions while $Re = 2000$. The sub-range region that clearly exists between $y/L = 1.0$ and $y/L = 6.0$ decreases gradually towards the downstream of the second stenosis. Further downstream this region is very small as this is the recovery zone.

8.4 Conclusion

In this Chapter, a Large Eddy Simulation has been performed to investigate physiological pulsatile flow through the model of a double stenosis. The results presented in various forms show the effects of the presence of the second stenosis in an artery. For $Re = 2000$, the maximum Smagorinsky constant obtained is $C_s \approx 0.2$ which is almost double the case of a single stenosis in Chapter 7 (Fig. 7.8d). The maximum contribution of the SGS model also increases at the region of the second stenosis.

The upper wall pressure and stress drops increase rapidly in the second stenosis for all the Reynolds numbers which are consistent with the results of Talukder *et al* . [147] and Damodaran *et al* . [60].

Furthermore, due to the presence of the second stenosis the turbulent intensity of the flow increases significantly. From the pathological point of view, the increment in the turbulent fluctuations are more dangerous as they damage the material of blood cells and the inner surface of a blood vessel. The permanent re-circulation zone found in the downstream of the second stenosis will also increase the risk of thrombosis or blood clotting, and consequently, increase the risk of heart attack or brain stroke.

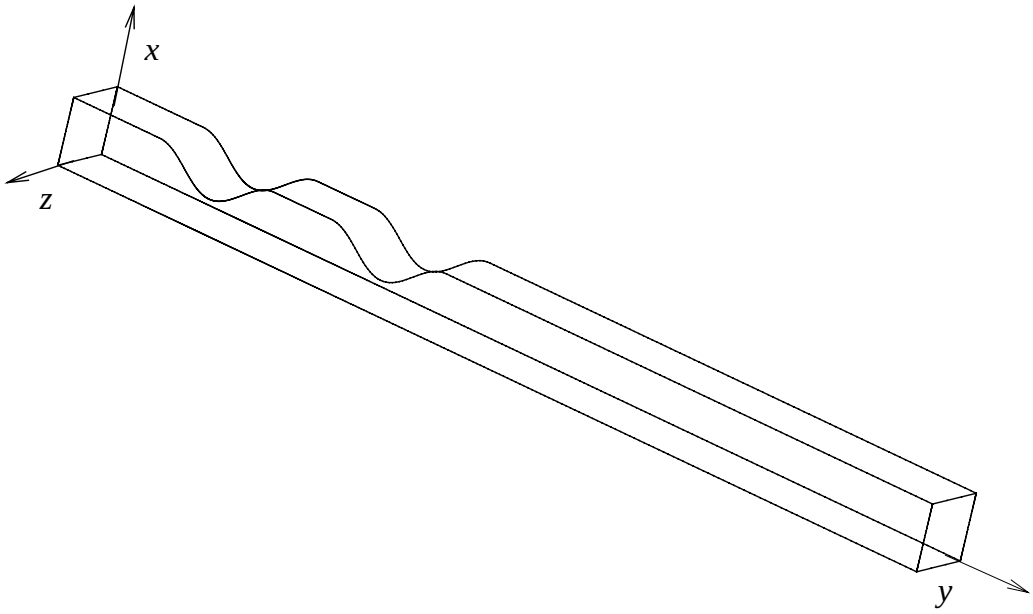

Figure 8.1: A schematic of the model with coordinate system.

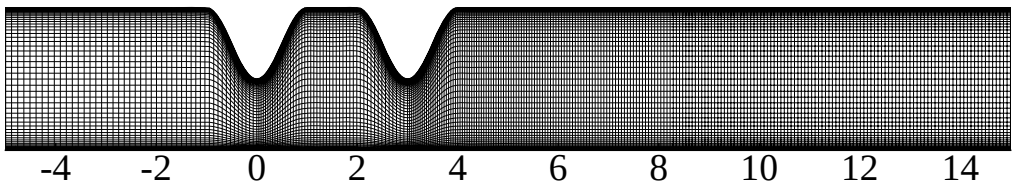

Figure 8.2: A crude mesh distribution in $x - y$ plane.

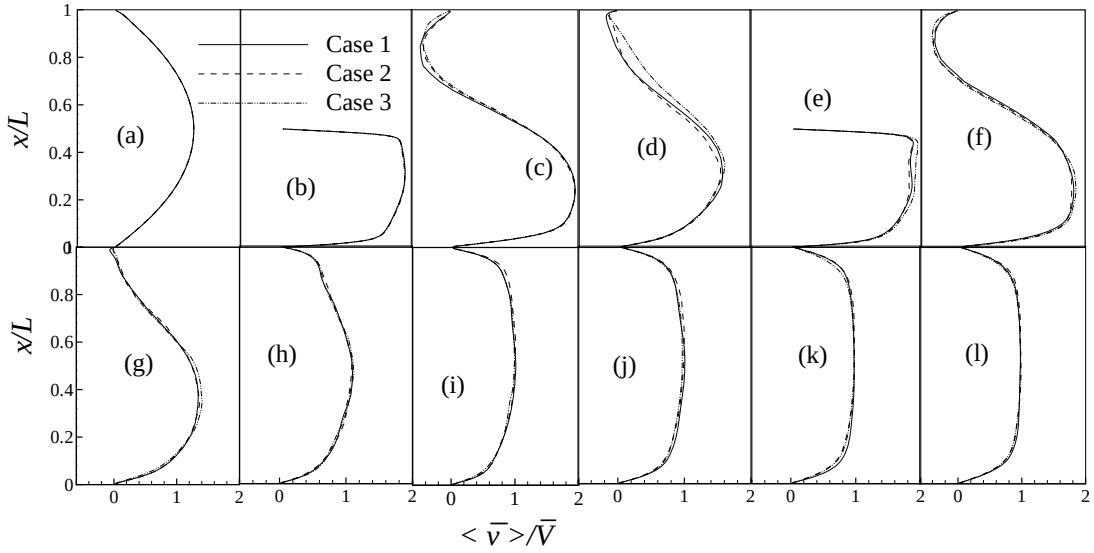

Figure 8.3: Grid independence test for the mean streamwise velocity, $< \bar{v} > /\bar{V}$, at (a) $y/L =$ inlet, (b) $y/L = 0.0$, (c) $y/L = 1.0$, (d) $y/L = 2.0$, (e) $y/L = 3.0$, (f) $y/L = 4.0$, (g) $y/L = 5.0$, (h) $y/L = 6.0$, (i) $y/L = 8.0$, (j) $y/L = 10.0$, (k) $y/L = 12.0$ and (l) $y/L =$ outlet, while $Re = 2000$.

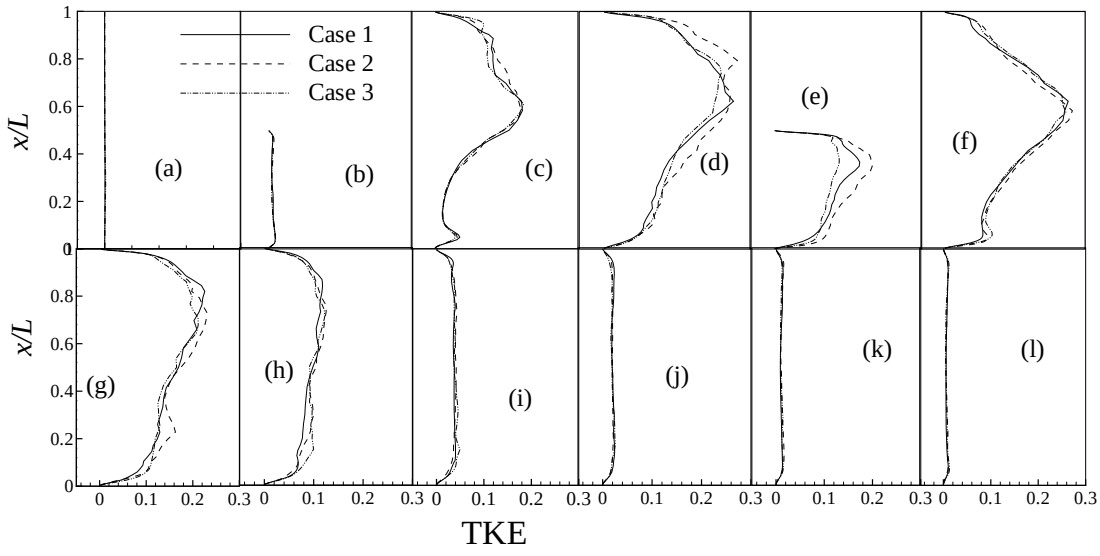

Figure 8.4: Grid independence test for the turbulent kinetic energy (TKE), $\frac{1}{2} < u_j'' u_j'' > /\bar{V}^2$, (a) $y/L =$ inlet, (b) $y/L = 0.0$, (c) $y/L = 1.0$, (d) $y/L = 2.0$, (e) $y/L = 3.0$, (f) $y/L = 4.0$, (g) $y/L = 5.0$, (h) $y/L = 6.0$, (i) $y/L = 8.0$, (j) $y/L = 10.0$, (k) $y/L = 12.0$ and (l) $y/L =$ outlet, while $Re = 2000$.

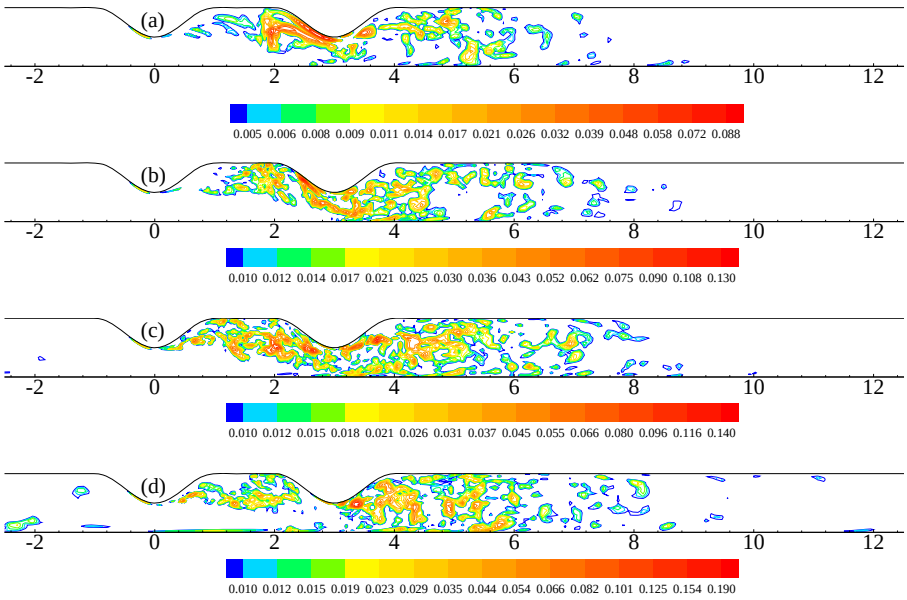

Figure 8.5: Dynamic Smagorinsky constant, C_s, for (a) $Re = 1000$, (b) $Re = 1400$, (c) $Re = 1700$ and (d) $Re = 2000$ at $t/T = 10.25$.

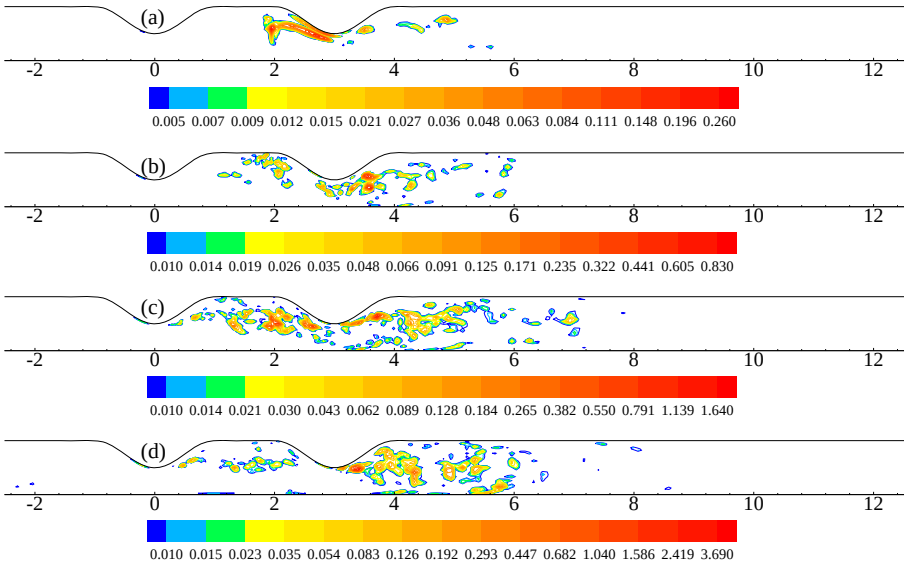

Figure 8.6: Normalised SGS eddy viscosity, μ_{sgs}/μ, for (a) $Re = 1000$, (b) $Re = 1400$, (c) $Re = 1700$ and (d) $Re = 2000$ at $t/T = 10.25$.

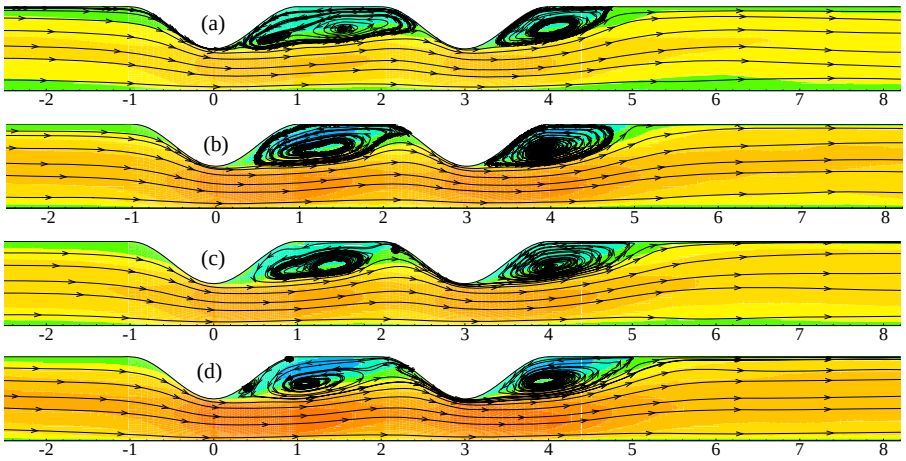

Figure 8.7: Mean streamwise streamlines appended on the mean streamwise velocity ,$< \bar{v} > /\bar{V}_{max}$, for (a) $Re = 1000$, (b) $Re = 1400$, (c) $Re = 1700$ and (d) $Re = 2000$.

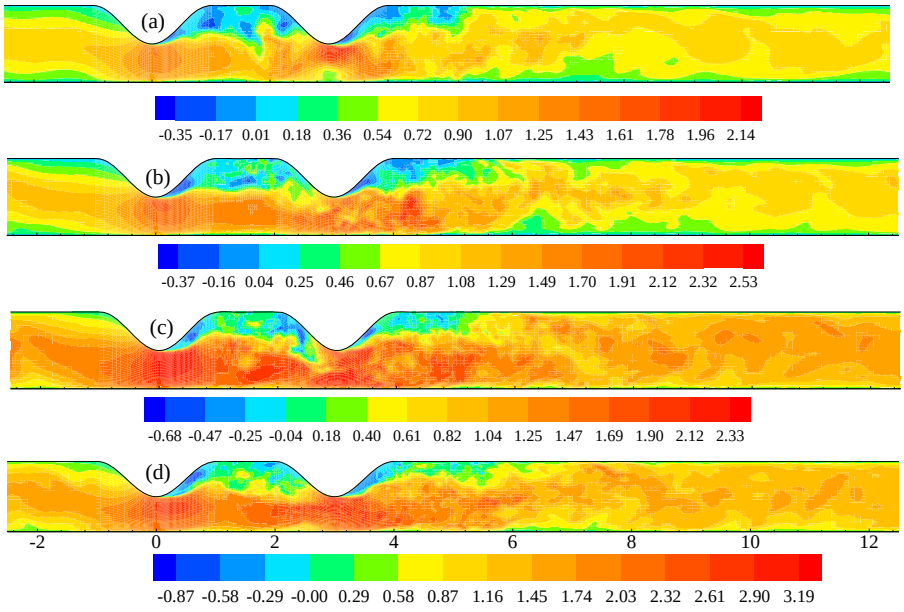

Figure 8.8: Contour plot of the instantaneous streamwise velocity, $\bar{v}/\bar{V}_{max}$, for (a) $Re = 1000$, (b) $Re = 1400$, (c) $Re = 1700$ and (d)$Re = 2000$ at $t/T = 10.25$.

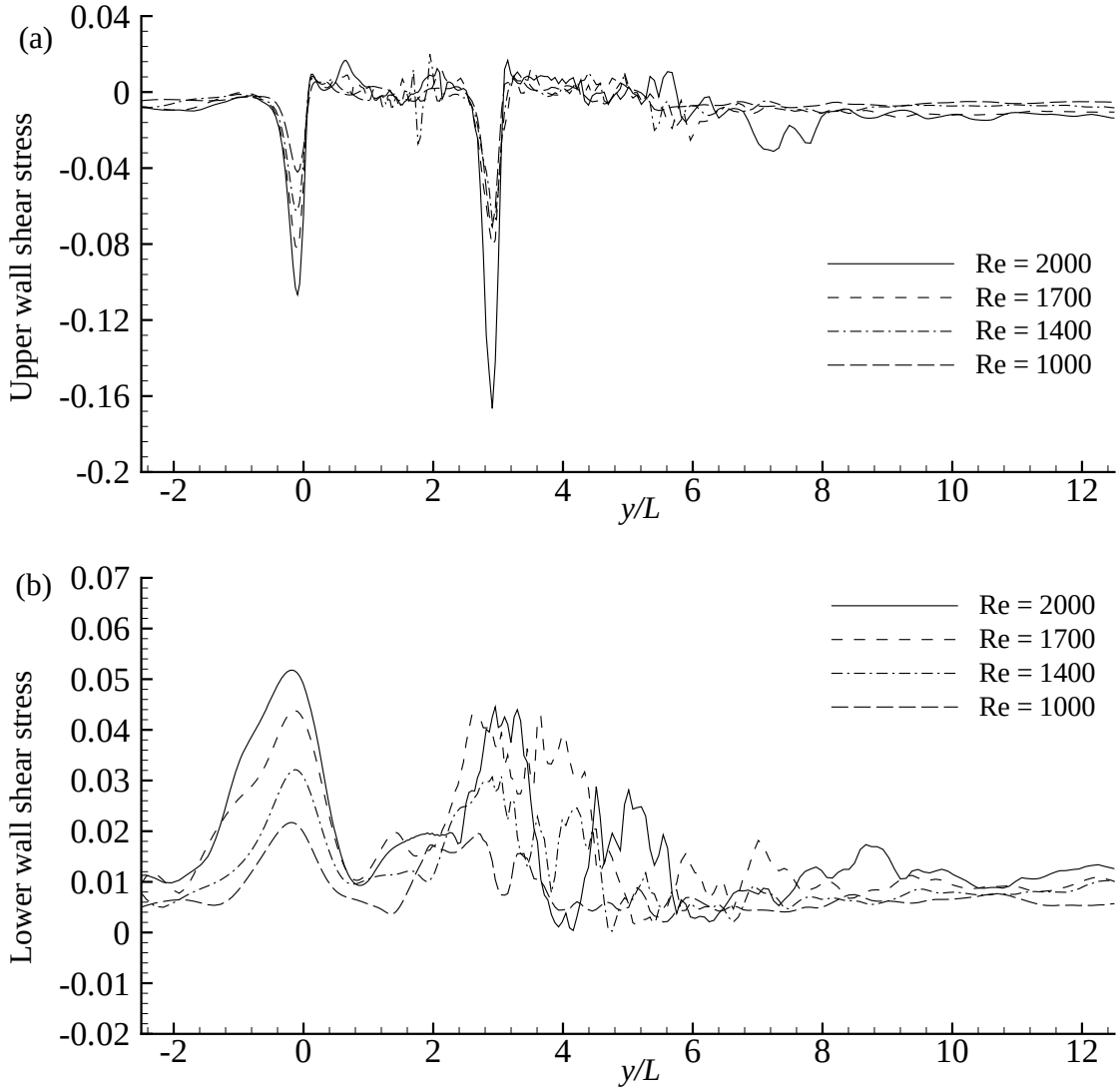

Figure 8.9: Instantaneous wall shear stress, $\tau_{xy}/\rho\bar{V}^2_{max}$, at the (a) upper wall and (b) lower wall for the different Reynolds numbers at $t/T = 10.25$.

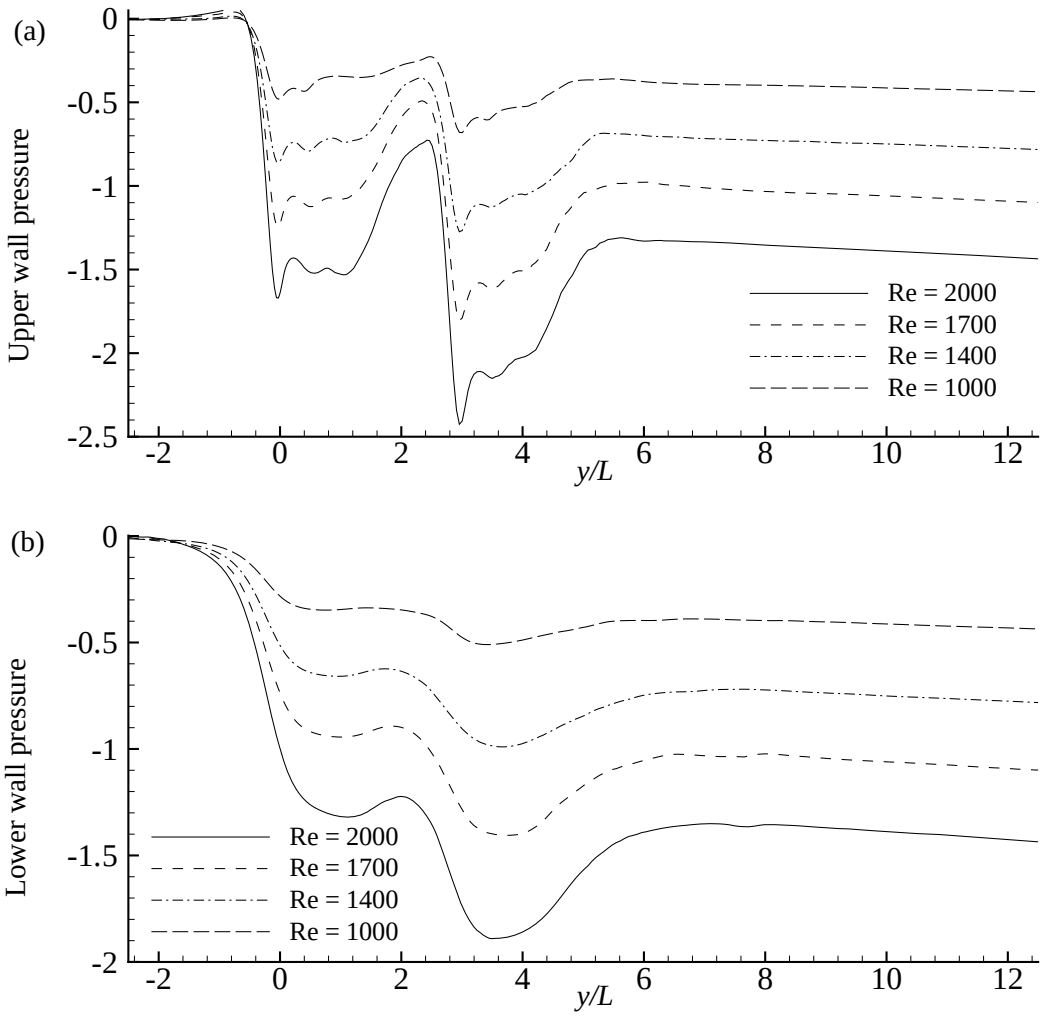

Figure 8.10: Time-mean pressure, $< \bar{p} > /\rho \bar{V}_{max}^2$, at the (a) upper wall and (b) lower wall for the different Reynolds numbers.

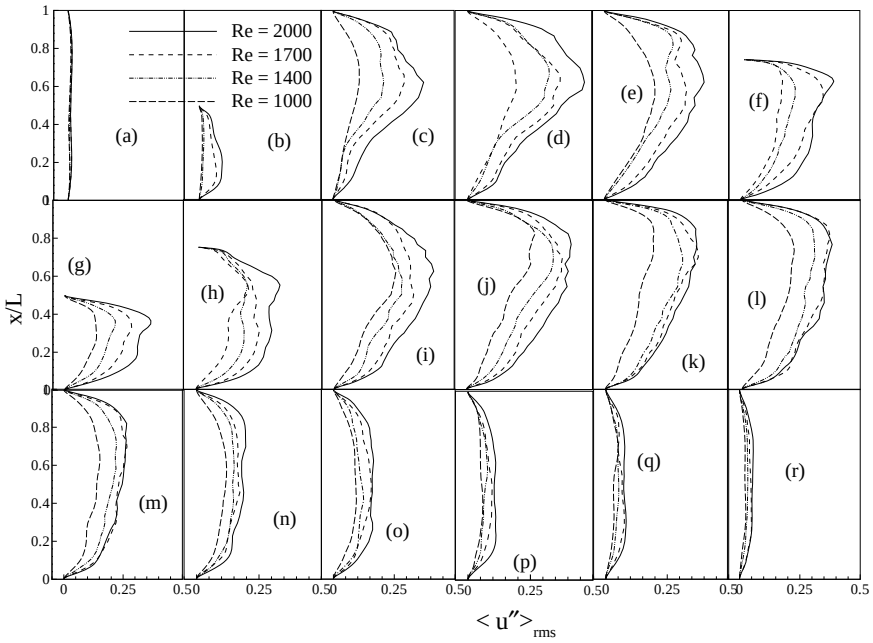

Figure 8.11: rms of the cross-stream velocity fluctuations, $< u'' >_{rms} /\bar{V}_{max}$, at the different axial locations: (a) $y/L =$ inlet, (b) $y/L = 0.0$, (c) $y/L = 1.0$, (d) $y/L = 1.5$, (e) $y/L = 2.0$, (f) $y/L = 2.5$, (g) $y/L = 3.0$, (h) $y/L = 3.5$, (i) $y/L = 4.0$, (j) $y/L = 4.5$, (k) $y/L = 5.0$ (l) $y/L = 5.5$, (m) $y/L = 6.0$, (n) $y/L = 7.0$, (o) $y/L = 8.0$, (p) $y/L = 10.0$, (q) $y/L = 12.0$ and (r) $y/L =$ outlet for the different Reynolds numbers.

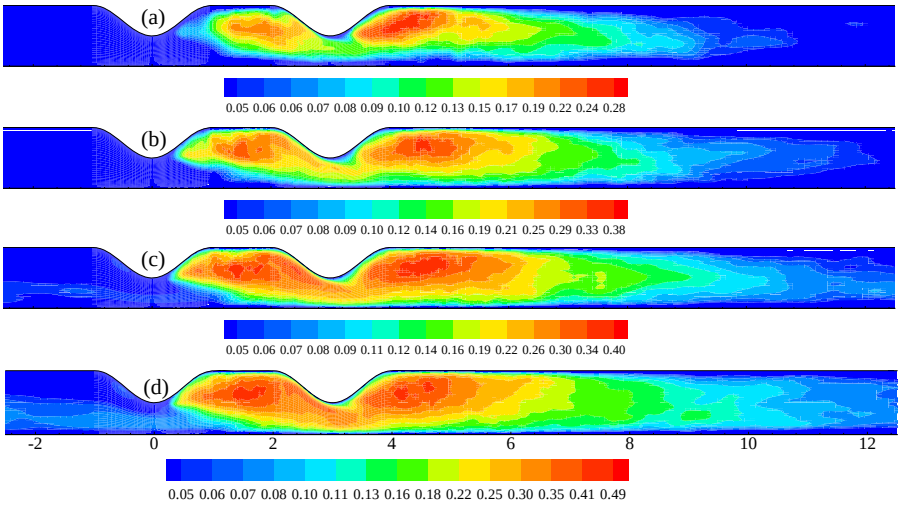

Figure 8.12: Contour plot of $< u'' >_{rms} /\bar{V}_{max}$, for (a) $Re = 1000$, (b) $Re = 1400$, (c) $Re = 1700$ and (d) $Re = 2000$.

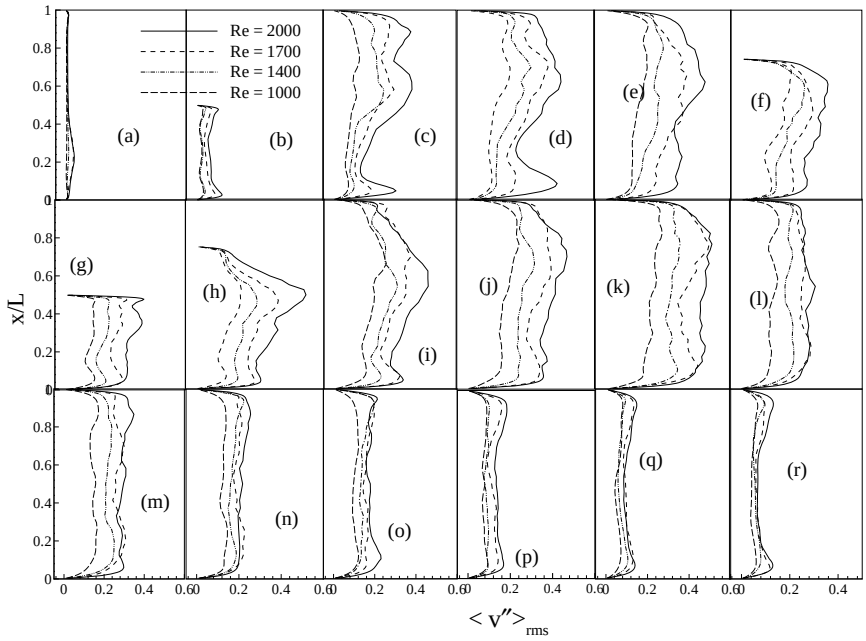

Figure 8.13: rms of the streamwise velocity fluctuations, $< v'' >_{rms} /\bar{V}_{max}$, at the different axial locations: (a) $y/L =$ inlet, (b) $y/L = 0.0$, (c) $y/L = 1.0$, (d) $y/L = 1.5$, (e) $y/L = 2.0$, (f) $y/L = 2.5$, (g) $y/L = 3.0$, (h) $y/L = 3.5$, (i) $y/L = 4.0$, (j) $y/L = 4.5$, (k) $y/L = 5.0$ (l) $y/L = 5.5$, (m) $y/L = 6.0$, (n) $y/L = 7.0$, (o) $y/L = 8.0$, (p) $y/L = 10.0$, (q) $y/L = 12.0$ and (r) $y/L =$ outlet for the different Reynolds numbers.

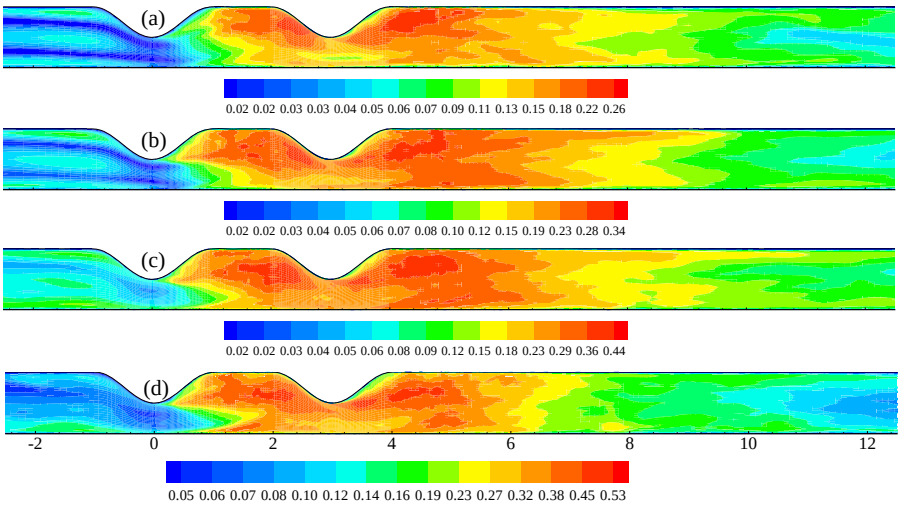

Figure 8.14: Contour plot of $< v'' >_{rms} /\bar{V}_{max}$, for (a) $Re = 1000$, (b) $Re = 1400$, (c) $Re = 1700$ and (d) $Re = 2000$.

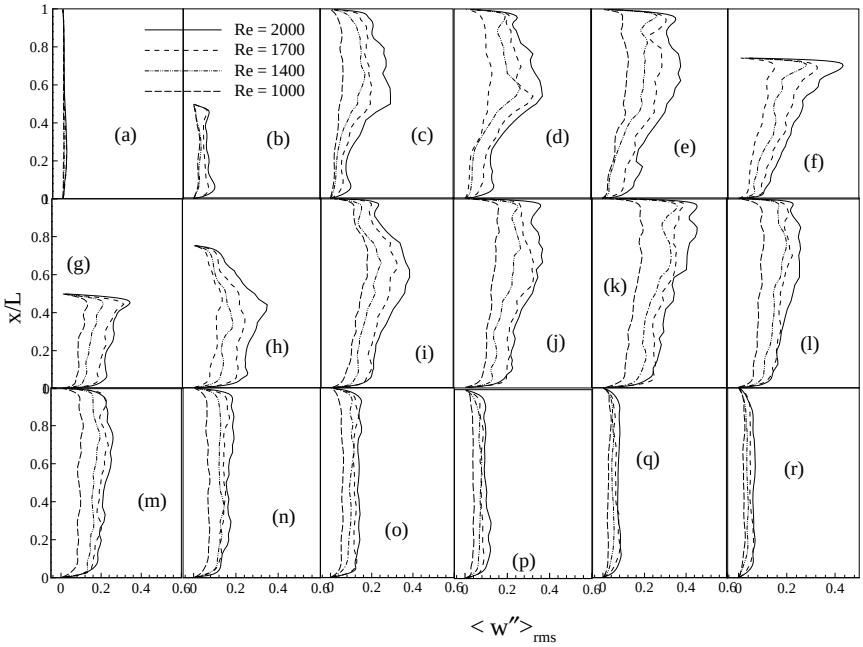

Figure 8.15: rms of the spanwise velocity fluctuations, $< w'' >_{rms} / \bar{V}_{max}$, at the different axial locations: (a) $y/L =$ inlet, (b) $y/L = 0.0$, (c) $y/L = 1.0$, (d) $y/L = 1.5$, (e) $y/L = 2.0$, (f) $y/L = 2.5$, (g) $y/L = 3.0$, (h) $y/L = 3.5$, (i) $y/L = 4.0$, (j) $y/L = 4.5$, (k) $y/L = 5.0$ (l) $y/L = 5.5$, (m) $y/L = 6.0$, (n) $y/L = 7.0$, (o) $y/L = 8.0$, (p) $y/L = 10.0$, (q) $y/L = 12.0$ and (r) $y/L =$ outlet for the different Reynolds numbers.

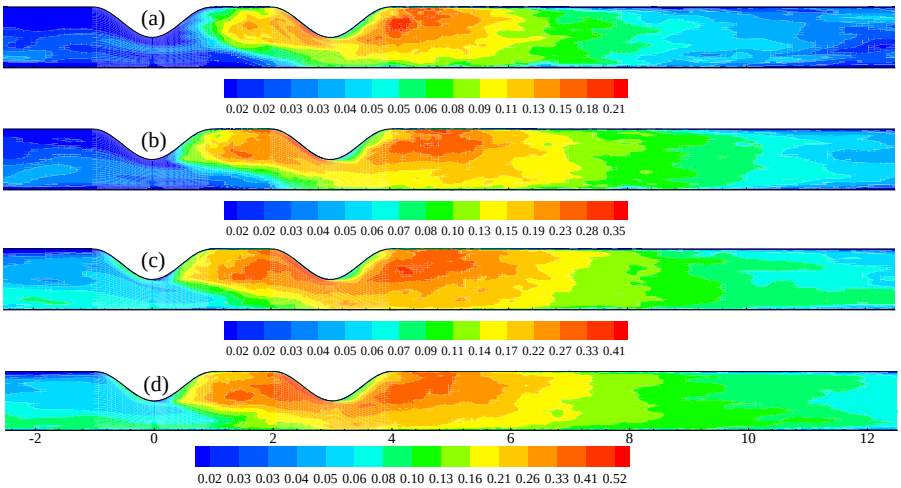

Figure 8.16: Contour plot of $< w'' >_{rms} / \bar{V}_{max}$, for (a) $Re = 1000$, (b) $Re = 1400$, (c) $Re = 1700$ and (d) $Re = 2000$.

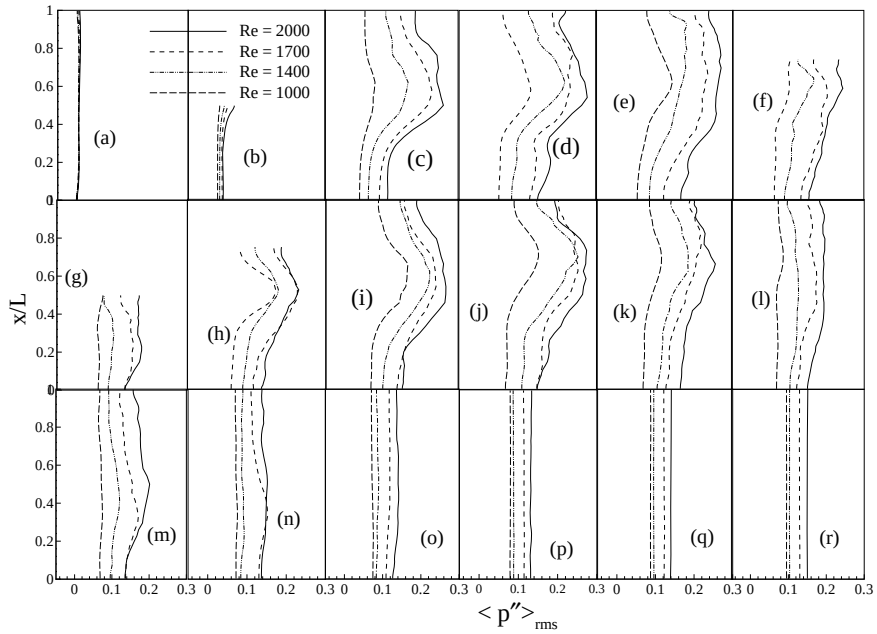

Figure 8.17: rms of the pressure fluctuations, $< p'' >_{rms} / \rho \bar{V}^2_{max}$, at the different axial locations: (a) $y/L =$ inlet, (b) $y/L = 0.0$, (c) $y/L = 1.0$, (d) $y/L = 1.5$, (e) $y/L = 2.0$, (f) $y/L = 2.5$, (g) $y/L = 3.0$, (h) $y/L = 3.5$, (i) $y/L = 4.0$, (j) $y/L = 4.5$, (k) $y/L = 5.0$ (l) $y/L = 5.5$, (m) $y/L = 6.0$, (n) $y/L = 7.0$, (o) $y/L = 8.0$, (p) $y/L = 10.0$, (q) $y/L = 12.0$ and (r) $y/L =$ outlet for the different Reynolds numbers.

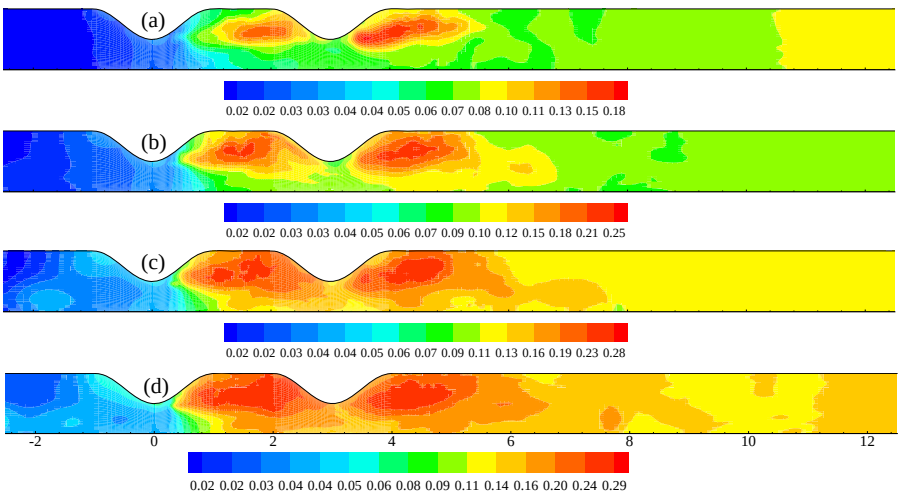

Figure 8.18: Contour plot of $< p'' >_{rms} / \rho \bar{V}^2_{max}$, for (a) $Re = 1000$, (b) $Re = 1400$, (c) $Re = 1700$ and (d) $Re = 2000$.

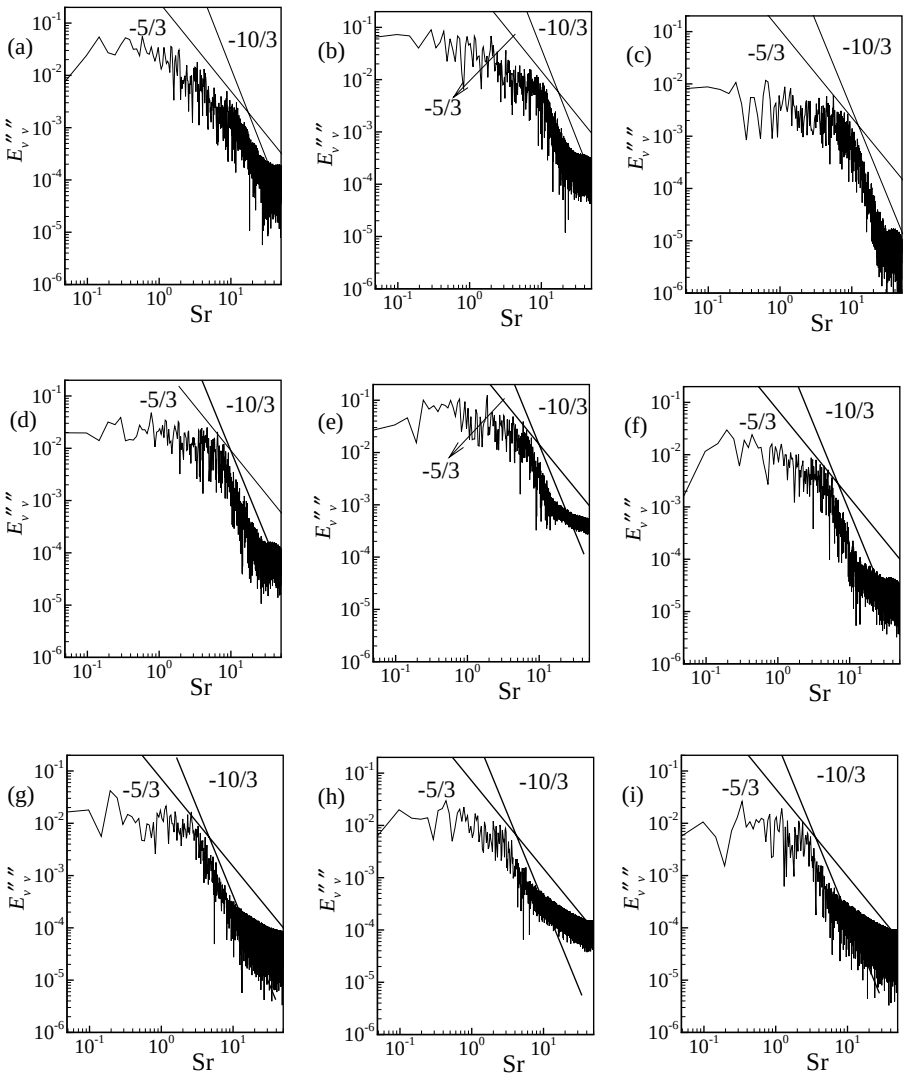

Figure 8.19: Energy spectrum of v'' at (a) $y/L = 1.0$, (b) $y/L = 2.0$, (c) $y/L = 3.0$, (d) $y/L = 4.0$, (e) $y/L = 5.0$, (f) $y/L = 6.0$, (g) $y/L = 7.0$, (h) $y/L = 8.0$ and (i) $y/L = 9.0$ while $Re = 2000$.

Chapter 9

LES of Physiological Pulsatile Flow in a Model Aneurysm

9.1 Introduction

Aneurysms pose a great health risk due to their potential for thrombus formation and more importantly rupture. If left untreated, aneurysm may continue to expand until rupture, causing haemorrhage, complications to local organ function, and possibly death. Aneurysm ruptures have high rates of mortality and morbidity (Kassell *et al* . [149]). In this Chapter, a Large Eddy Simulation (LES) is employed to study the transition-to-turbulent pulsatile flow through a 3D model of an arterial aneurysm. A physiological pulsatile flow where the pressure pulse consists of first four harmonics is used at the inlet to generate the pulsatile flow. The inlet velocity profiles which are physiologically realistic have already been presented in Chapter 7. The flow Reynolds number (Re) and the Womersley number (α) are fixed at 2000 and 10.5 respectively in this Chapter.

The numerical results are presented in terms of the velocity, vorticity, sequential streamlines, pressure and shear stress distributions, root mean square velocity and pressure fluctuations as well as the energy spectra. A qualitative comparison of the streamlines with experimental results which was obtained by Egelhoff *et al* . [5] of the flow visualisation photographs in the asymmetric aortic aneurysm are made at the different phases of time period. Moreover, a grid independence test has been done for the two different sets of grid arrangement. To the best of our knowledge, from the literature review, it is noted that most of the previous studies in aneurysm are restricted to laminar flow only.

9.2 Model Geometry

In Fig. 9.1, the geometry of the model aneurysm is shown, which consists of a 3D channel with one sided balloon-shaped dilation on the upper wall centred at $y/L = 0.0$, where y is the horizontal distance or the distance along the flow and L is the height of the channel. In the model, the height (x) of the channel and its width (z) are kept the same, giving a square cross-section upstream and downstream of the stenosis. The length of the aneurysm region is taken as $4L$ according to the investigation of Neofytou *et al* . [150] on a model aortic aneurysm. They considered the aneurysm segment length as 4 times the diameter of the model tube. The upstream length of the aneurysm is $2L$ while the downstream region is $10L$. The shape of the aneurysm is chosen for this study as

$$\frac{x}{L} = 1 + \delta_c \left(1 + \cos\frac{y\pi}{L}\right), \quad -2L \leq y \leq 2L \tag{9.1}$$

where δ_c is the parameter that controls the percentage of the aneurysm. In the present study, δ_c is fixed at 1, which gives a 100% dilation of the cross-sectional area at the centre of the aneurysm. For convenience of computation and setting the outlet boundary condition, the post aneurysm length has been extended sufficiently.

No slip boundary conditions are used for the lower and upper walls of the model. At the outlet a convective boundary condition is used. In the spanwise boundaries, a periodic boundary condition is applied. Non-uniform dense meshes are used near the top and bottom walls of the model to capture the thin shear layer developed in the vicinity of the walls. The meshes are also concentrated inside the aneurysm where the high re-circulations generate. A crude mesh distribution is plotted in the $x - y$ plane and shown in Fig. 9.2.

9.3 Results and Discussion

The computational results of LES presented here have been obtained by using the mesh arrangements of $120 \times 350 \times 90$ and $90 \times 300 \times 90$ (along $x \times y \times z$) for the Reynolds number of 2000, the Womersley number of 10.5 and $A = 0.4$. The simulations are carried out up to the peak phase of the 11th cycle of pulsation as it

has been shown that the mean results are eventually become stationary after $t/T = 9$ time periods. In terms of the contribution of the SGS model in LES, we have found that the normalised SGS, μ_{sgs}/μ, is approximately 0.1, that is, a maximum of 10% contribution comes from the SGS model.

9.3.1 Instantaneous and mean flow

The contour plots of the three velocity components, $\bar{u}/\bar{V}_{max}$, $\bar{v}/\bar{V}_{max}$ and $\bar{w}/\bar{V}_{max}$, are presented in Fig. 9.3(a-c) respectively at the peak phase of the last pulsation, i.e. $t/T = 10.25$. The irregular forms of velocity appearing in the far downstream region of the aneurysm are visible in these plots. The flow takes on the chaotic form inside the aneurysm near the upper wall, consequence of this will be discussed later in terms of the flow streamlines and wall shear stresses.

The corresponding contour plot of the spanwise-averaged vorticity, $< \omega_z >_s$, is depicted in Fig. 9.4 with the unequal fourteen contour levels of vortices as shown in the colour bar. The dashed lines in the plot represent anti-clockwise vortices while the solid lines represent clockwise vortices. The results show that the severe re-circulated regions produced inside the aneurysm impose a perturbation on the fluid, as a result the flow in the far downstream region becomes highly disturbed.

Experimental results of Egelhoff *et al* . [5] presented in Fig. 9.5 show flow visualisation photographs of the asymmetric abdominal aortic aneurysm at the different phases of time period while $Re_{peak} = 3308$. The experimental results show that the core of the re-circulation region which generates in the aneurysm at the early systole (a) changes with time, and the severity of this re-circulation is quite prominent at the phases from mid systole (c) to early diastole (e). The nature of the re-circulated flow inside the aneurysm, as reported in the paper, is turbulent.

Similar types of flow pattern with re-circulation regions are observed in the present study as shown in Fig. 9.6(a-g) in terms of the streamline plots in the aneurysm section at the different phases over a time period along with the mean streamline plot in frame (h). In frame (a), at $t/T = 9.0$, the primary re-circulation zone is very small, and is situated near the upper wall in the immediate downstream region of the centre of the aneurysm where the fluid experiences an impediment by the arterial wall.

The primary re-circulated region increases at $t/T = 9.125$ but it moves towards the centre of the aneurysm. In addition, a secondary as well as a small tertiary re-circulated zone is visible in the region between $y/L \sim 0.5$ and $y/L \sim 1.5$. The streamlines in frame (c) show that the primary re-circulated zone moves further upstream at the peak systole ($t/T = 9.25$) and is now situated between $y/L \sim -2.0$ and $y/L \sim 0.0$, while the secondary and tertiary flow vortices at this phase expand and get stronger. After the peak of the pulsation, the two large re-circulations occupy almost the whole aneurysm as seen in frame (d). Besides, another re-circulation zone is created at this phase near the lower wall between $y/L \sim 1.5$ and $y/L \sim 2.0$ due to the backward flow near the upper wall. Up to phase $t/T = 9.625$, the re-circulated zone near the lower wall continues to develop, but the size of this zone decreases gradually as the flow pulsation goes up.

In the final frame 9.6(h), we show the mean streamlines which gives a summary of the flow field over the full time cycle of pulsation. It is interesting to note that there is no re-circulation region near the lower wall, but a large re-circulated zone created inside the aneurysm is permanent where the potential blood clot or thrombosis may occur (Rayz *et al* . [90]).

Fig. 9.7 shows the results of the mean streamwise velocity, $< \bar{v} > /\bar{V}_{max}$, at different axial positions and comparison between the aforementioned two grid arrangements. The agreement between the two grid orientations is excellent for the mean velocity distributions. The velocity at the inlet is parabolic in shape due to the laminar flow. However, inside the aneurysm the velocity profiles take on a slightly deformed parabolic form due to the re-circulations observed earlier. Moreover, the velocity near the upper wall located between $y/L \sim -1.0$ and $y/L \sim 1.0$ is negative because of the adverse pressure gradient. After the aneurysm the velocity profiles take a shape which is different from the parabolic found at the inlet.

The instantaneous and mean pressure distributions at the upper and lower wall are compared in Fig. 9.8. Frame (a) shows that the upper wall pressure is large in the aneurysm region and an extreme rise in pressure occurs just before the end of the aneurysm region. But pressure drops occur at $y/L = 2.0$ where the aneurysm region is over, and the instantaneous pressure takes on an oscillatory form downstream due to the turbulent nature of the flow already seen in Fig. 9.3. Although the instantaneous pressure at the lower wall as seen frame (b) oscillates downstream,

the extreme rise in both the instant and mean pressure occurs just prior to the centre of aneurysm.

The corresponding shear stress distributions are presented in Fig. 9.9. The shear stress at the upper wall is higher inside the aneurysm, but the acute stress drop occurs just prior to the post edge of the aneurysm, followed by the oscillation towards the downstream. On the other hand, the lower wall shear stress inside the aneurysm is smaller than that of the outer region, but it is clearly observed that the upper wall shear stress is always smaller than the stress at lower wall. From the pathological point of view, these high and low shear stresses are harmful for the patient. Salsac [151] reported that platelets may become activated in the regions of high shear stress, and then be transported to the low shear stresses regions where they will accumulate on the wall of the aneurysm, initiating the formation of the endothelial thrombus. Lasheras [14] explained that the high shear stress activates the endothelial mechanism which accelerates the expansion process of the aneurysm and an endoluminal thrombus forms early in the expansion process. This thrombus covers the whole aneurysm's wall and causes the destruction of the endothelial layer by hypoxia-a pathological condition in which a region of the body is deprived of adequate oxygen supply.

9.3.2 Turbulent characteristics

The root mean square (rms) of the velocity turbulent fluctuations, $< u'' >_{rms} /\bar{V}_{max}$, $< v'' >_{rms} /\bar{V}_{max}$ and $< w'' >_{rms} /\bar{V}_{max}$, are represented in Figs. 9.10, 9.11 and 9.12, respectively at the different axial locations. The sensitivity of using the two different sets of grid arrangement on the rms results is not very large, which is acceptable for the turbulent results as already discussed in the previous chapters. In particular, frames (a-r) in Fig. 9.10 show that the u-velocity turbulent fluctuations inside the aneurysm are higher than those of any other locations, so the maximum turbulence occurs inside the aneurysm, which also corresponds to the presence of the strong re-circulations in the aneurysm already seen in Fig. 9.6. However, in frame (h), at position $y/L = 2.0$, where the post segment of the aneurysm ends, the turbulent fluctuations are very low due to the pressure drop at that location. After $y/L = 2.0$, the flow becomes fully developed turbulent.

Figs. 9.11 and 9.12 also show that the maximum turbulent fluctuations occur inside the aneurysm and they are extreme at $y/L = 1.5$. Similarly, at $y/L = 2.0$ the v and w-velocity fluctuations are very small and their magnitudes increase again downstream.

Fig. 9.13 represents the rms of the pressure turbulent fluctuations, $< p'' >_{rms} /\rho \bar{V}^2_{max}$, at the upper wall. The results again clearly show that the maximum pressure fluctuations occur inside the aneurysm. As in velocity fluctuations, the pressure fluctuation drops after the aneurysm segment in between $y/L = 2.0$ and $y/L = 4.5$, followed by the gradual increase downstream. The contour plots of the rms of the velocity and pressure fluctuations are depicted in Fig. 9.14 to show the turbulent region with the magnitudes of the rms results in the mid plane. From this figure, it is seen again that the extreme level of turbulence occurs inside the aneurysm between $y/L = 0.0$ and $y/L = 2.0$.

To further ensure the presence of turbulent flow inside the aneurysm, the energy spectra of the streamwise velocity fluctuations $v''^2/\bar{V}^2_{max}$ along with the straight lines of the Strouhal number $Sr^{-5/3}$ are plotted in Fig. 9.15 at the different positions inside and immediate post region of the aneurysm. In frame (a) of Fig. 9.15, the inertia sub-range region is very small, so the flow is slightly turbulent before the centre of the aneurysm. However, in frames (b-c), at $y/L = 0.0$ and $L = 1.0$, the sub-range region is quite large which further confirms that the flow in this region is turbulent. Towards the downstream of the aneurysm, frames (d-f), the sub-range region decreases as the intensity of turbulent decreases there.

9.4 Conclusion

Large Eddy Simulation with the localized dynamic model of Piomelli and Liu [4] is used to investigate the physiological blood flow in the model of arterial aneurysm for $Re = 2000$, $\alpha = 10.5$ and $A = 0.4$. In this Chapter, it is found that the normalised SGS viscosity is approximately 0.1, which indicates that the SGS contribution is very small. So, the solutions are close to those of a coarse DNS. Inside the aneurysm a large recirculation region is found where the flow gets the negative velocities. The maximum upper wall pressure inside the aneurysm is found after the centre and the pressure drop takes place just at the end of the aneurysm.

The upper wall shear stress inside the aneurysm is smaller than that of the lower wall and the stress drop in the upper wall is strongly correlated with the pressure drop. The extreme turbulent intensity inside the aneurysm occurs after the centre, and because of that, the root mean square of velocities and pressure fluctuations are large inside the aneurysm. Moreover, the energy spectra inside the aneurysm also show the presence of large sub-range region.

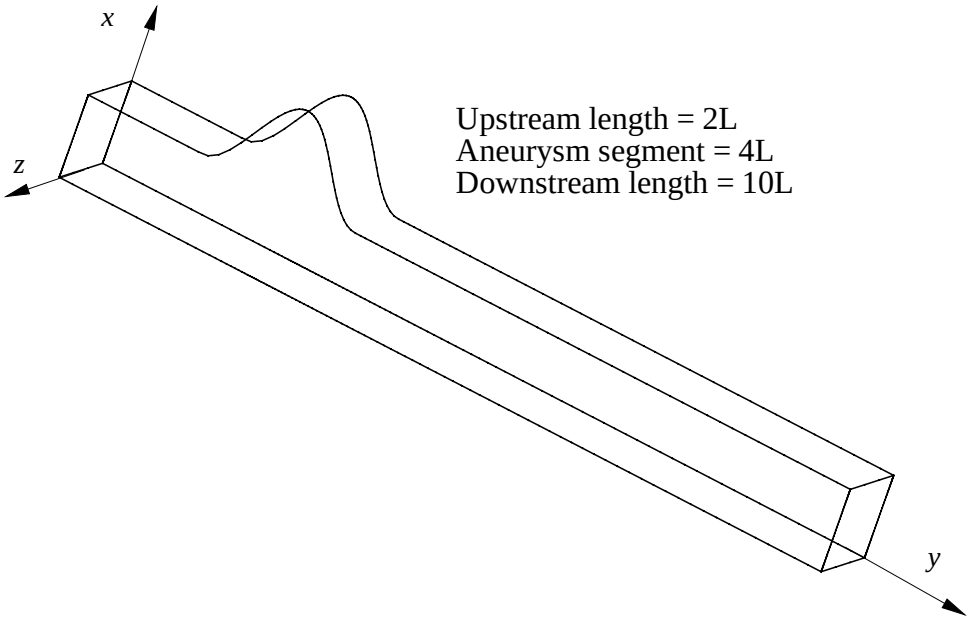

Figure 9.1: A schematic of the model of aneurysm and coordinate system.

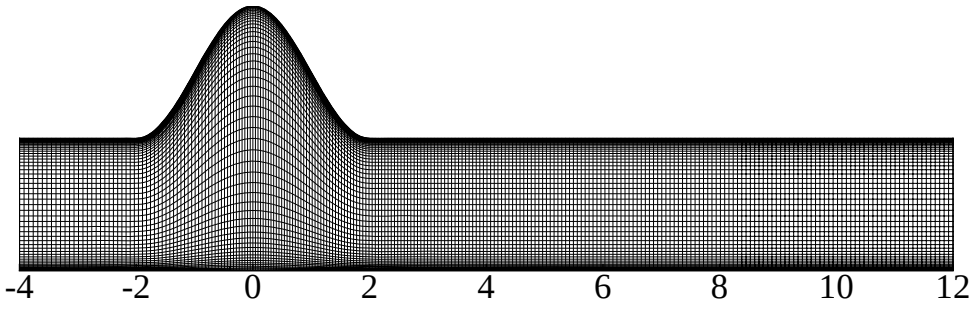

Figure 9.2: A crude mesh distribution on $x - y$ plane.

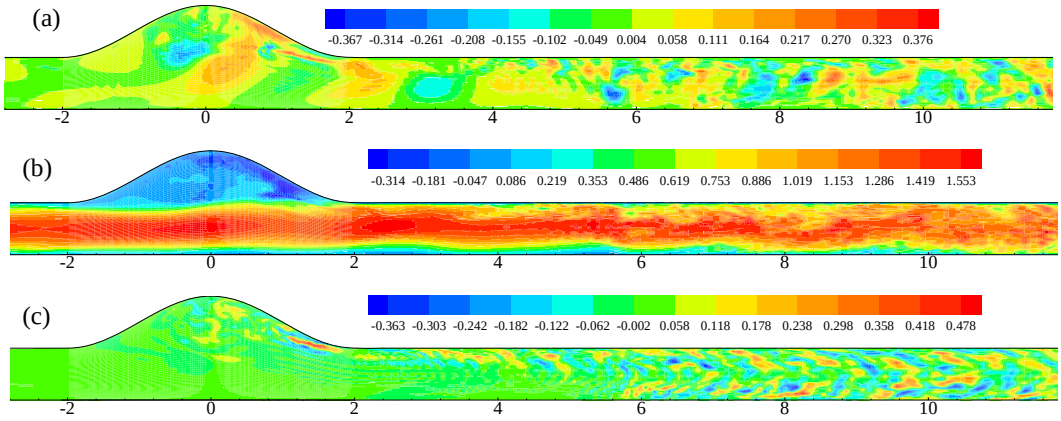

Figure 9.3: Instantaneous velocity: (a) $\bar{u}/\bar{V}_{max}$ (b) $\bar{v}/\bar{V}_{max}$ and (c) $\bar{w}/\bar{V}_{max}$ at $t/T = 10.25$ and $z/L = 0.5$.

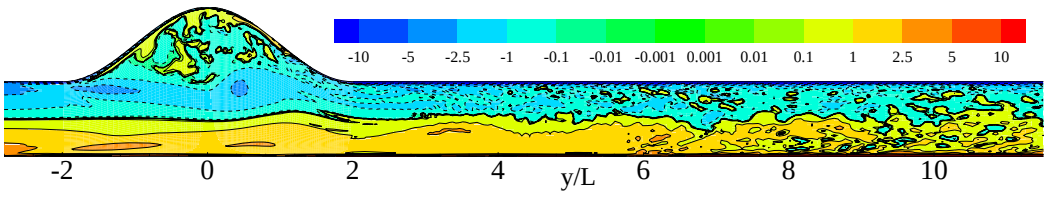

Figure 9.4: Spanwise averaged vorticity, $< \omega_z >_s$, at $t/T = 10.25$.

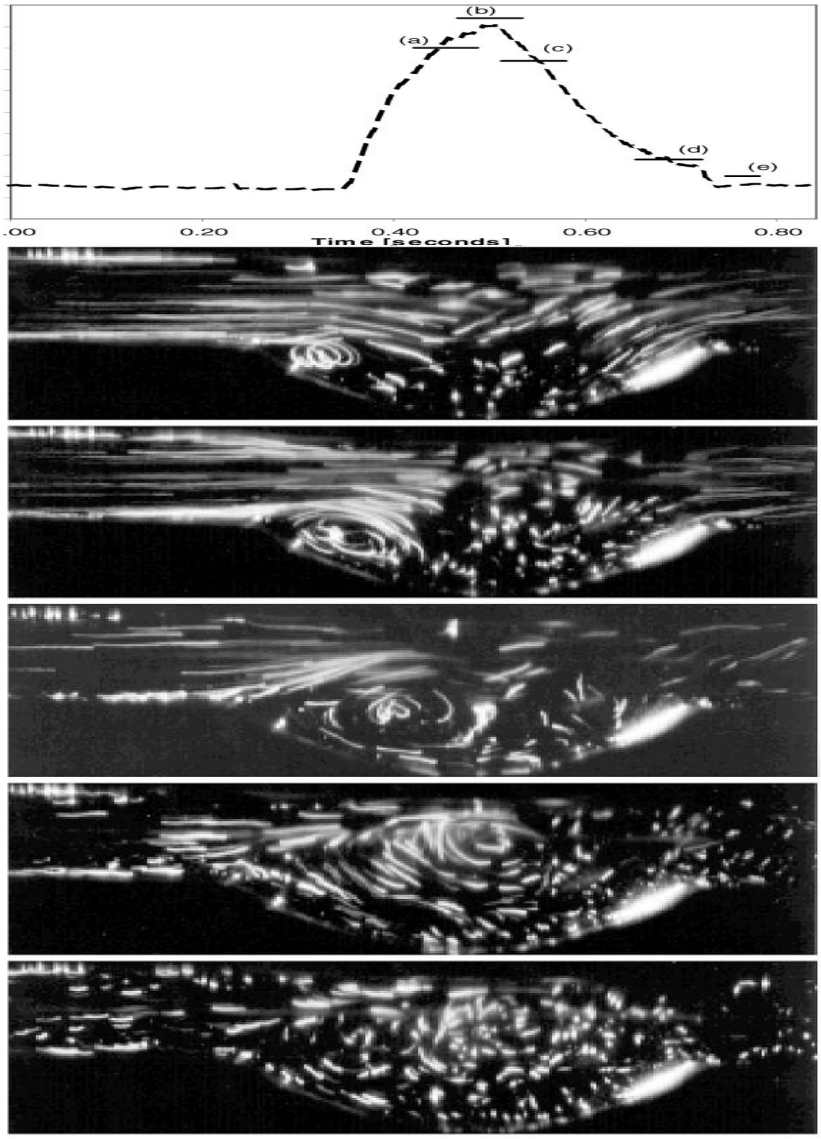

Figure 9.5: Experimental results of Egelhoff *et al* . [5]: flow visualisation photographs in the asymmetric abdominal aortic aneurysm during the (a) early systole, (b) peak systole, (c) mid systole, (d) late systole and (e) early diastole while the peak Reynolds number is 3308.

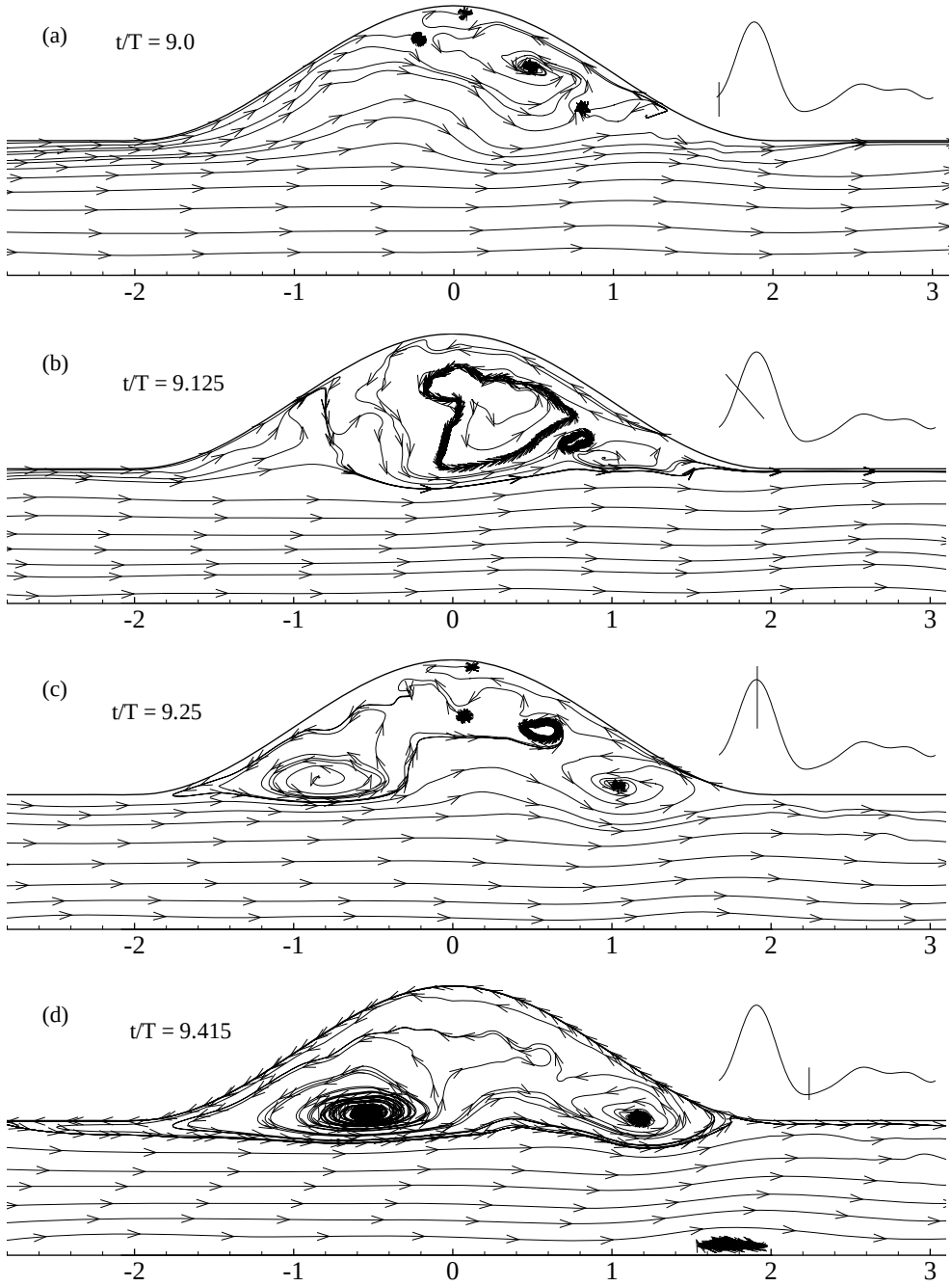

Figure 9.6: Streamlines showing the re-circulation region in the aneurysm at the different phases over a time cycle: (a) $t/T = 9.0$, (b) $t/T = 9.125$, (c) $t/T = 9.25$, (d) $t/T = 9.415$, (e) $t/T = 9.5$, (f) $t/T = 9.625$ and (g) $t/T = 9.75$. Time-mean results are in (h).

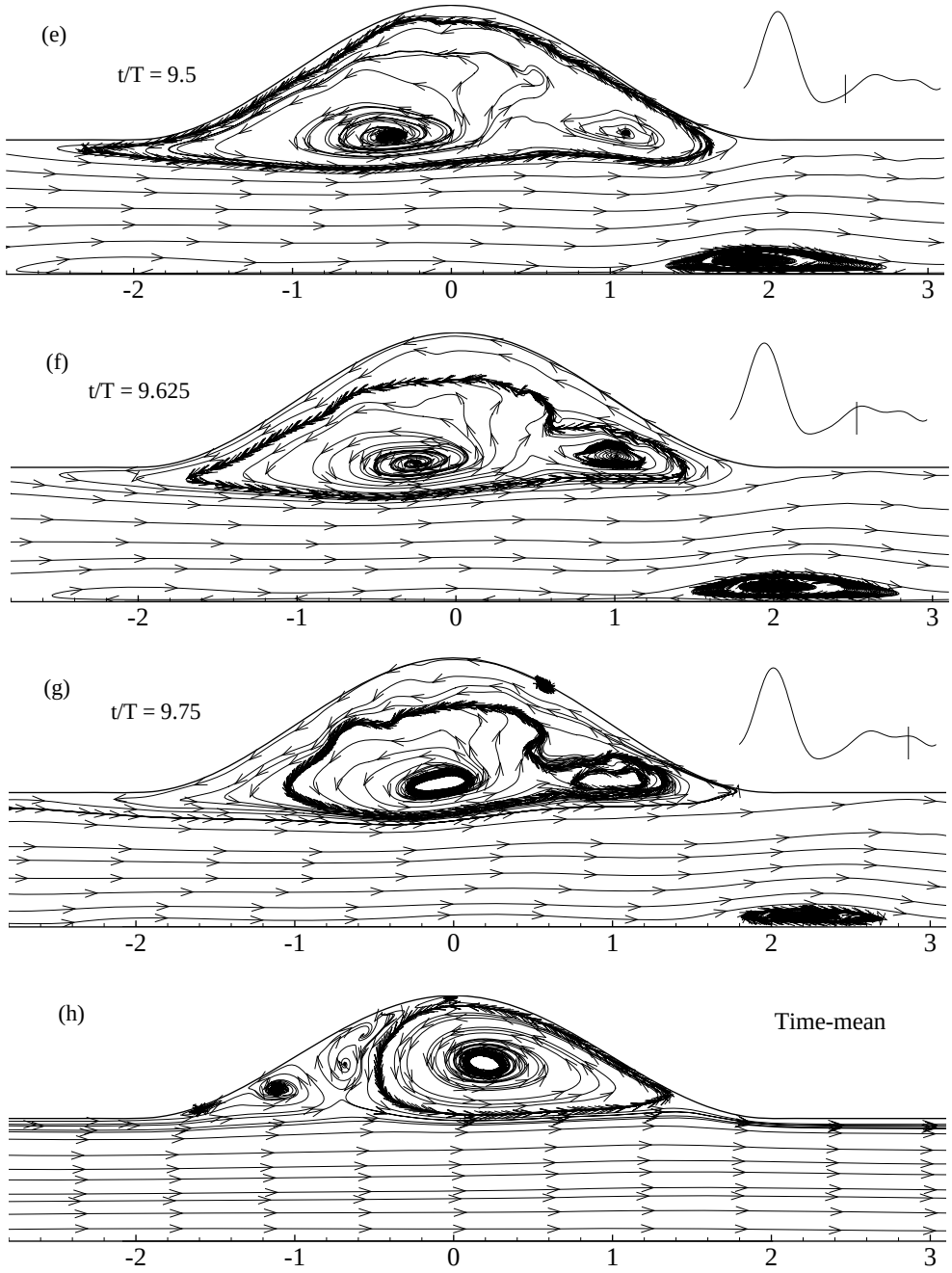

Figure 9.6: (continued)

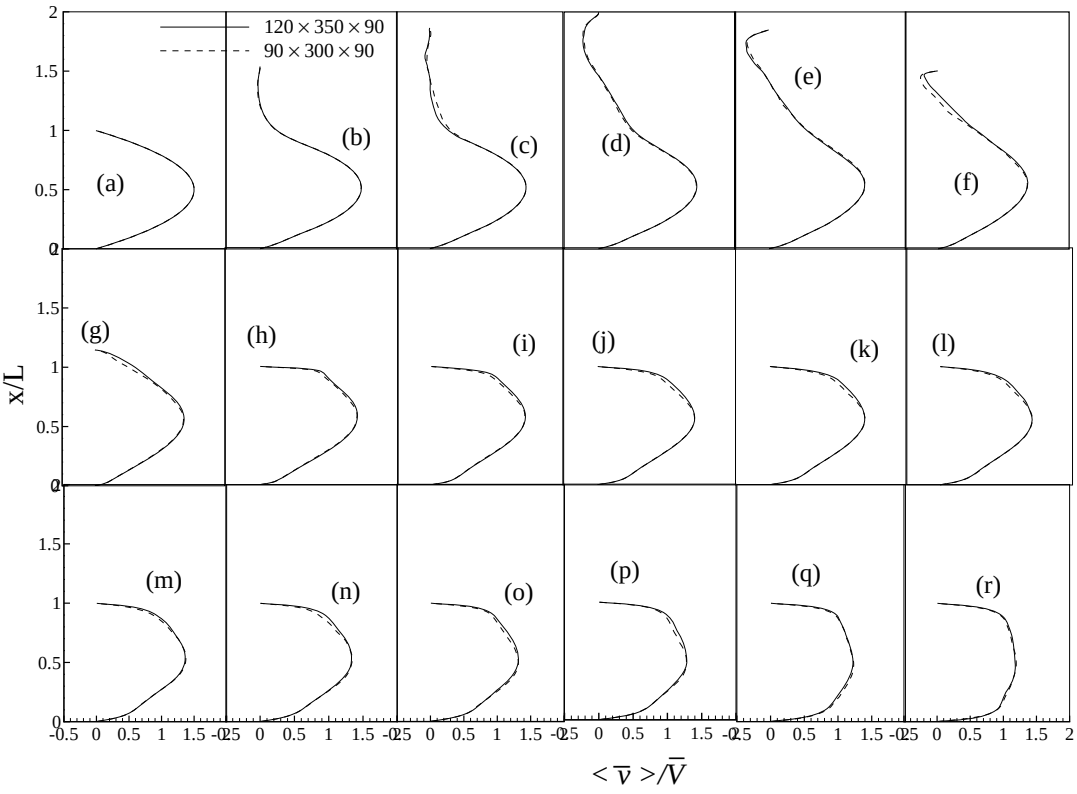

Figure 9.7: Mean streamwise velocity, $< \bar{v} > /\bar{V}$, at $z/L = 0.5$ and different axial locations: (a) $y/L =$ inlet, (b) $y/L = -1.0$, (c) $y/L = -0.5$, (d) $y/L = 0.0$, (e) $y/L = 0.5$, (f) $y/L = 1.0$, (g) $y/L = 1.5$, (h) $y/L = 2.0$, (i) $y/L = 2.5$, (j) $y/L = 3.0$, (k) $y/L = 3.5$ (l) $y/L = 4.0$, (m) $y/L = 5.0$ (n) $y/L = 6.0$, (o) $y/L = 7.0$, (p) $y/L = 8.0$, (q) $y/L = 10.0$ and (r) $y/L =$ outlet.

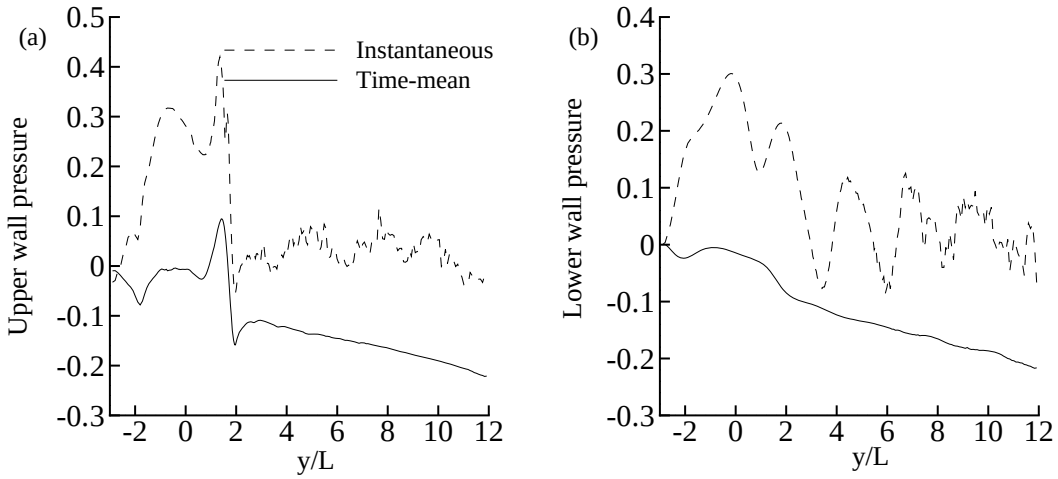

Figure 9.8: Instantaneous and mean pressure in the (a) upper wall and (b) lower wall at $t/T = 10.25$.

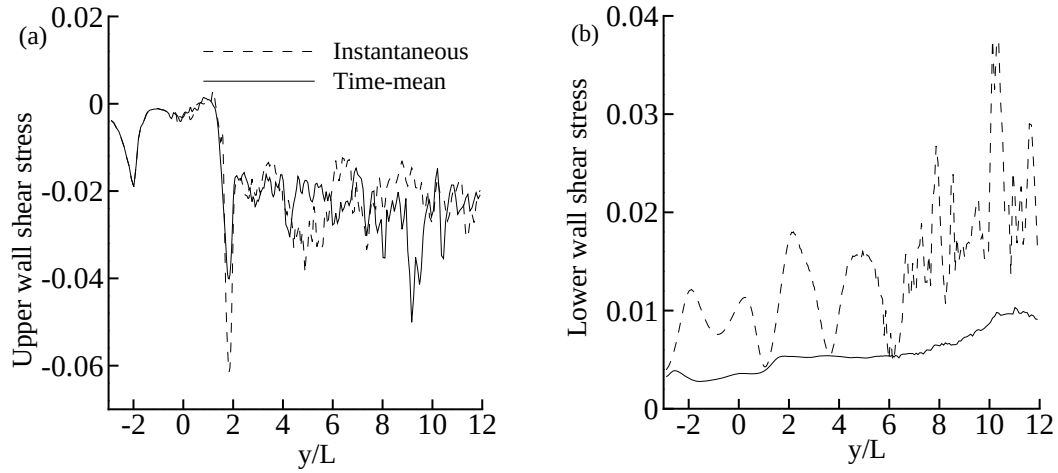

Figure 9.9: Instantaneous and mean shear stress in the (a) upper wall and (b) lower wall at $t/T = 10.25$.

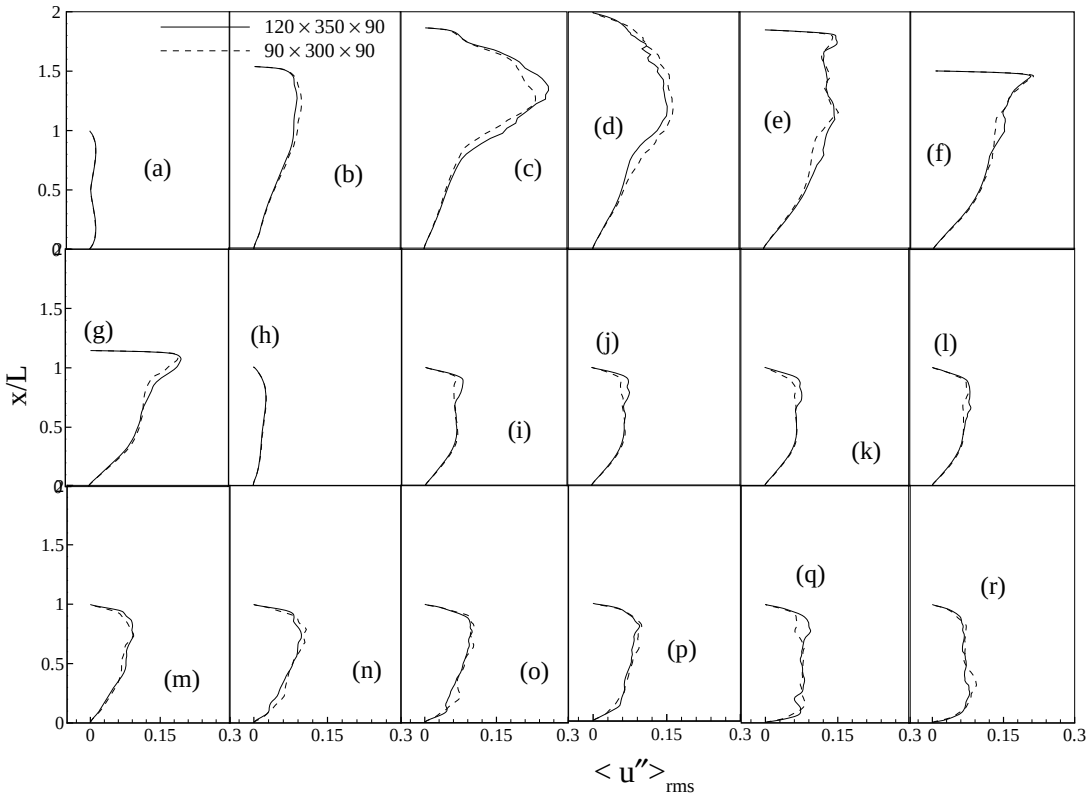

Figure 9.10: rms of the cross-stream velocity fluctuations, $< u'' >_{rms} /\bar{V}_{max}$, at $z/L = 0.5$ and different axial locations: (a) $y/L =$ inlet, (b) $y/L = -1.0$, (c) $y/L = -0.5$, (d) $y/L = 0.0$, (e) $y/L = 0.5$, (f) $y/L = 1.0$, (g) $y/L = 1.5$, (h) $y/L = 2.0$, (i) $y/L = 2.5$, (j) $y/L = 3.0$, (k) $y/L = 3.5$ (l) $y/L = 4.0$, (m) $y/L = 5.0$ (n) $y/L = 6.0$, (o) $y/L = 7.0$, (p) $y/L = 8.0$, (q) $y/L = 10.0$ and (r) $y/L =$ outlet.

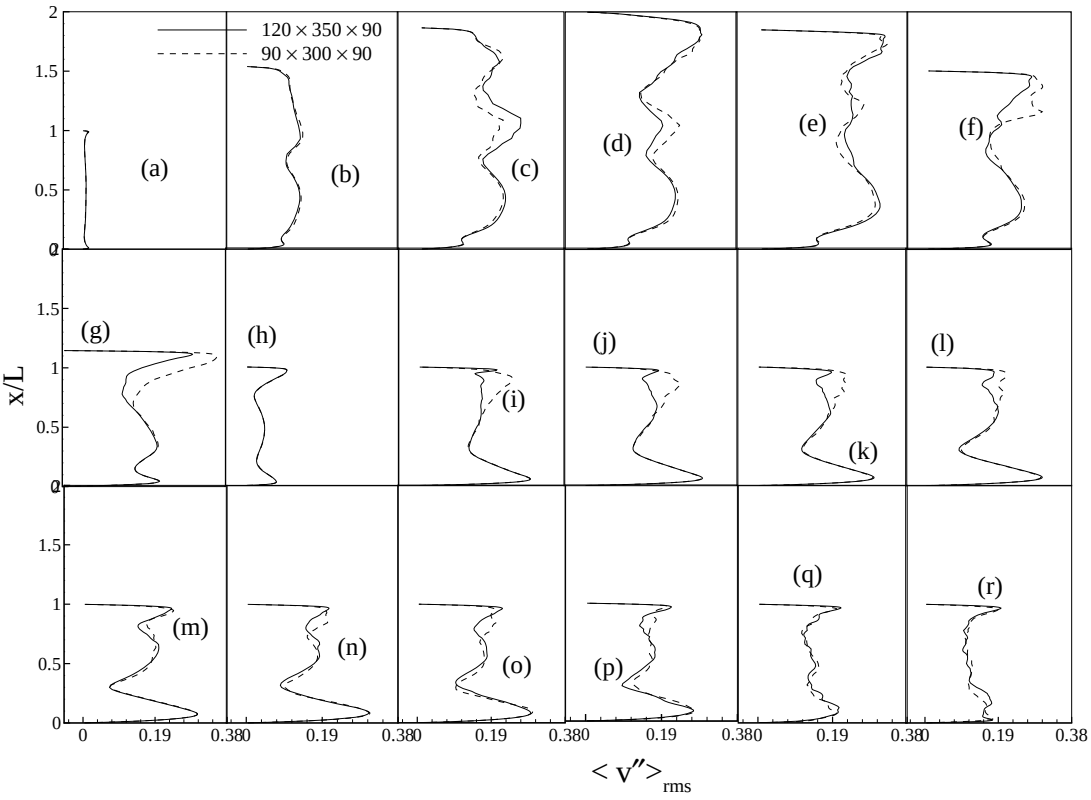

Figure 9.11: rms of the streamwise velocity fluctuations, $< v'' >_{rms} /\bar{V}_{max}$, at $z/L = 0.5$ and different axial locations: (a) $y/L =$ inlet, (b) $y/L = -1.0$, (c) $y/L = -0.5$, (d) $y/L = 0.0$, (e) $y/L = 0.5$, (f) $y/L = 1.0$, (g) $y/L = 1.5$, (h) $y/L = 2.0$, (i) $y/L = 2.5$, (j) $y/L = 3.0$, (k) $y/L = 3.5$ (l) $y/L = 4.0$, (m) $y/L = 5.0$ (n) $y/L = 6.0$, (o) $y/L = 7.0$, (p) $y/L = 8.0$, (q) $y/L = 10.0$ and (r) $y/L =$ outlet.

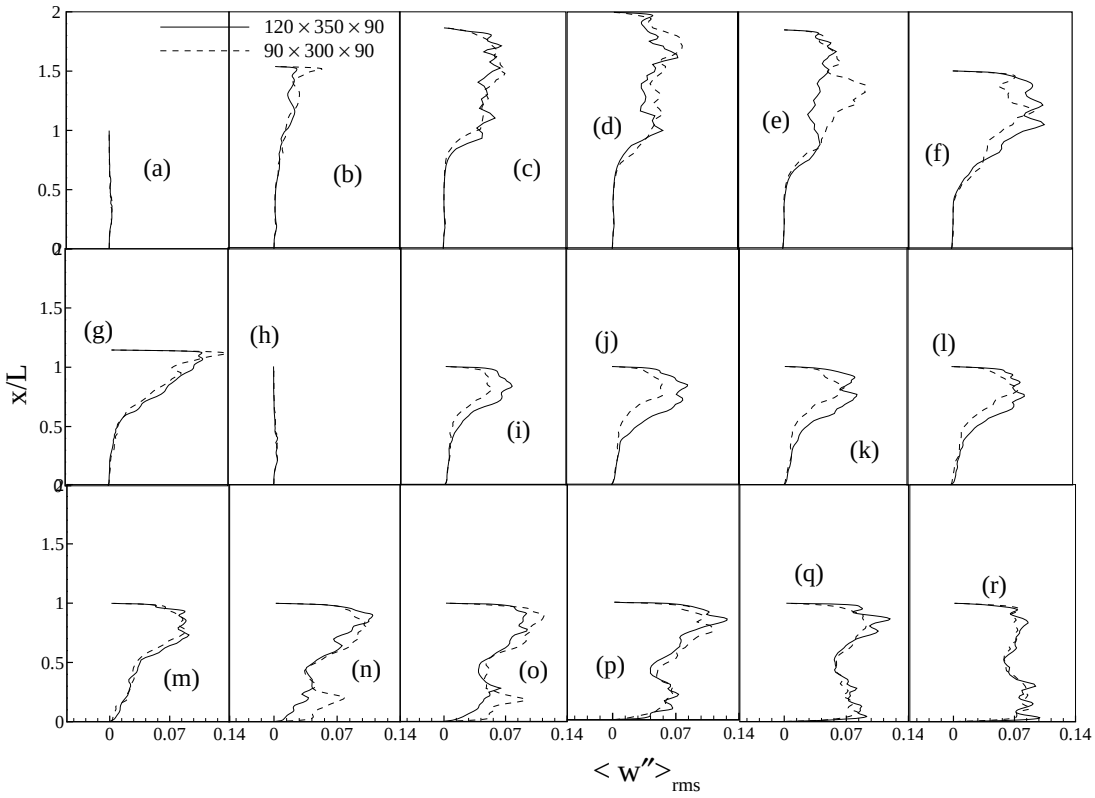

Figure 9.12: rms of the spanwise velocity fluctuations, $< w'' >_{rms} / \bar{V}_{max}$, at $z/L = 0.5$ and different axial locations: (a) $y/L =$ inlet, (b) $y/L = -1.0$, (c) $y/L = -0.5$, (d) $y/L = 0.0$, (e) $y/L = 0.5$, (f) $y/L = 1.0$, (g) $y/L = 1.5$, (h) $y/L = 2.0$, (i) $y/L = 2.5$, (j) $y/L = 3.0$, (k) $y/L = 3.5$ (l) $y/L = 4.0$, (m) $y/L = 5.0$ (n) $y/L = 6.0$, (o) $y/L = 7.0$, (p) $y/L = 8.0$, (q) $y/L = 10.0$ and (r) $y/L =$ outlet.

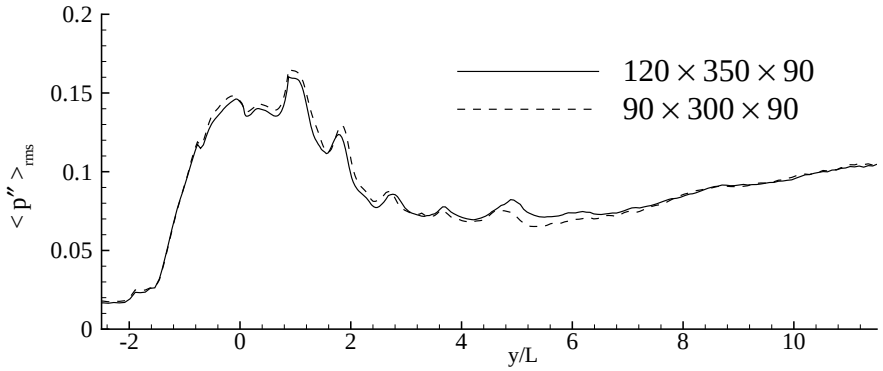

Figure 9.13: rms of the pressure fluctuations, $< p'' >_{rms} / \rho \bar{V}_{max}^2$, at the upper wall.

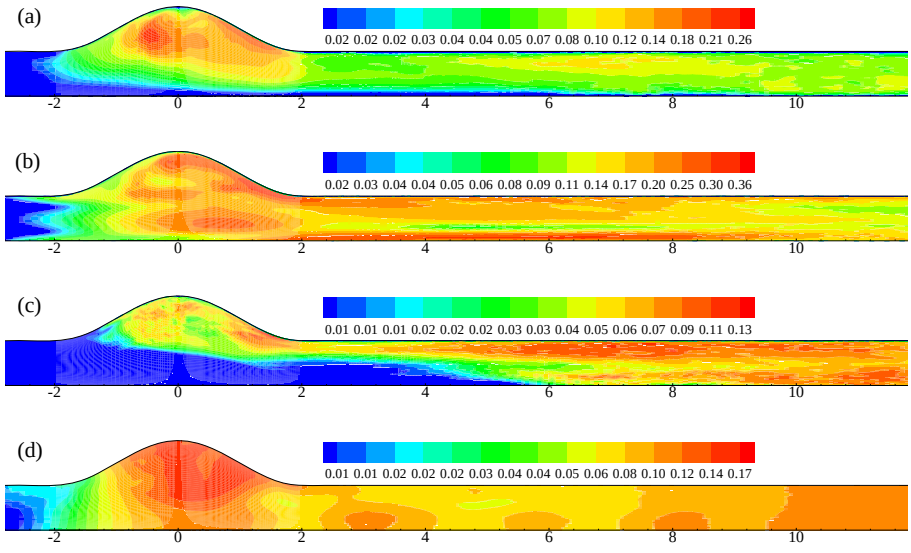

Figure 9.14: Contour plots of the rms of velocity and pressure fluctuations: (a) $< u'' >_{rms} / \bar{V}_{max}$, (b) $< v'' >_{rms} / \bar{V}_{max}$, (c) $< w'' >_{rms} / \bar{V}_{max}$ and (d) $< p'' >_{rms} / \rho \bar{V}_{max}^2$ at $z/L = 0.5$.

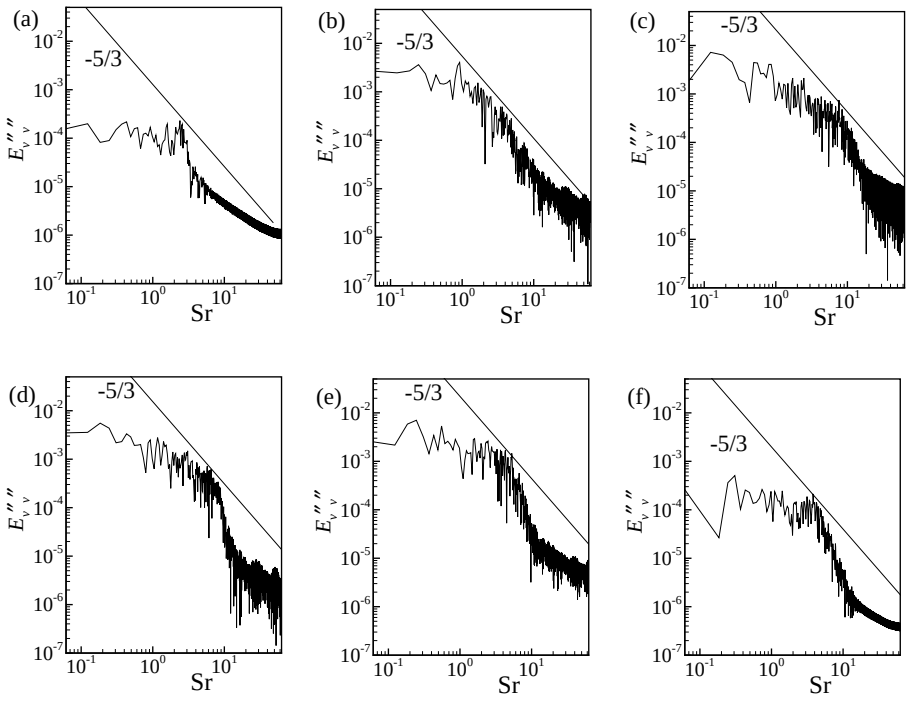

Figure 9.15: Energy spectrum of v'' at (a) $y/L = -1.0$, (b) $y/L = 0.0$, (c) $y/L = 1.0$, (d) $y/L = 2.0$, (e) $y/L = 3.0$ and (f) $y/L = 4.0$.

Chapter 10

Non-Newtonian Physiological Pulsatile Flow in a Model Stenosis

10.1 Introduction

Blood is a non-Newtonian incompressible viscoelastic fluid (Fung [94], pp.53). At a shear rate above about $100\ \text{s}^{-1}$, the blood viscosity tends towards an asymptotic value, μ_∞; but if the shear rate falls below that asymptotic level, the viscosity of blood increases and non-Newtonian properties are exhibited by blood (Berger and Jou [95]). Moreover, when the shear rate drops below $10\ \text{s}^{-1}$ the effect of the non-Newtonian viscosity is quite prominent (Huang *et al* . [152]).

In the previous chapters, the investigation was done by assuming that blood is a Newtonian fluid with constant viscosity. However, we have recently re-examined the data of the shear rate in Chapter 7 and found that the global maximum shear rate during some periods in a time cycle becomes less that $100\ \text{s}^{-1}$, as shown in Fig. 10.1. So, to gain more accurate insight on the transition-to-turbulent post stenotic flow phenomena account must be taken in the computation for the non-Newtonian nature of the fluid.

The model of stenosis in this Chapter remains the same as was used in Chapter 4 (Fig. 4.1). Large Eddy Simulation technique is applied to study the transition of the physiological pulsatile non-Newtonian blood flow in the model by using five different blood viscosity models: (i) Power-law (ii) Carreau (iii) Quemada (iv) Cross and (v) modified-Casson model.

The mesh arrangement in the simulation is taken as $50 \times 200 \times 50$ (Case 1 of Chapter 7) for $Re = 2000$. The results obtained by the various non-Newtonian

blood viscosity models are compared with those of the Newtonian blood viscosity model presented in Chapter 7 for the fourth harmonic of the physiological pressure pulse.

10.2 Filtered Governing Equations

The filtered Navier-Stokes equations of motion for the non-Newtonian fluid flow may be written as

$$\frac{\partial \bar{u_j}}{\partial x_j} = 0, \tag{10.1}$$

$$\frac{\partial \rho \bar{u_i}}{\partial t} + \frac{\partial \rho \bar{u_i} \bar{u_j}}{\partial x_j} = -\frac{\partial \bar{p}}{\partial x_i} + \frac{\partial}{\partial x_j}\left[\mu(|\dot{\gamma}|)\left(\frac{\partial \bar{u_i}}{\partial x_j} + \frac{\partial \bar{u_j}}{\partial x_i}\right)\right] - \frac{\partial \tau_{ij}}{\partial x_j}. \tag{10.2}$$

Here $\mu(|\dot{\gamma}|)$ is the blood viscosity which depends on the shear rate, $\dot{\gamma}_{ij} = \frac{1}{2}\left(\frac{\partial \bar{u_i}}{\partial x_j} + \frac{\partial \bar{u_j}}{\partial x_i}\right)$, and the magnitude of the shear rate is defined as $|\dot{\gamma}| = \sqrt{2\dot{\gamma}_{ij}\dot{\gamma}_{ji}}$ (Tu and Delville [97], Barth *et al* . [153], and Miranda *et al* . [154]). In the Newtonian model, $\mu(|\dot{\gamma}|)$ tends to a constant value for the blood viscosity which is denoted by μ_∞. But for the non-Newtonian models the relations between the viscosity and shear rate are presented in the section below. The subgrid-scale term is modelled using the Piomelli-Liu [4] localized dynamic model.

10.3 Non-Newtonian Blood Viscosity Model

Five different widely used non-Newtonian constitutive relationships for the blood viscosity model depending on the shear rate are given below.

10.3.1 Power-law Model

The Power-law model was proposed by Wlaburn and Schneck [155]. The model takes into account of the haemotocrit which is the volume percentage of red blood cells in whole blood. The viscosity model is given by

$$\mu(|\dot{\gamma}|) = k|\dot{\gamma}|^{n-1}, \tag{10.3}$$

where $k = 14.67 \times 10^{-3}$ and $n = 0.7755$ are the model constants.

10.3.2 Carreau Model

Carreau [156] proposed a four-parameter non-Newtonian viscosity model which is known as the Carreau model. The viscosity model is given by

$$\mu(|\dot{\gamma}|) = \mu_\infty + (\mu_0 - \mu_\infty)[1 + (\lambda\dot{\gamma})^2]^{(n-1)/2}, \tag{10.4}$$

where $\mu_0 = 0.056$ Pa.s is the blood viscosity at zero shear rate, $\lambda = 3.131$ is the time constant associated with the viscosity that changes with the shear rate, and $n = 0.3568$.

10.3.3 Quemada Model

This model was developed by Quemada [157] to predict the viscosity of concentrated systems, which is based on the shear rate and haematrocrit. The viscosity model is given by

$$\mu(|\dot{\gamma}|) = \mu_p \left(1 - \frac{1}{2}\frac{k_0 + k_\infty\sqrt{|\dot{\gamma}|/\gamma_c}}{1 + \sqrt{|\dot{\gamma}|/\gamma_c}}\phi\right)^{-2}, \tag{10.5}$$

where $\mu_p = 1.2 \times 10^{-3}$ Pa.s is the viscosity of plasma and for haematocrit $\phi = 0.45$. The values of the model parameters are $\gamma_c = 1.88\text{s}^{-1}$, $k_\infty = 2.07$ and $k = 4.33$.

10.3.4 Cross Model

Cross [158] proposed a shear rate dependent viscosity model which is known as the Cross model. The viscosity model is given by

$$\mu(|\dot{\gamma}|) = \mu_\infty + \frac{(\mu_0 - \mu_\infty)}{\left[1 + \left(\frac{\dot{\gamma}}{\dot{\gamma}_c}\right)^n\right]}, \tag{10.6}$$

where $\mu_0 = 0.0364$ Pa.s is the blood viscosity at very low shear rate, $\gamma_c = 2.63\text{s}^{-1}$ is the reference shear rate and $n = 1.45$ is the model constant.

10.3.5 Modified Casson Model

The Casson model was originally introduced in Casson [159] for the prediction of the flow behaviour of pigment-oil suspension. The Casson viscosity model is given by

$$\mu(|\dot{\gamma}|) = \frac{\left[\sqrt{\tau_0} + \sqrt{\eta_c \dot{\gamma}}\right]^2}{\dot{\gamma}}. \tag{10.7}$$

However, Merrill *et al* . [160] found that the rheological properties of human blood were consistent with the Casson model at shear rates of $0.1 - 1.0$ s^{-1}, but deviated to some extent in the range of $1 - 40$ s^{-1}. Bate [161] believed that the blood flow through tubes is best described by the Casson model in the shear rate range of $15 - 6400$ s^{-1}. Therefore, for large-diameter vessels, like arteries, a modified and more-general Casson model was formulated by Gonzalez and Moraga [162] as

$$\mu(|\dot{\gamma}|) = \left(\sqrt{\eta_c} + \frac{\sqrt{\tau_0}}{\sqrt{\lambda} + \sqrt{\dot{\gamma}}}\right), \tag{10.8}$$

where $\eta_c = 3.45 \times 10^{-3}$ Pa.s is the Casson viscosity, $\tau_0 = 2.1 \times 10^{-2}$ s^{-1} is the yield stress and $\lambda = 11.5$ s^{-1} is a constant when the shear rate tends to zero.

10.4 Results and Discussion

The relationship between the apparent shear rates and viscosity for the above mentioned five non-Newtonian blood viscosity models along with the Newtonian viscosity model is presented in Fig. 10.2. From this figure, it is seen that for low shear rates (e.g. < 100s^{-1}) the non-Newtonian blood viscosity is higher than that of the Newtonian model. In the Newtonian model the viscosity is constant which is shown by the solid line.

The Power-law model shows that the blood viscosity at the low shear rates increases but decreases at large shear rates. The limitation of the Power-law model is that it fails to describe the viscosity of blood at very low and higher level of shear rates. In the Carreau and modified-Casson models the viscosity tends to the asymptotic constant viscosity μ_∞ at the shear rate $\dot{\gamma} > 10^4$. The Quemada and Cross models exhibit the non-Newtonian properties of blood at shear rate $\dot{\gamma} < 10^2$.

Moreover, in the Cross model the viscosity asymptotically matches the constant viscosity at the shear rates $\dot{\gamma} > 10^2$ but the Quemada model shows the asymptotic nature below the constant viscosity μ_∞.

Milnor [163] argued that the blood viscosity using the above mentioned viscosity models becomes infinite at the very lowest rate of shear, which is impossible in the practical sense. To get the true effect of the non-Newtonian blood viscosity, following Johnston *et al* . [101], the lowest shear rate used in the whole computation is 0.1s^{-1} (see Fig. 10.2). The necessity for using the non-Newtonian model is made clear by observing the range of global maximum shear rate $|\dot{\gamma}|$ plotted in Fig. 10.3 and 10.4 for the different models. From all the figures it is seen that the global maximum shear rates lie in the range of non-Newtonian shear rate, $\dot{\gamma} < 10^2$, during some part of the time cycle the non-Newtonian properties of blood are important.

Fig. 10.5 depicts the post-stenotic re-circulation zone in terms of the mean streamlines for the different models. From this figure, it can be seen that the length of the re-circulation region is enlarged in the non-Newtonian models, which is an alarming condition at the pathological point of view, since the blood in the re-circulation region is re-circulated for a long time and stagnant in this region which could cause the blood clot or thrombosis.

The mean shear stress, $\tau_{xy}/\rho\bar{V}^2_{max}$, distributions are plotted in Fig. 10.6(a-c) respectively at the upper wall, centreline and lower wall. At the upper wall the stress drop is higher in the case of non-Newtonian model than that of the Newtonian model and the maximum stress drop is found in the Power-law model. The magnitude of this stress drop is -0.07730 which is about 32% higher than the Newtonian model for which it is -0.05869. Interestingly, the stress drop in all the models occurs at a same streamwise location, $y/L = -0.12505$. The difference between the non-Newtonian and Newtonian models of the shear distribution is distinguishable in the post-stenotic turbulent region. However, in the laminar region the differences are very small. Moreover, further downstream region the upper wall shear stresses for non-Newtonian models are always smaller than the case of Newtonian model.

At the centreline the shear stress drops located at $y/L = 0.78$ are higher for the non-Newtonian models. At the centreline, the largest stress drop occurs in the Carreau model with a magnitude of -0.01136 and the corresponding smallest value of the stress drop for the Newtonian model is -0.00287. On the other hand, the

maximum shear stress at the lower wall occurs at $y/L = -0.059$ for all the models, but the largest value is found for the Power-law model which is 0.04989. In contrast to the upper wall, the non-Newtonian models give higher shear stress at the lower wall in the further downstream region.

Fig. 10.7(a-c) depict the mean pressure, $\bar{p}/\rho\bar{V}^2_{max}$, at the upper wall, centreline and at the lower wall respectively. From these figures, it can be seen again that the differences in the pressure distributions between the Newtonian and non-Newtonian models are clearly visible, but among the non-Newtonian models the differences are very small. The pressure drop at the throat of the stenosis is slightly higher in the case of the Newtonian model than in the case of non-Newtonian models. Further downstream the pressure for the non-Newtonian models is higher than the case of Newtonian model.

Fig. 10.8(a-b) illustrates the centreline mean kinetic energy (MKE), $\frac{1}{2} < \bar{u}_j\bar{u}_j > /\bar{V}^2_{max}$, and the turbulent kinetic energy (TKE), $\frac{1}{2} < u''_j u''_j > /\bar{V}^2_{max}$, for the different models. In frame (a), the MKE is almost identical at the upstream of the stenosis for all the models, where the flow is laminar. At the turbulent region ($1.0 \leq y/L \leq 6.0$) the MKE varies in the non-Newtonian models with magnitude that is slightly higher in the Carreau and Quemada models compared to the Newtonian model. Significant effects are reported on the results of the turbulent kinetic energy in frame (b). The peak of TKE in the post-stenotic region ($1.0 < y/L < 3.0$) occurs in the Newtonian model, while all the non-Newtonian models produce higher TKE downstream ($3.0 < y/L < 9.0$) because of the fact that the physiological oscillation which is reduced by the high viscosity in the non-Newtonian models causes delay in the transition process. Interestingly, this result compares well with that of Chapter 4 (Fig. 4.26) that the transition to turbulent happens earlier when the percentage of oscillation is increased.

Due to the effects of the non-Newtonian blood viscosity the flow field also varies significantly which is clearly shown in Figs. 10.9 in terms of the streamwise velocity, $\bar{v}/\bar{V}_{max}$, at the different post-stenotic streamwise locations, $y/L = 1.0$ and 2.0, over the last two time periods.

The numerical values of the global maximum Smagorinsky dynamic constant C_s, the normalised SGS viscosity μ_{sgs}/μ, and the streamwise velocity $\bar{v}/\bar{V}_{max}$ for the different non-Newtonian models along with Newtonian model are compared in

Table 10.1: Global maximum values of C_s and the normalised SGS viscosity μ_{sgs}/μ for the different models at $t/T = 10.25$.

Model	C_s	x/L	y/L	z/L	μ_{sgs}/μ	x/L	y/L	z/L
Newtonian	0.12	0.58	1.85	0.67	0.97	0.70	2.44	0.78
Power-law	0.14	0.23	2.81	0.43	0.81	0.79	2.44	0.43
Carreau	0.12	0.58	2.37	0.02	0.72	0.58	2.37	0.02
Quemada	0.13	0.70	2.37	0.28	0.95	0.70	2.37	0.27
Cross	0.12	0.62	2.72	0.35	0.66	0.62	2.72	0.35
Mod-Casson	0.12	0.62	2.51	0.39	0.84	0.54	2.51	0.39

Table 10.2: Global maximum values of streamwisee velocity $\bar{v}/\bar{V}_{max}$ for the different models at $t/T = 10.2$.

Model	$\bar{v}/\bar{V}_{max}$	x/L	y/L	z/L
Newtonian	2.81343	0.37	2.11	0.22
Power-law	2.54959	0.58	2.58	0.43
Carreau	2.38454	0.42	2.88	0.02
Quemada	2.53122	0.42	2.73	0.12
Cross	2.39409	0.42	2.51	0.18
Mod-Casson	2.50988	0.54	2.80	0.35

Tables 10.1 and 10.2, respectively. From Table 10.1, it is seen that the maximum values of C_s for the non-Newtonian models are found in the post stenotic region between $2.0 < y/L < 3.0$ but for the Newtonian model the maximum C_s lies between $1.0 < y/L < 2.0$. On the other hand, the maximum values of μ_{sgs}/μ and $\bar{v}/\bar{V}$ occur in the post-stenotic region between $2.0 < y/L < 3.0$ and the magnitude of these quantities are smaller in the non-Newtonian cases than the Newtonian case.

10.5 Conclusion

Non-Newtonian physiological flow in a model arterial stenosis has been investigated by using the LES technique. The global maximum shear rate for the different viscosity models lies in the non-Newtonian ranges, which means less than 100s^{-1}, which clearly indicates the necessity of using the non-Newtonian blood viscosity

model in the investigation.

The results show that for the non-Newtonian models the global maximum SGS viscosity and the streamwise velocity are smaller than the Newtonian model and the post-stenotic re-circulation region extends slightly further for the non-Newtonian models, which increases the possibility of blood clot or thrombosis.

The maximum and minimum wall stresses occur for the non-Newtonian models at the lower and upper walls respectively and the pressure drop is slightly smaller in the case of non-Newtonian models. The peak turbulent intensity is higher for the Newtonian model, but in the non-Newtonian model it is higher in the further downstream region than the Newtonian model. Overall, the flow distribution is significantly changed due to the non-Newtonian nature of the blood.

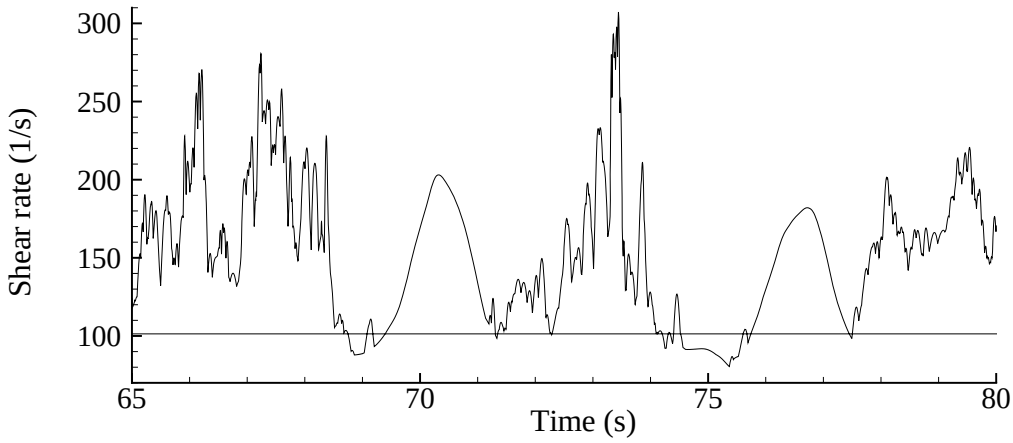

Figure 10.1: Global maximum shear rate $|\dot{\gamma}|$ against time for the Newtonian model while $Re = 2000$.

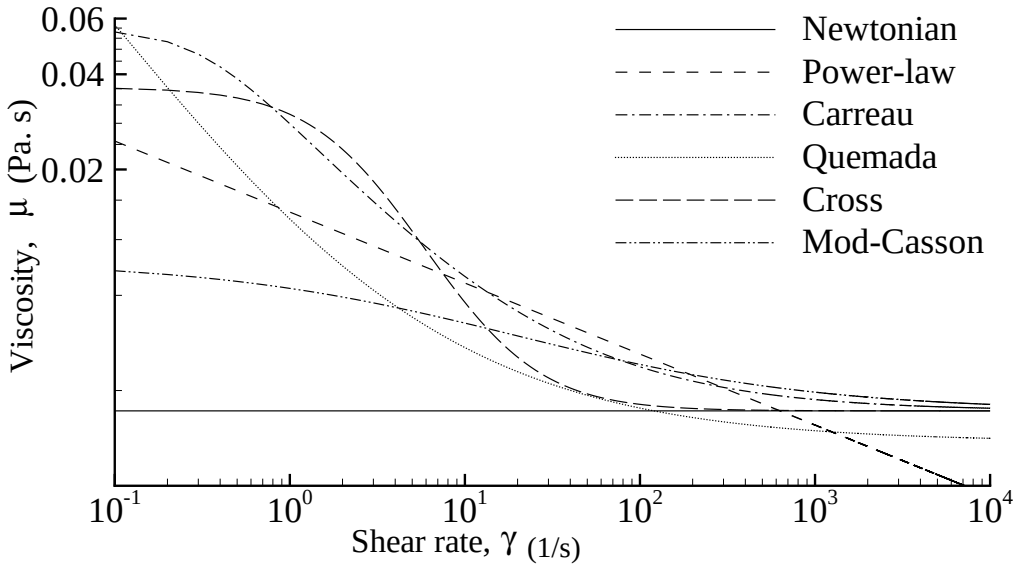

Figure 10.2: Relations between the shear rate and the apparent blood viscosity for the different models.

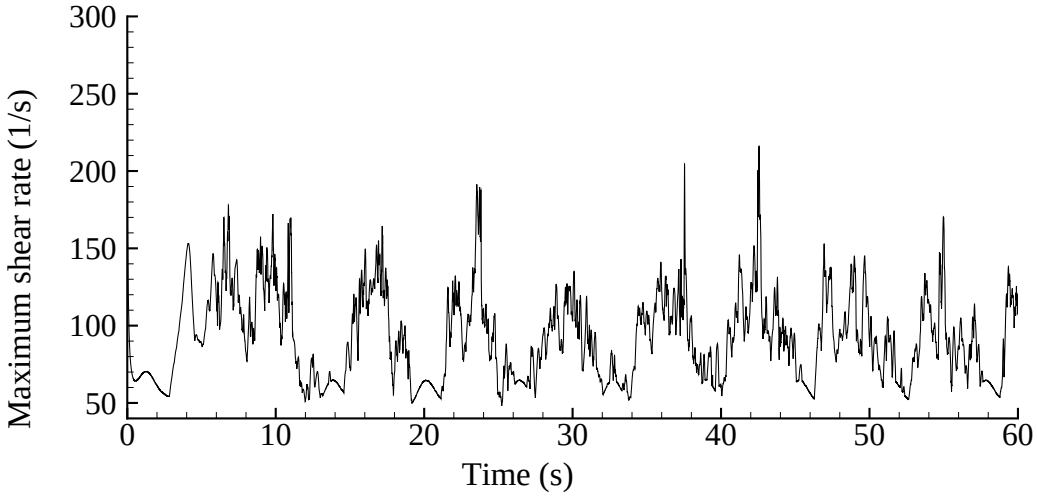

Figure 10.3: Global maximum shear rate $|\dot{\gamma}|$ against time for the Power-law model.

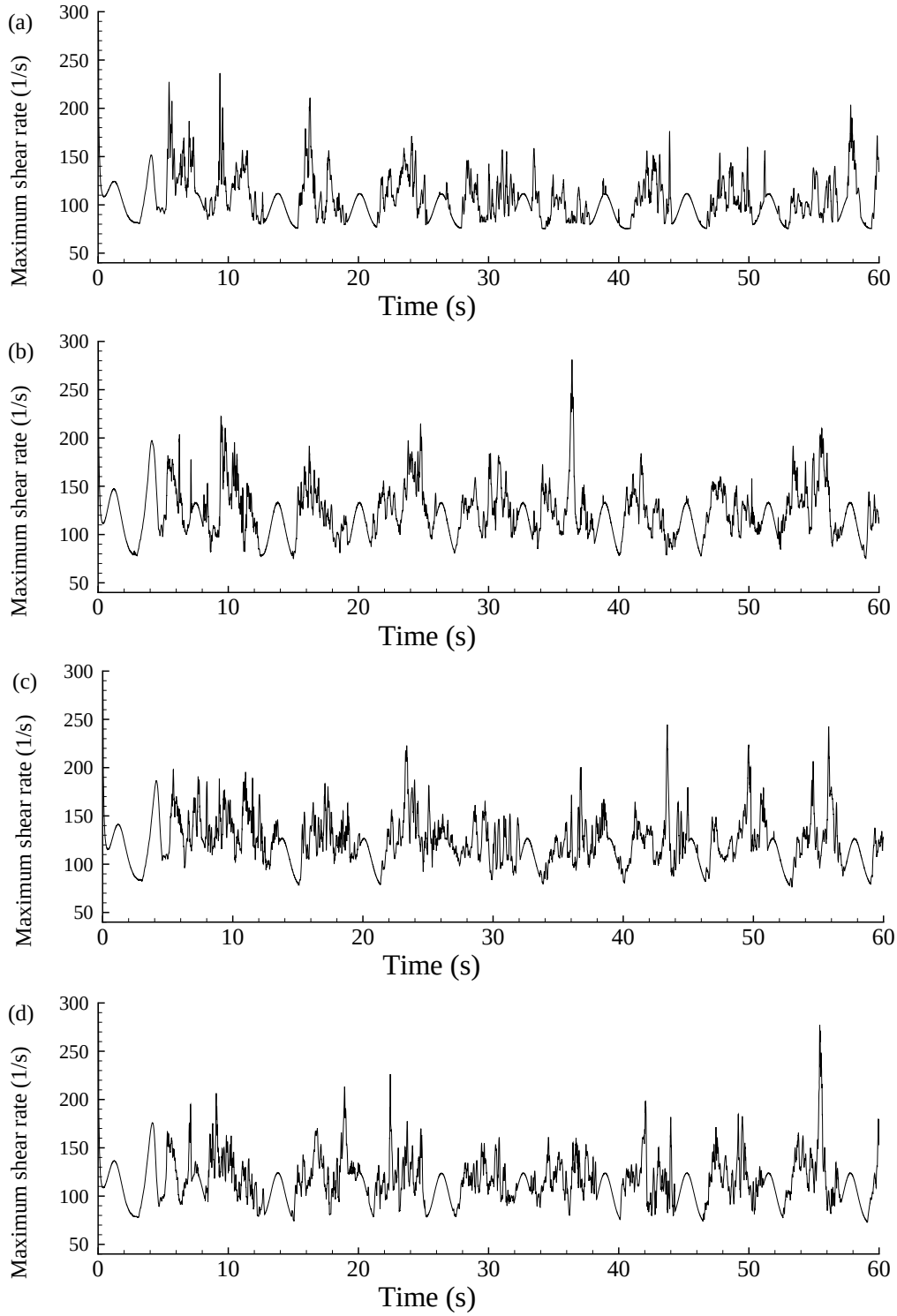

Figure 10.4: Global maximum shear rate $|\dot{\gamma}|$ against time for (a) Carreau (b) Quemada (c) Cross and (d) modified-Casson models.

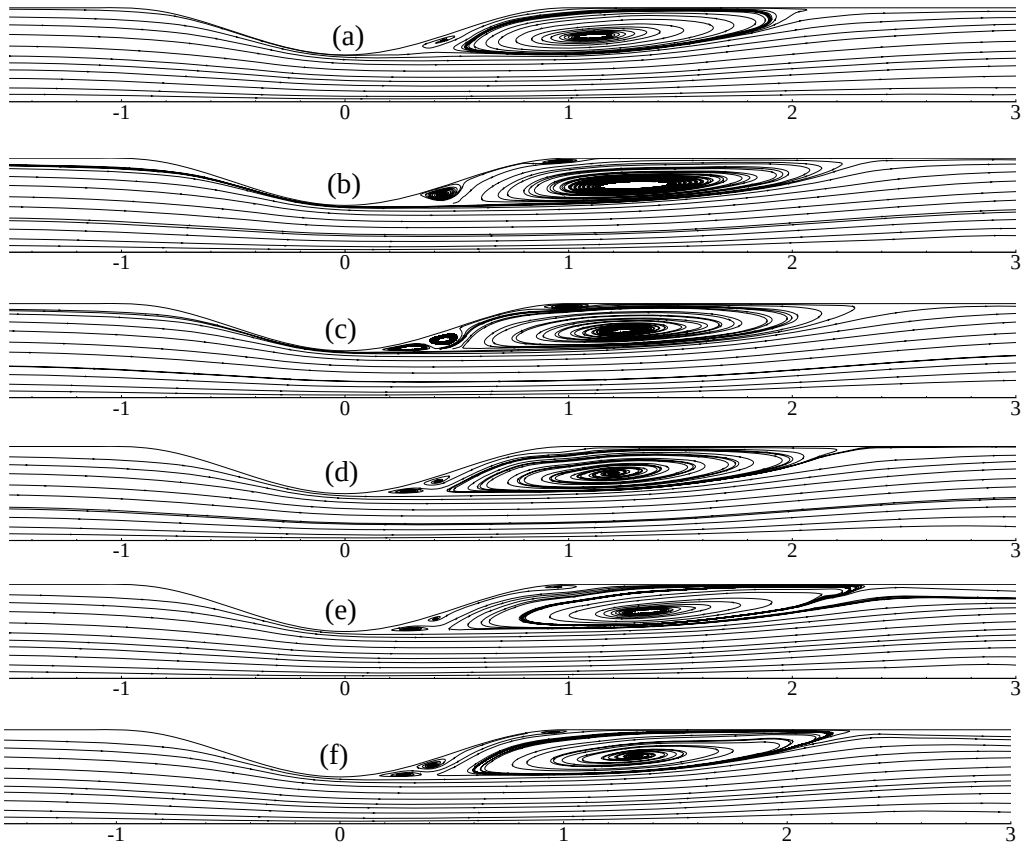

Figure 10.5: Mean post-stenotic recirculation zone, (a) Newtonian (b) Power-law (c) Carreau (d) Quemada (e) Cross and (f) modified-Casson models.

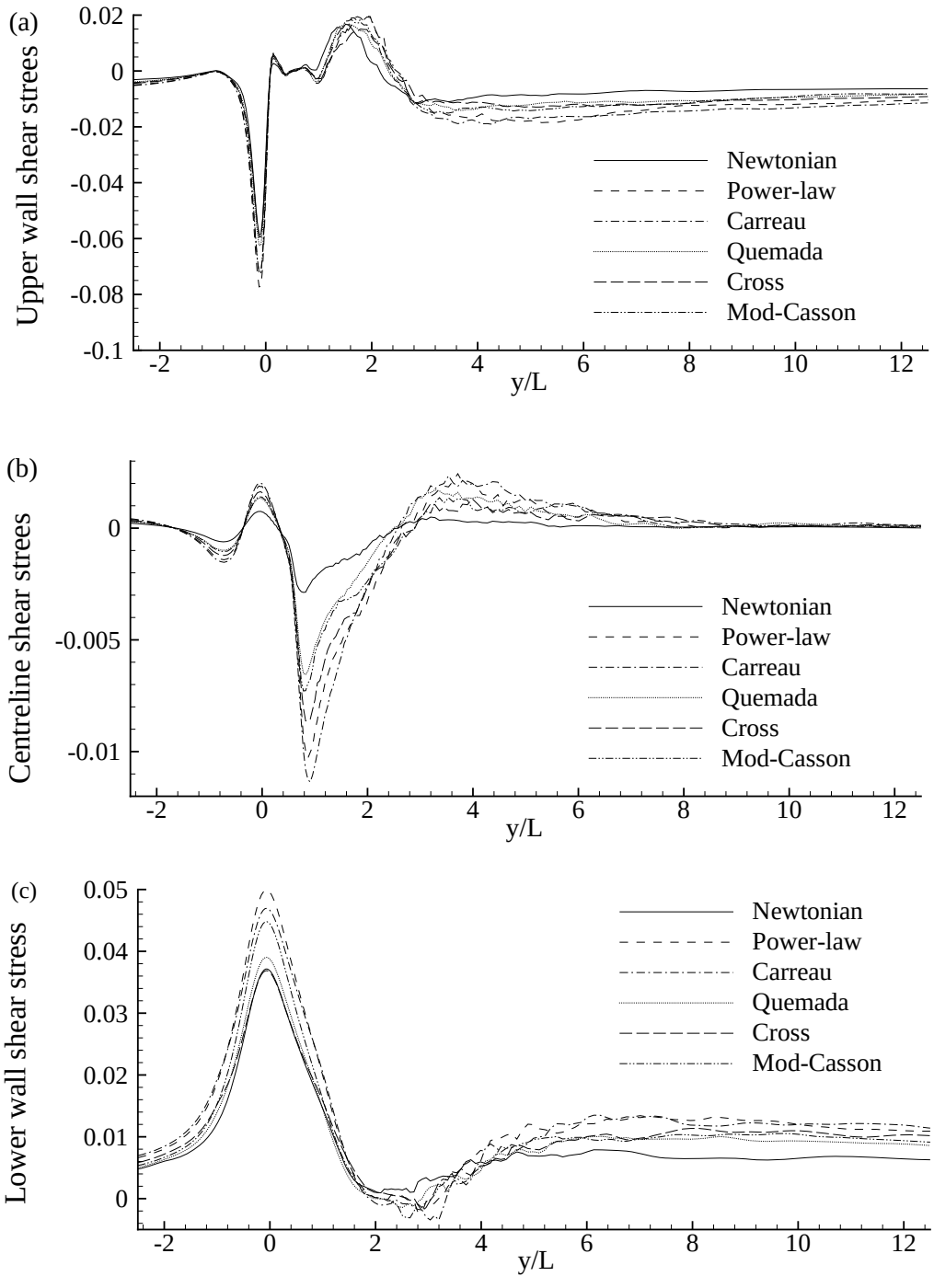

Figure 10.6: Mean shear stress, $\tau_{xy}/\rho\bar{V}_{max}^2$, at the (a) upper wall (b) centreline and (c) lower wall for the different blood viscosity models.

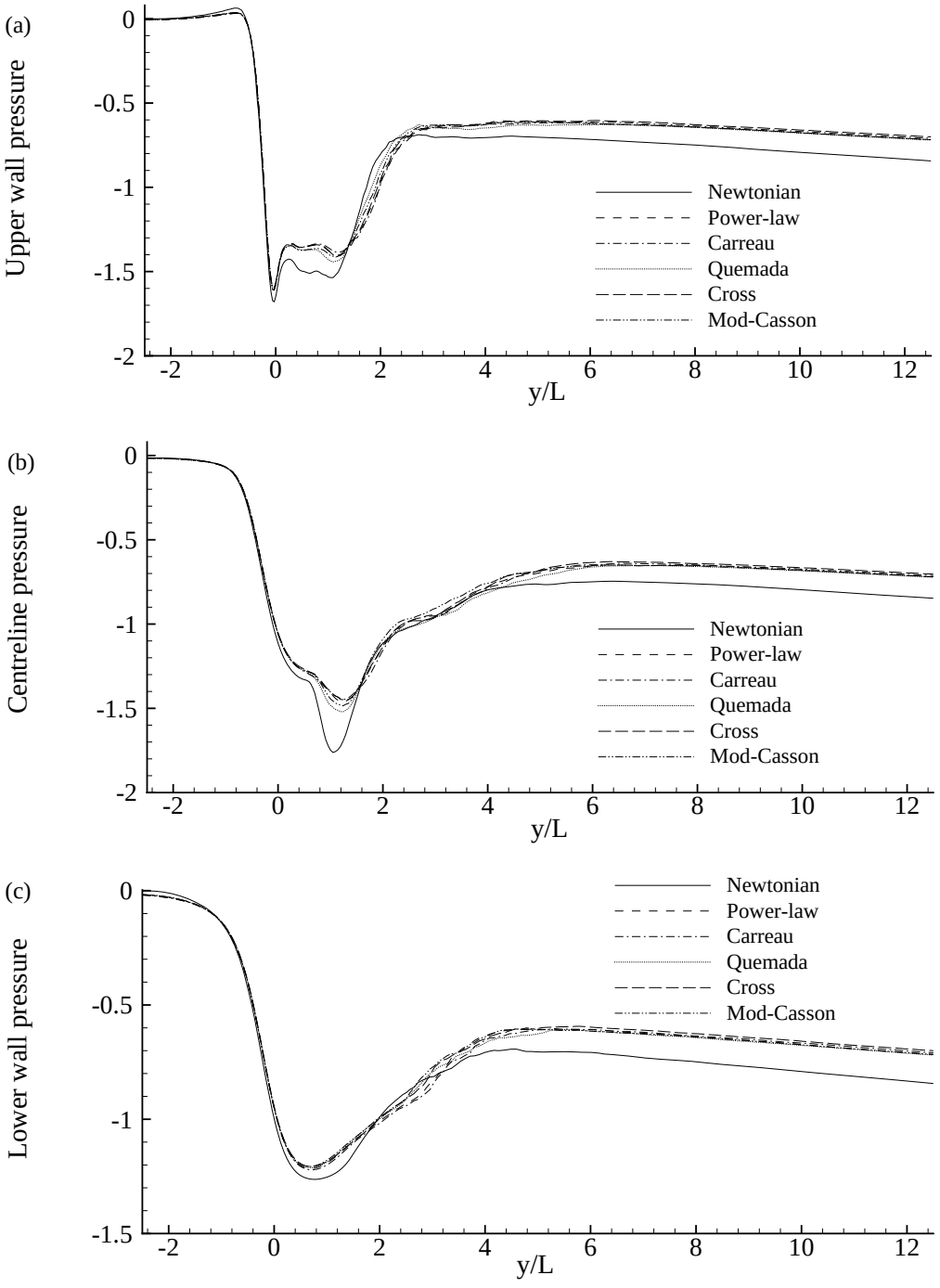

Figure 10.7: Mean pressure, $\bar{p}/\rho\bar{V}_{max}^2$ at the (a) upper wall (b) centreline and (c) lower wall for the different blood viscosity models.

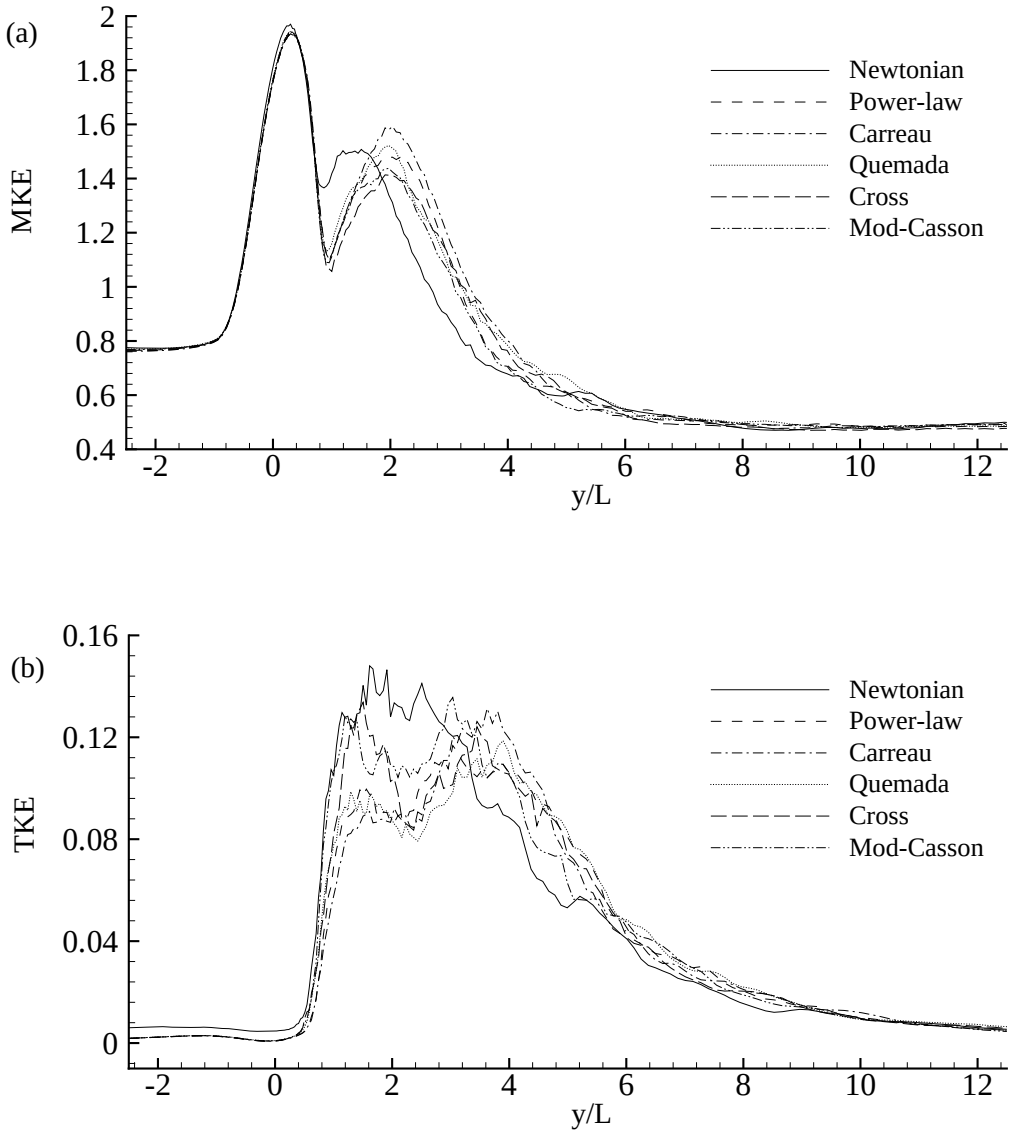

Figure 10.8: (a) Mean kinetic energy, $\frac{1}{2} < \bar{u}_j \bar{u}_j > /\bar{V}^2_{max}$, and (b) turbulent kinetic energy, $\frac{1}{2} < u''_j u''_j > /\bar{V}^2_{max}$, at $x/L = z/L = 0.5$ for the different blood viscosity models.

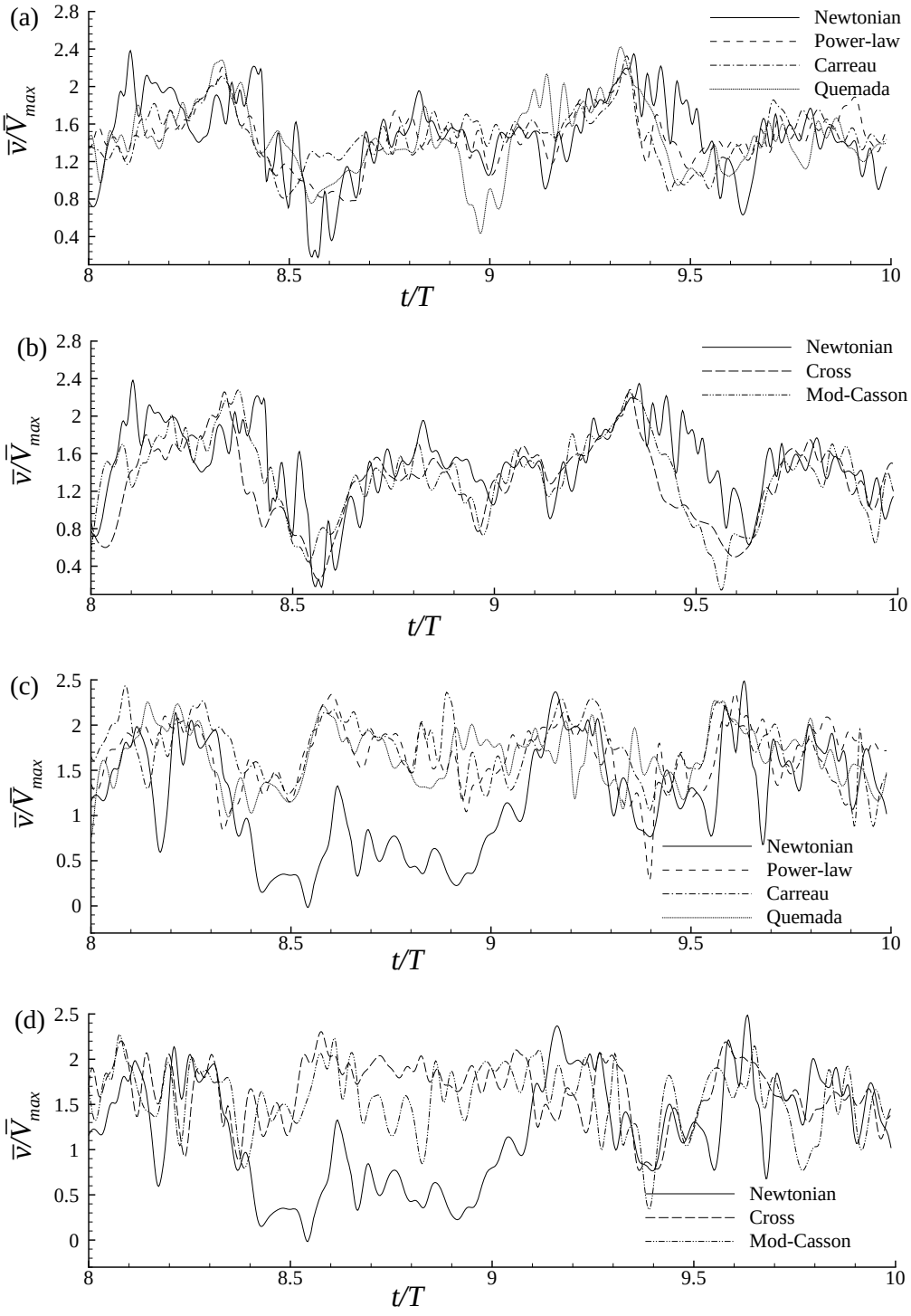

Figure 10.9: Streamwise velocity, $\bar{v}/\bar{V}_{max}$, (a-b) at $y/L = 1.0$, (c-d) at $y/L = 2.0$ over the last two cycles of pulsation at $x/L = z/L = 0.5$.

Chapter 11

Conclusions and Suggestions for Future Research

In this chapter, the findings of the present study have been summarised and some suggestions for future work are made.

11.1 Conclusions

Large Eddy Simulation technique has been applied to analyse the transition-to-turbulent flow in models of arterial stenosis and aneurysm with different types of pulsatile flows. In the stenosed model, a cosine shaped stenosis is placed eccentrically at the upper wall of a 3D channel which reduces the cross-sectional area, whereas the aneurysm which is also placed at the upper wall dilates the channel cross-sectional area. In LES, a top-hat spatial $grid$-filter is applied to the Navier-Stokes equations of motion to separate the large scale flows from the sub-grid scale (SGS). The large scale flows are resolved fully while the unresolved SGS motions are modelled dynamically. The findings of this study are summarised chapter-wise, which are given below.

In Chapter 4, LES with the Germano-Lilly [2; 3] dynamic model has been used to investigate the simple sinusoidal additive type pulsatile flow through a 3D model of arterial stenosis. With increasing Reynolds number, we found an increase in the turbulent kinetic energy and wall shear stress. For the peak Reynolds number Re_p of 1950, the maximum ratio of the SGS to molecular viscosity is 0.709, which indicates that the contribution from the SGS model is 70.9%, however, for $Re \leq 1200$ the SGS model contribution is very small and the simulated results could be treated as

a DNS solutions. The maximum stress drop occurred at the upper wall just prior to the centre of the stenosis, which is opposite to the findings of Mittal *et al* . [79], but is consistent with the results of Ojha *et al* [81], Mallinger and Drikakis [72] and Frydrychowicz *et al* [12]. The break frequency of the energy spectra is found from $-5/3$ to $-10/3$ for the velocity fluctuations and the corresponding break frequency for the pressure fluctuations is from $-5/3$ to $-7/3$. In addition, we have shown that for the large ratio of oscillation at the inlet, transition-to-turbulent happenes at the immediate post-stenosis region and the maximum turbulent intensity occurred for the highly pulsatile flow when the amplitude of the oscillation is relatively large.

In Chapter 5, the non-additive type pulsatile flow in the same model has been investigated by applying LES. A maximum 78% contribution is received from the sub-grid to large scale motion for $Re = 2000$. The results of the non-additive pulsatile case have been compared with those of both the additive pulsatile and steady flow cases and we have found that the post-stenotic flow patterns in different pulsations are quite different. In the non-additive case the length of the re-circulation region is smaller than the additive case, and the intensity of the stress and pressure drop at the throat of the stenosis is always larger in the additive case than non-additive.

In Chapters 4 and 5, simple sinusoidal additive and non-additive oscillations were imposed at the inlet of the model respectively, but the objective of Chapter 6 was to consider a physiological pulsatile flow, at the inlet of the model geometry. In this chapter, LES with the Piomelli and Liu [4] localized dynamic model was applied to the study of physiological pulsatile flow through the stenosis, whereas in the previous chapters the Germano-Lilly [2; 3] dynamic model was used. A maximum 37.4% contribution is recorded from the SGS model while $Re = 2000$. A comparison of the results obtained from the LES and coarse DNS is drawn and excellent agreement is found in the primary flow features but some variations are found in the turbulent characteristics. This is quite reasonable and is caused by the effects of the subgrid models. The level of turbulent fluctuations found in the downstream, between $y/L = 1.0$ and $y/L = 6.0$, is high, which is responsible for the damaging of blood cells and thrombosis in the post-stenotic region. The break frequency of the energy spectra from $-5/3$ to $-10/3$ for the velocity fluctuations and from $-5/3$ to $-7/3$ for the pressure fluctuations are also observed in the post-stenosis

region. We have compared the results between the sinusoidal additive (Chapter 4) and physiological pulses, and the comparisons show that the shear stress and the turbulent kinetic energy are higher in the case of the additive sinusoidal pulsatile case than the physiological pulsation.

In Chapter 7, the effects of various harmonics of the pressure pulse in the physiological pulsatile flow are investigated in the same model geometry. The Germano-Lilly [119; 3] dynamic model and the Piomelli-Liu [4] localized dynamic model are used in LES technique to investigate the effects of the first four harmonics of the physiological pressure pulse in the model. The first harmonic results are slightly different from the results of the last three harmonics, but the variation among the results of the second to fourth harmonics are very small. The contributions of the Germano-Lilly dynamic model and the Piomelli-Liu localized dynamic model are 74% and 97%, respectively, for $Re = 2000$. Due to less backscattering and less CPU time, the Piomelli-Liu model is found better than the Germano-Lilly. For the higher area reduction of the stenosis, the stress drop at the upper wall, the maximum shear stress at the lower wall and the turbulent kinetic energy increased. On the other hand, the intensity of the shear stress and the turbulent kinetic energy decreased when the length of the stenosis is increased.

In Chapter 8, physiological pulsatile flow through the model of a double stenosis is investigated using the LES with the Piomelli-Liu [4] localized dynamic model. The contribution from the SGS model is almost double for $Re = 1700$ and 2000 in comparison with the results of a single stenosis. Due to the presence of the second stenosis, the stress drop, the adverse pressure gradient and the turbulent intensity of the flow enhance significantly. The increased shear stress and turbulent fluctuations are more dangerous as they usually damage the material of blood cells and the inner side of the blood vessels. Moreover, a second re-circulation zone seen downstream of the second stenosis enhances the probability of thrombosis or blood clotting, and consequently, increases the chance of heart attack or brain stroke.

In Chapter 9, LES with the Piomelli-Liu [4] model is applied to study the physiological pulsatile flow inside the model of arterial aneurysm for only $Re = 2000$. Inside the aneurysm a large re-circulation region exists and the flow is turbulent, which is totally consistent with the experimental results of Egelhoff *et al* . [5]. The upper wall pressure and stress drop are located at the end of the segment of the

aneurysm, whereas the maximum turbulent intensity occurs between the centre and the ending segment of the aneurysm.

In Chapter 10, physiological pulsatile flow in a model arterial stenosis is investigated using various non-Newtonian blood viscosity models and the results are compared with the Newtonian model in Chapter 7. In the non-Newtonian case the length of the re-circulation region increases slightly, which increases the time that the blood remains at the post-lip region. This is potentially dangerous from the pathological point of view, as this stagnation could be a factor in the genesis of thrombosis in the post-stenosis region. The maximum lower wall shear stress and the stress drops at the upper wall occur for the non-Newtonian blood viscosity models, but the pressure drop is slightly larger in the Newtonian case than with the non-Newtonian models. The maximum turbulent intensity occurs in the Newtonian model, since in the non-Newtonian models the intensity of the physiological oscillation decreases as the blood viscosity increases.

Despite the simplicity in the model of arterial stenosis and aneurysm studied here, we believe that the simulated results presented in this thesis give a better insight and in-depth knowledge to a pathologist or medical surgeon on the important fluid dynamics aspects of transient blood flow that are usually present in a real-life biological stenosis and aneurysm e.g. pathological atherosclerotic or diseased arteries. Modelling accurately the complex form of transitions of physiological blood flow in stenosis, aneurysm or heart requires an accurate numerical approach. LES has the capability of modelling instantaneous transition-to-turbulent pulsatile flow, as demonstrated in the present thesis and also by Mittal *et al* . [79], Scotti and Piomelli [68] and Liang and Papadakis [118]. Therefore, we believe that the researchers in this field will benefit significantly from the LES approach.

11.2 Future Research

The application of LES in bio-fluid mechanics is very limited as discussed in the review chapter (Chapter 2). We think that the LES could be an ideal simulation technique to model the transitional blood flow in various bio-fluid applications including fluid-structure interaction. The recommendations for future work, based on the findings in the thesis, are given below

- For simplicity, a vessel of square cross-section has been studied in the present study unlike a biological vessel which is usually circular in cross-section. So, in future, more realistic biological vessel should be considered and the transition-to-turbulent flow through it should be investigated.

- We have considered the rigid wall for the model arterial stenosis and aneurysm, but the arterial walls in real biological system are compliant. The effects of the arterial wall vibration is very important factor for generating the arterial murmur sound in presence of the arterial stenosis. So, future simulation should involve the fluid-structure interactions using the LES technique.

- Atherosclerosis most commonly affects arterial bifurcations, so the LES could be applied in the investigation of transient-to-turbulent flow in a model of arterial bifurcations.

- In-vivo flows in large arteries are spiral-laminar due to the twisting element imparted by the heart as it contracts around its own axis (Stonebridge and Brophy [164]), but the flow studied in the thesis is laminar pulsatile prior to the stenosis and aneurysm. Spiral-laminar flow should be introduced at the inlet of the model geometry to investigate the transient-to-turbulent flows through the stenosis and aneurysm.

- We have assumed that the stenosis is formed by a smooth mathematical function, for example, the cosine curve. But in reality, this is not generally the case. Back *et al* . [165] defined the outline of the stenosis from a casting of a left circumflex coronary artery with mild atherosclerotic disease, which contains many small valleys and ridges - this suggests that the more realistic biological stenosis wall is rough rather than smooth . So, in future, the irregular arterial stenosis should be considered and the transient-to-turbulent flows through this should be investigated.

References

[1] S. A. Ahmed, D. P. Giddens, Velocity measurement in steady flow through axisymmetric stenosis at moderate Reynolds number, *J. Biomechanics*, 16 (7) (1983) 505–516.

[2] M. Germano, U. Piomelli, W. Cabot, A dynamic subgrid-scale eddy viscosity model, *Phys. Fluids A*, 3 no. 7 (1991) 1760–1765.

[3] D. K. Lilly, A Proposed Modification of the Germano Subgrid-Scale Closure Method, *Physics of Fluids A*, 4 (3) (1992) 633–635.

[4] U. Piomelli, J. Liu, Large-eddy simulation of rotating channel flows using a localized dynamic model, *Physics of Fluids*, 7(4) (1995) 839–848.

[5] V. Deplano, Y. Knapp, E. Bertrand, E. Gaillard, Flow behaviour in an asymmetric compliant experimental model for abdominal aortic aneurysm, *J. Biomechanics*, 40 (2006) 2406–2413.

[6] J. R. Womersley, Method for the calculation of velocity, rate of flow and viscous drag in arteries when the pressure gradient is known, *J. Physiology*, 155 (1955) 553–563.

[7] D. N. Ku, B. N. McCord, Cyclic stress causes rupture of the atherosclerotic plaque cap, *Suppl. to Circulation*, 88 (1) (1993) 1362–1375.

[8] D. M. Wootton, D. N. Ku, Fluid mechanics of vascular systems, diseases, and thrombosis, *Annu. Rev. Biomed. Eng.*, 01 (1999) 299–329.

[9] D. N. Ku, Blood flows in arteries, *Annu. Rev. Fluid Mechanics*, 29 (1997) 399–434.

[10] W. W. Nichols, M. F. O'Rourke, *McDonald's Blood Flow in Arteries: Theoretical, Experimental and Clinical Principles*, 4th Edition, Oxford University Press, 1998.

[11] A. M. Malek, S. L. Alper, S. Izumo, Hemodynamic shear stress and its role in atherosclerosis, *J. Ameriacn Medical Association (JAMA)*, 282 (1999) 2035–2042.

[12] A. Frydrychowicz, A. Harloff, B. Jung, M. Zaitsev, E. W. Eigang, T. A. Bley, M. Langer, J. Henning, M. Markl, Time-resolved, 3-Dimensional magnetic resonance flow analysis at 3 T: visualization of normal and pathological aortic vascular hemodynamics, *J. Comput. Assist. Tomogr.*, 31(1) (2007) 9–15.

[13] B. V. R. Kumar, K. B. Naidu, Hemodynamics in aneurysm, *Computers and Biomedical Research*, 2 (1996) 119–139.

[14] J. C. Lasheras, The biomechanics of arterial aneurysms, *Annual Review of Fluid Mechanics* , 39 (2007) 239–319.

[15] C. Clark, The fluid mechanics of aortic stenosis–I. Theory and steady flow experiments, *J. Biomechanics*, 9 (1976) 521–528.

[16] C. Clark, The fluid mechanics of aortic stenosis–II. Unsteady flow experiments, *J. Biomechanics*, 9 (1976) 567–573.

[17] R. A. Cassanova, D. P. Giddens, Disorder distal to modeled stenosis in steady and pulsatile flow, *J. Biomechanics*, 11 (1978) 441–453.

[18] D. F. Young, F. R. Tsai, Flow characteristics in models of arterial stenosis -I. steady flow, *J. Biomechanics*, 6 (1973) 395–410.

[19] D. F. Y. W. Yongchareon, Initiation of turbulence in model arterial stenosis, *J. Biomechanics*, 12 (1979) 185–196.

[20] D. F. Young, F. R. Tsai, Flow characteristics in models of arterial stenosis -II. unsteady flow, *J. Biomechanics*, 6 (1973) 547–559.

[21] A. M. A. Khalifa, D. P. Giddens, Analysis of disorder in pulsatile flows with application to poststenotic blood velocity measurement in dogs, *J. Biomechanics*, 11 (1978) 129–141.

[22] A. M. A. Khalifa, D. P. Giddens, Characterization and evolution of poststenotic flow disturbances, *J. Biomechanics*, 14 (5) (1981) 279–296.

[23] L. J. D'Luna, V. L. Newhouse, D. P. Giddens, In vitro Doppler detection of axisymmetric stenosis from transverse velocity measurements, *J. Biomechanics*, 15(9) (1982) 647–660.

[24] S. A. Ahmed, D. P. Giddens, Flow disturbances measurements through a constricted tube at moderate Reynolds number, *J. Biomechanics*, 16 (12) (1983) 955–963.

[25] L. Back, E. Roschke, Shear layer flow regimes and wave instabilities and reattachment lengths downstream of an abrupt circular channel, *J. Applied Mechanics*, 39 (1972) 677–681.

[26] S. A. Ahmed, D. P. Giddens, Pulsatile poststenotic flow studies with Laser Doppler Anemometer, *J. Biomechanics*, 17 (9) (1984) 695–705.

[27] S. A. Ahmed, An experimental investigation of pulsatile flow through a smooth constriction, *Exp. Therm. Fluid Sci.*, 17 (1998) 309–318.

[28] D. L. Burns, A general theory of the cause of murmurs in the cardiovascular system, *American J. Medicine*, 27 (1959) 360–374.

[29] E. L. Yelling, Hydraulic noise in submerged and bounded liquid jets, *ASME Biomedical Fluid mechanics Symposium*, (1966) 209–221.

[30] R. S. Lees, C. F. Dewey, Phonoangiography: a new noninvasive diagnostic method for studying arterial disease, *Procsedings of the National Academy of Science*, 67(2),October (1970) 935–942.

[31] D. L. Fry, Acute vascular endothelial changes associated with increased blood velocity gradients, *Circulation Res.*, 22 (1968) 165–197.

[32] S. P. Sutera, M. H. Mehrjardi, Deformation and fragmentation of human red blood cells in turbulent flow, *Biophysical J.*, 15 (1975) 1–10.

[33] J. D. Folts, E. B. Crowell, G. G. Rowe, Platelet aggregation in partially obstructed vessels and its elimination with aspirin, *Circulation* 54 (1976) 365–370.

[34] P. Stein, F. J. Walburn, H. N. Sabbah, Turbulent stresses in the region of aortic and pulmonary valves, *J. Biomechanics Engineering*, 104 (1982) 238–244.

[35] M. H. Friedman, G. M. Hutchins, C. B. Nargeron, O. J. Deters, F. Mark, Correlation between intimal thickness and fluid shear in human arteries, *Atherosclerosis*, 39 (1981) 425–436.

[36] D. N. Ku, D. P. Giddens, C. K. Zarins, S. Glagov, Pulsatile flow and atherosclerosis in the human carotid bifurcation, *Atherosclerosis*, 5 (1985) 293–302.

[37] T. A. Salam, A. B. Lumsden, W. D. Suggs, D. N. Ku, Low shear stress promotes intimal hyperplasia thickening, *J. Vasc. Invest.*, 2 (1996) 12–22.

[38] X. He, D. N. Ku, Pulsatile flow in the human left coronary artery bifurcation: average conditions, *J. Biomechanical Engineering*, 118 (1996) 74–82.

[39] B. M. Kim, W. H. Corcona, Experimental measurements of turbulence spectra distal to stenosis, *J. Biomechanics*, 7 (1974) 335–342.

[40] C. Clark, Turbulent velocity measurements in a model of aortic stenosis, *J. Biomechanics*, 9 (1976) 677–687.

[41] C. Clark, Turbulent wall pressure measurements in a model of aortic stenosis, *J. Biomechanics*, 10 (1977) 461–472.

[42] P. C. Lu, D. R. Gross, H. C. Hwang, Intravascular pressure and velocity fluctuations in palmonic arterial stenosis, *J. Biomechanics*, 13 (1980) 291–300.

[43] P. C. Lu, C. N. Hui, H. C. Hwang, A model investigation of velocity and pressure spectra vascular murmurs, *J. Biomechanics*, 16(11) (1983) 923–931.

[44] R. J. Tobin, I. D. Cheng, Wall pressure spectra scaling downstream of stenosis in steady tube flow, *J. Biomechanics*, 9 (1976) 633–640.

[45] D. P. Giddens, R. F. Mabon, R. A. Cassanova, Measurements of disordered flows distal to subtotal vascular stenosis in the thoracic aortas of dogs, *Circulation Research*, 39 (1976) 112–119.

[46] S. A. Jones, A. Fronk, Analysis of break frequencies downstream of a constriction in a cylindrical tube, *J. Biomechanics*, 20(3) (1987) 319–327.

[47] J. S. Lee, Y. C. Fung, Flow in locally constricted tubes at low Reynolds numbers, *J. Applied Mechanics*, 37 (1970) 9–16.

[48] M. D. Deshpande, D. P. Giddens, R. F. Mabon, Steady laminar flow through modelled vascular stenosis, *J. Biomechanics*, 9 (1976) 165–174.

[49] L. C. Cheng, M. E. Clark, J. M. Robertson, Numerical calculations of oscillating flow in the vicinity of square wall obstacles in plane conduits, *J. Biomechanics*, 5 (1972) 467–484.

[50] B. J. Daly, A numerical study of pulsatile flow through stenosed canine femoral arteries, *J. Biomechanics*, 9 (1976) 465–475.

[51] V. O'Brien, L. W. Ehrlich, I. Simple pulsatile flow in an artery with a constriction, *J. Biomechanics*, 18 (2) (1985) 117–127.

[52] S. Cavalcanti, Hemodynamics of an artery with mild stenoses, *J. Biomechanics*, 28 (4) (1995) 387–399.

[53] G. R. Zendehbudi, M. S. Moayeri, Comparison of physiological and simple pulsatile flows through stenosed arteries, *J. Biomechanics*, 32 (1999) 959–965.

[54] P. F. Marques, M. C. Oliveira, A. S. Frabca, M. Pinotti, Modelling and simulation of pulsatile blood flow with a physiologic wave pattern, *Artificial Organs*, 27 (5) (2003) 478–485.

[55] J. S. Stroud, S. A. B. D. Saloner, Influence of stenosis morphology on flow through severely stenotic vessels: implications for plaque rupture, *J. Biomechanics*, 33 (2000) 443–455.

[56] M. C. Melaaen, Analysis of fluid flow in constricted tubes and ducts using body-fitted non-staggered grids, *Int. J. Nume. Meth. Fluids*, 15 (1991) 895–923.

[57] C. Bertolotti, V. Deplano, Three dimensional numerical simulations of flow through a stenosed coronary bypass, *J. Biomechanics*, 33 (2000) 1011–1022.

[58] A. S. Dvinsky, M. Ojha, Simulation of three-dimensional pulsatile flow through an asymmetric stenosis, *Med. Biol. Eng. Comput.*, 32 (1994) 138–142.

[59] Q. Long, X. Y. Xu, K. V. Ramnarine, P. R. Hoskins, Numerical investigation of physiologically realistic pulsatile flow through arterial stenosis, *J. Biomechanics*, 34 (2001) 1229–1242.

[60] V. Damodaran, G. W. Rankin, C. Zhang, Numerical study of steady laminar flow through tube with multiple constriction using curvilinear co-ordinates, *Int. J. Numer. Meth. Fluids*, 23 (1996) 1021–1041.

[61] T. S. Lee, Numerical study of fluid flow through double bell-shaped constrictions in a tube, *Int. J. Numer. Meth. Heat and Fluid flow*, 12 (3) (2002) 258–289.

[62] H. Huang, T. S. Lee, C. Shu, Lattice-BGK simulation of steady flow through vascular tubes with double constrictions, *Int. J. Numerical Methods for Heat and Fluid Flow*, 16 (2) (2006) 185–203.

[63] F. Ghalichi, X. Deng, A. D. Champlain, Y. Douville, M. King, R. Guidoin, Low Reynolds number turbulence modeling of blood flow in arterial stenosis, *Biorheology*, 35 (4,5) (1998) 281–294.

[64] S. S. Varghese, S. H. Frankel, Numerical Modeling of pulsatile turbulent flow in stenotic vessels, *J. Biomechanical Engineering*, 124 (2003) 445–460.

[65] T. S. Lee, W. Liao, H. T. Low, Numerical simulation of turbulent flows through series stenoses, *Int. J. Numer. Meth. Fluids*, 42 (2003) 717–740.

[66] T. S. Lee, W. Liao, H. T. Low, Numerical study of physiological turbulent flows through series arterial stenoses, *Int. J. Numer. Meth. Fluids*, 46 (2004) 315–344.

[67] M. X. Li, J. J. B-Brandt, P. R. Hoskins, W. J. Easson, Numerical Analysis of pulsatile blood flow and vessel wall mechanics in different degrees of stenoses, *J. Biomechanics*, 40 (2007) 3715–3724.

[68] A. Scotti, U. Piomelli, Turbulent models in pulsatile flows, *AIAA Journal*, 40 (3) (2002) 573–544.

[69] P. R. Splart, S. R. Allmaras, A one-equation turbulence model for aerodynamics flows, *La Recherche Aerospatiale*, 1 (1) (1994) 5–21.

[70] P. G. Saffman, D. C. Wilcox, Turbulence model predictions for turbulent boundary layer, *AIAA Journal*, 12 (1974) 541–550.

[71] P. A. Dublin, Separated flow computations with the k-ϵ-v^2 model, *AIAA Journal*, 33 (1995) 659–664.

[72] F. Mallinger, D. Drikakis, Instability in three-dimensional, unsteady, stenotic flows, *Int. J. Heat and Fluid Flow*, 23 (2002) 657–663.

[73] F. Mallinger, D. Drikakis, Laminar-to-turbulent transition in pulsatile flow through a stenosis, *Biorheology*, 39 (2002) 437–441.

[74] S. J. Sherwin, H. M. Blackburn, Three-dimensional instabilities and transition of steady and pulsatile flows in an axisymmetric stenotic tube, *J. Fluid Mechanics*, 533 (2005) 297–327.

[75] H. M. Blackburn, S. J. Sherwin, Instability modes and transition of pulsatile stenotic flow: pulse-period dependence, *J. Fluid Mechanics*, 573 (2007) 57–88.

[76] S. S. Varghese, S. H. Frankel, P. F. Fischer, Direct numerical simulation of stenotic flows. Part 1. Steady flow, *J. Fluid Mechanics*, 582 (2007) 253–280.

[77] S. S. Varghese, S. H. Frankel, P. F. Fischer, Direct numerical simulation of stenotic flows. Part 2. Pulsatile flow, *J. Fluid Mechanics*, 582 (2007) 281–318.

[78] R. Mittal, S. P. Simmons, H. S. Udaykumar, Application of Large-eddy simulation to the study of pulsatile flow in a modelled arteria stenosis, *J. Biomechanical Engineering*, 123 (2001) 325–332.

[79] R. Mittal, S. P. Simmons, F. Najjar, Numerical study of pulsatile flow in a constricted channel, *J. Fluid Mech.*, 485 (2003) 337–378.

[80] O. R. Tutty, Pulsatile flow in a constricted channel, *J. Biomech. Eng.*, 114 (1992) 50–54.

[81] M. Ojha, R. S. Cobbold, K. W. Johnston, R. L. Hummel, Pulsatile flow through constricted tubes: an experimental investigation using photochromic tracer methods, *J. Fluid Mechanics*, 203 (1989) 173–197.

[82] P. W.Scherer, Flow in axisymmetrical glass model aneurysms, *J. Biomechanics*, 6 (1973) 695–700.

[83] A. V. Salsac, S. R. Sparks, J. M. Chomaz, J. C. Lasheras, Evolution of the wall shear stresses during the progressive enlargement of symmetric abdominal aortic aneurysm, *J. Fluid Mechanics*, 560 (2006) 19–51.

[84] V. Deplano, Y. Knapp, E. Bertrand, E. Gaillard, Flow behaviour in an asymmetric compliant experimental model for abdominal aortic aneurysm, *J. Biomechanics*, 40 (2006) 2406–2413.

[85] S. O. Wille, Finite element simulations of the pulsatile blood flow patterns in arterial abnormalities, *Finite Elements in Biomechanics (R. H. Gallagher et al . Eds.)*, (1982) 39–60.

[86] K. Perktold, K. Gruber, T. H. Kenner, H. Florion, Calculation of pulsatile flow and particle paths in an aneurysm-model, *Basic Research Cardiology*, 7 (1984) 253–261.

[87] K. Perktold, On the paths of particles in an axisymmetrical aneurysm, *J. Biomechanics*, 20 (3) (1985) 311–317.

[88] B. V. R. Kumar, A space-time analysis flow in a 3D vessel with multiple aneurysm, *Computation Mechanics*, 32 (2003) 16–28.

[89] B. Utter, J. S. Rossmann, Numerical simulation of saccular hemodynamics: Influence of morphology on rupture risk, *J. Biomechanics* , 40 (2007) 2716–2722.

[90] V. L. Rayz, L. Boussel, M. T. Lawton, G. A-Bolton, L. Ge, W. L. Y. R. T. Higashida, D. Saloner, Numerical modeling of the flow intracranial aneurysms: prediction of regions prone to thrombus formation, *Annals of Biomedical Engineering* , 36 (11) (2008) 1793–1804.

[91] I. Chatziprodromou, A. Tricoli, D. Poulikakos, Y. Ventikos, Haemodynamics and wall remodelling of a growing cerebral aneurysm: A computational model, *J. Biomechanics* , 40 (2007) 412–426.

[92] A. Valencia, H. Morales, R. Rivera, E. Bravo, M. Galvez, Blood flow dynamics in patient-specific cerebral aneurysm models: The relationship between wall shear stress and aneurysm area index, *Medical Engineering and Physics*, 30 (2008) 329–340.

[93] K. M. Khanafer, J. L. Bull, R. Berguer, Fluid-structure interaction of turbulent pulsatile flow within a flexible wall axisymmetric aortic aneurysm model, *European J. Mechanics B/Fluids*, (2007) doi:10.1016/j.euromechflu.2007.12.003.

[94] Y. C. Fung, *Biomechanics: Circulation*,, 2nd edition, Springer,1997.

[95] S. A. Berger, L.-D. Jou, Flows in stenotic vessels, *Annu. Rev. Fluid Mechanics*, 32 (2000) 347–382.

[96] J. R. B. Jr, C. Kleinstreuer, J. K. Comer, Rheological effects on pulsatile hemodynamics in a stenosed tube, *Computers and Fluids*, 29 (2000) 695–724.

[97] C. Tu, M. Delville, Pulsatile flow of non-Newtonian fluids through arterial stenosis, *J. Biomechanics*, 29 (7) (1996) 899–908.

[98] P. Neofytou, S. Tsangaris, Flow effects of blood constitutive equation in 3D models of vascular anomalies, *Int. J. Numer. Meth. Fluids*, 51 (2006) 489–510.

[99] P. Neofytou, D. Drikakis, Effects of blood models on flows through a stenosis, *Int. J. Numer. Meth. Fluids*, 43 (2003) 597–635.

[100] P. Neofytou, D. Drikakis, Non-Newtonian flow instability in a channel with a sudden expansion, *J.Non-Newtonian Fluid Mechanics*, 111 (2003) 127–150.

[101] B. M. Johnston, P. R. Johnston, S. Corney, D. Kilpatrick, Non-Newtonian blood flow in human right coronary arteries: steady state simulations, *J. Biomechanics* , 37 (2004) 709–720.

[102] B. M. Johnston, P. R. Johnston, S. Corney, D. Kilpatrick, Non-Newtonian blood flow in human right coronary arteries: transient simulations, *J. Biomechanics* , 39 (2006) 1116–1128.

[103] X. Y. Luo, Z. B. Kuang, A study on the constitutive equation of blood , *J. Biomechanics* , 25 (8) (1992) 929–934.

[104] J-B.Zhang, Z. B. Kuang, Study on blood constitutive parameters in different blood constitutive equations , *J. Biomechanics* , 33 (2000) 355–360.

[105] J. Hron, J. Malek, S. Turek, A numerical investigation of flows shear-thinning fluids with applications to blood rheology, *Int. J. Numerical Methods in Fluids* , 32 (2000) 863–879.

[106] A. Valencia, A. Zarate, M. Galvez, L. Badilla, Non-Newtonian blood flow dynamics in a right internal carotid artery with a saccular aneurysm, *Int. J. Numerical Methods in Fluids*, 50 (2006) 751–764.

[107] D. Nag, A. Datta, Steady laminar flow of blood through successive restrictions in circular conduits of small diameter, *Proc. IMechE, Part C: J. Mechanical Engineering Science* , 222 (2008) 1557–1573.

[108] A. Valencia, M. Villanueva, Unsteady flow and mass transfer in models of stenotic arteries considering fluid-structure interaction, *Int. Communication Heat and Mass Transfer*, 33 (2006) 966–975.

[109] T. J. Pedley, *The fluid mechanics of large blood vessels*,, Cambridge University Press, 1980.

[110] G. Grotzbach, Spatial resolution requirements for Direct Numerical Simulations of the Rayleigh-Bernard convection, *J. Computational Physics*, 49(2) (1983) 241–264.

[111] W. C. Reynolds, The potential and limitations of direct and large eddy simulations, In J. L Lumley, editor, Whither Turbulence? Turbulence at the Crossroads 357 in Lecture Notes in Physics, Springer-Verlag (1990) 313–343.

[112] A. N. Kolmogorov, Dissipation of energy in the locally isotropic turbulence, Proceedings of the Royal Society of London A: Mathematical and Physical Science 434 (1991) 15–17.

[113] H. Tennekes, J. L. Lumley, *A first course in turbulence*, The MIT press, 1972.

[114] A. Leonard, Energy cascade in Large-Eddy Simulations of turbulent fluid flows, *Adv. Geophys.*, 18A (1974) 237–248.

[115] S. Ghosal, P. Moin, The basic equations for the Large Eddy Simulation of turbulent flows in complex geometry, *J. Computational Physics*, 118 (1995) 24–37.

[116] L. di Mare, W. P. Jones, LES of turbulent flow past a swept fence, *Int. J. Heat and Fluid Flow*, 24 (2003) 606–615.

[117] W. P. Jones, M. Wille, Large-eddy simulation of a plane jet in a cross-flow, *Int. J. Heat and Fluid flow*, 17 (1996) 296–306.

[118] C. Liang, G. Papadakis, Large eddy simulation of pulsatile flow over a circular cylinder at subcritical Reynolds number, *Computers and Fluids*, 36 (2007) 299–312.

[119] J. Smagorinsky, General circulation experiment with the primitive equations. i. the basic experiment, *Monthly Weather Rev.*, 91 (1963) 99–164.

[120] T. S. Lund, On the use of discrete filters for large eddy simulation, *Center for Turbulence Research*, Annual Research Briefs (1997) 83–95.

[121] R. Vichnevetsky, Invarience theorems concerning reflection at numerical boundaries , *J. Computational Physics*, 63 (2) (1986) 268–282.

[122] G. Jin, M. Braza, A non-reflecting boundary condition for incompressible unsteady Navier-Stokes calculation, *J. Computational Physics*, 107 (1993) 239–253.

[123] L. L. Pauley, P. Moin, W. C. Reynolds, The structure of two dimensional separation, *J. Fluid Mechanics*, 220 (1990) 397–411.

[124] F. Mare, W. P. Jones, K. R. Menzies, Large eddy simulation of a model gas turbine combustor, *Combustion and Flame*, 137 (2004) 278–294.

[125] M. C. Paul, Performance of the various Sn approximations of DOM in a 3D combustion chamber, *ASME J. Heat Transfer*, 103 (7) (2008) 072701–1–7.

[126] S. C. Paul, M. C. Paul, W. P. Jones, Large eddy simulation for turbulent non-premixed fuel-rich combustion in a cylindrical combustor , In, P. Wesseling, E. Onate and J. Periaux Eds. Proceedings of the European Conference on Computational Fluid Dynamics (ECCOMAS CFD), 5-8 September, The Netherlands, (2006) 1–15.

[127] W. P. Jones, M. C. Paul, Combination of DOM with LES in a gas turbine combustor, *Int. J. Engineering Science*, 43 (6) (2006) 379–397.

[128] N. Branley, W. P. Jones, Large eddy simulation of turbulent non-premixed flame, *Combustion and Flame*, 127 (2001) 1914–1934.

[129] M. Wille, Large Eddy Simulation of Jets in Cross Flows, PhD Thesis, Imperial College of Science, Technology and Medicine, London, 1997.

[130] J. F. Thomson, F. Thames, C. Mastin, Automatic numerical generation of body-fitted curvilinear coordinates system for field containing any number of arbitrary two dimensional bodies, *J. Computational Physics*, 15 (1974) 299–319.

[131] Y. Morinishi, Conservation prperties of finite difference schemes for incompressible flow, *Center for Turbulence Research*,) (1995) 121–132.

[132] H. Choi, P. Moin, Effect of the computational time step on numerical solutions of turbulent flow, *J. Computational Physics*, 111 (1994) 1–4.

[133] C. M. Rhie, W. L. Chow, Numerical study of the turbulent flow past an airfoil with trailing edge separation, *AIAA Journal*, 21(11) (1983) 1525–1532.

[134] H. A. D. Vorst, BI-CGSTAB: a first and smoothly converging variant of BI-CG for the solution of the nonsymmetric linear systems, *SIAM J. Sci. Stat. Comput.*, 13 (2) (1992) 631–644.

[135] D. S. Kershaw, The Incomplete Cholesky-Cojugate Gradient method for the iterative solution of systems, *J. Computational Physics*, 26 (1978) 43–65.

[136] A. K. M. Hussain, W. C. Reynolds, The mechanics of an organized wave in turbulent shear flow, *J. Fluid Mechanics*, 41 (2) (1970) 241–258.

[137] B. B. Lieber, D. P. Giddens, Post-stenotic core flow behavior in pulsatile flow and its effects on wall shear stress, *J. Biomechanics*, 23 (6) (1990) 597–605.

[138] MATLAB, The Language of Technical Computing , The Mathworks Inc., 2007, August.

[139] P. Moin, J. Kim, Numerical investigation of turbulent channel flow, *J. Fluid Mechanics*, 118 (1982) 341–377.

[140] D. L. P. Ask, B. Hok, H. Terio, Bio-acoustic signals from stenotic tube flow: state of the art and perspectives for future methodological development, *Med. Bio. Engn. Comput.*, (1995) 669–675.

[141] T. S. Lee, T. W. NG, Z. D. Shi, Numerical study of effects of pulsatile amplitude on unsteady laminar lows in rigid pipe with ring-type constrictions, *Int. J. Numer. Meths. Fluids*, 24 (1997) 275–290.

[142] T. J. Pedley, High Reynolds number flow in tubes of complex geometry with application to wall shear stress in arteries, In: Biological Fluid Dynamics, Edited by Ellington C P and Pedley T J, Cambridge: The Company of Biologists, Limited (1995) 219–241.

[143] K. B. Chandran, *Cardiovascular Biomechanics,*, New York University Press, 1992.

[144] C. Loudon, A. Tordesillas, The use of the dimensionless Womersley number to characterize the unsteady nature of internal flow, *J. Theor. Biol.*, 191 (1998) 63–78.

[145] D. R. Gross, P. Lu, K. T. Dodd, H. C. Hwang, Physical characteristics of pulmonary artery stenosis murmurs in claves, *Am. J. Physiology*, 238 (Heart Circ. Physiol. 7) (1980) H876–H885.

[146] W. Heisenberg, Zur statistischen theorie der turbulenz, *Z. Phys.* 124 (1948) 628–657.

[147] N. Talikder, P. E. Karayannacos, R. M. Nerem, J. S. Vasco, An experimental study of fluid mechanics of arterial stenosis, *ASME J. Biomechanical Engineering*, 99 (1977) 74–82.

[148] H. Huang, T. S. Lee, C. Shu, Lattice-BGK simulation of steady flow through vascular tubes with double constriction, *Int. J. Numer. Meth. Heat and Fluid flow*, 16 (2) (2006) 185–203.

[149] N. F. Kassell, J. C. Torner, E. C. Haley, The international cooperative study on the timing of aneurysm surgery. 1. Overall management results, *J. Neurosurgery* , 73 (1) (1990) 18–36.

[150] P. Neofytou, S. Tsangaris, M. Kyriakidis, Vascular wall flow-induced forces in a progressively enlarged aneurysm model, *Computer Methods in Biomechanics and Biomedical Engineering* , 11 (6) (2008) 612–626.

[151] A. V. Salsac, S. R. Sparks, J. C. Lasheras, Hemodynamic changes occurring during the pogressive enlargement of abdominal aortic aneurysm , *Annals Vascular Surgery*, 18 (1) (2004) 14–21.

[152] C. R. Huang, W. D. Pan, H. W. Chen, A. L. Copley, Thixotropic properties of whole blood from healthy human subjects, *Biorheology* , 24 (1987) 795–801.

[153] W. L. Barth, L. V. Branets, G. F. Carey, Non-Newtonian flow in branched pipes and artery models, *Int. J. Numerical Methods in Fluids* , 57 (2008) 531–553.

[154] A. I. P. Miranda, P. J. Oliveira, F. T. Pinho, Steady and unsteady laminar flows of Newtonian and generalised Newtonian fluids in a planar T-junction, *Int. J. Numerical Methods in Fluids* , 57 (2008) 295–328.

[155] F. J. Wlaburn, D. J. Schneck, A constitutive equation for whole human blood, *Biorheology*, 13 (1976) 201–210.

[156] P. J. Carreau, Rheological Equation from Molecular Network Theories, *J. Rheology*, 16 (1) (1972) 99–127.

[157] D. Quemada, Rheology of concentrated disperse system III. General features of the proposed non-Newtonian model. Comparison with experimental data, *Rheology Acta*, 17 (1977) 643–653.

[158] M. M. Cross, Rheology of non-Newtonian fluids: A new flow equation for viscoelastic systems, *J. Collied Science*, 20 (1965) 417.

[159] N. Casson, *Rheology of Disperse System*, Pergamon press, London, 1959 84–104.

[160] E. W. Merrill, G. R. Cokelet, A. Britten, R. E. Wells, Non-Newtonian rheology of human blood-effect of fibrinogen deduce by subtraction, *Circulation Reserach*, 13 (1963) 48–55.

[161] H. Bate, Blood viscosity at different shear rates in capillary tubes, *Biorheology*, 14 (1977) 267–275.

[162] H. A. Gonzalez, N. O. Moraga, On predicting unsteady non-Newtonian blood flow, *Applied Mathematics and Computations*, 170 (2) (2005) 909–923.

[163] W. R. Milnor, *Hemodynamics*, Williums and Wilkins, Baltimore, 1982, 49-55 .

[164] P. A. Stonebridge, C. M. Brophy, Spiral laminar flow in arteries?, *The Lancet*, 338 (1991) 1360–1361.

[165] L. Back, Y. Cho, D. Crawford, R. Cuffel, Effect of mild atherosclerosis on flow resistance in a coronary artery casting of man, *J. Biomechanical Engineering*, 106 (1984) 48–53.

[166] W. P. Jones, F. di Mare, A. J. Marquis, LES-BOFFIN: User's Guide, *Imperial College London, UK*,) (2002) 1–66.

[167] S. V. Patankar, *Numerical Heat Transfer and Fluid Flow*, Hemisphere Publishing Corporation, 1980.

Appendix A

Numerical Procedure

As mentioned in § 3.7 in Chapter 3, the BOFFIN code (LES-BOFFIN: User's Guide [166]) , employed in our computation uses a finite volume approach where the filtered governing equations are integrated over the mesh control volume to obtain an algebraic finite difference approximation for those partial differential transport equations. To facilitate calculation, the governing equations are transformed into curvilinear coordinates. The approach is described briefly in this chapter.

A.1 Coordinate Transformation

Thompson *et al* [130] introduced an approach where the finite difference equations are formulated in a transformed curvilinear coordinate system that coincides with the boundaries of the flow domain. In this approach, the flow domain in physical space is mapped onto a rectangular domain in computational space, as shown in Fig. A.1, where a two-dimensional case is represented for simplicity.

Fot the map $x_j \rightarrow \xi_j$, if J_{ij} represents the elements of the Jacobian matrix, **J**, of the transformation then

$$J_{ij} = \frac{\partial x_i}{\partial \xi_j} \tag{A.1}$$

The determinant of the Jacobian matrix, **J**, is denoted by $|\mathbf{J}|$ and given by

$$|\mathbf{J}| = \frac{\partial x_i}{\partial \xi_j} A_{ij}, \tag{A.2}$$

where A_{ij} are the elements of the cofactor matrix, **A**, of the Jacobian, defined as

$$|\mathbf{A}| = |\mathbf{J}|\mathbf{J}^{-1} \tag{A.3}$$

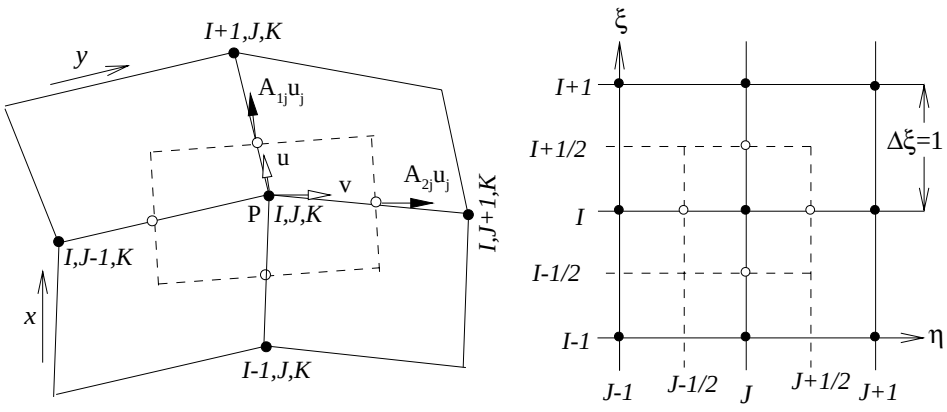

Figure A.1: Grid arrangement and notation in two-dimensional case in both physical space (left), and in computational space (right). Solid lines indicate the grid lines, dashed lines the faces of the control volume.

By applying the chain rule, the derivatives can now be expressed in the transformed space in the following way

$$\frac{\partial \phi}{\partial x_i} = \frac{\partial \phi}{\partial \xi_j}\frac{\partial \xi_j}{\partial x_i} = \frac{A_{ij}}{|\mathbf{J}|}\frac{\partial \phi}{\partial \xi_j}, \tag{A.4}$$

where ϕ is a generic variable.

The filtered governing equations (3.34)-(3.35) in general curviliear co-ordinates can be written as,

$$\frac{\partial}{\partial \xi_k}\left(\frac{A_{kj}}{|\mathbf{J}|}\bar{u}_j\right) = 0, \tag{A.5}$$

$$\begin{aligned}\frac{\partial(\rho\bar{u}_i)}{\partial t} + \frac{\partial}{\partial \xi_k}\left(\frac{A_{kj}}{|\mathbf{J}|}\rho\bar{u}_i\tilde{u}_j\right) &= -\frac{A_{kj}}{|\mathbf{J}|}\frac{\partial \bar{p}}{\partial \xi_k} \\ &+ \frac{\partial}{\partial \xi_k}\left[\frac{A_{kj}}{|\mathbf{J}|}\left(\mu_e\frac{A_{lj}}{|\mathbf{J}|}\frac{\partial \bar{u}_i}{\partial \xi_l} + \mu_e\frac{A_{li}}{|\mathbf{J}|}\frac{\partial \bar{u}_j}{\partial \xi_l}\right)\right],\end{aligned} \tag{A.6}$$

where theeffective viscosity, μ_e, is the sum of the molecular and sub-grid eddy viscosity defined as

$$\mu_e = \mu + \mu_{sgs}. \tag{A.7}$$

The finite volume method uses the integral form of the transport equations as the starting point. Integrating the transformed equations over a single control volume, ΔV, gives,

Continuity:

$$\int_{\Delta S} G_k n_k ds = 0, \tag{A.8}$$

Momentum:

$$\int_{\Delta V} \frac{\partial(\rho \bar{u}_i)}{\partial t} |\mathbf{J}| dV + \int_{\Delta S} G_k \bar{u}_i n_k dS = -\int_{\Delta V} A_{kj} \frac{\partial \bar{p}}{\partial \xi_k} dV + \int_{\Delta S} \left[\mu_e \left(\frac{A_{lj} A_{kj}}{|\mathbf{J}|} \frac{\partial \bar{u}_i}{\partial \xi_l} + \frac{A_{li} A_{kj}}{|\mathbf{J}|} \frac{\partial \bar{u}_j}{\partial \xi_l} \right) \right] n_k dS, \tag{A.9}$$

where $G_k = A_{ij} \rho \bar{u}_j$, are the mass fluxes. n_k is the unit normal pointing in the outward direction of the cell surface, ΔS, of the cell volume, ΔV.

A.2 Discretisation Scheme Used in BOFFIN

The grid arrangement used is shown in Fig A.1, where the mesh spacing in the transformed space is uniform, i.e. $\Delta \xi = 1$. The control volume (CV) faces lie midway between nodes. According to the collocated arrangement, all the variables e.g. velocity and pressure stored at the CV centres are assumed to be uniform over the CV. A linear variation of variable values between grid nodes is assumed in such a way that the value of the variables at the cell faces are obtained as averages of the values at the appropriate adjacent nodes.

In order to illustrate the discretisation scheme adopted, we have considered the u-momentum equation of the Navier-Stokes equations. The convective term is approximated by,

$$\begin{aligned} \int_{\Delta S} G_k \bar{u} n_k dS \approx & \left[G_1 \bar{u} \right]_{I+\frac{1}{2},J,K} - \left[G_1 \bar{u} \right]_{I-\frac{1}{2},J,K} \\ & + \left[G_2 \bar{u} \right]_{I,J+\frac{1}{2},K} - \left[G_2 \bar{u} \right]_{I,J-\frac{1}{2},K} \\ & + \left[G_3 \bar{u} \right]_{I,J,K+\frac{1}{2}} - \left[G_3 \bar{u} \right]_{I,J,K-\frac{1}{2}} . \end{aligned} \tag{A.10}$$

For instance, the first term of the equation (A.10), $\left[G_1 \bar{u} \right]_{I+\frac{1}{2},J,K}$, is approximated

as follows:

$$[G_1\bar{u}]_{I+\frac{1}{2},J,K} = \frac{1}{2}\,[G_1]_{I+\frac{1}{2},J,K}\,([\bar{u}]_{I,J,K} + [\bar{u}]_{I+1,J,K})\,, \tag{A.11}$$

The linear variation of variables between node points has been assumed. The mass fluxes are expressed as

$$[G_1]_{I+\frac{1}{2},J,K} = \rho \times \left([A_{11}\bar{u}]_{I+\frac{1}{2},J,K} + [A_{12}\bar{v}]_{I+\frac{1}{2},J,K} + [A_{13}\bar{w}]_{I+\frac{1}{2},J,K}\right), \tag{A.12}$$

where the term like $[A_{11}\bar{u}]_{I+\frac{1}{2},J,K}$ is discretised as,

$$[A_{11}\bar{u}]_{I+\frac{1}{2},J,K} = \frac{1}{2}\,([\bar{u}]_{I,J,K} + [\bar{u}]_{I+1,J,K}) \times \left(\left[\frac{\partial y}{\partial \eta}\right]_{I+\frac{1}{2},J,K}\cdot\left[\frac{\partial z}{\partial \zeta}\right]_{I+\frac{1}{2},J,K} - \left[\frac{\partial y}{\partial \zeta}\right]_{I+\frac{1}{2},J,K}\cdot\left[\frac{\partial w}{\partial \eta}\right]_{I+\frac{1}{2},J,K}\right), \tag{A.13}$$

and,

$$\left[\frac{\partial y}{\partial \eta}\right]_{I+\frac{1}{2},J,K} = \frac{1}{2}\left(\frac{[y]_{I,J+1,K} - [y]_{I,J-1,K}}{2} + \frac{[y]_{I+1,J+1,K} - [y]_{I+1,J-1,K}}{2}\right). \tag{A.14}$$

The diffusive terms are approximated in a similar manner. The cross derivative terms arising from the non-orthogonality of the transformed co-ordinate system are treated explicitly.

Time derivatives are discretised by a three point backward difference scheme with a constant time step of δt which is represented by

$$\frac{\partial \bar{u}}{\partial t} \approx \frac{3}{2}\left(\frac{\bar{u}^{n+1} - \bar{u}^{n}}{\delta t}\right) - \frac{1}{2}\left(\frac{\bar{u}^{n} - \bar{u}^{n-1}}{\delta t}\right), \tag{A.15}$$

where n is the number of timestep.

The discretisation scheme described above leads to a quasi-linear system of

equations for the velocity, $\bar{u}$, that can be written as,

$$a_{I,J,K}\bar{u}^{n+1}_{I,J,K} = \sum_{neighbours} a_\alpha \bar{u}^{n+1}_\alpha + S_{I,J,K}, \tag{A.16}$$

where $S_{I,J,K}$ represents a source term containing all terms that can not be expressed as face fluxes and can be dependent on $\bar{u}$; and a_α account for both the convective and diffusive terms. The summation being taken over the immediate neighbours of I, J, K (i.e. $I \pm 1$, $J \pm 1$, $K \pm 1$).

A.3 Velocity and Pressure Calculation

Once the governing equations are discretised, the pressure and velocity fields are obtained by employing a pressure correction method which is similar to the SIMPLE algorithm of Patankar [167]. This method can be illustrated as follows.

The finite difference equations (fde), for instance, the u-momentum equation to within a second order accuracy can be written in the following quasi-matrix form assuming a constant time step

$$\mathbf{u}^{n+1} - \mathbf{u}^n + \frac{2}{3}\delta t \mathbf{T}^{n+1}\mathbf{u}^{n+1} = -\frac{2}{3}\delta t \mathbf{D}\mathbf{p}^{n+1} + \mathbf{S}. \tag{A.17}$$

where $\mathbf{u}$ is the vector of the unknown u nodal values, $\mathbf{T}^{n+1}$ represents the coefficient matrix for the convection and diffusion terms at $n+1$, $\mathbf{D}$ arises from the discretisation of the pressure term, and the source term $\mathbf{S}$ contains all the terms resulting from the time discretisation. The cross-derivative diffusion terms are given explicit treatment in order to reduce the computational cost. Evaluating these cross derivatives at time level n and adding them to $\mathbf{S}$ introduces an error of $O(\delta t^2)$ into equation (A.17). Therefore, the fde (A.17) can be written as

$$\mathbf{u}^{n+1} + \frac{2}{3}\delta t \mathbf{T}^{n}\mathbf{u}^{n+1} = -\frac{2}{3}\delta t \mathbf{D}\mathbf{p}^{n+1} + \mathbf{S} + O(\delta t^2). \tag{A.18}$$

where $\mathbf{S}$ now contains additionally those cross-derivative terms which are not included in $\mathbf{T}^n$ and treated explicitly. The bar in velocity is disregarded in order to simplify the notation.

The solution to equation (A.18) obtained by neglecting the error term $O(\delta t^2)$ is

a second order accurate approximation to $\mathbf{u}^{n+1}$. In order to achieve second order accuracy, the equation (A.17) is solved in two stages. In the first stage, a solution to (A.18) is sought. Denoting this solution as $\mathbf{u}^m$, having a corresponding pressure field $\mathbf{p}^m$, and introducing a pressure increment, $\Delta\mathbf{p}^m = \mathbf{p}^m - \mathbf{p}^n$, equation (A.18) becomes

$$\mathbf{u}^m + \frac{2}{3}\delta t\mathbf{T}^n\mathbf{u}^m + \frac{2}{3}\delta t\mathbf{D}\delta\mathbf{p}^m = -\delta t\mathbf{D}\mathbf{p}^n + \mathbf{S}, \tag{A.19}$$

where m represents an intermediate time level between $n+1$, at which the solution is sought, and n, the most recent update.

Applying an approximate factorisation, equation (A.19) can be recast as

$$(\mathbf{I} + \frac{2}{3}\delta t\mathbf{T}^n)\underbrace{(\mathbf{u}^m + \frac{2}{3}\delta t\mathbf{D}\boldsymbol{\Delta}\mathbf{p}^m)}_{\mathbf{u}^*} = -\frac{2}{3}\delta t\mathbf{D}\mathbf{p}^n + \mathbf{S}. \tag{A.20}$$

A Taylor series analysis gives, $\mathbf{D}\boldsymbol{\Delta}\mathbf{p}^m \sim O(\delta t)$. So, the error introduced by the approximate factorisation is $(\delta t)^2\mathbf{T}^n\mathbf{D}\boldsymbol{\Delta}\mathbf{p}^m \sim O(\delta \mathbf{t})^3$ and can be neglected. The equation (A.20) is then solved in two steps:

$$\mathbf{u}^* = (\mathbf{I} + \frac{2}{3}\delta t\mathbf{T}^n)^{-1}(-\frac{2}{3}\delta t\mathbf{D}\mathbf{p}^n + \mathbf{S}) \tag{A.21}$$

$$\mathbf{u}^m = \mathbf{u}^* - \frac{2}{3}\delta t\mathbf{D}\delta\mathbf{p}^m. \tag{A.22}$$

The vectors of unknown v and w nodal values, $\mathbf{v}$ and $\mathbf{w}$, are obtained in the similar way. However, none of these velocity fields at time level m can be obtained since $\Delta\mathbf{p}^m$ is not known.

In order to obtain the pressure increment, $\Delta\mathbf{p}^m$, the velocity fields $\mathbf{u}^m$, $\mathbf{v}^m$ and $\mathbf{w}^m$ are subsituted into the continuity equation, which gives a Poisson-type equation for the pressure increment and this will be discussed in the following subsection.

Since $\mathbf{u}^m$ is a 2nd order accurate approximation to $\mathbf{u}^{n+1}$, in the second stage, a second order accurate solution at the time level $n+1$ is obtained by rewriting the equation (A.19) for the time level $n+1$, with the coefficient matrix evaluated using values from the intermediate time level m,

$$\mathbf{u}^{n+1} + \frac{2}{3}\delta t\mathbf{T}^m\mathbf{u}^{n+1} + \frac{2}{3}\delta t\mathbf{D}\boldsymbol{\Delta}\mathbf{p}^{n+1} = -\frac{2}{3}\delta t\mathbf{D}\mathbf{p}^m + \mathbf{S}, \tag{A.23}$$

where the pressure increment, $\Delta\mathbf{p}^{n+1} = \mathbf{p}^{n+1} - \mathbf{p}^{m}$, is introduced. Using the approximate factorisation, equation (A.23) is written as,

$$(\mathbf{I} + \frac{2}{3}\delta t\mathbf{T}^{m})\underbrace{(\mathbf{u}^{n+1} + \frac{2}{3}\delta t\mathbf{D}\boldsymbol{\Delta}\mathbf{p}^{n+1})}_{\mathbf{u}^{**}} = -\frac{2}{3}\delta t\mathbf{D}\mathbf{p}^{m} + \mathbf{S}. \tag{A.24}$$

$$\mathbf{u}^{**} = (\mathbf{I} + \frac{2}{3}\delta t\mathbf{T}^{m})^{-1}(-\frac{2}{3}\delta t\mathbf{D}\mathbf{p}^{m} + \mathbf{S}) \tag{A.25}$$

$$\mathbf{u}^{n+1} = \mathbf{u}^{**} - \frac{2}{3}\delta t\mathbf{D}\boldsymbol{\Delta}\mathbf{p}^{n+1}. \tag{A.26}$$

The pressure increment is again computed from the Poisson-type equation which will be discussed in the next section.

A.3.1 Pressure Smoothing

As mentioned in the previous section, a Poisson-like equation for the pressure increment, now defined as $\Delta p^{m} = p^{m} - p^{m-1}$, where $m-1$ indicates the most recent calculated values and m the intermediate time level at which the solution being sought, is obtained by substituting equation (A.21) in the continuity equation. For illustration purpose, considering only the flux component arisen from the integration over the cell faces in the ξ direction, this substitution gives

$$\begin{aligned}\frac{2\delta t}{3}\left[\frac{A_{1j}A_{kj}}{|\mathbf{J}|}\frac{\partial\Delta p^{m}}{\partial\xi_{k}}\right]_{I+\frac{1}{2},J,K} - \frac{2\delta t}{3}\left[\frac{A_{1j}A_{kj}}{|\mathbf{J}|}\frac{\partial\Delta p^{m}}{\partial\xi_{k}}\right]_{I-\frac{1}{2},J,K} \\ = \left[\rho A_{1j}u_{j}^{m-1}\right]_{I+\frac{1}{2},J,K} - \left[\rho A_{1j}u_{j}^{m-1}\right]_{I-\frac{1}{2},J,K},\end{aligned} \tag{A.27}$$

where u_{j}^{m-1} is the velocity field corresponding to the pressure field p^{m-1}. Using the central difference interpolated onto cell faces, for instance, the pressure increment gradient at $I+\frac{1}{2}, J, K$ is approximated by

$$\begin{aligned}\left[\frac{A_{kj}}{|\mathbf{J}|}\frac{\partial\Delta p^{m}}{\partial\xi_{k}}\right]_{I+\frac{1}{2},J,K} = \frac{1}{2}\left[\frac{A_{kj}}{|\mathbf{J}|}\right]_{I+\frac{1}{2},J,K} \\ \left(\left[\frac{\partial\Delta p^{m}}{\partial\xi_{k}}\right]_{I+1,J,K} + \left[\frac{\partial\Delta p^{m}}{\partial\xi_{k}}\right]_{I,J,K}\right),\end{aligned} \tag{A.28}$$

where

$$\left[\frac{A_{kj}}{|\mathbf{J}|}\right]_{I+\frac{1}{2},J,K}\left[\frac{\partial\Delta p^m}{\partial\xi_k}\right]_{I,J,K} = \left[\frac{A_{1j}}{|\mathbf{J}|}\right]_{I+\frac{1}{2},J,K}\left(\frac{\Delta p^m_{I+1,J,K}-\Delta p^m_{I-1,J,K}}{2}\right) + \left[\frac{A_{2j}}{|\mathbf{J}|}\right]_{I+\frac{1}{2},J,K}\left(\frac{\Delta p^m_{I,J+1,K}-\Delta p^m_{I,J-1,K}}{2}\right) + \left[\frac{A_{3j}}{|\mathbf{J}|}\right]_{I+\frac{1}{2},J,K}\left(\frac{\Delta p^m_{I,J,K+1}-\Delta p^m_{I,J,K-1}}{2}\right), \quad \text{(A.29)}$$

The above interpolations lead to an oscillatory pressure field which is decoupled from the velocity field at even and odd grid nodes. To remedy this problem, the finite difference operators are redefined so that pressure increment derivatives normal to the cell faces are evaluated using values at nodes adjacent to the cell faces, and the cross derivatives interpolated from gradients calculated at adjacent nodes, giving

$$\left[\frac{A_{kj}}{|\mathbf{J}|}\frac{\partial\Delta p^m}{\partial\xi_k}\right]_{I+\frac{1}{2},J,K,1\delta} = \left[\frac{A_{1j}}{|\mathbf{J}|}\right]_{I+\frac{1}{2},J,K}\left(\Delta p^m_{I+1,J,K}-\Delta p^m_{I,J,K}\right) + \left[\frac{A_{2j}}{|\mathbf{J}|}\right]_{I+\frac{1}{2},J,K}\left(\frac{\Delta p^m_{I+1,J+1,K}-\Delta p^m_{I-1,J-1,K}+\Delta p^m_{I,J+1,K}-\Delta p^m_{I,J-1,K}}{4}\right) + \left[\frac{A_{3j}}{|\mathbf{J}|}\right]_{I+\frac{1}{2},J,K}\left(\frac{\Delta p^m_{I+1,J,K+1}-\Delta p^m_{I-1,J,K-1}+\Delta p^m_{I,J,K+1}-\Delta p^m_{I,J,K-1}}{4}\right) \quad \text{(A.30)}$$

where the subscript 1δ denotes the compact stencil. It can be demonstrated that this approach is equivalent to adding a smoothing term, $\sigma(\Delta p^m)$, to the RHS of equation (A.27), of the form

$$\sigma(\Delta p^m) = \frac{2\delta t}{3}\left\{\left[\frac{A_{1j}A_{kj}}{|\mathbf{J}|}\frac{\partial\Delta p^m}{\partial\xi_k}\right]_{I+\frac{1}{2},J,K} - \left[\frac{A_{1j}A_{kj}}{|\mathbf{J}|}\frac{\partial\Delta p^m}{\partial\xi_k}\right]_{I+\frac{1}{2},J,K,1\Delta} + \left[\frac{A_{1j}A_{kj}}{|\mathbf{J}|}\frac{\partial\Delta p^m}{\partial\xi_k}\right]_{I-\frac{1}{2},J,K,1\Delta} - \left[\frac{A_{1j}A_{kj}}{|\mathbf{J}|}\frac{\partial\Delta p^m}{\partial\xi_k}\right]_{I-\frac{1}{2},J,K,1\Delta}\right\} \quad \text{(A.31)}$$

This smoothing term involves known and unknown components, and can be written as

$$\sigma(\Delta p^m) = \sigma(p^m) - \sigma(p^{m-1}). \quad \text{(A.32)}$$

The Rhie and Chow [133] approach is to add the unknown term, $\sigma(p^m)$, to the RHS of the equation (A.27). Adding this unknown term, the pressure increment equation becomes,

$$\frac{2\delta t}{3}\left[\frac{A_{1j}A_{kj}}{|\mathbf{J}|}\frac{\partial \Delta p^m}{\partial \xi_k}\right]_{I+\frac{1}{2},J,K,1\Delta} - \frac{2\delta t}{3}\left[\frac{A_{1j}A_{kj}}{|\mathbf{J}|}\frac{\partial \Delta p^m}{\partial \xi_k}\right]_{I-\frac{1}{2},J,K,1\Delta} = \left[\rho A_{1j}u_j^{m-1}\right]_{I+\frac{1}{2},J,K} - \left[\rho A_{1j}u_j^{m-1}\right]_{I-\frac{1}{2},J,K} + \frac{2\delta t}{3}\left\{\left[\frac{A_{1j}A_{kj}}{|\mathbf{J}|}\frac{\partial p^{m-1}}{\partial \xi_k}\right]_{I+\frac{1}{2},J,K} - \left[\frac{A_{1j}A_{kj}}{|\mathbf{J}|}\frac{\partial p^{m-1}}{\partial \xi_k}\right]_{I+\frac{1}{2},J,K,1\Delta} + \left[\frac{A_{1j}A_{kj}}{|\mathbf{J}|}\frac{\partial p^{m-1}}{\partial \xi_k}\right]_{I-\frac{1}{2},J,K} - \left[\frac{A_{1j}A_{kj}}{|\mathbf{J}|}\frac{\partial p^{m-1}}{\partial \xi_k}\right]_{I-\frac{1}{2},J,K,1\Delta}\right\}. \quad \text{(A.33)}$$

The mass flux, for instance at $I+\frac{1}{2}, J, K$, is then updated from

$$\left[\rho A_{1j}u_j^m\right]_{I+\frac{1}{2},J,K} = \left[\rho A_{1j}u_j^{m-1}\right]_{I+\frac{1}{2},J,K} + \frac{2\delta t}{3}\left\{\left[\frac{A_{1j}A_{1j}}{|\mathbf{J}|}\frac{\partial p^{m-1}}{\partial \xi_k}\right]_{I+\frac{1}{2},J,K} - \left[\frac{A_{1j}A_{1j}}{|\mathbf{J}|}\frac{\partial p^{m-1}}{\partial \xi_k}\right]_{I+\frac{1}{2},J,K,1\Delta}\right\} + \frac{2\delta t}{3}\left[\frac{A_{1j}A_{1j}}{|\mathbf{J}|}\frac{\partial \Delta p^m}{\partial \xi_k}\right]_{I-\frac{1}{2},J,K,1\Delta} \quad \text{(A.34)}$$

and the velocity field stored at the cell centres is updated from the original discrete approximation, so that

$$\left[u_j^m\right]_{I,J,K} = \left[u_j^{m-1}\right]_{I,J,K} - \frac{2\delta t}{3}\left[\frac{A_{kj}}{|\mathbf{J}|}\frac{\partial \Delta p^m}{\partial \xi_k}\right]_{I,J,K}. \quad \text{(A.35)}$$

A.3.2 Solution Algorithm and Convergent Condition

The system of algebraic equations resulting from the above discretisation are solved according to the folloing algorithm:

- Compute $\mathbf{u}^*$, $\mathbf{v}^*$ and $\mathbf{w}^*$ from equation (A.21) using most recently updated $\mathbf{G}^n$ and $\mathbf{p}^n$.

- Solve for $\Delta\mathbf{p}^m$ from equation (A.33) with Rhie and Chow [133] pressure smoothing.
- Update mass fluxes and velocities using equations (A.34) and (A.35) respectively to obtain $\mathbf{G}^m$, $\mathbf{u}^m$, $\mathbf{v}^m$ and $\mathbf{w}^m$.

- Compute $\mathbf{u}^{**}$, $\mathbf{v}^{**}$ and $\mathbf{w}^{**}$ from equation (A.25) using the updated $\mathbf{G}^m$ and $\mathbf{p}^m$.
  - Solve for $\Delta\mathbf{p}^{n+1}$ from equation (A.33) with Rhie and Chow [133] pressure smoothing.
  - Update mass fluxes and velocities using equations (A.34) and (A.35) respectively to obtain $\mathbf{G}^{n+1}$, $\mathbf{u}^{n+1}$, $\mathbf{v}^{n+1}$ and $\mathbf{w}^{n+1}$.

The maximum residuals, representing the errors associated with the entire solution procedure, are calculated within the solvers as a part of the solution procedure. For velocity, the normalised residual is,

$$||\mathbf{u}^{n+1}||^{\#} = \frac{t^{\#}\left(R^{u}_{ijk}\right)_{max}}{\left[max\left(\rho^2 u^2_{ijk} + \rho^2 v^2_{ijk} + \rho^2 w^2_{ijk}\right)\right]^{1/2}}, \tag{A.36}$$

where the time scale $t^{\#}$ depends on the flow under investigation and is defined using a length and a velocity scale representative of conditions at the inlet; ijk represents the location in the computational domain. The normalised residual for the pressure increment is

$$||\Delta\mathbf{p}^{n+1}||^{\#} = \frac{t^{\#}\left(R^{p}_{ijk}\right)_{max}}{\left(\frac{1}{N_{grid}}\sum_{N_{grid}}\rho^2\right)^{1/2}}, \tag{A.37}$$

where N_{grid} is the total number of grid points. Here R^{u}_{ijk} and R^{p}_{ijk} are the dimensional residuals for the velocity and pressure respectively.

The momentum equations are iterated until $||\mathbf{u}^{n+1}||^{\#} < 10^{-7}$. The tolerance for the pressure increment equation is reduced so that the iterative procedure does not terminate until $||\Delta\mathbf{p}^{n+1}||^{\#} < 10^{-8}$. For clarity, a separate list of symbols for this appendix is given in §B.3.

Appendix B

Physiological Flow

The physiological pulsatile velocity profile is obtained from the solution of a one-dimensional Navier-Stokes equation where the pressure gradient is the Fourier series of time. Womersley [6] first calculated the physiological velocity profile for a tube by using this pressure gradient. A similar approach has been applied by Loudon and Tordesillas [144] to calculate the physiological pulsatile velocity profiles between the two parallel flat plates. Some calculations for the physiological solutions are given below.

B.1 Physiological Flow Solution

Following [6] and [144], a one dimensional equation is considered as

$$\frac{\partial^2 \bar{v}}{\partial x^2} - \frac{\rho}{\mu}\frac{\partial \bar{v}}{\partial t} = \frac{1}{\mu}\frac{\partial \bar{p}}{\partial y}, \quad 0 \leq x \leq L \tag{B.1}$$

where

$$\frac{\partial \bar{p}}{\partial y} = \frac{2}{3}A_0 + A\sum_{n=1}^{NH} M_n e^{i(n\omega t + \phi_n)}. \tag{B.2}$$

Here A_0 and A are the constants corresponding to the steady and oscillatory pressure gradient, M_n and ϕ_n are the respective coefficients and the phase angle of the different harmonics, which are known from Womersley [6], N is the number of harmonics and $\omega = \frac{2\pi}{T}$ is the frequency of the unsteady flow. After solving eq. (B.1), the solution takes the following form:

$$\bar{v}(x,t) = 4\bar{V}_{max}\frac{x}{L}\left(1-\frac{x}{L}\right) + A\sum_{n=1}^{NH}\frac{iM_nL^2}{\mu\alpha^2 n}$$
$$\left[\cosh(\alpha\sqrt{in}\frac{x}{L}) - \frac{\cosh(\alpha\sqrt{in})-1}{\sinh(\alpha\sqrt{in})}\sinh(\alpha\sqrt{in}\frac{x}{L}) - 1\right]e^{i(n\omega t+\phi_n)}. \quad \text{(B.3)}$$

The real part of this solution is used as the inlet condition to generate the physiological velocity profiles. In this solution, $\bar{V}_{max}$ is the bulk velocity which depends on the flow Reynolds number defined as $Re = \frac{\bar{V}_{max}L}{\nu}$ and $\alpha = L\sqrt{\frac{\rho\omega}{\mu}}$ is the unsteady Reynolds number or the Womersley number.

B.2 Real Part of the Solution

For separating the real part of the solution (B.3), the De Moivre's theorem of complex numbers is applied with some trigonometric formulas.

De Moivre's theorem:

$$(\cos\theta + i\sin\theta)^m = [\cos(m\theta) + i\sin(m\theta)], \quad \text{(B.4)}$$

If $z = x + iy$, then

$$\sinh z = \sinh x\cos y + i\cosh x\sin y,$$
$$\cosh z = \cosh x\cos y + i\sinh x\sin y, \quad \text{(B.5)}$$

Using the De Moivre's theorem, it can be written as

$$\begin{aligned}\sqrt{i} &= \left[\cos(\frac{\pi}{2}) + i\sin(\frac{\pi}{2})\right]^{\frac{1}{2}} \\ &= \left[\cos(\frac{\pi}{4}) + i\sin(\frac{\pi}{4})\right] \\ &= \frac{1}{\sqrt{2}}(1+i) \end{aligned} \quad \text{(B.6)}$$

So,

$$\begin{aligned}\cosh\left(\alpha\sqrt{in}\frac{x}{L}\right) &= \cosh\left[\alpha\sqrt{n}\frac{1}{\sqrt{2}}(1+i)\frac{x}{L}\right] \\ &= \cosh\left(\alpha\frac{x}{L}\sqrt{\frac{n}{2}}\right)\cos\left(\alpha\frac{x}{L}\sqrt{\frac{n}{2}}\right) \\ &+i\sinh\left(\alpha\frac{x}{L}\sqrt{\frac{n}{2}}\right)\sin\left(\alpha\frac{x}{L}\sqrt{\frac{n}{2}}\right) \end{aligned} \tag{B.7}$$

and

$$\begin{aligned}\sinh\left(\alpha\sqrt{in}\right) &= \sinh\left[\alpha\sqrt{n}\frac{1}{\sqrt{2}}(1+i)\right] \\ &= \sinh\left(\alpha\frac{x}{L}\sqrt{\frac{n}{2}}\right)\cos\left(\alpha\frac{x}{L}\sqrt{\frac{n}{2}}\right) \\ &+i\cosh\left(\alpha\frac{x}{L}\sqrt{\frac{n}{2}}\right)\sin\left(\alpha\frac{x}{L}\sqrt{\frac{n}{2}}\right) \end{aligned} \tag{B.8}$$

Similarly,

$$\begin{aligned}\cosh\left(\alpha\sqrt{in}\right) &= \cosh\left[\alpha\sqrt{n}\frac{1}{\sqrt{2}}(1+i)\right] \\ &= \cosh\left(\alpha\sqrt{\frac{n}{2}}\right)\cos\left(\alpha\sqrt{\frac{n}{2}}\right) \\ &+i\sinh\left(\alpha\sqrt{\frac{n}{2}}\right)\sin\left(\alpha\sqrt{\frac{n}{2}}\right) \end{aligned} \tag{B.9}$$

and

$$\begin{aligned}\sinh\left(\alpha\sqrt{in}\right) &= \sinh\left[\alpha\sqrt{n}\frac{1}{\sqrt{2}}(1+i)\right] \\ &= \sinh\left(\alpha\sqrt{\frac{n}{2}}\right)\cos\left(\alpha\sqrt{\frac{n}{2}}\right) \\ &+i\cosh\left(\alpha\sqrt{\frac{n}{2}}\right)\sin\left(\alpha\sqrt{\frac{n}{2}}\right) \end{aligned} \tag{B.10}$$

Substituting the relations (B.6-B.10) into Eq. (B.3) and separating the real part,

gives

$$\begin{aligned}\bar{v}(x,t) = {} & 4\bar{V}_{max}\frac{x}{L}\left(1-\frac{x}{L}\right) \\ & + A\sum_{n=1}^{4}\frac{M_n L^2}{\mu\alpha^2 n}\left\{1 - P_1 + D(P_2 - P_3)\right\}\sin(n\omega t + \phi_n) \\ & + A\sum_{n=1}^{4}\frac{M_n L^2}{\mu\alpha^2 n}\left\{D(P_4 - P_5) - P_6\right\}\cos(n\omega t + \phi_n) \end{aligned} \tag{B.11}$$

where

$$P_1 = \cosh\Phi_1 \cos\Phi_1 \tag{B.12}$$

$$P_2 = \sinh\Phi_1 \sinh\Phi_2 \cos\Phi_1 \tag{B.13}$$

$$P_3 = \sin\Phi_2 \sin\Phi_1 \cosh\Phi_1 \tag{B.14}$$

$$P_4 = \sinh\Phi_1 \sin\Phi_2 \cos\Phi_1 \tag{B.15}$$

$$P_5 = \sinh\Phi_2 \sin\Phi_1 \cosh\Phi_1 \tag{B.16}$$

$$P_6 = \sinh\Phi_1 \sin\Phi_1 \tag{B.17}$$

$$Dr = \sinh^2\Phi_2 \cos^2\Phi_2 + \cosh^2\Phi_2 \sin^2\Phi_2 \tag{B.18}$$

$$Nr = \cosh\Phi_2 - \cos\Phi_2 \tag{B.19}$$

$$D = \frac{Nr}{Dr} \tag{B.20}$$

$$\Phi_1 = \alpha\frac{x}{L}\sqrt{\frac{n}{2}} \tag{B.21}$$

$$\Phi_2 = \alpha\sqrt{\frac{n}{2}} \tag{B.22}$$

B.3 List of Symbols for Appendix A and B

Roman Symbols

a_α	coefficients in discretisation equations
A	amplitude of the physiological oscillation, m
$\mathbf{A}$	matrix of cofactors of Jacobian matrix
A_{ij}	elements of $\mathbf{A}$
$\mathbf{D}$	pressure term coefficient matrix
$\mathbf{G}$	mass fluxes vector
G_k	mass flux in ξ_k coordinate direction
$\mathbf{I}$	identity matrix
I, J, K	grid indexes
$\mathbf{J}$	Jacobian matrix of coordinate transformation
J_{ij}	elements of $\mathbf{J}$
m	intermediate time level
n	time level
$\mathbf{P}$	vector of nodal pressure values
$\mathbf{S}$	source term vector
S_α	source term in discretisation equations
t	time
$\mathbf{T}$	convective and diffusive terms coefficient matrix
u	a constant convective velocity
u_i	velocity component, m/s
$\mathbf{u}, \mathbf{v}, \mathbf{w}$	vectors of velocity components
$\mathbf{u}^\star, \mathbf{v}^\star, \mathbf{w}^\star$	vectors of intermediate velocity components
$\mathbf{u}^{\star\star}, \mathbf{v}^{\star\star}, \mathbf{w}^{\star\star}$	vectors of intermediate velocity components
x_i	physical space coordinates, m

Greek Symbols

α	Womersley number
δt	time step
ΔV	computational cell volume
ΔS	computational cell surface

$\Delta\xi$	mesh specing in computational space
Δp	pressure increment
$\Delta\mathbf{p}$	vector of nodal pressure increments
μ	molecular viscosity, $kg.m^{-1}.s^{-1}$
μ_e	effective viscosity, $kg.m^{-1}.s^{-1}$
μ_{sgs}	subgrid scale eddy viscosity, $kg.m^{-1}.s^{-1}$
ξ_i	computational space coordinates
ρ	density, kg/m^3
σ	pressure smoothing term
ϕ_n	phase angle of the physiological oscillation

Mathematical Accents

$\bar{.}$	spatial filtering
$\|.\|$	determinant
$\|\|.\|\|$	norm

Appendix C

Publications and Presentations

Publications

1. **Md. Mamun Molla**, Manosh C. Paul: LES of additive and non-additive pulsatile flows in a model arterial stenosis, *Computer Methods in Biomechanics and Biomedical Engineering (2009) (In press)*.

2. Manosh C. Paul, **Md. Mamun Molla**, Giles Roditi: LES of Blood Flow Simulation, *Medical Engineering and Physics, 31 (2009) 153-159* .

3. **Md. Mamun Molla**, Manosh C. Paul, Giles Roditi: Physiological Flow in a Model stenosis, *Journal of Biomechanics, 41(S1) (2008) S243*.

4. **Md. Mamun Molla**, Manosh C. Paul: A Study of Transition to Turbulent flow in a model arterial stenosis using Large Eddy Simulation. *Theoretical and Computational Fluid Dynamics,(2009) (submitted)*.

5. **Md. Mamun Molla**, Manosh C. Paul: LES of physiological pulsatile flow in a model of arterial stenosis. Part 1. Results of the first harmonic pressure pulse, *(In preparation for the International Journal)*.

6. **Md. Mamun Molla**, Manosh C. Paul: LES of Physiological pulsatile flow in a model of arterial stenosis. Part 2. Effects of various harmonics, *(In preparation the International Journal)*.

7. **Md. Mamun Molla**, Manosh C. Paul: Physiological pulsatile flow through a double stenosis using LES, *(In preparation the International Journal)*.

8. **Md. Mamun Molla**, Manosh C. Paul: LES of physiological pulsatile flow through a model aneurysm, *(In preparation the International Journal).*

9. **Md. Mamun Molla**, Manosh C. Paul: Physiological pulsatile non-Newtonian flow in a model arterial stenosis, *(Accepted by the* 1^{st} *International Conference on Mathematical and Biomedical Engineering-CMBE2009, Swansea, UK).*

Conference/Seminar Presentations

1. LES of Physiological Pulsatile Flow in a Model Stenosis, Presented in the *7th EUROMECH Fluid Mechanics Conference 2008 (EFMC7 2008)*, Manchester, UK, 14-18 September 2008

2. Physiological Pulsatile Flow in a Model Stenosis, Presented in the *16th European Congress Society of Biomechanics (ESB 2008)*, Lucerne, Switzerland, 6-9 July 2008

3. Transition to Turbulent Pulsatile Flow in a Model Stenosis Using Large eddy Simulation, Presented in the *1st Postgraduate Engineering Conference 2007*, University of Glasgow, UK, 30 April-1 May 2007

4. Large Eddy Simulation on the Pulsatile Flow in a Model Stenosis, Presented in the Colloquium, Department of Mechanical Engineering, University of Glasgow, June 2006.

5. Transition to Turbulent Blood Flow Simulation in a Model Stenosis using LES, Presented a poster in the *9th British Applied Mathematics Colloquium 2006*, Keele University, UK, 24-27 April 2006